DOCTOR OF PHILOSOPHY

High-Speed Optical Sampling Techniques Enabled By Ultrafast Semiconductor Lasers

Bajek, David J.

Award date:
2016

HIGH-SPEED OPTICAL SAMPLING TECHNIQUES ENABLED BY ULTRAFAST SEMICONDUCTOR LASERS

David J. Bajek

A thesis submitted for the degree of Doctor of Philosophy

University of Dundee

December 2016

For my wife,

and our beautiful children

CONTENTS

ACKNOWLEDGEMENTS

From a very young age it has been my dream to become a scientist. As the years passed, and I gradually progressed down the long winding road, I came to regard the PhD as one of the most defining achievements of a scientist's career, representing an incredible journey of discovery – and it has not disappointed. I feel truly honoured to be in the position to earn not just this degree, but the incredible opportunities which came with it. I have travelled the world in my journey during both my Masters in Astrophysics in St Andrews and my PhD here in Dundee, and have witnessed the birth of incredible new research in some fantastic academic institutions. I have met people with immense talent and outstanding commitment to their fields who I am proud to call my friends, and have learned more about life, the Universe, and myself due to these unforgettable experiences.

Firstly, my thanks to the EPSRC Doctoral Training Account and Philip Leverhulme Prize (Leverhulme Trust, PLP-2011-172) which funded this project, and therefore not only all the original science and research that resulted, but also all the fantastic experiences gained.

My sincere appreciation goes out to all staff and students who have made this experience so special at the University of Dundee, but in particular to my supervisor, Maria Ana Cataluna. There is no mistaking her extensive knowledge, intuition and dedication to her field. For their invaluable moral support I would like to also thank Paul Campbell, Steve Reynolds, David McGloin, Mike MacDonald, David Keeble, Sam Swift, Kees Weijer, Amin Abdolvand, Alan Gillespie, and Keith Wilcox. To my friends; Lauren Fleming, Stella Corsetti, Claire Davies, Stephen Grant and especially Adam Forrest - the sheer amount I have laughed with you all these last years has made every struggle worthwhile.

I would also like to thank my family; my brothers Andrew, Stephen and Michael, my sister Janine, and my nephews Marcus and Jaxon for their love and support throughout. In particular I would like to send my love to my parents, Henryk and Jane, who during my childhood had a bigger part in fuelling my scientific career than they may realise. My mother would bring me junior chemistry sets, microscopes and slides with organisms to view, whilst my father would take me on regular trips to Dundee's Mill's Observatory and encourage me with my very own telescope. Unconsciously, these moments opened my

eyes to the importance of questioning the world around me, and without a doubt paved the way to my love of both physics and astronomy. Thank you, from the bottom of my heart, for a creative, curious and open-minded start to life. I would like to proudly mention my grandparents, Henryk and Evelyn Bajek (née Davidson) and Stephen and Margaret Dempster (née MacAulay), who in their own individual wonderful ways have given me a lifetime of unconditional love and encouragement in pursuing a career which, above all else, simply makes me happy. To my Father-In-Law, James (Jim) Johnson, I would like to thank you for all the love and support you have given us all the way from the United States, and to my soon-to-be Mother-In-Law, Soosan (Suzi) Najafabadi, I would like to welcome you to the whole family; we love you both dearly.

For my beautiful wife, Kyle, there are no words to fully express my eternal gratitude and love for her unending support, untiring encouragement, inexhaustible patience and utterly selfless spirit in guiding me through this journey in my life. She has been there every minute of every day without a break; always ready to listen, to soothe and to love. I can only hope to repay her for everything she has brought to my life, by spending the rest of mine making her dreams come true too. During this project our lives were made complete by the birth of both of our daughters, Alice Evelyn Bajek, born on the 4th of October 2014, and Violet Jane Bajek, born on the 1st of March 2016. There is no question that this new chapter was yet another boost for the project, knowing that before I left for the lab in the morning, and when I returned home from the office, theirs would be the gorgeous smiling faces waiting for me. I don't think it is possible to beat that type of motivation; to work as hard as possible to make your darling daughters proud of you, to want to succeed and give yourself the best chance of providing for your family. Beautiful girls, you made all the difficult times more than worth it, and you made all of the good times the best times. I spent many days and nights in the laboratory and writing in the office looking at your pictures and imagining the life of adventures awaiting you. And so to my wife and all my children: I love you all, always and forever.

DECLARATION

I, David Bajek, hereby declare that this thesis has been compiled by me, that it is a record of work completed by me, all references cited have been consulted by me and that it has not previously been accepted for a higher degree at this University or any other institution of learning.

David J. Bajek

I state that the condition of the relevant ordinance and regulations have been fulfilled

Maria Ana Cataluna (supervisor)

ABSTRACT

In this thesis, novel optical sampling techniques are theorised and demonstrated using quantum dot two-section passively mode-locked laser diodes (MLLDs) as an inexpensive and compact source of ultrashort light pulses on the order of a few picoseconds duration.

The first technique, OSBERT (Optical Sampling By Electronic Repetition-Rate Tuning) is a single-laser optical sampling technique which was demonstrated using a MLLD whose repetition rate may be modulated electronically by varying the reverse bias applied to the saturable absorber section, whilst a constant forward bias is applied to the gain section. This is compared to standard repetition rate tuning which is typically performed by varying an internal or external laser cavity length, often using a motorised mirror. Splitting the pulse train into two copies and directing them through a highly imbalanced Michelson interferometer then gives rise to a temporal scan range which is proportional to the repetition rate modulation, scaled by the length of the passive delay line (the longer of the two interferometer arms). The technique was proven as an entirely non-mechanical alternative to traditional motorised translation stage methods of optical sampling as both a single and a two-photon absorption cross-correlator. Whilst scan ranges of up to 200ps were realised, the OSBERT method also successfully demonstrated distance measurements at scan rates of 10kHz, where target displacements between 100µm and 1.0mm were detected at effective free-space distances of over 3m and 36m respectively, exhibiting accuracies of 10µm and 100µm respectively. Finally, the ability to detect cross-correlations at up to 1MHz scan rates was shown, suggesting great potential for MHz level scan rates under future development.

The second technique, SLECOPS (Single Laser Electronically Controlled OPtical Sampling) was developed from a theoretical basis. Whilst OSBERT is a technique specifically invented for the use of MLLDs, SLECOPS is potentially suited to any type of laser whose repetition rate may be varied via square wave modulation, and thus could be adopted by a vast variety of laser systems and their respective optical sampling applications. The theory outlines the potential to contend with the OSBERT technique in scan rate and in minimising characteristic laser output differences between pulse pairs used during each cross-correlation event.

SLECOPS is particularly interesting in that the technique involves asynchronous-type scanning (such as that used in two-laser sampling systems such as Asynchronous Optical Sampling and Electronically Controlled Optical Sampling) but uses only one laser. This led to the conceptualisation of the ‘virtual laser’, where just one laser can be said to function as two within the context of optical sampling.

The selectable scan range and competitive scan rates of both OSBERT and SLECOPS as single laser optical sampling techniques thus pave the way for two section passively MLLDs to be deployed in fast, low-cost and compact optical sampling systems.

LIST OF PUBLICATIONS

The work published and presented at conferences related to and during this project are referenced here for citation throughout the thesis, numbered 1 – 6 when used.

Peer-Reviewed Publications

[1] Li, M.F., Ni, H.Q, Ding, Y., Bajek, D., Kong, L., Cataluna, M.A., and Niu, Z.C., *Optimization of InAs/GaAs quantum-dot structures and application to 1.3-μm mode-locked laser diodes.* Chinese Physics B, 2014. **23**(2): p. 027803.

[2] Wang, H.L., Kong, L., Forrest, A.F., Bajek, D., Haggett, S., Wang, X., Cui, B.F, Pan, J.Q., Ding, Y., Cataluna, M.A., *Ultrashort pulse generation by semiconductor mode-locked lasers at 760 nm*. Optics Express, 2014. 22(21): p. 25940-25946.

[3]Kong, L., Wang, H.L., Bajek, D., White, S.E., Forrest, A.F., Wang, X.L., Cui, B.F., Pan, J.Q., Ding, Y., and Cataluna, M.A., *Deep-red semiconductor monolithic mode-locked lasers.* Applied Physics Letters, 2014. **105**(22): p. 221115.

Peer-Reviewed Conference Contributions

[4] Kong, L., Wang, H., Bajek, D., Haggett, S., Forrest, A., Wang, X., Cui, B., Pan, J., Ding, Y., Cataluna, M. A., *Semiconductor monolithic mode-locked laser for ultrashort pulse generation at 750 nm*. 24th IEEE International Semiconductor Laser Conference. 2014. Palma de Mallorca, Spain.

[5] Wang, H., Kong, L., Bajek, D., Haggett, S., Wang, X., Cui, B., Pan, J., Ding, Y., Cataluna, M. A., *760-nm Semiconductor Passively Mode-Locked Monolithic Laser for Picosecond Pulse Generation* CLEO: 2013. 2013. San Jose, California: Optical Society of America.

[6] Cataluna, M.A., Ding, Y., White, S.E., Bajek, D., Krakowski, M., *High-power ultrafast and broadly-tunable quantum-dot lasers*. SPIE Photonics West: Quantum Sensing and Nanophotonic Devices XII. 2015. San Francisco; United States.

Posters Presented

Bajek, D. and Cataluna, M. A., *Ultra-Novel Applications of Ultrafast Photonics*, Winter College on Optics: Trends in Laser Development and Multi-disciplinary Applications to Science and Industry, ICTP, Trieste, Italy, 4th February 2013

Bajek, D., Kong, L., Wang, H.L., White, S.E., Forrest, A.F., Wang, X.L., Cui, B.F., Ding, Y., Cataluna, M.A., *Deep-Red Semiconductor Monolithic Mode-Locked Lasers*, Annual SU2P Symposium, University of St Andrews, Scotland, 23rd March 2015

Papers for publication which are currently in draft:

Bajek, D., Cataluna, M.A., *OSBERT: Optical Sampling by Electronic Repetition-Rate Tuning*

Bajek, D., Cataluna, M.A., *SLECOPS: Single Laser Electronic Optical Sampling*

Patents for submission which are currently in draft:

Bajek, D., and Cataluna, M.A., *SLECOPS: Single Laser Electronically Controlled Optical Sampling*, 2015

Bajek, D., and Cataluna, M.A., *OSBERT: Optical Sampling By Electronic Repetition-Rate Tuning*, 2015

LIST OF ABBREVIATIONS

AC	Autocorrelation
AlGaAs	Aluminium Gallium Arsenide
AR	Anti-Reflective
ASOPS	Asynchronous Optical Sampling
ECOPS	Electronically Controlled Optical Sampling
EM	Electromagnetic
EOS	Electro-Optic Sampling
EPSRC	Engineering and Physical Sciences Research Council
FFT	Fast Fourier Transform
FWHM	Full-Width at Half-Maximum
GaAs	Gallium Arsenide
GSLD	Gain Switched Laser Diode
InAs	Indium Arsenide
IR	Infra-Red
LD	Laser diode
MLLD	Mode-Locked Laser Diode
MOCVD	Metal Organic Chemical Vapour Deposition
ND	Neutral density
OSBERT	Optical Sampling By Electronic Repetition Rate Tuning
OSCAT	Optical Sampling by Cavity Tuning
OSREFM	Optical Sampling by Repetition Frequency Modulation
OST	Optical Sampling Technique
PDL	Passive Delay Line
PPS	Pump Probe Spectroscopy
QD	Quantum Dot
QW	Quantum Well
RF	Radio Frequency
SLASOPS	Single-Laser Asynchronous Optical Sampling
SLECOPS	Single-Laser Electronically Controlled Optical Sampling
SNR	Signal-to-Noise Ratio
SOA	Semiconductor Optical Amplifier
TDS	Time Domain Spectroscopy
THz	Terahertz
Ti:Sapp	Titanium Sapphire laser

1. INTRODUCTION

In this chapter, a brief overview of pulsed lasers is discussed, followed by a review of various optical sampling techniques and their achievements in a number of state of the art applications for reference throughout the thesis. A collection of these techniques are contrasted and graphically compared for their scan rates and scan ranges, and the potential for ultrafast semiconductor laser diodes in such systems is discussed. The research goals of the project are defined, and an outline of the thesis structure is provided.

1.1. Ultrafast Photonics Overview

First theorised by Albert Einstein in 1917 [7], the development of the laser since its eventual demonstration in the 1960s [8] has had a formidable impact on the shaping of the scientific world. From surgery and medical imaging, to computing and telecommunications, to distance and speed measurements and weapons and military applications, it is difficult to imagine the modern world without lasers in a great many aspects of even everyday life. In particular, the invention of techniques giving rise to pulsed lasing has led to immense scientific advances in the field of ultrafast photonics, where lasers emit a train of ultrashort pulses of duration $\Delta\tau$ at some repetition rate f_{rep}, rather than continuous wave (cw) emission, see Figure 1-1.

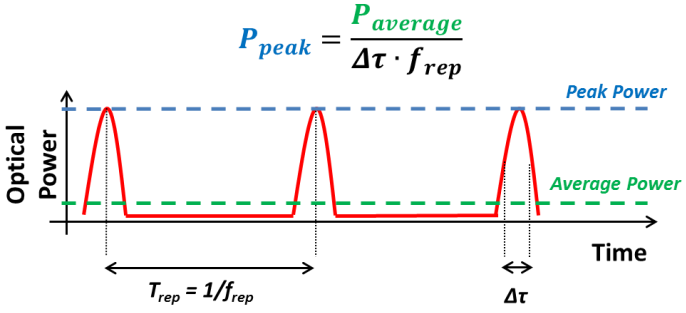

Figure 1-1 – A laser which emits a train of ultrashort pulses does so at some repetition rate f_{rep} giving rise to distinct peak and average optical powers.

In particular, as can be seen, for shorter pulse durations and lower repetition rates, higher peak powers may be accessed, an advantage for reaching high instantaneous excitation energies required for example in non-linear optics (including two photon absorption (TPA) and second and third harmonic generation (SHG and THG)) compared to the equivalent average power of cw emission required. The characteristic pulsed output depends on both

the type of laser and the pulsing technique involved, which among others may include pulsed pumping, gain switching [9], q-switching or mode-locking [10], the latter of which is of particular interest and is discussed in greater detail in chapter 2. Active mode-locking [11] for pulse formation requires an external signal such as an acousto-optic modulator to modulate the intra-cavity dynamics to generate a pulsed output, whilst passive mode-locking [12] involves an optical element such as a saturable absorber [13] or a Kerr lens [14] to be placed within the cavity itself. The ultrashort pulses generated from such techniques are of particular interest because in applications such as time-resolved spectroscopy[15], events occurring over significantly short durations (nanoseconds down to attoseconds) may be studied. As such, the temporal dynamics of biological, chemical or other physical reactions may be imaged, measured and analysed on a time-scale orders of magnitude faster than high speed cameras are capable of, due to the measurement windows being framed by light itself.

Therefore, in recent decades there has been a drive towards the demonstration of ever-shorter light pulse durations, see Figure 1-2. In fact, prior to the invention of the laser, flash lamps were being utilised for timing measurements and even flash photolysis [16], which is an early form of pump-probe spectroscopy. Ultimately, the shorter the pulse produced, the shorter the timescale accessible for scrutiny; to date the shortest pulse of light reported has a 67 attosecond duration [17].

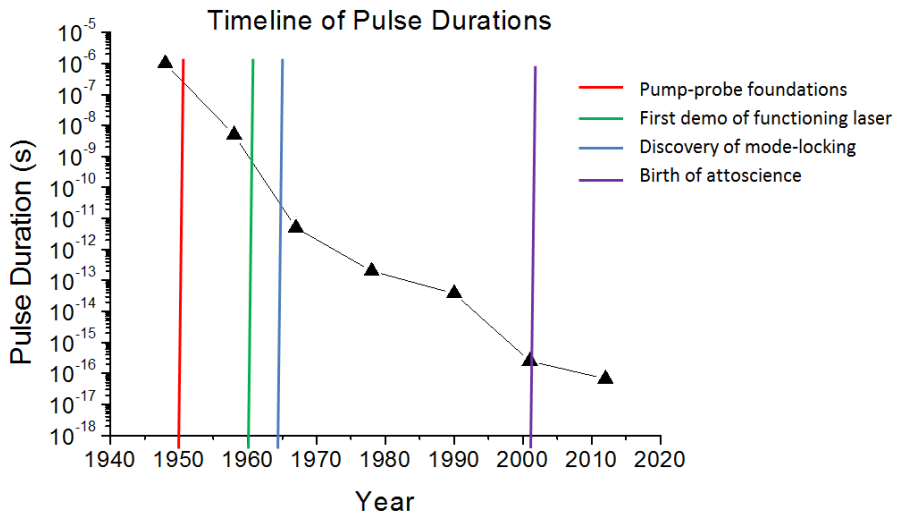

Figure 1-2 - Optical pulse durations decreasing over recent decades alongside several milestones: pump-probe experimental Foundations (flash photolysis) [16], first demonstration of a functioning laser [8], discovery of mode-locking [10], and the birth of Attoscience [18]. Data points in order from left to right: [19-23] [17, 18].

Ultrashort pulses not only come in various intensities and durations, but are produced by a wide variety of competing laser systems and their respective techniques, from highly commercialised doped fibre [24] or Titanium:Sapphire laser systems [25], to the semiconductor-based mode-locked laser diodes (MLLDs) used throughout this project. In contrast, MLLDs offer a highly attractive alternative to the bulk, complexity and expense of such commercial systems. These devices (which may be designed and grown in multiples in a clean room) offer a wide selection in terms of wavelength (which are accessible due to the ability to engineer the bandgap of the semiconductor material [3, 26, 27]), pulse repetition rate, optical power and pulse duration in a significantly more cost-effective and compact package than their commercially available counterparts. Additionally, many solid state lasers must be optically pumped using semiconductor laser diodes, which are then electrically pumped. Due to the vast variety of material composition and structures available, particularly of two-section passively mode-locked laser diodes, their output characteristics are also readily tunable over varying degrees on account of the semiconductor device's response to electrical biasing conditions and operational temperature of each section, discussed further in Chapter 2. If we consider a commercially available system such as the Insight DeepSee+ [28], a Titanium:Sapphire laser with a combined optical parametric oscillator which may access a wide range of wavelengths, we bear in mind that not only do such systems come with a hefty price tag on the order of tens to hundreds of thousands of pounds, but require a complex cooling system and a great deal of electrical power to run. Such a system could conceivably be replaced by an array of versatile semiconductor laser diodes of various wavelengths at a fraction of the cost, operating under superior wall plug efficiency.

As such, *mode-locked laser diodes* are becoming increasingly attractive sources when considered alongside steadily advancing *optical sampling* techniques and *pump-probe* spectroscopy applications within *ultrafast* photonics. The number of occurrences of scientific publication topics which include the above italicised phrases within the 'Web of Knowledge' since the 1950s were plotted per decade alongside the previous plot of decreasing pulse durations, see Figure 1-3.

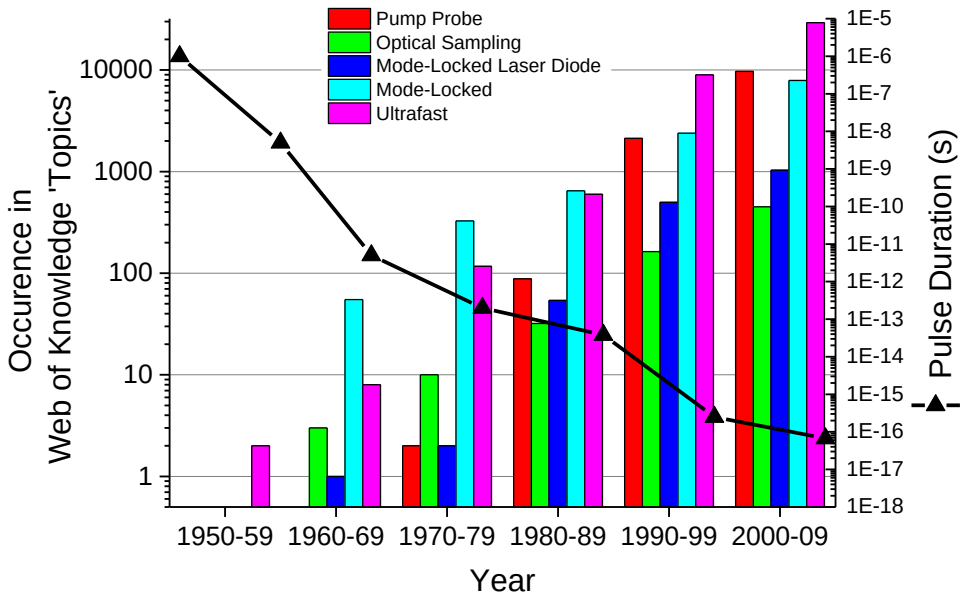

Figure 1-3 - A historical snapshot illustrating the exponential increase in scientific studies involving mode-locked laser diodes, optical sampling and pump probe measurements in the field of ultrafast photonics, alongside the ever-decreasing pulse durations being achieved in the state of the art. .

Delving deeper into the demonstrated applications of such versatile and appealing laser diodes, we find they are being deployed very popularly within optical communications and data communications [29-31], and increasingly so within biophotonics and other biomedical applications [26, 32].

However, limitations in both output powers (on the order a few watts peak power) and pulse durations (of a few picoseconds) mean that such devices are less regularly adopted for such techniques. In addition, the monolithic nature of mode-locked laser diodes as stand-alone lasers tends to give rise to very short cavity lengths, typically producing repetition rates of several GHz, meaning the pulse energy is also limited compared to the several killwatts, femtosecond pulse duration and 80MHz repetition rate of a Titanium:Sapphire system. These drawbacks can, however, be compensated for externally. The output power may be boosted by the use of a Semiconductor Optical Amplifier (SOA), whilst the pulse duration may be compressed, and the cavity length extended to an external cavity operation, leading to greater peak powers, shorter pulse durations, lower repetition rates and consequently greater pulse energies. Such external optics do then, however, detract from the compact and simple nature of a stand-alone monolithic MLLD.

1.2. Motivation and current trends

Many optical sampling techniques have been under rigorous development in recent years due to their major impact in a number of important fields, including applications within attoscience [33], femtochemistry [34], and biomedical sciences [35]. As the work presented in this thesis surrounds the development of optical sampling techniques, several major examples in the field are detailed here for reference throughout the thesis.

Adopting pump-probe spectroscopy as an example of an optical sampling technique, we consider a laser source capable of producing a pulse of light (the pump) typically with a duration that could range between femtoseconds and picoseconds. The pump pulse is directed towards a target of interest, exciting the phenomenon to be observed in the sample, and arrives there at time t_{pump}. A much weaker second pulse (the probe, which for example may originate from a second laser or can be a copy of the pump pulse) follows after a desired delay in time t_{probe} such that $\Delta t = t_{probe} - t_{pump}$, and is used to investigate the effects of the initial pump pulse at this offset time. This process is repeated at a variety of delay times in order to assess the sample's response over the time window of interest known as the scan range; the smaller the delay step-size, the more detail in the response curve, see Figure 1-4.

In addition, it is necessary to differentiate between the pump and probe after interaction with the target sample, which, depending on the setup, could be achieved by introducing a difference in the pump and probe's respective polarisation or wavelength which can potentially remove the pump at the detector if it is passed through an appropriate filter, leaving only the resultant probe available to detect. The technique has been used (among other applications) to probe the ultrafast gain dynamics of semiconductor optical amplifiers [36] as well as the imaging of nodular melanoma in human skin with the potential to map tumour margins during excision [37].

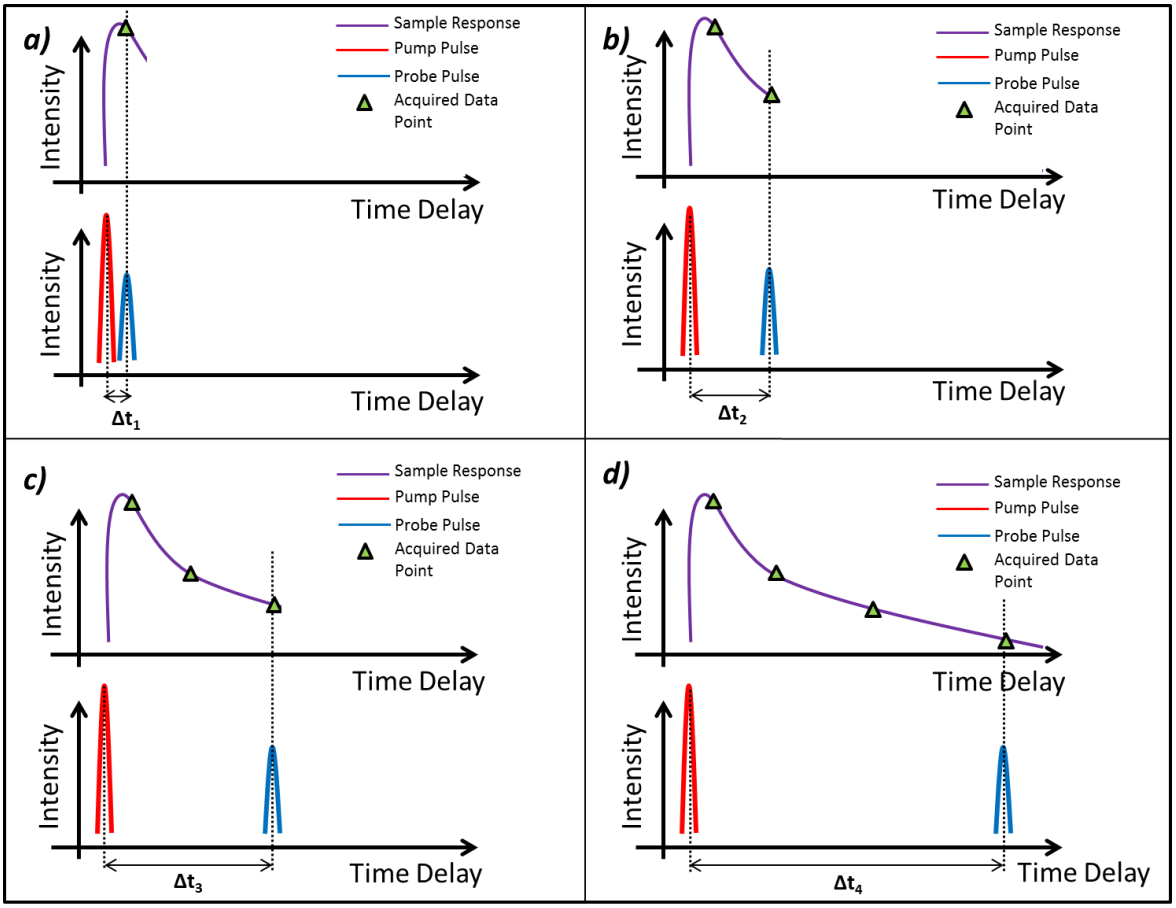

Figure 1-4 – Pump Probe Spectroscopy; the temporal response of a target sample which has been excited by a high intensity pump pulse is sensed by temporally delaying the probe pulse with respect to the pump at increasing time delay intervals, a) to d).

The state of the art is fuelled by a variety of techniques which may be adopted in order to introduce the delay between pump and probe, however most carry drawbacks in terms of cost, complexity, footprint or speed. Conventional delay line methods use an interferometer, where the pulsed beam from a single laser source is split into two paths; the pump is sent directly to the target on a stationary path, while the probe is sent through a variable delay line. If the delay line is composed of a mirror mounted on a mechanical translation stage, the delay between pump and probe interacting with the target may be adjusted from a delay of zero (whereby both arms are of the same length) to the maximum translatable range of the stage, see Figure 1-5. The translation distance in space Δx corresponds with a delay time Δt between pump and probe pulses at the target in the temporal domain such that $\Delta x = \frac{1}{2}\Delta t \cdot c$, where c is the speed of light.

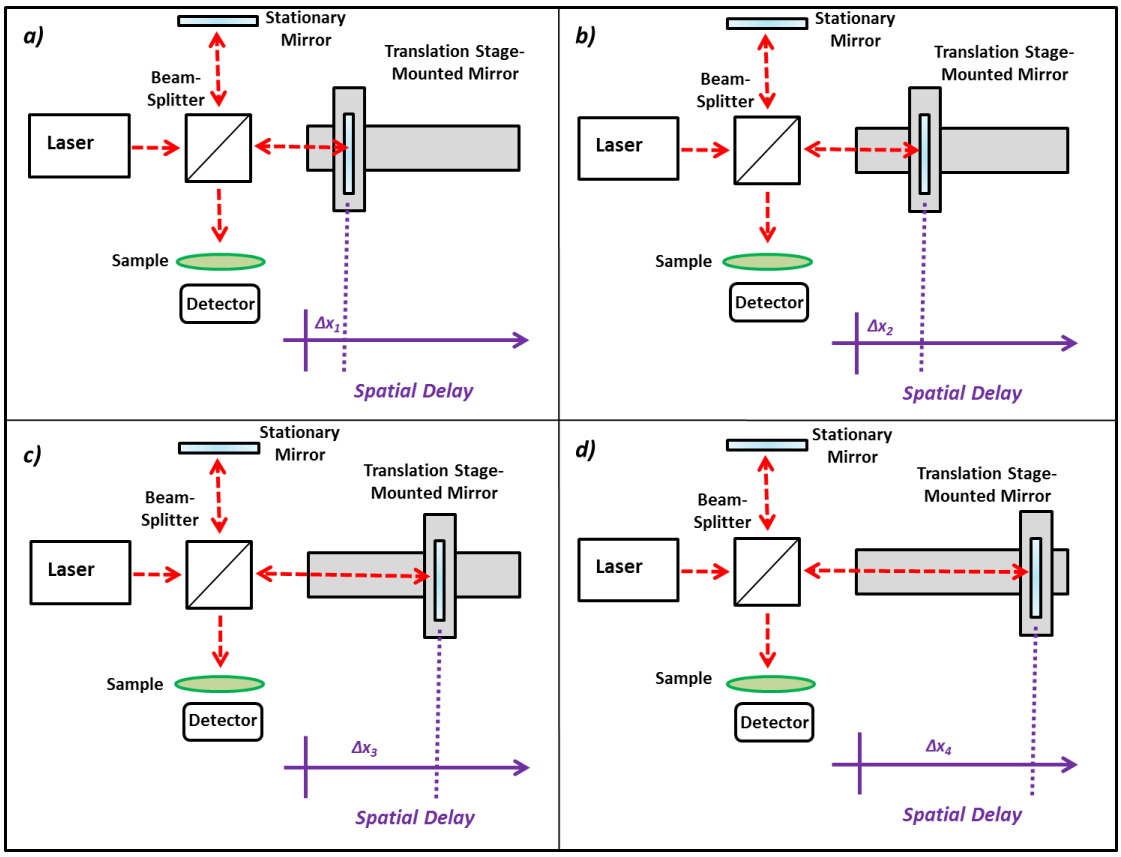

Figure 1-5 – The pump pulse in the stationary arm meets with the probe pulse from the mechanical translation stage arm at some target sample at a temporal delay proportional to the extension of the delay line length a) – d). This spatial domain schematic may be compared with the temporal domain schematic outlined in Figure 1-4.

However, due to the high demand in stability and optical adjustment of mechanical translation stages, this method is unlikely to ever contend with non-mechanical alternatives; long delay lines require extremely accurate alignment over the entire scanning space, which dependent on the length, may lead to a difference in spot size across the scan. For example if a temporal dynamic of even a nanosecond is to be examined, a delay stage would need a total translatable distance of at least 15cm. Finally, in order to accurately read a temporal delay data point, the mechanical stage must precisely move a very small distance before the acquisition is made. This is ultimately limited by the speed of the physical motors involved, and as a result, scan rates are often limited to hundreds of Hz [38, 39].

An alternative, ASOPS [40-44] – Asynchronous Optical Sampling - is an optical sampling technique which introduces a delay between successive pump and probe pulses by instead utilising two pulsed lasers with a very small difference in repetition rate f_{rep} such that $\Delta f = f_{pump} - f_{probe}$, see Figure 1-6.

Figure 1-6 – Diagram illustrating the two-laser scanning system of ASOPS, using two slightly detuned repetition rates to investigate the sample.

If T_{rep} is the roundtrip period of a laser with repetition rate f_{rep} such that $f_{rep} = 1/T_{rep}$, it is the continual temporal offset between successive pump and probe pulses which causes them to interact with the target at a proportionally increasing delay time with respect to each other, thus eliminating the need to manually delay them at a desired step size. As a result of this difference, the pulses will overlap in time again at every $1 / \Delta f$, see Figure 1-7.

The sampling step-size is given by $\Delta f / f_{pump} \times f_{probe}$ and the number of points sampled is given by $f_{probe} / \Delta f$. This method improves upon the conventional mechanical translation stage by having no mechanical parts, and since two lasers are used, they may have different output wavelengths (two-colour spectroscopy) or polarisations and thus may easily be differentiated at the detector through the use of band-pass or polarising filters to block the pump.

The method is also self-repeating due to the nature of the periodicity of each laser's pulsed output, meaning that scanning repeats indefinitely once initiated, giving rise to the potential to quickly stack or average acquired scans, each of which will complete in a real time frame corresponding to $1 / \Delta f$. To date ASOPS has been practically demonstrated at scan rates of up tens of kHz [15].

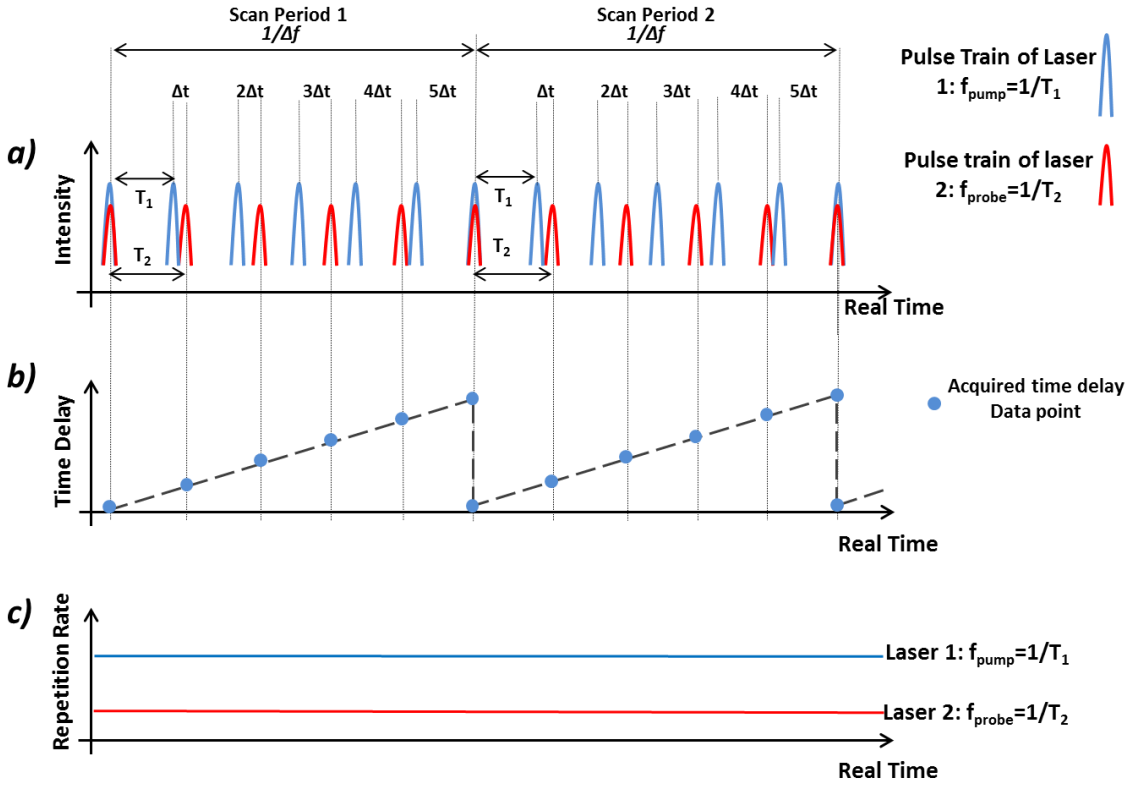

Figure 1-7 - The principle of ASOPS, whereby a) the pulses of one pulse train temporally 'walk around' the other, giving rise to b) a steadily increasing temporal delay between pump and probe pulses at a target position, due to c) the slight but constant difference in repetition rate of each laser.

However, the scan range is fixed, equalling the roundtrip period of the pump laser, and may not be easily altered. Although GHz-repetition-rate ASOPS systems have been developed [45, 46], the technique is commonly demonstrated using lasers with a repetition rate 10s to 100s of MHz [40, 47-50], giving rise to scan ranges of 10 to 100 nanoseconds. Given most time-resolved spectroscopy experiments are centred on the probing of ultrashort events which occur over the scale of picoseconds down to femtoseconds, such long temporal scan ranges tend to be in excess, leading to dead time while the scan completes. As stated, the step size is also limited to the offset dictated by the achievable difference in repetition rate, where too small a value for Δf will result in decreasing the scan rate. Additionally, the smallest achievable step sizes could be limited by the timing jitter in the system; if this results in too large a necessary step-size, the resolution may be too coarse to differentiate features within the dynamic target of choice [51]. Of course, the immediate drawbacks include that ASOPS requires two lasers, effectively doubling the costs and the complexity of locking electronics between them, as well as aligning and accurately desynchronising the repetition rate of the two beams at the target. Arbitrary Detuning ASOPS (AD-ASOPS) [52, 53] is a variant of the standard

technique developed recently, which claims to simplify the method by allowing both lasers to be free-running with no specific repetition rate requirements.

Another variation which may overcome some of ASOPS' drawbacks is ECOPS [54, 55] – Electronically Controlled Optical Sampling – which adopts some of the principles of ASOPS' two pulsed laser system, see Figure 1-8.

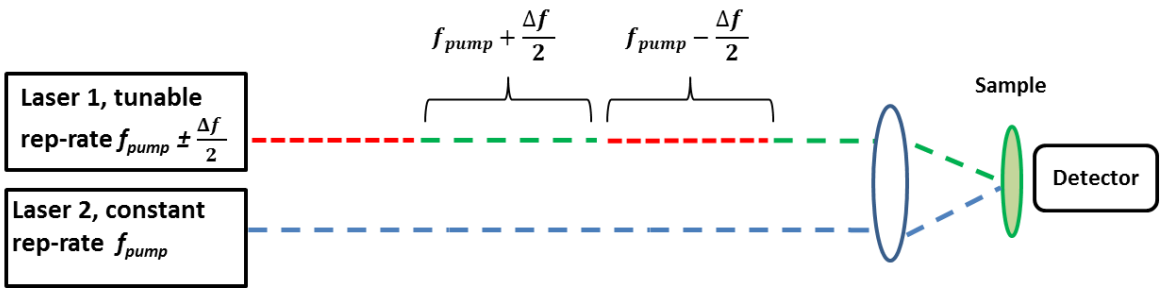

Figure 1-8 – Diagram illustrating ECOPS, whereby one laser repetition rate f_{pump} remains constant, whilst the other is switched repeatedly between two preferred repetition rate values, $f_{pump} = f_{pump} \pm \Delta f$.

Whilst one laser maintains a constant repetition rate f_{pump}, the repetition rate of the second laser is tunable using a mechanical piezo to vary the intra-cavity length, such that the frequency may be modulated in a square-wave regime between a user-defined maximum and minimum value with respect to the unmodulated laser, i.e. $f_{probe} = f_{pump} \pm \Delta f$ see Figure 1-9. As the tunable laser's repetition rate is switched from the maximum to minimum value, the resultant change with respect to the laser with a fixed repetition rate leads to the pump and probe pulses delaying asynchronously during the switch, which then repeats in reverse upon switching back to a maximum value.

Kim and Yee [56] demonstrated terahertz time-domain spectroscopy in both ECOPS and ASOPS, and found a reduction in the overall measurement time by a factor of 50 in the ECOPS regime due to the selectable scan range being confined only to that of interest, eliminating the wasteful dead time associated with ASOPS, showing ECOPS' potential to access increased scan rates, which to date however, has only been demonstrated up to 8 kHz [57] in comparison.

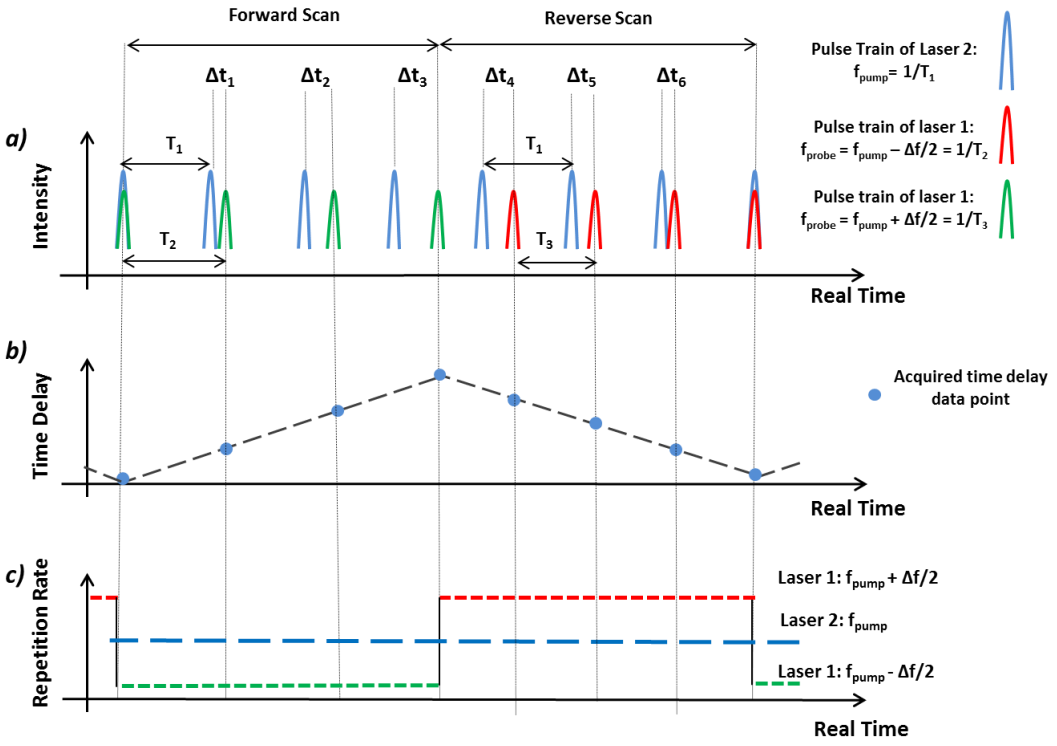

Figure 1-9 – The principle of ECOPS; a) a representation of how the temporal pulse positions vary over time, b) the time-delay which results over real time due to c) the pump laser having a constant repetition rate whilst the probe laser's repetition rate is modulated via square wave

Like ASOPS, this method shares the drawbacks of the expense of utilising two laser systems, and complicated locking electronics required to both set the required parameters and detect them. Additionally, the introduction of a piezo to vary the laser cavity length throughout the scan may actually remove one of ASOPS greatest features: the ability to scan without any limiting mechanical parts whatsoever. As such, ECOPS is physically limited by the maximum achievable speed of the motors involved, though often cites the potential for increasing piezo bandwidths as potential for future development [58].

We then consider the OSCAT technique [59, 60] – Optical Sampling by laser CAvity Tuning. This method uses only one laser in combination with an imbalanced interferometer, where the pump pulses are sent directly to the sample via a short arm, and the probe pulses are sent via a longer delay line, temporally delaying them with respect to the pump pulses. However unlike the conventional mechanical stage methods described above, the delay line is stationary and significantly longer than the other arm, see Figure 1-10.

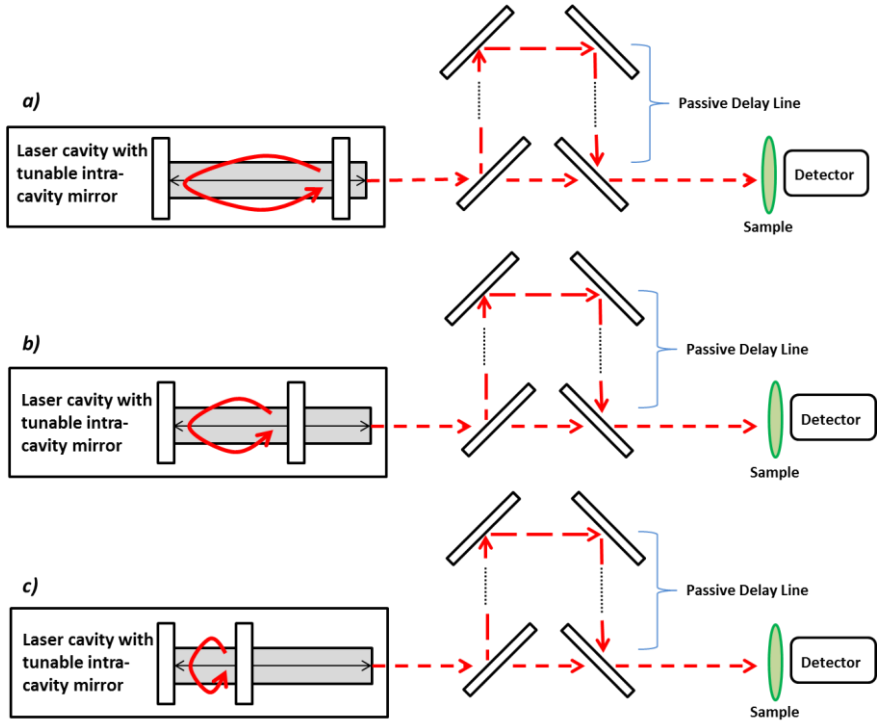

Figure 1-10 – Experimental setup of OSCAT; an interferometer design featuring a long delay line which is passive (no mechanical stage is required), whereby the temporal scanning instead comes about through the modulation of the lasers' intra-cavity length which in turn modulates the repetition rate, a) – c).

In this setup, the passive delay line (PDL) of length *l* and refractive index *n* is so long (spatially accommodating many roundtrip periods $T_{rep} = 1 / f_{rep}$) that tuning the repetition rate by Δf causes a change in the delay time Δt between pump and probe pulses, where

$$\Delta t = \frac{nlf_{rep}}{c}\left(\frac{1}{f_{rep}} - \frac{1}{f_{rep} + \Delta f}\right) \tag{1}$$

Upon each instance the repetition rate is varied (using a piezo stack to control the laser cavity length) the probe pulse is delayed further behind the pump pulse. If the mirror position is linearly ramped from a minimum to a maximum value (tuning the repetition rate inversely proportionally), this in turn linearly increases the temporal shift between successive pulses, and as such a continuous modulation (such as a triangular or saw tooth function) will give rise to repetitive scanning. Dependent upon the application, the choice of either a longer PDL length or greater repetition rate tunability may be selected in order to select the scan range, where optical fibre may serve as the PDL.

This method has been applied successfully in a variety of applications including terahertz spectroscopy, imaging and lidar [61-64], and whilst this single-laser design is far simpler

and potentially less expensive than ASOPS or ECOPS, fundamentally it still relies on a mechanically driven change in cavity length, meaning there are physical limitations on the potential for scan rate, which to date has mainly been practically demonstrated at a few hundred Hertz, with claims of cross-correlations acquired at rates approaching 1kHz [62].

Though semiconductor laser diodes (SLDs) are extremely popular throughout the scientific and commercial worlds due to their inexpensive, simple and compact nature, their involvement in optical sampling techniques is more often as the target of the study rather than the laser excitation source. Various forms of SLD have been the subject of pump probe measurements in order to study their gain and absorber or carrier dynamics [36], though In this case MLLDs were used as both pump and probe sources.

Momentum is gathering on the topic, however, as the search for semiconductor-based alternatives continues, such as in terahertz technology for example [65]. In 2008 Mihoubi *et al* [66] demonstrated an all-semiconductor Time-Domain Terahertz Spectroscopy (TDTS) system, where a mechanical delay stage was used to introduce the temporal delay between pump and probe pulses from a Vertical External Cavity Surface Emitting Laser (VECSEL). Similarly, Gebs *et al* [67] also demonstrated a TDTS system which was instead based upon the ASOPS technique. Being a two-laser method, they were successful in replacing one of the expensive and bulky Titanium:Sapphire lasers with an inexpensive and compact diode-pumped mode-locked VECSEL. Additionally, gain-switched laser diodes (GSLDs) have been successfully deployed as the laser excitation source in pump probe measurements, involving the slight detuning of two such laser's electronic driving conditions in order to probe a target in a similar fashion to the ASOPS technique [9, 68-70].

Finally, it is important to note that the OSCAT technique itself was similarly adopted for OSREFM [71-73] – Optical Sampling by Repetition Frequency Modulation – whereby the same OSCAT principles are applied in particular to the modulation of the repetition rate produced by a GSLD. Though only demonstrated to lower scan rates of up to 100Hz, this single-laser technique does remove the need for any external mirrors or mechanical parts, as the repetition rate is modulated directly from the diode itself via the modulation of an input electric signal. However, this technique (demonstrating a terahertz time-domain

spectrometer) also required complicated locking electronics to both set and lock the repetition rate and tune it. It was noted that the system also exhibited extremely high pulse-to-pulse jitter of around 10 picoseconds (compared to the 200 femtosecond compressed pulse duration), which caused severe broadening in their terahertz signal compared to their comparative study which adopted a conventional mechanical stage scanning system. The high jitter values were attributed to both the driving electronics and the gain switching mechanism, and the laser instability was attributed to amplified spontaneous emission during the formation of the pulse. A comparison of the described major optical sampling techniques are summarised and tabulated, as their advantages and disadvantages are referenced regularly throughout the thesis, see Figure 1-11.

Technique [References]	Scan rate dictated by:	Scan range dictated by	Advantages	Disadvantages
Delay Stage [38, 39]	The mechanical speed of a physical motor	The length of the translation stage	- 1 Laser - Simple setup - Scan range customisable	- Low scan rates limited by mechanical parts
ASOPS [40-44]	The offset Δf between both lasers	The roundtrip period $T = 1/f$	- Fast scan rates and long scan ranges (depending on laser characteristics) - No mechanical parts	- 2 Lasers - Double Costs - Complex phase-locking system -Scan range not customisable
ECOPS [54, 55]	The fraction of roundtrip period $T = 1/f$ selected by the offset Δf between both lasers, itself limited by Intracavity mirror motor speed	The offset Δf between both lasers	- Fast scan rates and long scan ranges (depending on laser characteristics) -Scan range customisable	- 2 Lasers - Double Costs - Complex phase-locking system - limited by mechanical parts
OSCAT [59, 60]	Intracavity mirror motor speed	- repetition rate f - repetition rate tunability Δf - PDL length l	- 1 Laser - Scan range customisable	- long PDLs lead to dispersion and jitter issues - limited by mechanical parts
OSREFM [71-73]	The ability to modulate the repetition rate and the carrier dynamics of the material concerned	- repetition rate f - repetition rate tunability Δf - PDL length l	- 1 Laser - Inexpensive SLD - Scan range customisable - No mechanical parts	- Complex phase locking electronics - low scan rates demonstrated - High pulse to pulse timing jitter

Figure 1-11 – Summary of the optical sampling techniques described, including how in each case the scan rate and scan range are determined, and the relative advantages and disadvantages of each system.

A selection of the demonstrated scan rates and scan ranges of the ASOPS, ECOPS, OSCAT and OSREFM techniques were then collected from an illustrative set of published works and plotted for comparison, see Figure 1-12. The data used to generate this figure[1] may be found in the Appendix, Section 7.1.1.

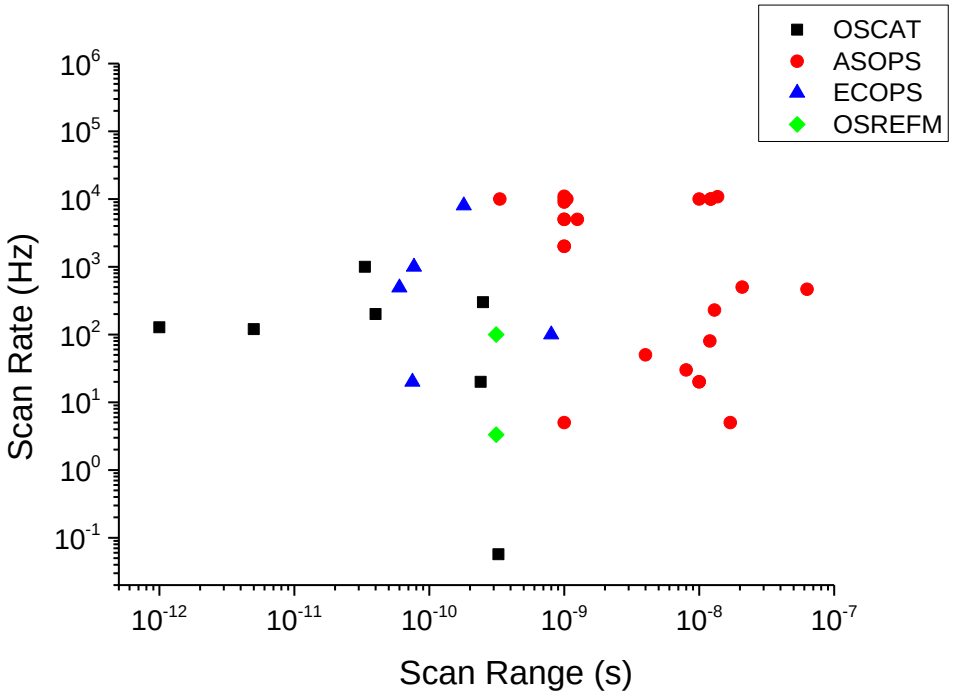

Figure 1-12 – A collection of scan ranges and scan rates from several optical sampling techniques including OSCAT, ASOPS, ECOPS and OSREFM are plotted together for an indicative comparison of their demonstrations to date.

Currently the ASOPS technique exceeds the others in scan rate, and has mostly been reported with fairly long scan ranges (though as discussed, this is not in practice always desirable, merely a result of the method). The ECOPS technique is a contender for scan rate, and as discussed, has the advantage of lowering the scan range to a custom value, reducing wasteful dead time found in ASOPS. The OSCAT (and OSREFM) techniques have mostly reported lower scan rates but a relatively wide variety of scan ranges (owed to the ability to simply extend or shorten the length of passive delay line for the preferred range, depending on the available repetition rate tunability). One of their main advantages over the asynchronous techniques, however, lies in the fact that they use only one pulsed laser source.

[1] Note that whilst other parameters such as laser type, pulse duration etc. were also tabulated and other works are discussed throughout the thesis, only those which had a clear scan range and scan rate value are plotted in Figure 1-12.

As discussed in the next section, it is clear that there remains a niche window for optical sampling techniques which can access both competitive scan rates at a wide variety of scan ranges. If the systems described could also be adapted for inexpensive and compact MLLDs rather than the expensive and bulky commercial systems most of these examples adopt, this would be another clear advantage.

1.3. Research Goals

The cutting-edge optical sampling techniques described contend with each other over scan rates and scan ranges, however their competitive edge sits on a delicate balance of additional considerations, including the number of lasers involved, the complexity in electronics required, the necessity for mechanically moving parts or indeed the cost of the laser type itself used for the application. As such, the main goal of this project was to develop novel optical sampling techniques which could take advantage of the highly customisable and versatile electronically-controlled nature of passively mode-locked two-section laser diodes, making use of the process of saturable absorption to generate ultrashort pulses and exploiting their diversity, compactness and cost-effectiveness when compared with typically used solid-state laser systems.

In particular, the laser's repetition rate and/or its ability to be modulated tend to be the more fundamental requirements of optical sampling techniques (particularly for both OSCAT and ECOPS), and as such the ability to achieve this through varying the electrical biasing conditions of two-section MLLDs which has been demonstrated in the literature (rather than using motorised laser cavity mirrors) sets the goal of achieving optical sampling techniques which require no limiting mechanical or moving parts whatsoever, and was therefore hypothesised to potentially be capable of faster scan rates.

Additionally, whilst some techniques in the literature achieve their fast scan rates without the requirement of mechanical parts, they may do so at the cost of an entire second laser system; therefore a further goal of this project was to achieve fast scan rates within optical sampling using only one mode-locked laser diode.

For contrast, comparative time-resolved mechanical translation stage techniques are also to be demonstrated, illustrating the MLLDs suitability for even standard methods of optical sampling. Additionally, both linear (single photon absorption) and non-linear (two-photon absorption) cross-correlation experiments will be demonstrated.

With these research goals in mind throughout the project, ultimately two unique optical sampling techniques are proposed:

Firstly, Optical Sampling By Electronic Repetition-Rate Tuning (OSBERT). This single-laser technique follows OSCAT in some aspects of the design, and follows the OSCAT expression (1), however absolutely no mechanical parts are required. The tuning of the repetition rate Δf is accomplished by varying the biasing conditions of a two-section mode-locked laser diode, and is entirely electronic, where a PDL of length l serves to scale the available scan range. Whilst the PDL can simply be free-space, there are advantages in using coiled optical fibre in order to save space and access greater lengths in the laboratory, and in addition (according to expression (1)) the greater refractive index will also scale the scan range. With no limiting physically moving parts, it was hypothesised that competitive scan rates could be reached.

Secondly, SLECOPS - Single-Laser Electronically Controlled Optical Sampling – is a theoretical technique which was partially conceived upon the principles of both ECOPS and OSCAT, and like OSBERT requires only one laser. Where MLLDs are used as the pulsed laser source this technique may also be entirely electronically controlled with absolutely no mechanical parts. However SLECOPS differs from OSBERT in that it is potentially also applicable to any pulsed laser source, and not limited to MLLDs, provided the repetition rate may be modulated via square wave, for example by varying the intracavity mirror distance using a stepper motor such as that of OSCAT or ECOPS. SLECOPS' major novelty is the ability to perform asynchronous type scans (such as that shown by two-laser systems including ASOPS and ECOPS) using only a single laser.

1.4. Thesis outline

The structure of the thesis following this introduction is as follows:

In Chapter 2 the literature review of the state of the art continues, and an introduction to the types of MLLDs used throughout the project is given, including an overview of their various structures and operation through biasing conditions. The role of carrier confinement within the devices, including the benefit of quantum dots in the active layer is also described. This section includes an introduction to passive mode-locking in such devices using the principle of saturable absorption, as well as an overview of the literature which explores the ability for MLLDs to have their repetition rates electronically tuned via the applied biasing conditions.

The resultant output characteristics of each device tested were then analysed in order to assess their potential in the optical sampling techniques developed for the project, which begins in Chapter 3 with a theoretical introduction to the concept of the first technique, OSBERT. This section continues with the first basic demonstrations of the principle in a number of proof-of-concept single and two photon absorption experiments which ultimately pave the way for the greater goal of significantly increasing the scan rate through fast modulation techniques in Chapter 4, alongside some demonstrated applications and a discussion of the accuracy and limitations of this technique.

The theorisation of the second technique, SLECOPS, begins in chapter 5 making use of the previous chapters for insight into its operation. The concept of the ‘virtual laser’ is introduced, where just one laser can be said to function as two in the context of optical sampling. Examples are calculated using the SLECOPS theory, then analysed and discussed for the potential to optimise the scan range and scan rate in order to compete with the state of the art techniques.

Finally, the experimental results of the project are contrasted with the research goals proposed above, conclusions on the role of two section quantum dot passively mode-locked MLLDs in optical sampling are drawn, and suggestions for future work then complete the thesis.

2. MODE-LOCKED LASER DIODES: Structure and Repetition Rate Tunability

In this chapter, the concept of mode-locking is introduced, and details of the two-section quantum dot monolithic passively mode-locked semiconductor laser diodes used throughout the project are discussed, whose outputs are fully characterised for their pulse duration, output power, repetition rate and emission wavelength. The phenomenon of electronically tuning the repetition rate of these devices is reviewed and then tested experimentally on the available devices, showing their potential for use in optical sampling in the subsequent chapters, particularly OSBERT which relies on this tunability.

2.1. Introduction to Mode-Locked Semiconductor Laser Diodes

In order to understand the foundations of the quantum-dot passively mode-locked semiconductor laser diodes used throughout this project, we shall examine each of these attributes individually.

2.1.1. The Laser Cavity and Mode-Locking

Mode-locking [10] is a technique widely used to generate ultrashort pulses from a laser. Consider the basic design of a laser, whereby a gain medium (which may either be optically or electrically pumped) is inserted within a Fabry-Pérot cavity. Light waves traverse the cavity and reflect to repeat the journey, interfering constructively and destructively with each other along the way, such that standing waves are created between the highly and partially-reflective mirrors. As such, only discrete frequencies are allowed to oscillate within the cavity, known as longitudinal modes, see Figure 2-1.

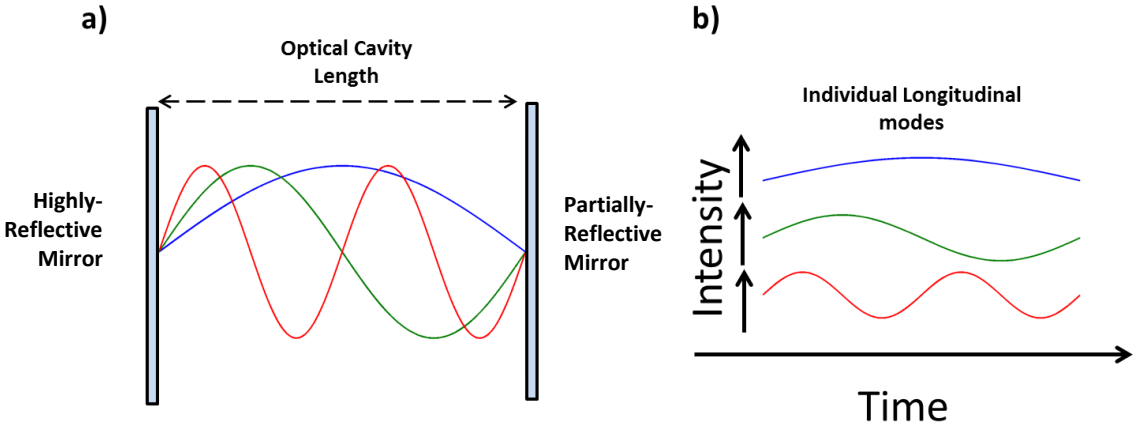

Figure 2-1 – a) An illustration of longitudinal modes within the optical cavity of a laser, and b) individual longitudinal modes

The only modes which are supported in the cavity of length L are those which are multiples of the half-wavelength of the oscillating light of speed c. In the frequency domain, the spacing of these modes is given by $\Delta\nu = c/2L$. We must then consider the bandwidth of the gain medium itself in conjunction with the modes which are supported within the optical cavity, see Figure 2-2.

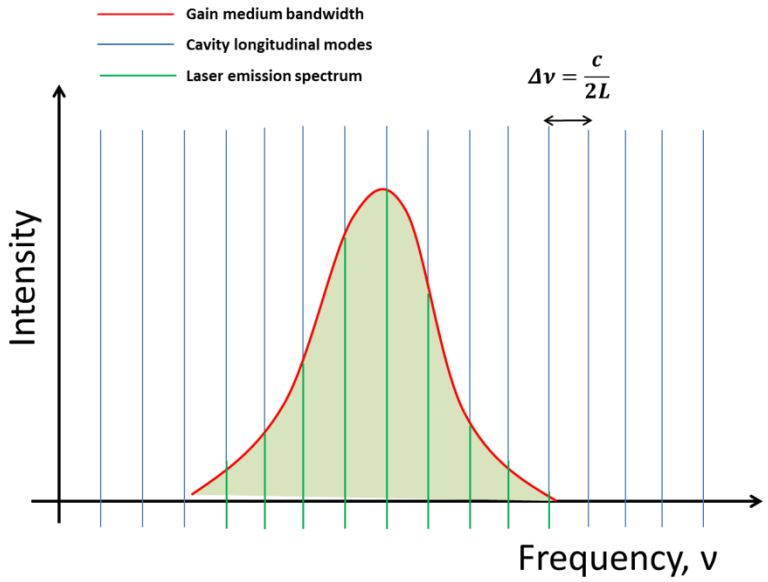

Figure 2-2 – Blue vertical lines represent the modes supported within a laser cavity of length *L*, red represents the gain medium's bandwidth, and green lines represent the allowed longitudinal modes leading to the laser emission spectrum.

Although only certain longitudinal modes are allowed spatially within a particular length of laser cavity, they may propagate in time with no fixed relationship between their relative phase. The result of the sum of multiple permitted longitudinal modes in a laser operating in cw (continuous wave) mode is illustrated in Figure 2-3.

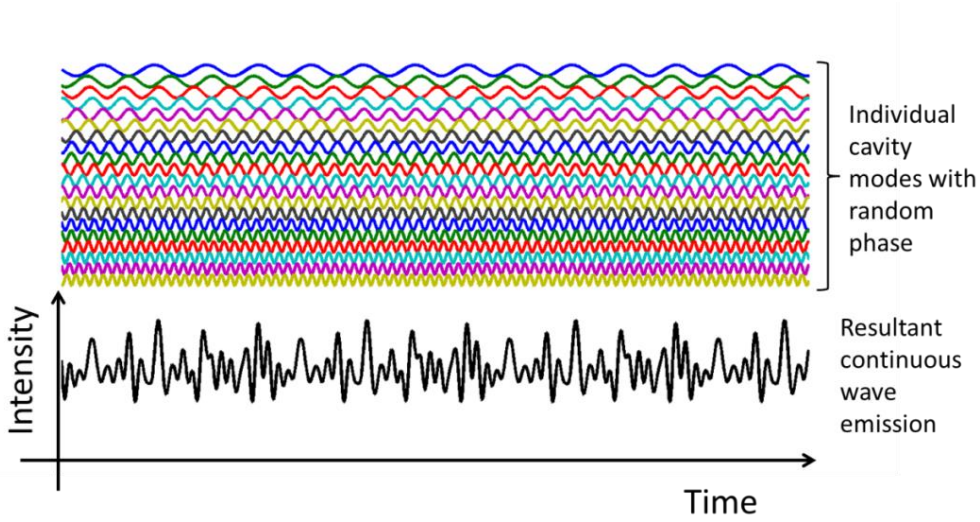

Figure 2-3 – Above, the oscillation of individually separated longitudinal modes with random phase within a laser cavity. Below, the summation of the longitudinal modes giving rise to cw emission.

The seemingly noisy output over time is typical of continuous wave emission from a laser, though observing carefully it is clear that even the noise pattern is periodic, due to the periodic nature of the longitudinal modes. Expanding upon this idea, if the exact same longitudinal modes were to have a fixed-phase relationship, the peaks of each wave would all periodically align, leading to a regular increase in constructive interference at this temporal point, surrounded by destructive interference elsewhere, see Figure 2-4.

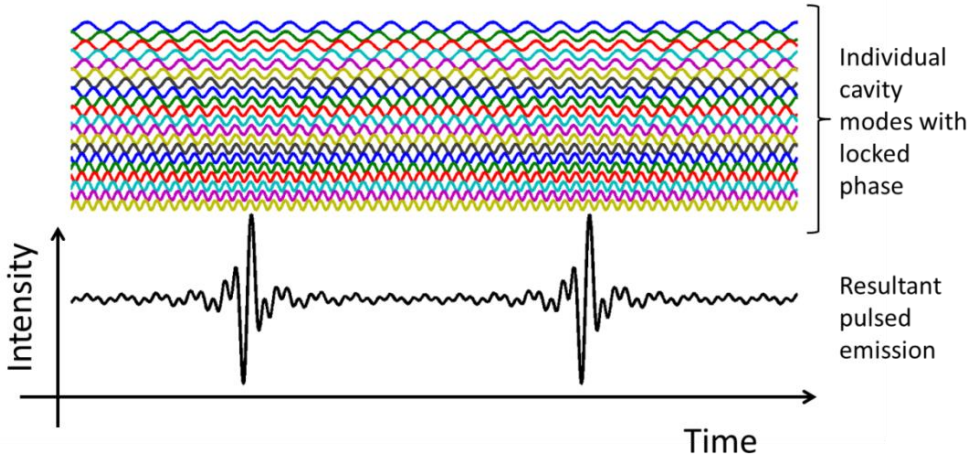

Figure 2-4 - Above, the oscillation of individually separated longitudinal modes with a fixed relative phase relationship within a laser cavity. Below, the summation of the locked modes giving rise to pulsed emission, i.e. mode-locking.

Comparing the emission of the pulsed and the continuous wave outputs, we find the mode-locked pulses exhibit significantly higher peak intensities (or optical powers) over a condensed time interval, compared to that of the continuous wave emission.

Given the nature of the locked modes, the pulses will form and emit in a periodicity known as the cavity roundtrip-time T_{rep}, proportional to the laser cavity length *L*, such that

$$T_{rep} = \frac{c}{2nL} \tag{2}$$

The inverse of the cavity roundtrip time is known as the laser's repetition rate f_{rep}, and may be related back to the mode-spacing $\Delta\nu_{spacing}$ such that

$$\Delta\nu_{spacing} = \frac{1}{T_{rep}} = f_{rep} = \frac{2nL}{c} \tag{3}$$

We may now also relate the peak and average powers, P_{pk} and P_{av} as a function of the pulse duration $\Delta\tau$ and the repetition rate f_{rep}, such that

$$P_{pk} = \frac{P_{av}}{\Delta\tau \cdot f_{rep}} \tag{4}$$

It is clear that lower repetition rates and shorter pulse durations (in conjunction with greater average power) will give rise to greater peak powers. It is also possible to determine the roundtrip period, and therefore both the repetition rate and the laser cavity length, by analysing a sample optical spectrum of a laser. Consider a pulsed laser of central emission wavelength $\lambda = 1266.5$nm measured using an Optical Spectrum Analyser (OSA), and its repetition rate of $f_{rep} = 5.079$GHz measured by a Radio Frequency Analyser (RFA), see Figure 2-5[2].

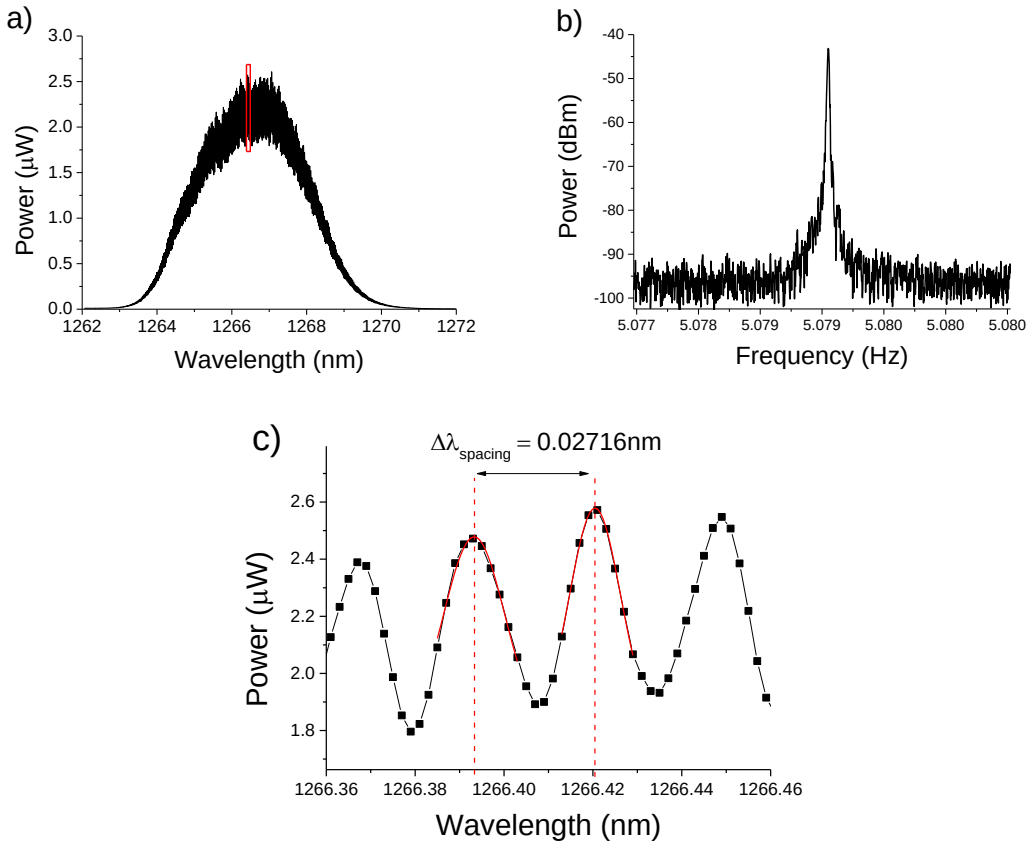

Figure 2-5 – a) The optical spectrum of a laser of central emission wavelength 1265.5nm with a highlighted (red) region of interest b) the radio frequency spectrum of the pulsed laser of repetition rate 5.079GHz and c) the mode spacing within the optical spectrum's highlighted region of interest

[2] Note, this experimental data in Figure 2-5 originates from a narrow-ridge device whose characteristics are detailed in section 2.5.1.

If we magnify a region of the optical spectrum trace at Figure 2-5*a* we find evenly distributed modes (Figure 2-5*c*) whose central wavelength may be measured by fitting a Gaussian function to their peaks. We then convert such that the wavelength mode spacing $\Delta\lambda_{spacing} = 0.02716\text{nm}$ is related to the frequency domain such that

$$\Delta\nu_{spacing} = \frac{c}{\lambda^2} \cdot \Delta\lambda_{spacing} = 5.079 \times 10^9 Hz \sim f_{rep} \tag{5}$$

Thus it is clear to see the important relationship between both the roundtrip period and the repetition rate of a pulsed laser in terms of the laser cavity length and the supported longitudinal modes. Finally it can be shown the greater the spectral bandwidth $\Delta\nu$ of the full optical spectrum, the shorter the resultant pulse duration $\Delta\tau$ shall be (assuming that the modes are locked in phase). This can be represented in terms of the Time-Bandwidth Product (TBP) as

$$\Delta\tau = \frac{TBP}{\Delta\nu} \tag{6}$$

Depending on the pulse shape, the TBP takes different values [74]; for an assumed Gaussian pulse shape, this value is 0.441. If the actual measured TBP of a pulsed laser exceeds this value, it can be assumed the pulse duration of the system is not as short as is theoretically allowed by the gain medium bandwidth and laser cavity combination. As such the pulses may for example have been stretched by the dispersion introduced by additional optical elements such as lenses or mirrors within the setup, whereby different spectral components of the pulse travel at different respective velocities.

It is also conceivable that a pulsed output could be achieved by quickly switching a laser on and off, and in semiconductor laser diodes this is known as gain switching [75] (This is the method used to generate the pulses in the laser used in the OSREFM technique [71] described in Chapter 1). An electrical signal is applied which only briefly brings the carrier density above threshold, before returning below threshold, meaning lasing occurs for a very short period. The benefits are a readily adjustable repetition rate due to the electrical signal, however, gain-switching as an alternative to mode-locking results in larger timing jitter, and without pulse compression tends to produce fairly broad pulses.

2.1.2. Quantum Confinement and the Laser Diode Structure

Fundamentally, the devices used in this work are based upon the same principles of semiconductor laser diodes and the typical P-i-N (p-type – intrinsic – n-type) structure where the active layer is embedded in the intrinsic layer. Metal contacts are deposited on the device for electrical biasing. Each side is cleaved and coated giving rise to the Fabry-Pérot cavity described above, see Figure 2-6. Upon forward biasing the laser diode, carriers (electrons from the n-side and holes from the p-side) are directed towards the active layer where they may recombine and give rise to photons in the form of spontaneous emission. As the forward current is increased, spontaneous emission builds up, and upon population inversion the rate of stimulated photon emission becomes greater than the photon absorption, and the light is now said to be amplified. As with any other type of laser, provided this gain amplification is greater than the losses induced within the cavity for feedback (imperfections in the structure and in the mirror reflectivities, scattering etc.) the threshold current I_{th} is met, above which lasing begins and the beam emits from the partially reflective mirror (or output coupler).

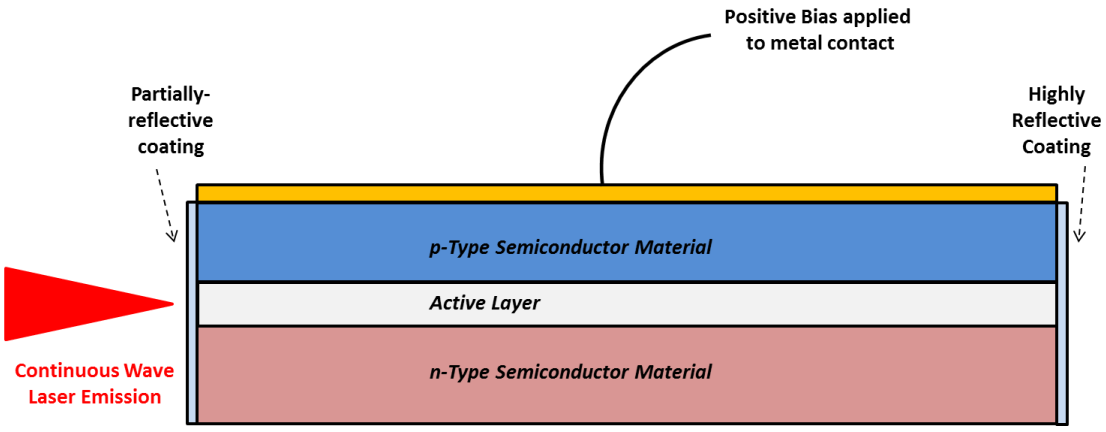

Figure 2-6 – A typical semicondcutor p-i-n laser diode structure which gives rise to cw emission.

Using this bulk semiconductor configuration, optical confinement is provided by the smaller refractive index of the surrounding n-type and p-type materials compared to that of the active layer, whilst the so-called double-heterostructure provides a degree of electrical confinement in the active layer of both the holes and electrons moving from the conduction and valence bands, E_C and E_V respectively. However, this confinement can be vastly improved upon by instead growing quantum wells, wires or dots in the active layer. In the case of the quantum well laser, the material grown in the active layer is sufficiently thin that quantum confinement now takes place in one of three spatial dimensions

because the density of states $D(E)$ takes an abrupt or step-wise form, see Figure 2-7. Similarly, quantum wires (or dashes) [76] allows quantum confinement to be extended into two dimensions, and for quantum dots three dimensions are confined [77].

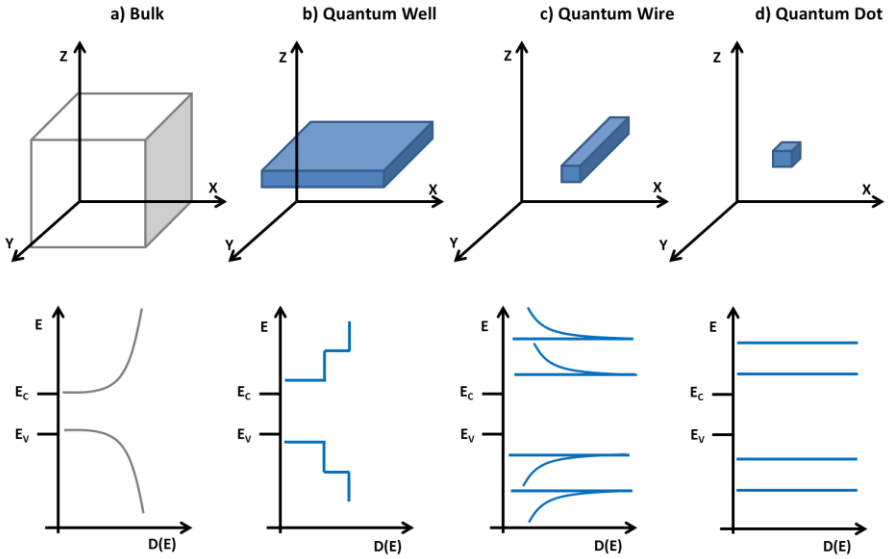

Figure 2-7 – The quantum confinement in three dimensions and density of states $D(E)$ with respect to the energy levels of the conduction and valence bands E_C and E_V for a) bulk semiconductor material b) quantum wells c) quantum wires and d) quantum dots

In fact it is possible to engineer the bandgap relatively robustly, and even grow quantum dots (QDs) within quantum wells (QWs) in a 'Dots in a Well' (DWELL) configuration [78]. As such, though difficult to illustrate in three dimensions, the confinement offered by QWs and QDs can be compared in terms of simplified band diagrams to that of the bulk material arrangement, see Figure 2-8.

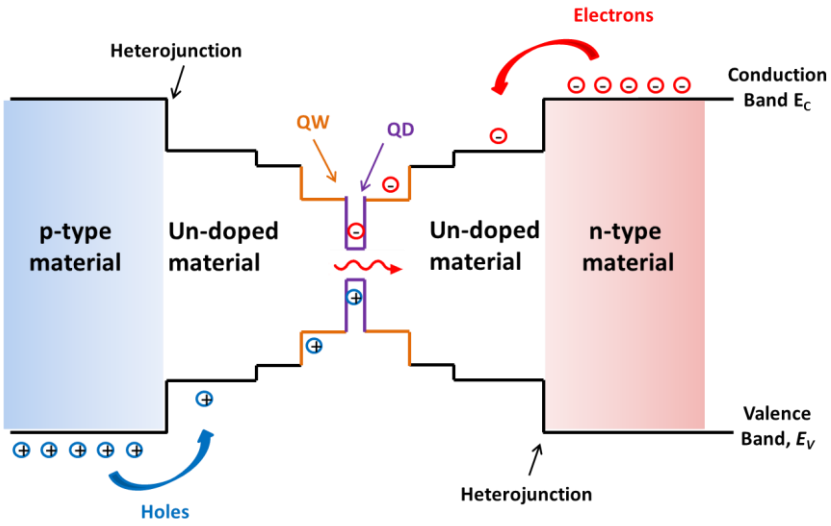

Figure 2-8 – Electrons from the n-type material and holes from the p-type material diffuse towards the active layer, aided by increasing confinement ranging initially from the doping profile, to the heterojunction boundary, to quantum wells (QW) and finally to quantum dots (QD).

As well as greater quantum confinement giving rise to greater quantum efficiency, since their invention [79] quantum dot lasers have demonstrated a number of advantages over quantum well lasers, including greater temperature insensitivity and lower threshold currents due to the far more discrete density of states [80, 81]. Throughout the project a number of devices were tested with various structural and chemical make-ups, including active regions comprising quantum wells or quantum dots, however ultimately those which gave rise to the work discussed in this thesis were quantum dot devices.

2.1.3. Saturable Absorption: Passive Mode-Locking in MLLDs

Mode-locking in laser diodes can be achieved using a number of methods; in particular these can include active, passive or hybrid techniques. In active mode-locking [11, 82], pulses are formed by directly modulating either the gain or loss mechanisms using an electronic signal with a frequency equal to that of the mode-spacing frequency. This technique results in a highly stable pulsing regime with low timing jitter, though typically broader pulses than other techniques. Active mode-locking also by definition needs to be controlled externally from the laser, adding a degree of complexity to the setup - a draw-back which is avoided by instead adopting passive mode-locking [83]. In this technique, a section within the laser cavity provides saturable absorption, where the light absorption decreases for increasing intensities. At some intensity the absorber will saturate, allowing only the transmission of higher intensities. Whilst initially this may only be a random noisy burst, after many roundtrips the process will dynamically create a better defined pulse at each roundtrip period. Such a saturable absorber may even be integrated monolithically into the laser; hence it may passively give rise to mode-locking of shorter pulses than that typically found in active mode-locking. Hybrid mode-locking [84] combines the active modulation of active mode-locking with the saturable absorption of passive mode-locking to produce ultrashort pulses.

This project and the optical sampling techniques investigated are entirely based around passive mode-locking of two-section monolithic quantum dot mode-locked laser diodes, where a saturable absorber can be integrated as a second (electrically isolated) section adjacent to the gain section, see Figure 2-9.

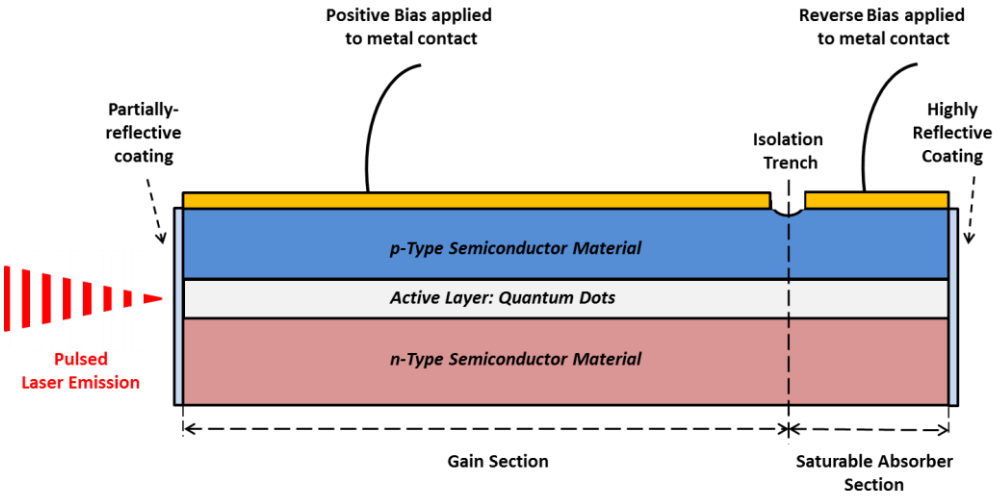

Figure 2-9 - Diagram of a 2-section MLLD, whereby a forward biased gain section is monolithically adjacent to a reverse biased absorber section, giving the total optical cavity length between two coated facets.

As described above, in cw operation, the supported longitudinal modes oscillate with random phase within the cavity. Due to the periodically noisy nature of the longitudinal modes in random phase, lower intensities will be absorbed more so than the periodically noisy bursts which exist, because ultimately the absorption decreases for increasing light intensity, and so only the greater intensities are allowed to transmit, forming the basis of a periodic pulse-like peak. This process continues, and upon each roundtrip the wings surrounding this peak are further attenuated, eventually giving rise to a pulsed output. For increasing the reverse bias applied to the absorber section, the carriers which are photo-generated by the high intensity pulse are swept out via the terminals. This leads to an important gain/loss dynamic between the gain and absorber sections which occurs periodically upon the saturation and recovery of the absorber, see Figure 2-10. Increasing the reverse bias to the absorber will therefore ultimately decrease its recovery time and therefore will further shorten the pulse duration.

It is clear that both the gain and absorber sections must have carrier recovery times shorter than that of the roundtrip period such that the process may repeat upon each instance the pulse meets the absorber section, which will have returned to a state of high loss.

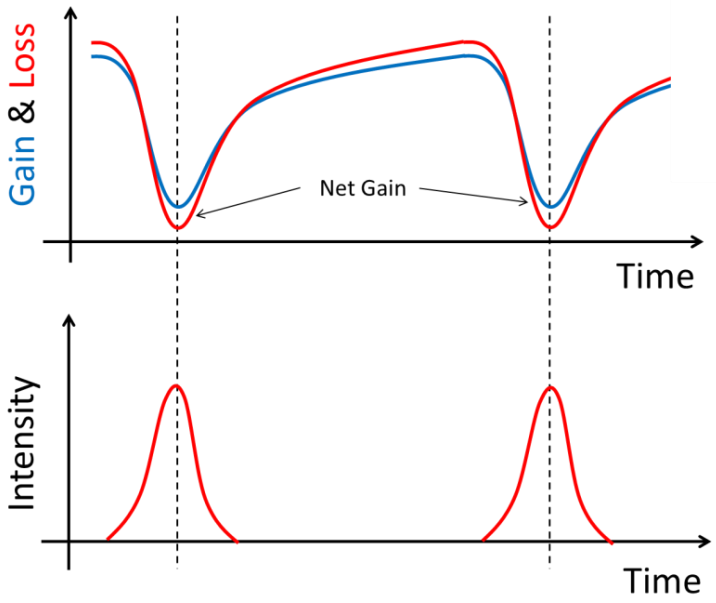

Figure 2-10 – Representation of the formation of pulses through gain and loss dynamics brought on by saturable absorption, based on a diagram from [85]. A reverse bias is applied to the absorber giving rise to a net gain window leading to a pulsed output.

In the case of the two-section MLLDs used throughout this project, we assume the characteristics are entirely unknown until they are examined, which is to say the duration of the pulses (and other output characteristics) will each depend upon not only the structural configuration of the device but also the variety of biasing conditions which may be applied across its sections.

2.2. Device Structure

Though several devices were studied for their suitability in the following work [1-3, 6], for the majority of the project, the most significant experimental work was carried out using two particular quantum-dot passively mode-locked laser diodes of slightly differing structures; namely a narrow-ridge waveguide and a tapered waveguide design.

2.2.1. Narrow-Ridge Device

Referring to Figure 2-11, the narrow-ridged waveguide device was fabricated by *Innolume GmbH* with a total length of 8.00mm corresponding to a repetition rate of approximately 5GHz, of which the absorber length was 900µm (11.25% of the full device length). The narrow ridge waveguide was 4µm wide. Both sections were electrically isolated from each other via an isolation trench. The highly-reflective (HR) rear facet coating has a reflectivity of 99%, whilst the anti-reflective (AR) front facet has a reflectivity of 10%.

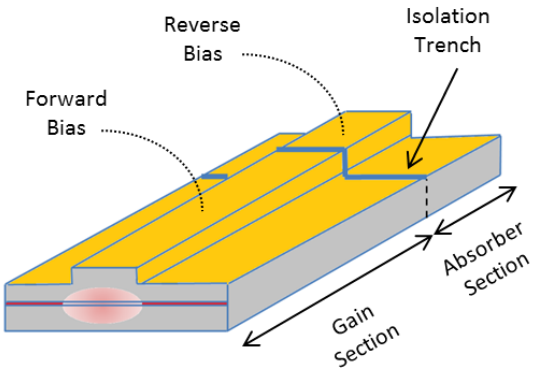

Figure 2-11 - Diagram[3] of the narrow-ridge device consisting of a reverse biased saturable absorber section which is electrically isolated from a forward biased gain section.

The quantum-dot structure, see Figure 2-12, was grown p-side up using molecular beam epitaxy on a 3 inch n^+GaAs substrate. P-type (Carbon doped) and N-type (Silicon doped) $Al_{0.15}Ga_{0.85}As$ cladding layers were respectively fabricated either side of the active region for optical and electrical confinement. The active layer comprised 10 layers of InAs quantum dots, topped by evenly-sized layers of $In_{0.15}Ga_{0.85}As$ and separated by 35nm-thick GaAs barriers.

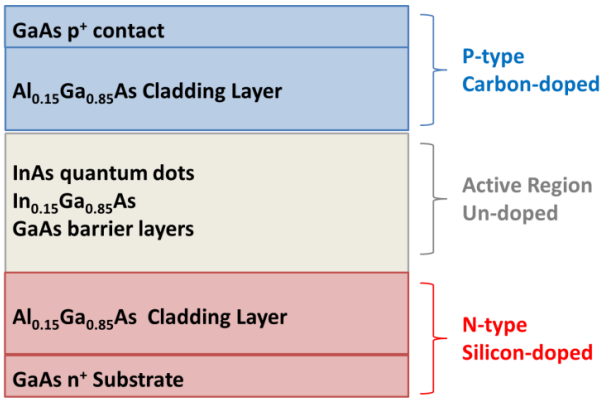

Figure 2-12 – Narrow-ridge device basic fabrication structure showing the PN junction enclosing the quantum dots in the active region (not to scale).

2.2.2. Tapered-Waveguide Device

The tapered-waveguide passively mode-locked semiconductor laser diode device was reported on at conference [6] during the project, and was fabricated by *III-V Lab* based on a quantum-dot structure grown by *Innolume GmbH*. A narrow-ridge waveguide was fabricated for the saturable absorber section, whilst instead a tapered waveguide with a full angle of 2° was used for the gain section, see Figure 2-13. The tapered waveguide

[3] Note, this diagram was reconstructed from one which was used in one of our publications regarding a quantum well structure of similar two-section design, which could emit at 760nm wavelength.

section was 2.40 mm long, whilst the narrow section's waveguide had a length of 600µm and a width of 14µm, giving a total device length of 3.00 mm. Both sections were electrically isolated from each other via a 5µm isolation trench. Whilst the straight section acts as a spatial filter within the cavity, the increasing width of the tapered section provides higher optical power [86, 87]. As such, tapered lasers offer a good solution in providing single spatial mode beams with high power and good beam quality showing suitable promise for applications in biophotonics [88].

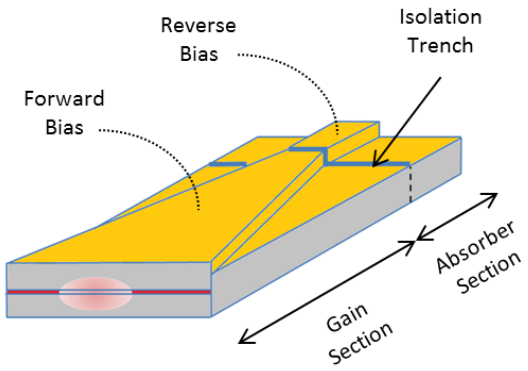

Figure 2-13 – Diagram of the tapered-waveguide device (not to scale in order to highlight features) consisting of a narrow reverse-biased saturable absorber section, which is electrically isolated from a tapered forward-biased gain section.

The quantum-dot tapered-waveguide device was fabricated with the same wafer structure as that of the narrow-ridge device (Figure 2-12), and therefore varies only in the physical structural dimensions, particularly the design of the tapered waveguide.

2.3. Device Characterisation

2.3.1. Characterisation setup

Such MLLDs must be fully characterised in order to understand their pulsed output dynamics, and importantly, their controllability under various biasing conditions.

A diagnostic setup is illustrated in Figure 2-14, where each device may be alternately placed into the configuration and fully characterised. A power supply (*Agilent E36447A*) provides the reverse bias required for the saturable absorber section, whilst a combined diode driver and thermoelectric cooler (TEC) (*Newport Laser Model 6100*) supplies the forward bias to the gain section and stabilises the temperature of the entire QD MLLD device.

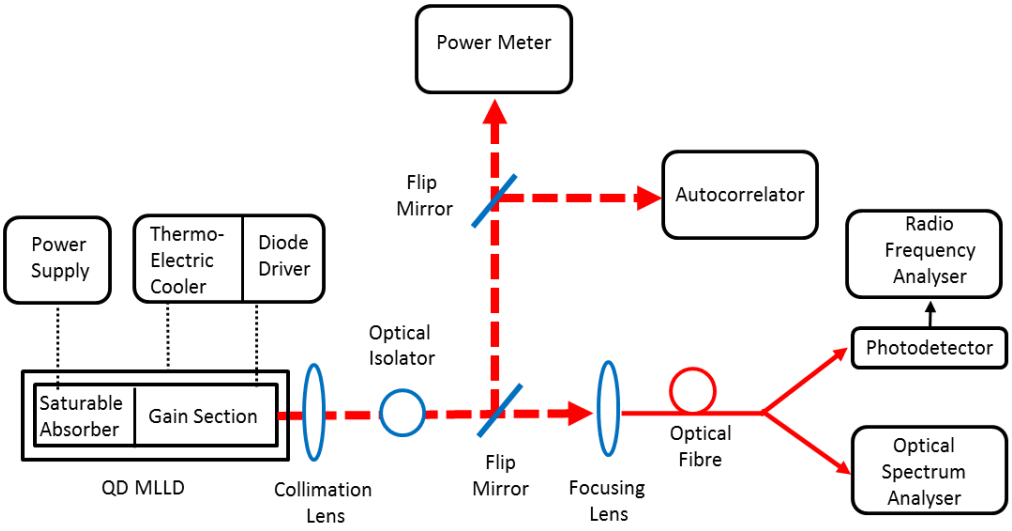

Figure 2-14 – Diagram of the diagnostic setup adopted for the characterisation of each QD MLLD device.

Typically the output laser beam of such MLLDs is highly divergent in the vertical axis, and as such a collimation lens (*Thorlabs C330TME-C aspheric lens, f=3.1mm*) is placed in the near-field of the device at the appropriate focal length in order to collimate the beam into an elliptical or near-circular shape. The beam is then sent into either one of two main paths by a flip-mirror (although it should be noted that beam splitters can readily replace flip mirrors in order to characterise several parameters at once, at the cost of reduced power to that piece of equipment).

Using a collimation lens (*Thorlabs C560TME-C aspheric lens, f =13.8mm*) one beam path is coupled into an optical fibre which is mounted on a 3-D translation stage in order to optimise fibre coupling. The fibre is then split into two lines and connected firstly to an *Anritsu MS9710C* Optical Spectrum Analyser (OSA) in order to measure the optical spectra from the device, and secondly to a *Picometrix D-15* photodetector of 21GHz bandwidth, which is in turn connected to an *Agilent E4407V ESA-A* Radio Frequency Analyser (RFA) of bandwidth 9kHz-26.5GHz in order to measure the radio frequency spectra of the device.

Regarding the radio frequency spectra, it should be noted that the optical isolator placed in front of the MLLD allows light to travel in only one direction in order to restrict (and therefore protect the source from) back-reflections which can interfere with the mode-locked output. A polariser at the input of the isolator allows only linearly polarised light into a Faraday rotator, which rotates the beam's polarization by 45° before exiting the device via another linear polarizer producing a 45° difference between the input and

output beams. When spurious back reflections are sent in the reverse direction from other optical elements in the light path, the Faraday rotator again rotates the light's polarization in the same direction that it did in the forward direction leading to a total rotation of 90° with respect to the input light, and thus unwanted optical feedback is stopped from re-entering the laser, which can cause instability and higher noise levels within the mode-locking regime. Therefore it is crucial these back-reflected signals are supressed.

The free-space beam path allows the measurement of the optical power, (using *Thorlabs integrating sphere S145C* in combination with *Thorlabs Power Meter PM100D*) and the pulse duration (using *APE PulseCheck Autocorrelator*). Autocorrelation is a technique which is used throughout the thesis in a number of configurations (described further in section 3.2). In an autocorrelator, the pulsed output is split using a beam-splitter, sending two exact copies of the same pulse on separate paths. One of the pulses is sent along a path which is variable in length, whilst the other is sent on a fixed delay path, and both are finally directed on a path towards the desired detection system, see Figure 2-15.

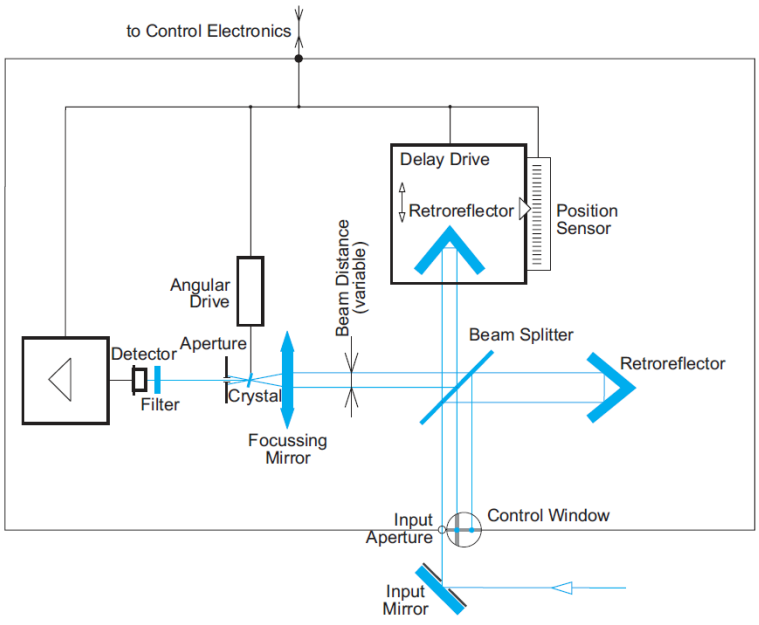

Figure 2-15 - Schematic of the second harmonic generation *APE Pulse-Check Autocorrelator* reproduced from [89], which was used to measure the pulse durations throughout the project.

The intensity of the nonlinear output signal depends on the relative temporal delay between the two pulses as one pulse increasingly overlaps the other in space with every step in the delay stage, until they have made a complete pass of each other. Summing all the output signal intensities over a wide range of delay times gives the resultant second-order autocorrelation intensity $A^{(2)}(\tau)$ for each instant in time:

$$A^{(2)}(\tau) = \int_{-\infty}^{\infty} I(t)I(\tau - t)dt \tag{7}$$

Where τ is the time delay between the pulse copies, $I(t)$ is the intensity of the non-delayed pulse and $I(\tau - t)$ is the intensity of the delayed pulse. In the case of Second Harmonic Generation (SHG) Autocorrelation [90], the combined pulse copies are then focused onto a thin crystal which doubles the frequency of the original input signal (i.e. halves the wavelength). The output signal is non-linearly dependent on the increasing intensity of the combined pulses as their peaks increasingly overlap. This output signal is then filtered out from any residual fundamental radiation and detected by a photodetector.

It is important to note, however, that if the original pulse is assumed to have a Gaussian shape, the autocorrelation of a Gaussian function does not result in an identical copy of that Gaussian function. In fact, it can be shown mathematically that the full width at half maximum (FWHM) of the autocorrelation will be broader than the original Gaussian-shaped pulse by some factor known as the autocorrelation co-factor [91]. Consider an Intensity varying as a function of time $I(t)$ to have a Gaussian shape

$$I(t) = exp\left[-\left(\frac{2\sqrt{ln2t}}{\Delta\tau_p^{FWHM}}\right)^2\right] \tag{8}$$

where $\Delta\tau_p^{FWHM}$ represents the original pulse width. Using expression (7) we find the autocorrelation function $A^{(2)}(t)$ will have a new FWHM of $\Delta\tau_A^{FWHM}$. The FWHM of the original pulse and its autocorrelation differ by the co-factor 1.41

$$\Delta\tau_A^{FWHM} = \mathbf{1.41}\Delta\tau_p^{FWHM} \tag{9}$$

We may prove this by mathematically simulating an autocorrelation[4]. An ultrashort pulse of 5 picosecond duration is assumed to have an intensity described by a Gaussian. Whilst this pulse remains stationary, a simulated copy of this pulse is allowed to traverse the time

[4] This simulation was written in MATLAB and the data was output to Origin Pro.

delay and overlap the original pulse – this simulates the concept of one pulse being delayed with respect to the other using, for example, a mechanical stage in one arm of non-collinear geometry setup, see Figure 2-16.

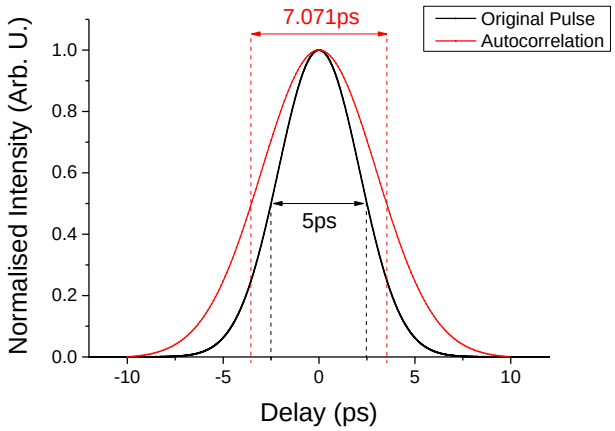

Figure 2-16 – MATLAB simulation of an autocorrelation. An original 5ps pulse was incrementally delayed in order to overlap a stationary copy of itself, giving an autocorrelation with a pulse duration 1.41 times broader (7.071ps) when a Gaussian pulse shape is assumed.

As can be seen, and predicted mathematically, the autocorrelation has a pulse duration of 7.071ps, which is 1.41 times longer than the original 5ps pulse. Therefore for the purposes of this project, when fitting a Gaussian function to each autocorrelation's pulse-width, the value is divided by the co-factor *1.41* in order to demonstrate the more likely original pulse duration (though if an alternative function such as a Lorentzian or a sech^2 better describes the pulse shape upon attempting to fit to the autocorrelation data, their co-factors of 1.54 and 2.0 respectively may be used instead using the same principle).

2.3.2. Power-Current Characterisation

Typical laser characteristics to be measured include P-I (Power-Current) curves, where the average optical power may be measured as a function of the forward bias applied to the gain section. This also provides us with information on the threshold current I_{th} (the current past which lasing may occur), and any indications of thermal rollover; the point at which the diode may begin to break down due to excess current. The study may be repeated whilst simultaneously applying various levels of reverse bias to the saturable absorber section in order to determine the loss in average power due to the increased absorption; useful for when the optimum mode-locking bias conditions are explored. P-I traces were gathered for both the narrow-ridge and tapered waveguide devices as a first comparison of their output power characteristics, see Figure 2-17 and Figure 2-18.

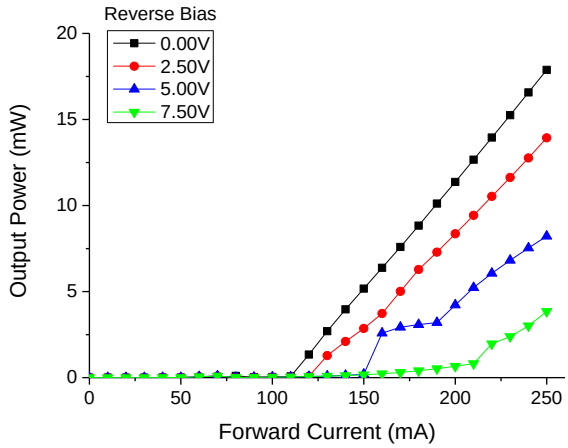

Figure 2-17 – P-I traces for the narrow-ridge-waveguide device for several values of reverse bias applied to the absorber section.

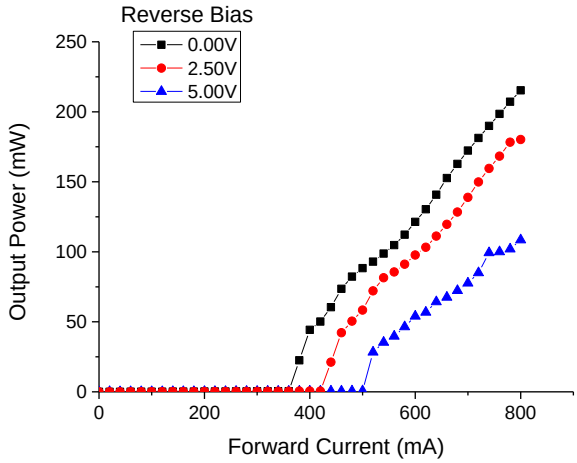

Figure 2-18 – P-I traces for the tapered-waveguide device for several values of reverse bias applied to the absorber section.

Evident in both P-I traces is the sudden increase in output power from hundreds of microwatts to tens of milliwatts at the threshold current, at which point lasing has been initiated. This threshold current is seen to increase for increasing reverse bias applied to the saturable absorber section. This occurs due to the fact that at higher reverse biases there is an increase in absorption and thus the cavity losses, resulting in a higher threshold gain. In particular, it is clear that the overall average output power is far greater in the tapered waveguide device than the narrow-ridge device (around a ten-fold increase), which is anticipated given the significantly greater volume of gain material in the tapered device, which of course additionally requires a greater applied forward current to realise.

Although the PI curves and other characteristic curves were acquired several times throughout the project in order to ensure the output remained consistent, error bars are typically not provided in the two-section passively mode-locked semiconductor laser diode field due to the great stability of such systems, provided the controlling conditions (the diode driver, power supply, temperature control) are also of a high standard and therefore as stable as possible. Because the laser is entirely electronically driven, any fluctuations in output would result in too many unpredictable inconsistencies, and therefore would not be used. Therefore, reproducibility of the results is ensured implicitly.

2.3.3. The Mode-Locking Region

The mode-locking characteristics may then be measured when the biasing conditions to the gain and absorber sections produce a steady train of ultrashort pulses. The repetition rate may be measured using a fast photodetector and RF analyser. Typically, a strong mode-locking region (MLR) is sought out; this is a 2-D region which can be mapped out for which various combinations of forward current ranges and reverse bias ranges lead to stable mode-locking such as that found in [92]. Strong mode-locking is generally indicated by sharp RF trace peaks (narrow linewidths and signal-to-noise ratio typically greater than 30dB [93]). This can be found by carefully varying one parameter through the other in a two-dimensional study. If the RF spectrum is carefully monitored simultaneously for sharp peaks, this region can then be mapped out for easier and more intense exploration of other parameters later, such as average power, optical spectra, pulse duration and peak power. When sharp peaks diminish and broaden on the RF analyser, mode-locking is considered to be weak or non-existent under those conditions. For the narrow-ridge device, strong mode-locking conditions were met within a forward bias range of 200-250mA and a combined reverse bias range of 4.60-7.80V, see Figure 2-19. The individual spectra which verify that these conditions constitute strong mode-locking are presented in *section 2.5*.

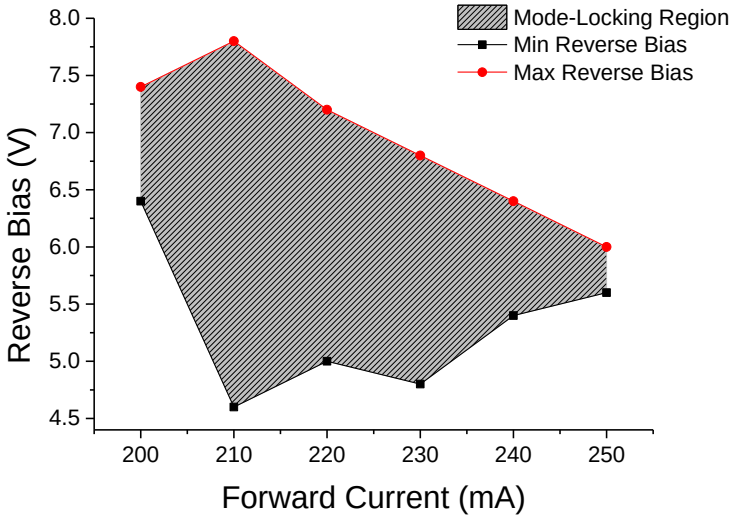

Figure 2-19 – Diagram of the mapped mode-locking region of the narrow-ridge device for varying bias conditions to each section of the device.

For the tapered device, strong mode-locking conditions were met within a forward bias range of 740-800mA and a combined reverse bias range of 3.7-4.4V, see Figure 2-20.

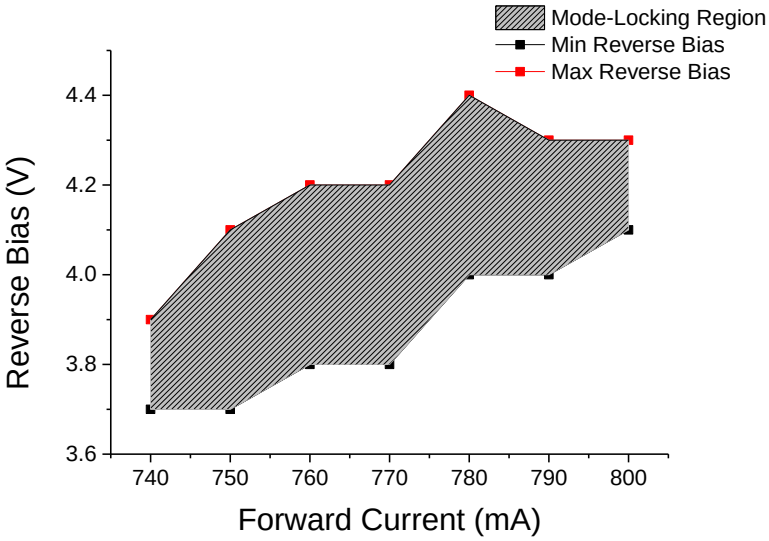

Figure 2-20 – Diagram of the mapped mode-locking region of the tapered device for varying bias conditions to each section of the device

With the biasing conditions now mapped for regions of strong mode-locking of the MLLD, they may now be investigated further for their degree of repetition rate tunability, as well as their impact on optical power, optical spectra and pulse duration at each point in order to determine the optimum conditions for optical sampling in the following chapters.

2.4. Introduction to Repetition Rate Tunability

As discussed in Chapter 1, a vital component of OSBERT is the ability to tune the MLLD's repetition rate electronically. To that end, a number of additional 2-section MLLDs were studied throughout the project under various regimes in order to determine their repetition rate tunability [3, 6] before finally opting for those used throughout the thesis. This section discusses the basis of repetition rate tunability in a number of configurations before discussing the experimental findings on the tuning capabilities of the devices themselves.

Typically if the repetition rate of a laser is to be varied, it may be done so by varying the length of the optical cavity itself, such as by introducing an output coupler mounted on a translation stage in the case of an external cavity laser [94]. Intriguingly, in the case of MLLDs, repetition rate tunability has been demonstrated instead via a variation of several combinations of temperature [76, 95, 96], gain current [76, 86, 97-100] or saturable absorber bias levels [76, 92, 95, 99-103]. The underlying process of such 'internal' repetition rate tunability has been widely discussed for various device types, attributing the phenomenon to a number of principles since trends in tunability vary greatly between device structures and compositions. One explanation is the Pockel's effect, whereby inherently the application of an electrical field across either section of the device may lead to variations in its refractive index [99], thus according to equation (2) this small variation in the gain's refractive index may replace the typical variation in cavity length *L*, and consequently vary the round-trip period within the cavity entirely non-mechanically. Similarly, the plasma effect [104, 105] - a change in the refractive index due to a change in carrier density - has been cited as a cause [98, 99, 101].

Another possible contribution to the repetition rate tunability lies with the Quantum Confined Stark Effect [106, 107], which describes the effect of an external electric field upon the light absorption spectrum or emission spectrum of quantum confinement in quantum wells, wires or dots [108]. Considering a quantum well under zero reverse bias, $V_{rev} = 0$, the electrons and the holes occupy states which are associated with a discrete set of energy bands. Consequently, only a discrete set of frequencies of light may be absorbed or emitted by the system. When a reverse bias $V_{rev} > 0$ is applied, the electron and hole states shift to lower and higher energies respectively [109] and thus the overlap

of the wave-function of each carrier decreases. This reduces the permitted light emission frequencies, and as such the wavelength of light generated may exhibit a red-shift due to the change in confined energy levels [110, 111], see Figure 2-21. Given that the refractive index of MLLDs is by extension wavelength-dependant, this could in turn slightly vary the group velocity, and thus, the detected repetition rate.

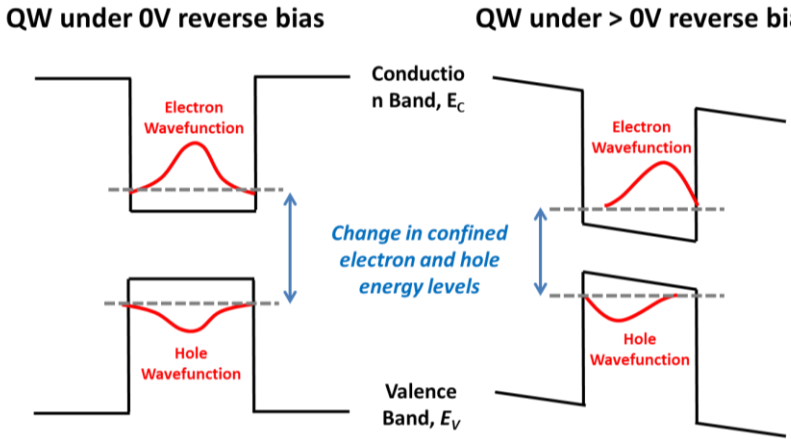

Figure 2-21 –The Quantum Confined Stark Effect (QCSE), where an applied reverse bias causes a decrease in the confinement energy difference in a quantum well.

The electrical repetition rate tuning effect within MLLDs has further been attributed to the so-called 'detuning time' associated with pulse-shaping; temporal shifts in the pulse position through reshaping within the oppositely biased absorber and gain sections, which cause the repetition rate to deviate slightly from the Fabry-Pérot round-trip time [76, 86, 99]. The level of allowable detuning was shown to be a function of pulse energy, pulse-width and complicated saturation and absorption dynamics which depend upon the particular device design and output characteristics. Ultimately, a number of refractive-index and non-refractive-index related phenomena are typically combined and cited in the literature as the cause for repetition rate tunability across a wide range of semiconductor laser diode device types.

Given the cleaving errors typically associated when cutting individual MLLDs after fabrication will vary the device length relating to repetition rate, this tunability provides a degree of electrical fine-tuning [103] for custom applications without the need to incorporate carefully adjusted external cavities to suit the repetition rate, allowing the device to retain its monolithic, stand-alone advantages at high frequencies; that is to say that an error in the length of the device may potentially be corrected by careful selection

of the bias conditions to bring the repetition rate to that expected by the desired length. Conversely, for applications which require longer round-trip times via external cavities, this tunability allows non-mechanical fine tuning of the lower repetition rate external cavity laser. Pulsed semiconductor lasers have also been featured in applications for microwave or millimetre-wave generation [112, 113], and in particular, the advantages in the ability to electrically tune the repetition rate of semiconductor laser devices in such systems have been described in optimising the signal generation [101, 114]. Furthermore, recent developments have demonstrated the benefits of repetition rate tunability in giving rise to wide and customisable RF locking ranges for use in frequency comb generation [76]. Whilst characterising additional devices for their use in this project, we published results showing 5MHz tunability by varying the absorber bias [6], and 30MHz tunability by varying both the gain and absorber bias levels [3].

A summary from the literature of studies on semiconductor laser diode devices which exhibit repetition rate tunability was tabulated for reference, see Figure 2-22. In particular only those studies which included both an account of the repetition rate tunability and an explanation of their findings are presented. In summary it is clear that there exists a degree of ambiguity regarding the exact mechanisms which govern repetition rate tunability in multi-section MLLDs, though as can be seen the detuning associated with pulse re-shaping does tend to be cited more often than the other possible causes. As such it is most likely that a number of the described phenomena are simultaneously responsible for the overall degree of tunability, giving rise to a complex dynamic of competing processes.

[Ref] Year	Laser Description	Rep. Rate (GHz)	Rep. Rate Tunability Enabled By	Total Rep. Rate Tunability (MHz)	Explanation Offered for Tunability
[103] 1997	3-section Quantum Well device with extended cavity, gain and absorber sections	9.3	Changes in bias to gain and absorber sections	87.5	Pulse shaping by the gain and saturable absorber media given as "most possible explanation"
[99] 1997	3-section Quantum Well device with extended cavity, gain and absorber sections	17.7	Changes in bias to extended cavity, gain and absorber sections	280	Pulse shaping (Pockel's effect considered partly responsible but calculated as too small an effect for their tunability)
[86] 2006	2-section Quantum Dot tapered waveguide MLLD with gain and absorber sections	24	Changes in bias to gain and absorber sections	50	Pulse shaping suggested, along with gain and absorber dynamics leading to refractive index variations
[98] 2013	2-section Quantum Dot MLLD with gain and absorber sections	20	Changes in bias to gain section	40	Pulse shaping and carrier density induced refractive index change "could be" responsible
[102] 2007	2-section Quantum Dot MLLD with gain and absorber sections	40	Changes in bias to gain and absorber sections	100	No explanation offered, however does cite [86] as having the same trends in tunability
[101] 1996	4-section Quantum Well MLLD device with phase control, gain, absorber and Distributed Bragg Reflector sections	37.45	Changes in bias to a phase control and absorber sections	1000	Plasma effect due to the variations in charge on each section
[76] 2012	2-section Quantum Dash MLLD with gain and absorber sections	21	Changes in bias to gain and absorber sections, and change of temperature to entire device	440	Pulse shaping given as a possibility as well as changes in the refractive index
[97] 2009	2-section Quantum Dot MLLD with gain and absorber sections	16	Changes in bias to gain and absorber sections	100	Complex dynamics of gain and absorption with varying pulse energies causing re-shaping
[95] 2005	3-section Quantum Well MLLD with gain and absorber sections, and a third selectable gain or absorber section	37	Changes in bias to absorber sections and change of temperature to entire device	57	Reduced group refractive index due to increased carrier density
[93] 2015	2-section Quantum Dot MLLD with gain and absorber sections	33.48	Changes in bias to gain and absorber sections	300	Thermal expansion of material and carrier escape reducing refractive index.
[6] 2015	**2-section Quantum Dot tapered waveguide MLLD with gain and absorber sections**	**15.96**	**Changes in bias to absorber section**	**5**	**Considered to likely be a combination of all described effects, particularly pulse shaping. For details on [6] see *Section 2.5.3*** **[3] 2014** | **2-section Quantum Well MLLD with gain and absorber sections** | **19.37** | **Changes in bias to gain and absorber sections** | **30**

Figure 2-22 – Table of devices from the literature which exhibited repetition rate tunability by varying the bias applied to one of their sections, or by varying the temperature of the device. The references highlighted in bold were regarding devices studied and published during this project.

2.5. Experimental Findings for Electronic Repetition Rate Tunability

In the following section the narrow-ridge waveguide and tapered waveguide devices are compared for their repetition rate tunability, and other corresponding laser output characteristics.

2.5.1. Narrow-Ridge Waveguide Device

As discussed in *Section 2.3*, the MLR of the device has been established; however the degree of repetition rate tunability varies across the biasing conditions. Exploring the previously determined MLR, the exact repetition rate was found at each point within the mapped region using individual RF spectra across each combination of bias parameters, see Figure 2-23.

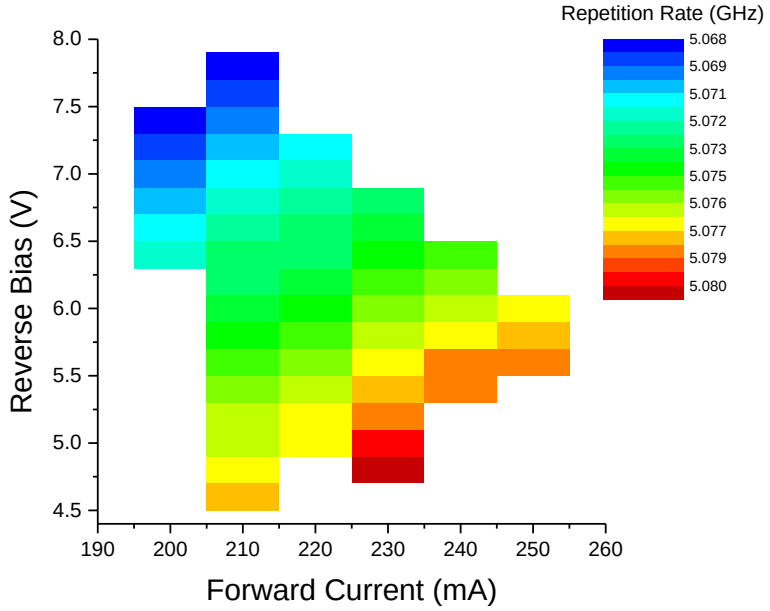

Figure 2-23 – The MLR as a contour map indicating the repetition rate in GHz found at each combination of biasing conditions to the absorber and gain sections.

As can be seen, the greatest repetition rate tunability range is found for a forward current to the gain section of 210mA, whilst the reverse bias to the saturable absorber is increased from 4.60V to 7.80V. Although experimentally the reverse bias and forward current changes were made in discrete steps (as shown by the contour plot), in reality the repetition rate is continuously tunable by these means. Individual RF spectra were then plotted for this region at representative 0.2V increments, see Figure 2-24.

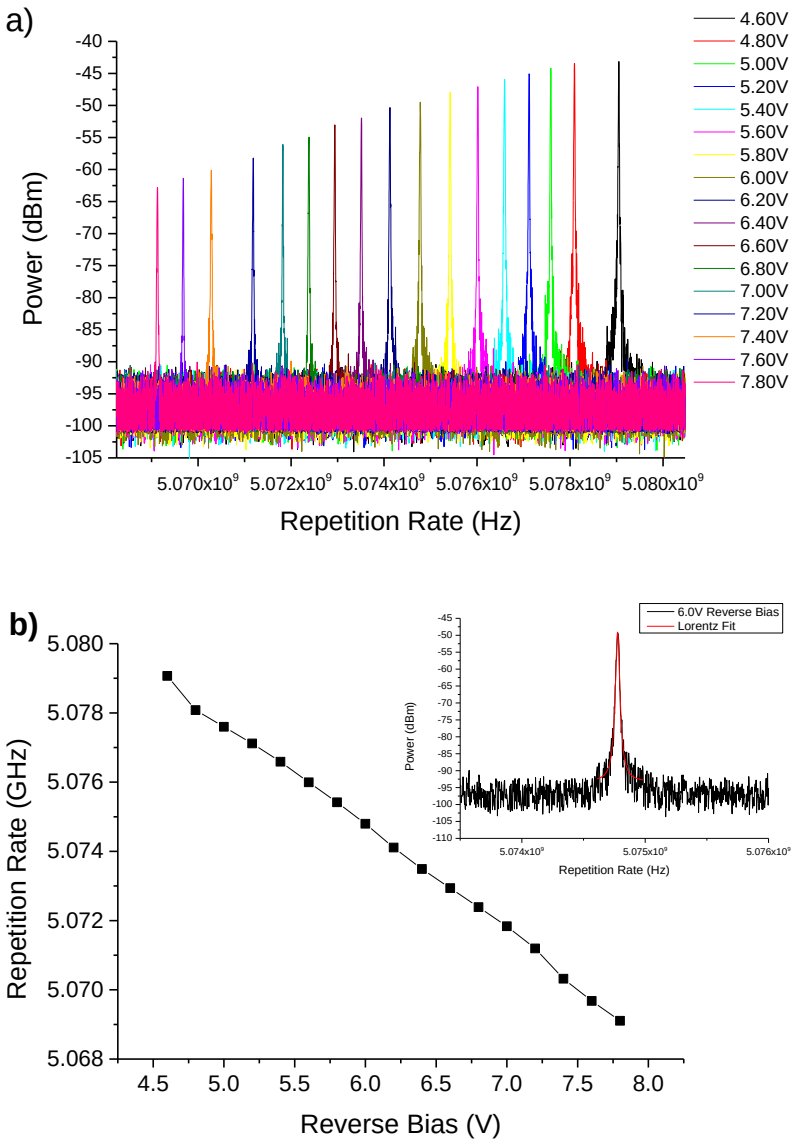

Figure 2-24 – a) RF Spectra at 210mA forward current to the gain section for increasing reverse bias to the absorber section across the MLR b) The Repetition Rate is seen to be tuned by approximately 10MHz; inset, an example spectrum is fit with a Lorentzian in order to mathematically determine the centre frequency of the trace

Each spectrum was fit with a Lorentzian function in order to mathematically determine each peak's central frequency. As such a repetition rate tunability of $\Delta f = \sim 10MHz$ is found for a change in reverse bias voltage to the absorber section of $\Delta V = 3.20V$. It is advantageous and important that the full span of the repetition rate tunability falls as linearly as possible with the variation in reverse bias. Optical sampling techniques such as OSCAT rely on the laser's repetition rate tunability giving rise to a proportional increase in delay; if this was a non-linear trend, it would be extremely difficult to deconvolve each step meaningfully through the development of OSBERT, described in Chapter 3 onwards.

As discussed throughout this chapter, varying the biasing conditions does not only affect the repetition rate; in fact these conditions are responsible for the entire output characteristics of the device, and as such varying the reverse bias by the 3.20V required to tune the repetition rate fully will have a knock-on effect on all other parameters.

Firstly, due to the increased absorption brought about by increasing the reverse bias to the absorber section, the average power will intrinsically fall, see Figure 2-25.

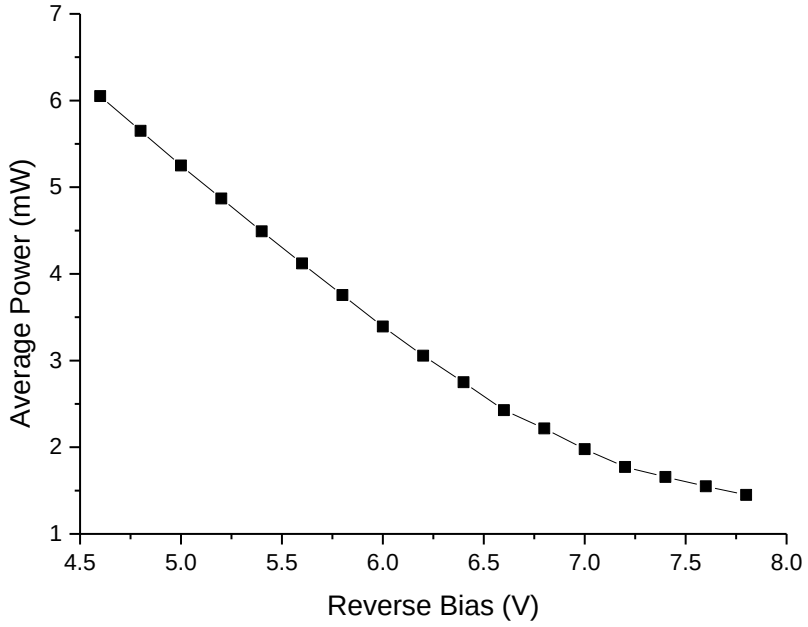

Figure 2-25 – The average optical power of the MLLD is seen to decrease due to increase of the reverse bias applied to the saturable absorber section.

Additionally, the change in applied electric field also leads to changes in the optical spectrum, see Figure 2-26.

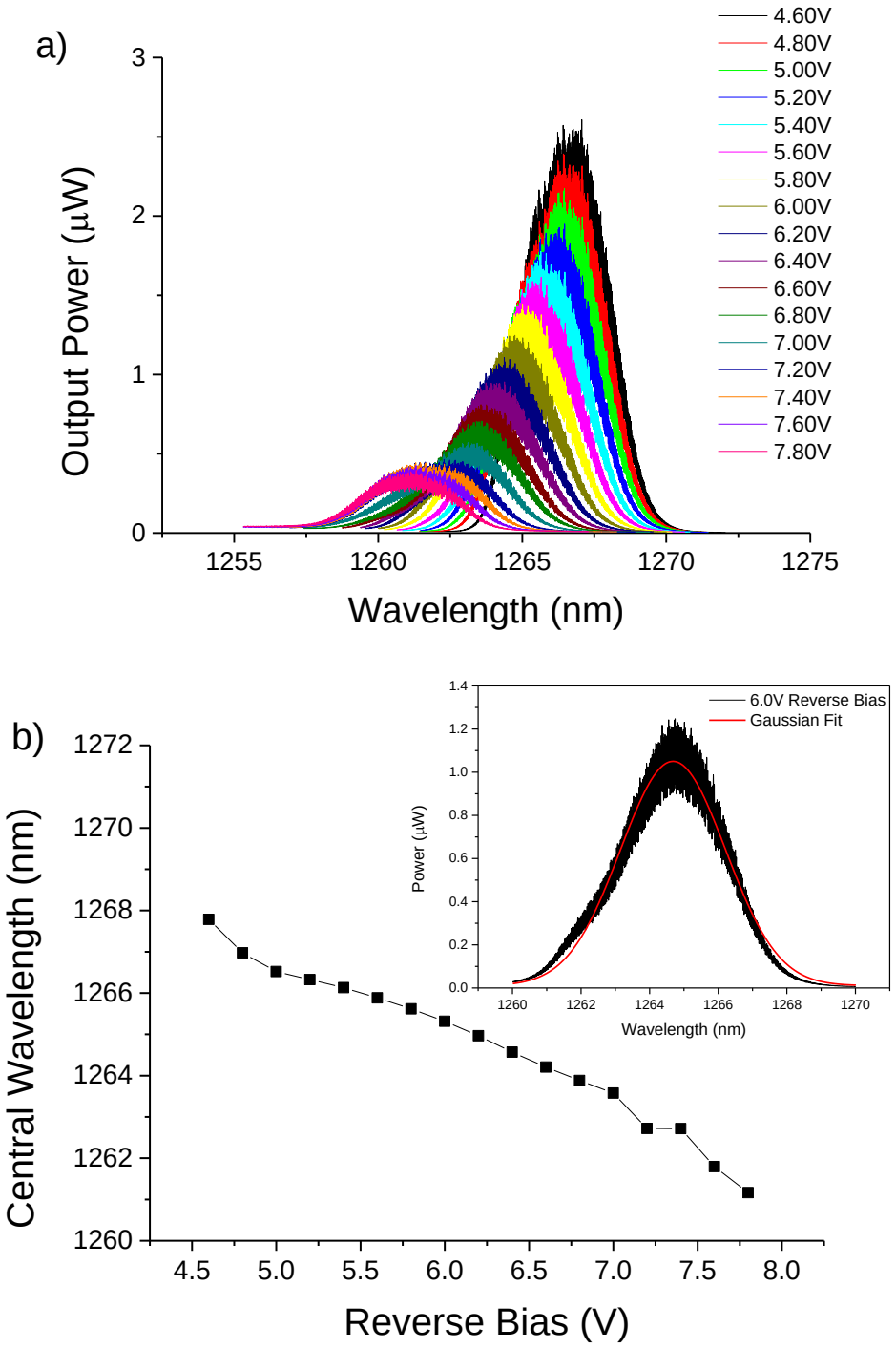

Figure 2-26 – a) Optical spectra traces showing the alteration in the optical spectrum as a result of increasing the reverse bias to the absorber section in order to tune the repetition rate. b) The general blue-shift of the central wavelength; inset, an example spectrum is fit with a Gaussian in order to mathematically determine the central wavelength.

As is demonstrated in Figure 2-27, the pulse shape is assumed to be Gaussian from the goodness of fit to the autocorrelations, and therefore this is also the fit used for the optical spectra. After fitting, each optical spectrum's central wavelength was plotted as a function of the applied reverse bias to reveal a blue shift. This would therefore not be directly supportive of the quantum confined Stark effect which as discussed, predicts a

red-shift in the optical spectrum, although (as is often cited in the literature) it is possible that QCSE is partially or fully countered-acted on by some of the many other described detuning factors; ultimately it is expected that any number of such effects exist together, dynamically balancing each other and producing a resultant net change in repetition rate.

We may then finally consider the effects of increasing the reverse bias applied to the absorber on the resultant pulse duration, see Figure 2-27.

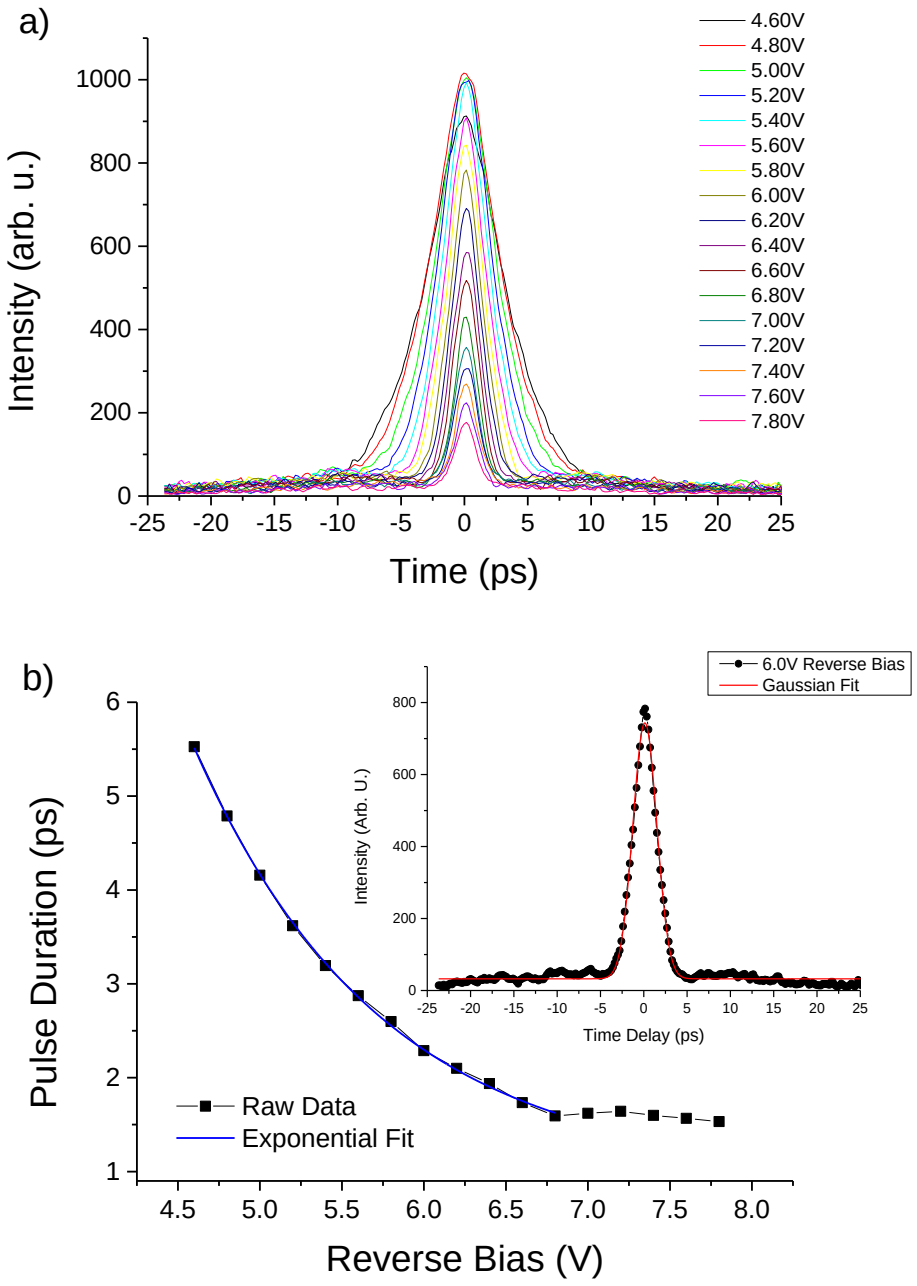

Figure 2-27 – a) Autocorrelation traces for increased reverse bias applied to the absorber b) the extracted pulse durations for each voltage step; inset, an example autocorrelation is fit with a Gaussian autocorrelation function in order to mathematically determine the pulse duration.

As the pulses in this work (acquired using the *APE PulseCheck Autocorrelator* described in *section 2.3.1*) are assumed to have a Gaussian shape, each autocorrelation is fit with a Gaussian whose measured FWHM is then divided by the Gaussian co-factor value, 1.41.

The pulse duration as expected has also reduced with each increase of reverse bias, initially following a trend well fitted by an exponential decay. This trend (which has been observed throughout the project in other devices ([3] for example) is in agreement with pump-probe studies [115] which have shown an exponential decrease in absorption recovery time with an increase in reverse bias applied. Thereafter, the pulse duration remains relatively unchanged. This limit in pulse duration despite increasing the absorber bias has previously been linked with weaker absorption saturation for increasing reverse bias levels [116].

As discussed, the benefit of pulsed laser output over continuous wave output is the ability to access higher instantaneous optical power with each intense pulse; this is the peak power and is calculated from the average power, the pulse duration and the repetition rate according to expression (4). Peak powers will therefore increase with increasing average powers, decreasing pulse durations and decreasing repetition rates. The maximum achievable peak power is of particular interest in non-linear optics. For example, second harmonic generation and two-photon absorption are both non-linear optical phenomena, whereby the desirable signal grows non-linearly with incident light intensity. The peak power was then calculated for increasing reverse bias according to expression (4), see Figure 2-28.

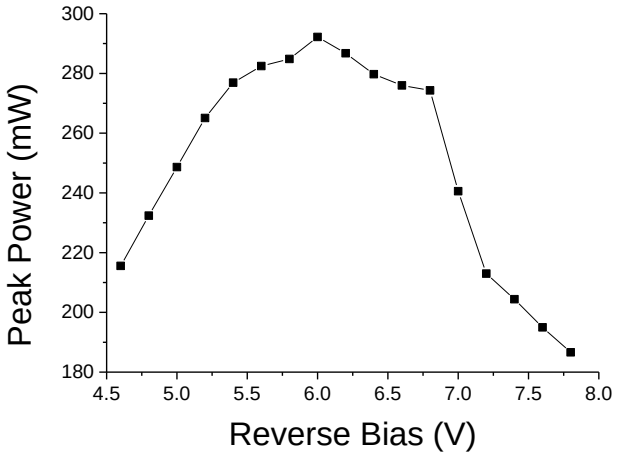

Figure 2-28 – Evolution of the calculated peak power as a result of increasing the reverse bias applied to the saturable absorber section.

The trend in peak power can be accounted for when considering that whilst the pulse duration is decreasing for increasing reverse bias, the average power is decreasing. Thus the turning point at the mid-way point of the MLR is indicative of the change in rate of these dynamics, reaching 292mW peak power at 6.0V, with just 3.4mW average power.

2.5.2. Repetition rate tuning with current and temperature

As was previously established from theory and from the generation of the laser's specific mode-locking region (Figure 2-23), the repetition rate may also be tuned by varying the forward current applied to the gain section, as well as the reverse bias applied to the absorber section. Also mentioned but not studied is the ability to do so by varying the operational temperature of the entire device. For a full cross-sectional analysis, both the forward current and temperature were independently varied in order to ascertain their degrees of tunability. In the case of the forward current study, the temperature remained at a constant 20°C and the reverse bias to the absorber remained constant at 5.90V, varying the forward current from 210mA to 250mA. In the temperature study, the forward current applied to the gain section remained constant at 210mA whilst the absorber was constantly biased with 5.90V, varying the temperature from 16°C to 24°C, see Figure 2-29.

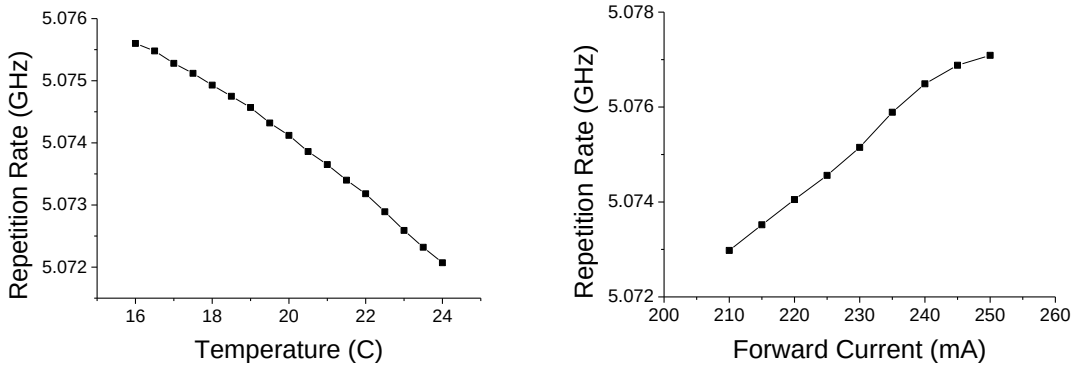

Figure 2-29 – Left, the change in repetition rate brought on by varying the temperature of the laser. Right, the change in repetition rate brought on by varying the forward current applied to the gain section. In each case the reverse bias to the absorber was constant at 5.90V.

The direction of 3.53MHz of repetition rate tuning is negative for increasing temperature, reported similarly in [76], however the opposite to that found in [95]. The positive 4.11MHz change in repetition rate for increasing forward current was found in both [76] and [97], however the opposite trend was found in [86, 98, 102], and as such we must conclude that without further comprehensive investigations of appropriate devices based

on a particular wafer structure, it is currently not possible to predict the direction or magnitude of repetition rate tunability within the scope of this project.

It is possible in the case of the temperature study that thermal expansion is taking place in the GaAs [117] which makes up the majority of the device. A similar part-explanation was given in [93], although this was not due to the direct variation of the devices operational temperature, but due to temperature induced carrier heating for increasing bias levels. In the case of the narrow-ridge laser, the absolute device length may perhaps be increased with increasing temperature provided by the Peltier cooling system, giving rise to a longer roundtrip period and thus a lower repetition rate. This was calculated, see *Appendix 7.2.1*, and was found to give rise to too small a change in the device to be solely responsible for the repetition rate tuning (250kHz compared to the 3.53MHz measured). However, as with all other tuning effects, it is possible that thermal expansion at least contributes partly, whilst complex carrier dynamics and pulse shaping are the most significant causes.

As with the reverse bias study, the forward current and temperature studies were examined in order to determine how the other output characteristics were affected in parallel with the repetition rate tuning, beginning with the changes in output average and peak powers, see Figure 2-30.

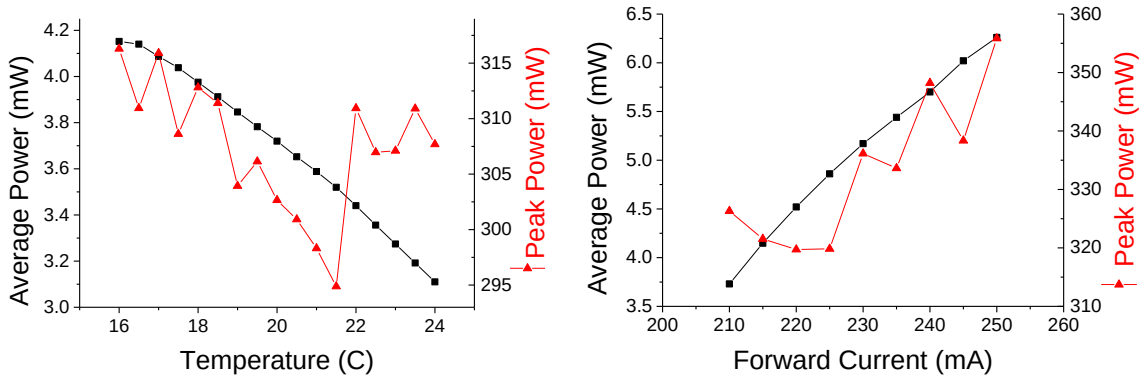

Figure 2-30 - The change in average and peak powers brought on by left, varying the operational temperature of the laser and right, varying the forward current applied to the gain section.

In the case of the temperature study, the average power drops for increasing temperature, and may be explained in terms of carrier dynamics. An increase in temperature will lead to a higher rate of Auger recombination, which is a non-radiative process. Higher temperatures will also more readily excite carriers out of the hetero-

structure, further reducing those available for radiative combination. The peak power varies somewhat, and given it is calculated from the repetition rate, average power and pulse duration across the tuning range, this is not surprising.

For the forward current study however, the average power steadily increases due to the increase in carriers made available for radiative recombination within the active region. The general trend is an increase in peak power, likely due to the greater average powers associated with each point. The change in pulse duration for the temperature and forward current study were also measured, see Figure 2-31.

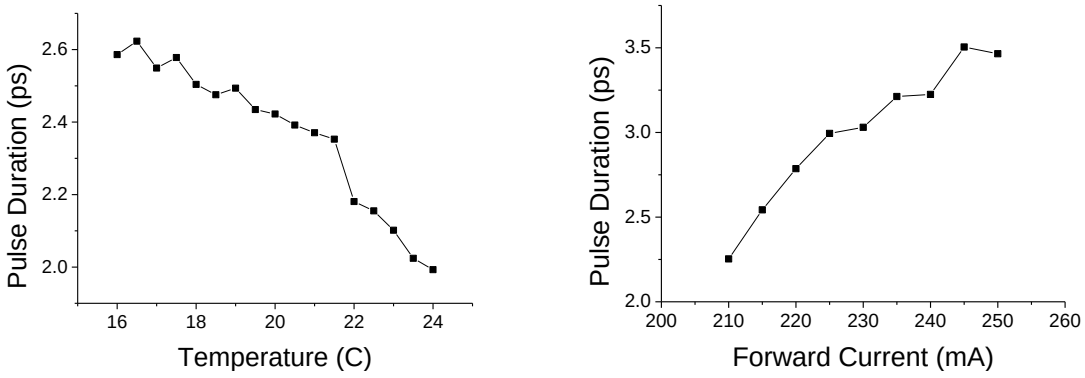

Figure 2-31 - Left, the change in pulse duration brought on by varying the operational temperature of the laser. Right, the change in pulse duration brought on by varying the forward current applied to the gain section.

For the temperature study, pump probe experiments [118] have shown that the decreasing pulse duration for increased temperatures is due to the associated stronger thermionic carrier emission, which gives rise to decreased absorption recovery times. In this sense the increased temperature can be seen to aid in the removal of photo-generated carriers. This is in contrast with the forward current study, in which the pulse duration increases for increasing current, and may be explained by an increase in self-phase modulation [119], a process where gain saturation causes changes in carrier density which in turn gives rise to changes in refractive index, dependent on the light intensities – ultimately this could broaden the pulses due to the changes within the optical spectra.

Finally the optical spectra of both the temperature and forward current studies were analysed for their shift in central wavelength, see Figure 2-32.

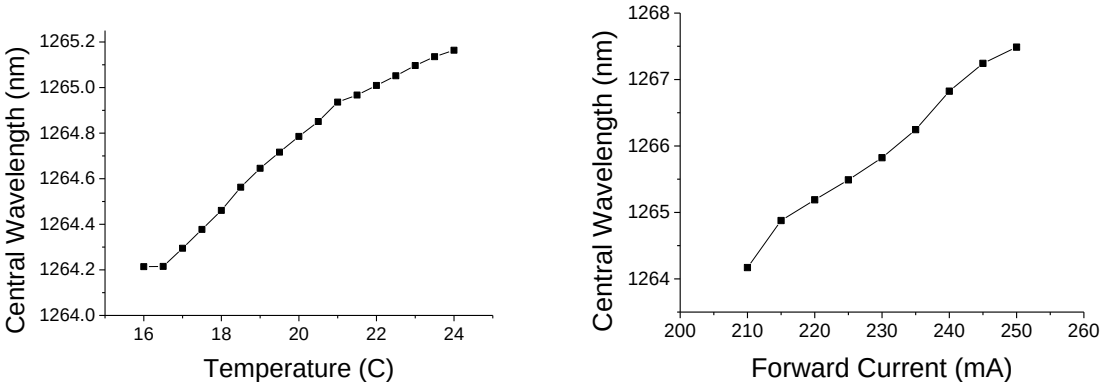

Figure 2-32 - Left, the change in the central wavelength of the optical spectra brought on by varying the operational temperature of the laser. Right, the change in the central wavelength of the optical spectra brought on by varying the forward current applied to the gain section.

During the temperature study, the optical spectra can be seen to red-shift towards longer wavelengths for increasing temperature. This is simply explained in terms of the band-gap energy E_g, which reduces for increasing temperature T according to the Varshni relation [120] such that

$$E_g(T) = E_g(0) - \frac{\alpha T^2}{T + \beta} \tag{10}$$

Where α and β represent fitting parameters specific to the semiconductor material, and as such the expression describes the difference expected in the band-gap energy at some temperature *T* and that expected at absolute zero.

In the case of the forward current study, a spectral red-shift was also observed. Given the gain section accounts for the majority volume of the entire device (compared to the significantly smaller absorber section), it is likely that a degree of Joule heating and other thermal effects due to non-radiative combination take place as the forward bias is applied across its length [121], leading to similar thermal effects found in the temperature study. These effects are likely exaggerated due to the fact the device is mounted p-side up, meaning the active region is physically further from the Peltier-cooler than if the device were mounted p-side down.

In order to assess the repetition rate tuning performance of all three tuning studies (reverse bias, temperature and forward current), the variation of each characteristic was plotted as a function of the magnitude of the change in repetition rate *Δf*, see Figure 2-33.

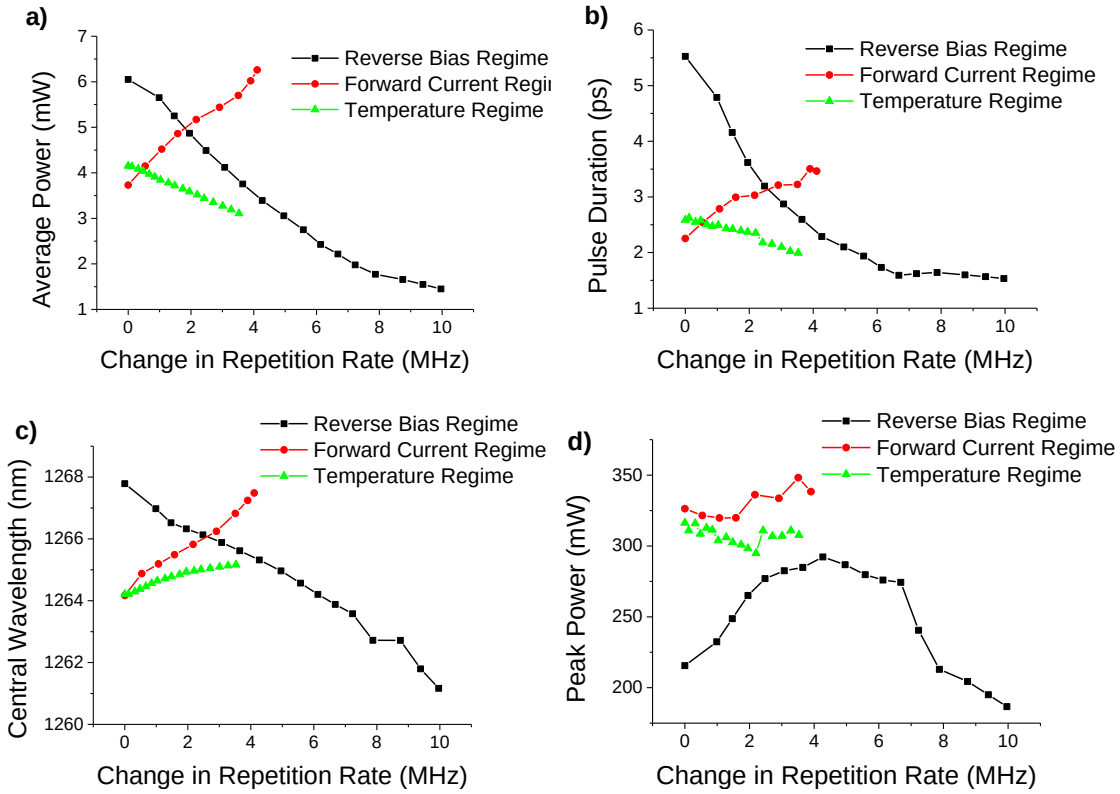

Figure 2-33 – Comparison of reverse bias, temperature and forward current studies of repetition rate tunability and their resultant trends in a) average power b) pulse duration c) central emission wavelength and d) peak power.

As can be seen, for the conditions examined, the available magnitude of absolute repetition rate tunability was far greater for the reverse bias study compared to both the temperature and forward bias cases, however this larger repetition rate tunability is accompanied by greater variations in the output characteristics.

As a reminder, one of the aims of this project is to achieve optical sampling based on a variation of the OSCAT technique, discussed in Chapter 1. According to expression (1) in order to build OSBERT, the repetition rate must be tunable by Δf, and (to complete another aim) this should ideally occur as quickly as possible in order to demonstrate fast scan rates. Therefore, we immediately exclude the notion of performing optical sampling based on repetition rate tuning by temperature, because stabilising the temperature of the device is a process which oscillates over several tens of seconds before settling; therefore each individual time delay point would have to be acquired on this time scale, leading to extremely slow scan rates – though it would be possible. Therefore, the repetition rate will be far more quickly tuned electronically via the gain or absorber biasing conditions.

Having now the choice of tuning either by variations in forward current to the gain section or in reverse bias to the absorber section, we finally exclude the former. The primary reason is simply that tuning via the gain section led to far lower repetition rate tunability, and ultimately this value needs to be as high as possible (discussed further in chapter 3). The secondary reason is that in order to quickly drive the change in repetition rate electronically a signal generator must be used (discussed further in chapter 4). In the case of the reverse bias to the saturable absorber, this requires only replacing the power supply with the signal generator, whereas in the case of the forward current to the gain section, this requires modulating the signal to the diode driver; a far less trivial task. On this basis, for the purposes of the remainder of this project, repetition rate tunability brought about by variations in the reverse bias supplied to the absorber section was adopted for all experiments.

An option for a future study may be to modulate the bias supplied to both the gain and absorber sections simultaneously in order to attempt to limit the changes in the output characteristics. Though non-trivial, a region could be mapped out where a variation in forward current applied to the gain section could compensate for output characteristic changes brought on by variations in the forward current applied to the gain section, whilst still allowing a linear change in repetition rate.

2.5.3. Tapered-waveguide laser

Similar output characteristic data was acquired and presented at a conference for the tapered-waveguide laser [6], focussing on the repetition rate tuning by variation in reverse bias applied to the absorber section, and using the same fitting techniques to mathematically determine the trends in the other corresponding output characteristics. These are briefly detailed here for contrast with the narrow-ridge device. Most importantly, we consider the repetition rate tunability which was maximised to 5MHz by fixing a forward current to the tapered gain section of 760mA, whilst tuning the reverse bias applied to the absorber section from 3.80V to 4.20V, see Figure 2-34.

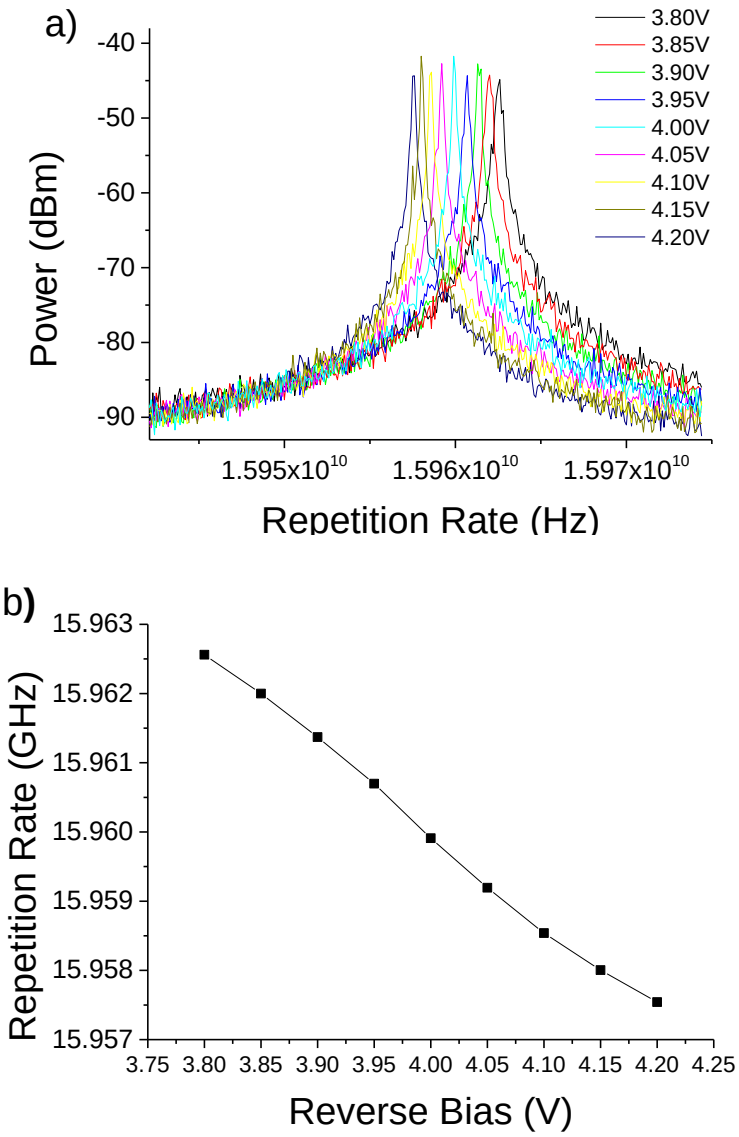

Figure 2-34 - a) RF Spectra at 760mA forward current to the gain section for increasing reverse bias to the absorber section across the MLR. b) The repetition rate is seen to be tuned by approximately 5MHz.

Similarly to that of the narrow-ridge device, the tapered device also exhibited a decrease in repetition rate (or negative tuning) for increasing reverse bias.

It is important to also remember that the corresponding output characteristics will also vary due to the change in biasing conditions. Similarly to that of the narrow-ridge waveguide device, the optical spectra collected across the reverse bias range were found to blue-shift, see Figure 2-35.

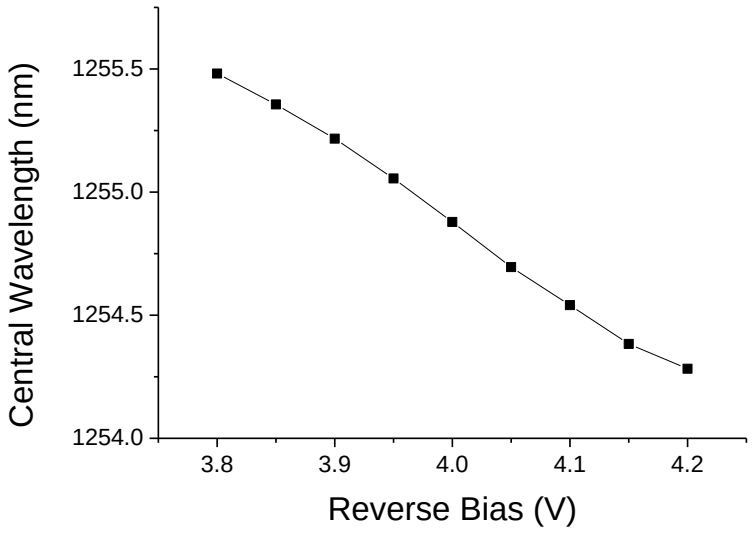

Figure 2-35 – A general blue-shift of the central wavelength of the optical spectra was brought on by increasing the reverse bias applied to the absorber section of the tapered waveguide device.

As with the narrow-ridge device, the pulse duration was found to decrease exponentially for increasing reverse bias applied to the saturable absorber section, see Figure 2-36.

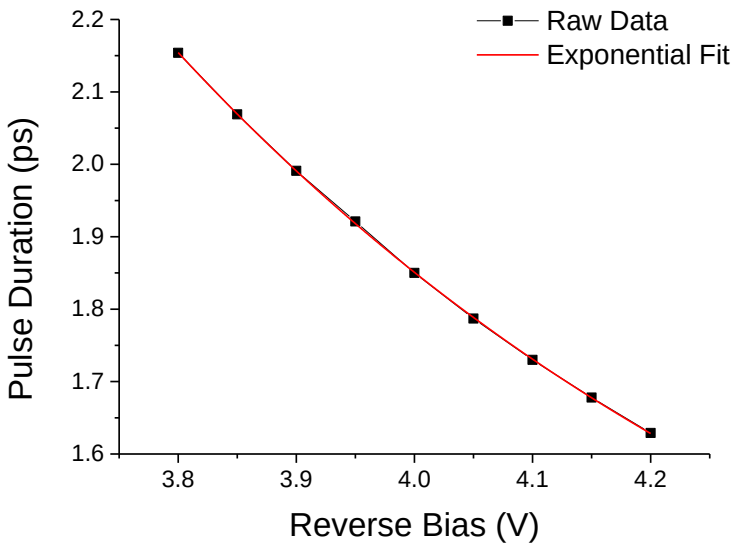

Figure 2-36 - The extracted pulse durations for each reverse bias value applied to the absorber section of the tapered waveguide laser.

Unlike the narrow-ridge device, however, a pulse duration limit is not reached here for higher reverse bias values. This is due to the fact that stable mode-locking ended abruptly within this particular regime of the device's MLR, and pulse durations were no longer measurable by autocorrelation.

Finally, also as with the narrow-ridge device, the average power decreased across the increasing reverse bias range due to the greater level of absorption in the saturable absorber, however the peak power continually increased, see Figure 2-37.

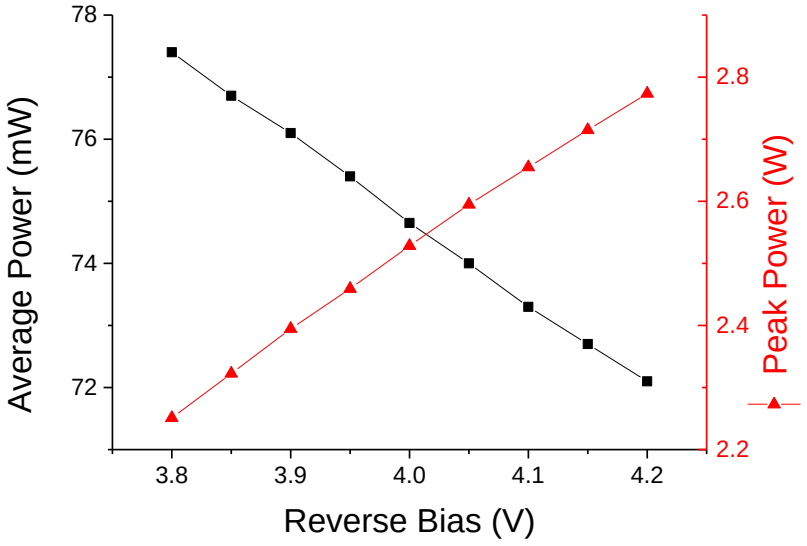

Figure 2-37 – Whilst the increase in reverse bias to the absorber section has the effect of decreasing the average output power, the peak power increases.

As with the narrow-ridge device, the achievable peak power is important for consideration in non-linear optics such as two-photon absorption, discussed further in chapter 3. Whereas the narrow-ridge device showed peak powers in the range of a few hundred mW, the inherent increased average power owed to the tapered gain section has also given rise to significantly higher peak powers of a few W, as expected from expression (4).

2.6. Conclusions

The narrow-ridge device was found to exhibit a maximum tunability of around 10MHz whilst a constant forward bias of 210mA was applied to the gain section, and a reverse bias of 4.60-7.80V was applied to the absorber section. By contrast, the tapered waveguide device exhibited a maximum tunability of around 5MHz whilst a constant forward bias of 760mA was applied to the tapered gain section, and a reverse bias of 4.60-7.80V was applied to the narrow absorber section. It was concluded that without either more comprehensive experimental and theoretical information in the literature, or more devices to systematically test, the exact mechanism for the repetition rate tuning may not be precisely pin-pointed, but attributed to a dynamic interplay of gain and absorber dynamics, refractive index changes, spectral shifts and pulse shaping. This tunability, as

discussed in Chapter 1, is vital to the development of the optical sampling technique OSBERT, which is similar to OSCAT and is studied in the following chapters.

Repetition rate tunability was also found for varying the temperature of the narrow-ridge device and for varying the forward current applied to the gain section. The level of tunability over these regimes was found to be lower than that of the reverse bias study, and as such was excluded from further experiments. An interesting idea for future experimentation would be to simultaneously modulate the biasing conditions in both the gain and absorber sections in order to attempt to maintain relatively constant output characteristics.

A parametric study of all major output characteristics across both the narrow-ridge and tapered waveguide devices demonstrated that whilst both exhibit many opportunities for repetition rate tunability via selected changes in the reverse bias, we must consider also that the average power, peak power, optical spectra and pulse durations will all be varying simultaneously. Consider the example of using this repetition rate tunability, in an OSCAT system as a replacement for a two-photon absorption mechanical stage optical sampling system. The mechanical stage system varies only the optical path length between two identical pulse trains, reading the nonlinear TPA signal at a detector; the laser parameters are held constant throughout. Adopting instead an OSCAT regime involves varying the repetition rate in order to produce the same results, whilst keeping the optical path length constant. If one of the described MLLD devices were used in such a configuration, we must consider the difference in results which may be expected.

For example, given TPA is a nonlinear phenomenon which is heavily dependent upon the laser excitation power and wavelength, driving the temporal delay via the reverse bias applied to the devices will likely impact not only the interaction, but the resultant traces. In particular the decrease in average power across the range will likely skew the baseline, whereas the increase in peak power due to shorter pulse durations will improve the nonlinearity effect, which due its wavelength-dependence, will also change with the slight blue shift of the optical spectra. The same can be said of a linear detection regime (such as single photon absorption) depending on the detector's (or the target's) spectral

responsivity, however in this case the peak power and pulse duration will have less of an impact than average power or central wavelength.

A summary of the change in output characteristics are generalised and tabulated for each device as they will be referred to throughout the subsequent chapters, see Figure 2-38.

NARROW-RIDGE WAVEGUIDE DEVICE		
Output Characteristic	**Description of response to change in reverse bias (4.60V to 7.80V) at 210mA forward current**	**Percentage Change**
Repetition Rate	Approximately 10MHz decrease from 5.079GHz to 5.069GHz	-0.20%
Average Power	Approximately 4.6mW decrease from 6mW to 1.4mW	-76.70%
Optical Spectrum	Central wavelength decrease of 7nm from 1268nm to 1261nm	-0.60%
	Rough increase in FWHM of ~1nm from ~3nm to ~4nm	+33.3%
Pulse Duration	Approximately 4ps decrease from 5.5ps to 1.5ps	-72.70%
Peak Power	Initial increase from 215mW up to 290mW at 6.0V, followed by a decrease to 185mW at 7.80V	+34.90%, -36.20%

TAPERED WAVEGUIDE DEVICE		
Output Characteristic	**Description of response to change in reverse bias (3.80V to 4.20V) at 760mA forward current**	**Percentage Change**
Repetition Rate	Approximately 5MHz decrease from 15.962GHz to 15.958GHz	-0.03%
Average Power	Approximately 5.5mW decrease from 77.5mW to 72mW	-7.10%
Optical Spectrum	Central wavelength decrease of ~1.25nm from 1255.5nm to 1254.25nm	-0.10%
	Rough increase in FWHM of ~0.45nm from ~3.5nm to ~3.95nm	+12.90%
Pulse Duration	Approximately 0.5ps decrease from 2.15ps to 1.65ps	-23.30%
Peak Power	Approximately 0.55W increase from 2.25W up to 2.8W	+24.40%

Figure 2-38 – Overview of the output characteristic changes induced by tuning the repetition rate via the reverse bias applied to the saturable absorber of both the narrow-ridge and the tapered device.

As can be seen, there are a number of important differences between the two devices; whilst they share a similar wavelength, the narrow-ridge device has a repetition rate approximately a third of that of the tapered device, and both are capable of producing pulses as short as a few picoseconds. However, the ultimate key difference in the devices is their difference in output powers. Whilst the narrow ridge device achieves a few hundred mW peak power, the tapered device achieves peak powers of several W. It is this key difference which will determine the devices' suitability for non-linear optics detection methods such as TPA when deployed in the optical sampling systems developed throughout this project.

Important to note is the percentage changes in the output characteristics over their repetition rate tunability range. Although the narrow-ridge device achieves a higher repetition rate tunability Δf of 10MHz versus the tapered devices' 5MHz, it occurs over a significantly broader range of the reverse bias to the absorber section (a total of 3.20V versus 0.4V respectively), and so it is clear to see the resultant output characteristic changes are also significantly greater in the narrow-ridge device. For the subsequent chapters we will refer to the device-specific ratio of repetition rate tunability to reverse bias amplitude as the 'characteristic tunability', $\Delta f_{rep}/\Delta V$, in units of MHz per V. As such, the narrow-ridge device has a characteristic tunability of 3.125 MHz/V whilst the tapered device quadruples this performance with 12.5 MHz/V. This value gives a strong numerical indication of the efficiency of each device for their deployment in optical sampling systems which require a change in repetition rate via biasing conditions; ultimately a large tunability over as narrow a sweep of the reverse bias as possible is preferred in order to minimise the alterations to the additional laser output characteristics. These factors are always taken into consideration in the following chapters.

3. OSBERT: Proving the Principle

This chapter discusses the fundamentals of the first optical sampling technique developed during the project. OSBERT (Optical Sampling By Electronic Repetition-Rate Tuning) is described from the basic theoretical background with regard to a viable replacement for optical sampling techniques which use mechanical stages, thus accomplishing the aim of scanning without any mechanical parts, owed to the electrical repetition rate tunability discussed in Chapter 2. The technique is then demonstrated experimentally and referred to in this section as S-OSBERT (Slow-OSBERT) due to the slow nature of the data acquisition, similar to that of the mechanical stage it replaces. The lack of any moving parts paves the way for a significant increase in scan rate which is discussed in the following chapter. Moreover, it is shown for the first time during this chapter that OSBERT requires only one laser, differentiating it further from the two-laser ASOPS and ECOPS techniques described in Chapter 1. OSBERT is tested in simple proof-of-concept applications, using both linear and non-linear optics approaches, and the results are contrasted with a conventional mechanical translation stage technique.

3.1. Theoretical introduction

As discussed in the introduction, the OSBERT method is based partially on the principle of OSCAT; a technique where a temporal delay between pump and probe pulses at some target position is brought about by varying the laser's repetition rate, and introducing a large passive imbalance between the two arms of an interferometric setup. The key difference is that unlike OSCAT which realises the repetition rate tunability through mechanical intra-cavity mirror variation, OSBERT achieves this by variations in electrical biasing, as demonstrated in chapter 2.

In an OSBERT setup, the passive delay line (PDL) which makes the long arm of an interferometer is long enough (accommodating many roundtrip periods, $T_{rep} = 1 / f_{rep}$), that adjusting the repetition rate of the source MLLD causes a change in the delay time between pump and probe pulses at some target position. Upon each instance the repetition rate is tuned, the probe pulse is delayed further behind the pump pulse. Depending on the application, either the PDL length l or the range of repetition rate tunability Δf may be adjusted to optimise the available scan range.

At first the MLLD is seen to be pulsing at some initial repetition rate f_1, whose roundtrip period is its inverse. Both resultant pulses (via the short arm and the PDL) upon recombination at some target position are found to have a fixed temporal delay over time. As the reverse bias to the absorber is increased, the repetition rate is detuned slightly to f_2. Whilst this new repetition rate has now encountered the same target position via the short arm, the train of pulses with the former repetition rate f_1 is still temporarily propagating at the target position, as the train of pulses with the new repetition rate has been delayed. When the temporal delay induced by the PDL is traversed, this results in both long and short arm beams conveying the same repetition rate to the target position. The fundamental difference in the final scenario is that the change in repetition rate via the long PDL has temporally offset the pulses at the final target position. This process may be repeated from a minimum repetition rate to a maximum repetition rate in user-defined steps in order to scan temporally across a maximum range.

Mathematically, restated here from [59, 60], consider that the short arm pulse train contains a reference pulse i which arrives at the target position at time $t = 0$, and a subsequent pulse $i + a$ arrives at some multiplication of the period T_{rep}, such that $t = a*T_{rep}$ (e.g. the fifth pulse after the first will arrive five repetition periods later, such that the index a denotes the number of pulses propagating in the PDL), see Figure 3-1.

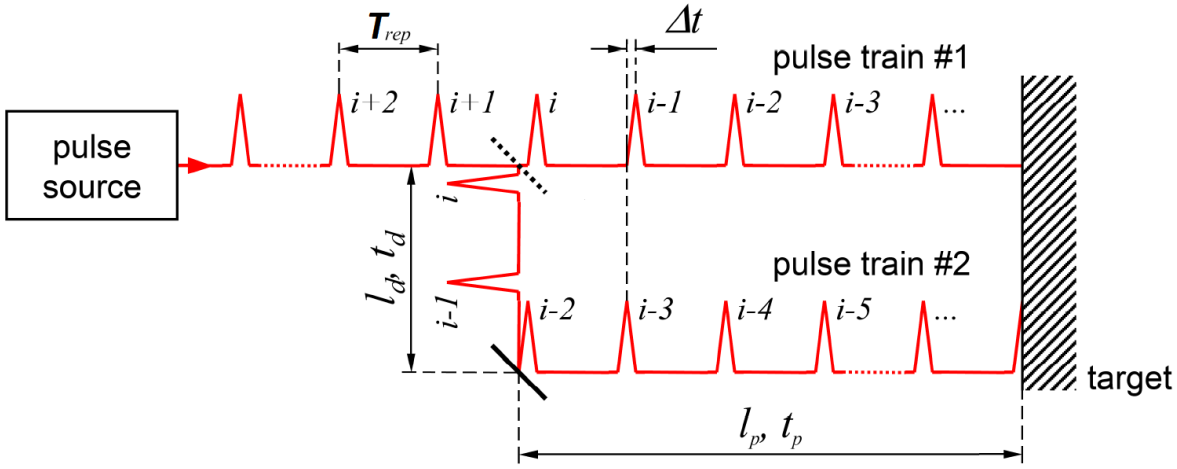

Figure 3-1 – The principle of OSCAT as adopted for OSBERT. Splitting the pulse train into a short and a long path allows a variation in the repetition rate to give rise to a temporal delay between pulses incident at a target position. Diagram reproduced and adapted from [59].

Within time t_p, a pulse from the short arm travels a distance l_p between the beam-splitter and the target position. The identical copy of this pulse in the PDL travels a longer distance $l_d + l_p$, such that it arrives at the target in time $t_p + t_d$. However, pulse $i + a$ will be delayed by time equal to $a * T_{rep}$ with respect to pulse i,

$$\Delta t = a * T_{rep} - a * \left(\frac{1}{f_{rep} + \Delta f}\right) \tag{11}$$

Substituting $T_{rep} = 1/f_{rep}$ and taking the common factor a, we then have

$$\Delta t = \frac{a}{f_{rep}} - \frac{a}{f_{rep} + \Delta f} = a\left(\frac{1}{f_{rep}} - \frac{1}{f_{rep} + \Delta f}\right) \tag{12}$$

We may now make the implicit equivalency whereby the component $l \cdot n \cdot f_{rep}/c$ is equal to the number of pulses a which may occupy the passive delay line length given the period between each pulse, where l is the length of PDL, n is the refractive index of the PDL, and c is the speed of light in a vacuum.

$$a = \frac{l \cdot n \cdot f_{rep}}{c} \tag{13}$$

As such equation (12) may be rewritten

$$\Delta t = \frac{l \cdot n \cdot f_{rep}}{c}\left(\frac{1}{f_{rep}} - \frac{1}{f_{rep} + \Delta f}\right) \tag{14}$$

From this expression it is clear to see that the maximum available scan range will increase linearly with an increase in available repetition rate tunability, scaled by any increase in the available PDL, see Figure 3-2. In this example the plots are calculated to give a scan range for increasing repetition rate tunabilities assuming a repetition rate of 10GHz and the refractive index of air $n = 1$, for three different PDL lengths; 1m, 2m and 3m.

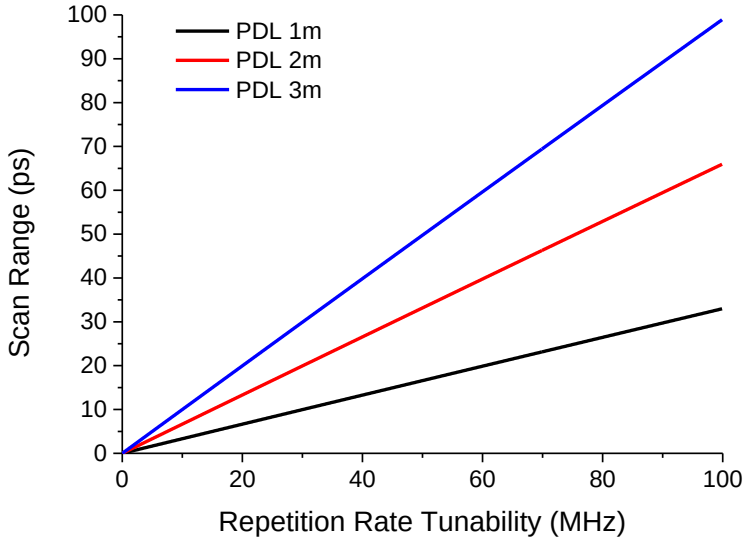

Figure 3-2 – For any given pulsed laser, a desired scan range may be achieved by any preferred combination of passive delay line (PDL) length or repetition rate tunability. In this simulated example the laser has a 10GHz repetition rate, and the passive delay line has the refractive index of air, *n = 1*.

Thus, in terms of the MLLDs adopted for OSBERT, linearly tuning the repetition rate by varying the reverse bias applied to the absorber section of the MLLD from a minimum to a maximum value will in turn linearly delay the pump and probe pulses with respect to each other over this tuning range, which will scale by increasing the PDL.

As such it is possible to trade one preferred parameter for another, depending on the application; a MLLD with low repetition rate tunability may make use of a longer passive delay line, whereas a laser with high repetition rate tunability can achieve the same scanning range using a far shorter passive delay line.

The final expression may alternatively be rewritten to find the passive delay length required given a known repetition rate and tunability, and the desired temporal scan range

$$l = \frac{\Delta t \cdot c \cdot \left(f_{rep} + \Delta f\right)}{n \cdot \Delta f} \tag{15}$$

We may also represent the expression for the special case where the entire period of the repetition rate is required as the temporal scan range (as in the case of ASOPS) by substituting Δt = scan range = $1/f_{rep}$

$$l = \frac{c \cdot \left(1 + \frac{\Delta f}{f_{rep}}\right)}{n \cdot \Delta f} \tag{16}$$

Upon further examination, the total scan range available to any given pulsed laser source is more limited by the ratio of repetition rate tunability to the fundamental repetition rate $\Delta f/f_{rep}$ which for this project we shall refer to as the *controllability factor* β. Rearranging expression (14) for Δf we can consider the case where the scan range and PDL length are fixed, and the user may need to determine the degree of repetition rate tunability required to fulfil these conditions, we find

$$\Delta f = \frac{c \cdot f_{rep} \cdot \Delta t}{(l \cdot n - c \cdot \Delta t)} \tag{17}$$

And as such, similarly if the ratio β must be determined to satisfy certain scanning criteria, it is simply expressed as

$$\frac{\Delta f}{f_{rep}} = \frac{c \cdot \Delta t}{(l \cdot n - c \cdot \Delta t)} = \beta \tag{18}$$

Finally, rearranging for the scan range Δt we now find that

$$\Delta t = \frac{\beta \cdot n \cdot l}{(c + \beta \cdot c)} = \frac{l \cdot n}{c} \cdot \frac{\beta}{1 + \beta} = \frac{a}{f_{rep}} \cdot \frac{\beta}{1 + \beta} \tag{19}$$

This gives some indications as to the difference in scanning potential between two lasers of equal repetition rate tunability, but different fundamental repetition rates. When the controllability factor β is considered alongside various passive delay line lengths *l* on logarithmic axes, we begin to see the full picture of their combined impact on scan range as a contour plot, see Figure 3-3, where any MLLD and its controllability factor could be mapped for the delay line required in order to achieve a desired scan range. If we take the example of the two devices discussed so far, we may calculate their controllability factor for comparison. The narrow-ridge device has a fundamental repetition rate of f_{rep} *~ 5 GHz* and a tunability of Δf *~ 10 MHz*, giving a controllability factor of $\Delta f/f$ *= 0.002* (or 0.2%

controllability). The tapered waveguide device has f_{rep} ~ *15.9 GHz* and a tunability of Δf ~ *5 MHz*, giving a controllability factor of $\Delta f/f_{rep} = 0.0003$ (or 0.03% controllability).

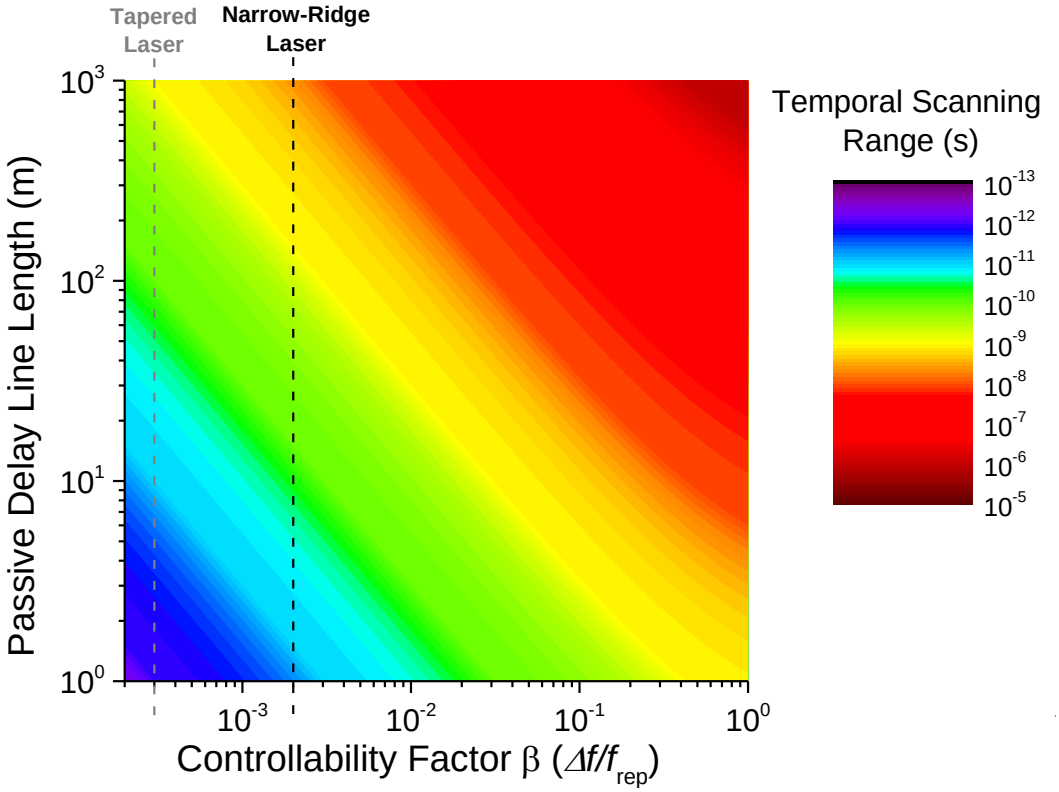

Figure 3-3 – Contour plot illustrating how the increasing controllability factor $\Delta f/f_{rep}$ of a pulsed laser source will effectively reduce the required length of passive delay line to achieve the desired scan range. The narrow-ridge and tapered waveguide lasers described in Chapter 2 are indicated for comparison.

It is therefore clear that the absolute value of the repetition rate tunability is not in itself the most important factor when choosing a device for this method; the controllability factor β places the tunability into the context of the repetition rate of a particular laser and helps to provide an indication of how long of a passive delay line will be required to access the particular scan range required for the study.

Finally, the advantages of using a fibre passive delay line over a free-space passive delay line are considered. Referring to expression (14) we consider that for many devices, depending on the required scan range, long passive delay lines may be difficult to realise in free space. Using an optical fibre as the PDL instead compresses the space required into a small spool, eliminating the need for long-distance beam alignment and knock on effects of any required beam shaping. Furthermore, the increased refractive index of optical

fibres (*n* ~ 1.46 in our studies, discussed further in Section 3.5.3) means a significant boost in scan range compared to that given by the same free space length, see Figure 3-4.

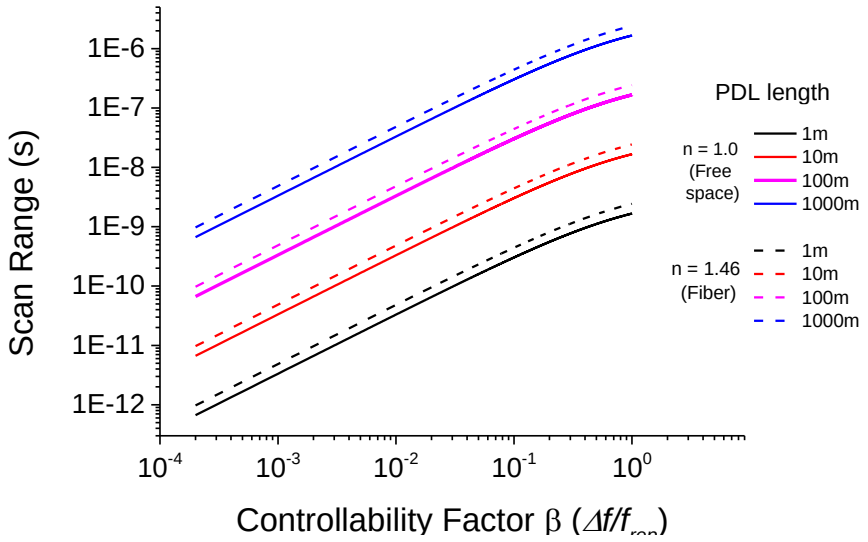

Figure 3-4 – Profile slices taken from the contour plot shown in Figure 3-3 demonstrating the benefit of using higher refractive index coiled fibre as a PDL when compared to the same length of free space PDL, giving rise to an increased temporal scan range for increasing controllability factor $\Delta f / f_{rep}$.

3.2. Introduction to Autocorrelation

Before testing a new optical sampling method on an application, a typical first proof of principle is often to perform a simple autocorrelation, or in the case of OSCAT, a cross-correlation; the key difference being that an autocorrelation involves the interference of one pulse with an exact copy of itself, whereas a cross-correlation interferes two pulses which are not copies. OSBERT relies on a great imbalance between the arms of the interferometer by way of a PDL, and so cross-correlation occurs when one pulse is interfered with a different pulse delayed by the length of the imbalance, and this shall be the primary proof of principle. Since the principles of both auto- and cross-correlation are similar, autocorrelation is described for clarity.

Depending on the requirements of the investigation, two main optical autocorrelation types were adopted throughout the project. The different resulting traces provide different information depending on the experimental conditions, including the setup geometry (collinear or non-collinear) and whether a linear or non-linear approach was used for the detection; (namely Single-Photon Absorption (SPA) or Two-Photon Absorption (TPA) [122] which are each described in section 3.2.1.

In both collinear and non-collinear geometries, the principle remains the same, as is outlined in [91] and discussed in chapter 2; an ultrashort pulse is split via a beam-splitter into two identical copies. One pulse copy traverses a stationary path, whilst the other traverses a path whose length may be varied, for example via a mirror mounted on a mechanical translation stage. The pulses recombine at a detector where the incremental delay in one arm walks the translatable pulse copy through the path of the stationary pulse copy, leading to an optical autocorrelation.

The first-order interferometric autocorrelation results when a linear detection method is adopted. The pulse copies from the stationary arm and the translation stage propagate through a collinear path towards the detector, allowing the beams to combine interferometrically, see Figure 3-5.

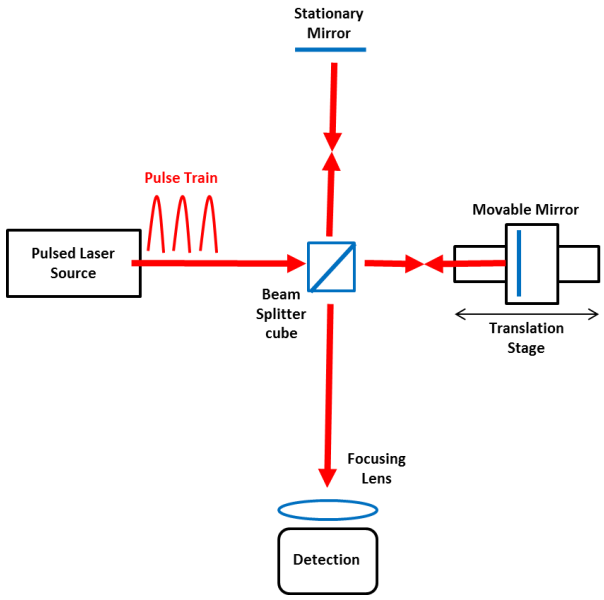

Figure 3-5 – Inteferometric autocorrelation setup. In the case of a linear detection regime, a first order autocorrelation results, whereas non-linear detection regimes (such as TPA or SHG) will result in an second-order interferometric autocorrelation.

Described in detail by Diels *et al* [123], the fundamental autocorrelation function of an electric field $E(t)$ over time is given by

$$A(\tau) = \int_{-\infty}^{+\infty} E(t)E(t-\tau)dt \tag{20}$$

Where τ represents the delay between both pulse copies resulting from the spatial displacement of the translation stage. The complex electric field corresponds to an

intensity $I(t) = |E(t)|^2$ such that the intensity of the addition of the input electric field $E(t)$ and its delayed copy $E(t-\tau)$ is given by

$$I_{(1)}(\tau) = \int_{-\infty}^{+\infty} |E(t) + E(t-\tau)|^2 dt \tag{21}$$

Expansion gives rise (amongst others) to the term $E(t)E(t-\tau)$. Since the electric field may be used to describe the pulse, in the linear autocorrelation regime, this interferometer may be used to measure the spectrum of a pulse, given the Fourier transform from the temporal to the frequency domain. Though used as a means of cross-correlation throughout the project, this method does not provide information on the pulse duration. In order to do so, a second-order detection method must be adopted, for example using non-linear optics.

An intensity autocorrelation is such a second-order process which results, for example, when the ultrashort pulse copies mix in either a collinear or a non-collinear (background-free) experimental geometry. In chapter 2, non-linear intensity autocorrelations were achieved using a commercial SHG autocorrelator, where the background (input signal) is filtered away from the non-linear signal by focussing both beams onto a nonlinear SHG crystal, i.e. a background-free intensity autocorrelation in a non-linear setup, see Figure 3-6.

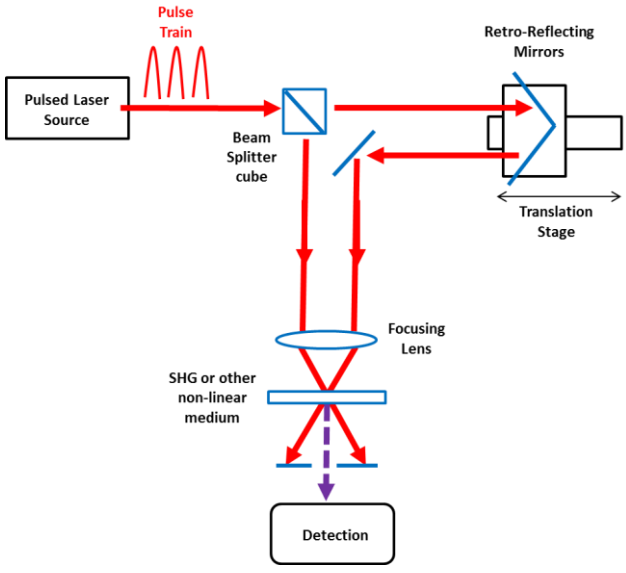

Figure 3-6 - Intensity autocorrelation setup: Both pulse copies are focussed onto a nonlinear crystal such that the resultant SHG signal only is directed towards the detector.

Both pulse copies are focussed down onto a non-linear crystal where the intensity of the autocorrelation grows non-linearly with the overlapped intensity of the input pulses, maximising when their peaks are precisely overlapped. The intensity autocorrelation gives a trace which may be used to estimate the original pulse duration, provided (as discussed in chapter 2) an appropriate co-factor is used depending upon the peak function used to fit to the trace. No phase information is retrievable from this intensity autocorrelation, for which a system which incorporates a spectral analyser such as FROG (Frequency-Resolved Optical Gating) must be adopted [124].

Finally, it should be noted that a second-order autocorrelation can also be interferometric if used in a collinear geometry, in which case (given great enough step resolution or fast enough detection), the fringes may also be resolved as with a first order trace, plus, like the intensity autocorrelation, the pulse duration is also retrievable. Ultimately, a collinear geometry was adopted for this project in terms of the proof of principle cross-correlations demonstrated, and are discussed further in this chapter.

3.2.1. Single-Photon Absorption and Two-Photon Absorption

The cross-correlator which was built for this project formed the basis of both the linear SPA and non-linear TPA OSBERT setups, depending on which combination of the two MLLD devices, and which of two detectors was used.

Like SHG, TPA is also a non-linear optical process, whereby two photons are absorbed simultaneously in order to excite an electron from a lower energy state to an upper energy state. This is in contrast with SPA where only a single photon is required to excite the electron between lower and upper states. According to the Planck relation, as in the case of a semiconductor's band-gap energy E_g between valence and conduction bands, an electron may make the transition directly between energy bands upon the absorption of a single photon having a corresponding frequency ν (or wavelength λ) where

$$E_g = h\nu = \frac{hc}{\lambda} \tag{22}$$

where *c* is the speed of light in a vacuum and *h* is Planck's constant. This photodiode arrangement is not unlike the reverse biased saturable absorber section of an MLLD discussed in chapter 2, where an absorbed photon creates an electron-hole pair and leads to a photo-current. TPA however occurs where the frequency of a single photon would not allow the direct transition between the bands, but instead two photons whose combined energy at a non-corresponding frequency is sufficiently great to excite the electron firstly from a ground state to a virtual state (situated part way between states) before the second absorption concludes the transition to the upper state. The intensity required to conduct a transition is significantly greater than that required by SPA (hence non-linear), as the probability of two-photon absorption grows with the square of the incident light intensity. As such, pulsed lasers with high peak powers (owed primarily to ultrashort pulse durations) are significantly more likely to give rise to TPA than a continuous wave laser of equal average power.

TPA is an attractive alternative to SHG because a semiconductor phototodiode may itself serve as both the non-linear TPA medium and the detector [125]. In fact, in 1998 D. Reid *et al* summarised a number of commercially available semiconductor-based photodiode devices which were capable of producing TPA under suitable conditions in the context of autocorrelation [126]. Their work stipulated that provided the bandgap of the semiconductor material used to create the detector was sufficiently greater than the photon energy of the laser excitation (given by expression (22)), a non-linear response could arise, given a sufficiently high incident light intensity. As such, practically speaking, an excitation wavelength which coincides with the detectors spectral response will have a far greater probability of giving rise to a linear SPA response, whereas a longer wavelength is more likely to give rise to the non-linear TPA response, see Figure 3-7.

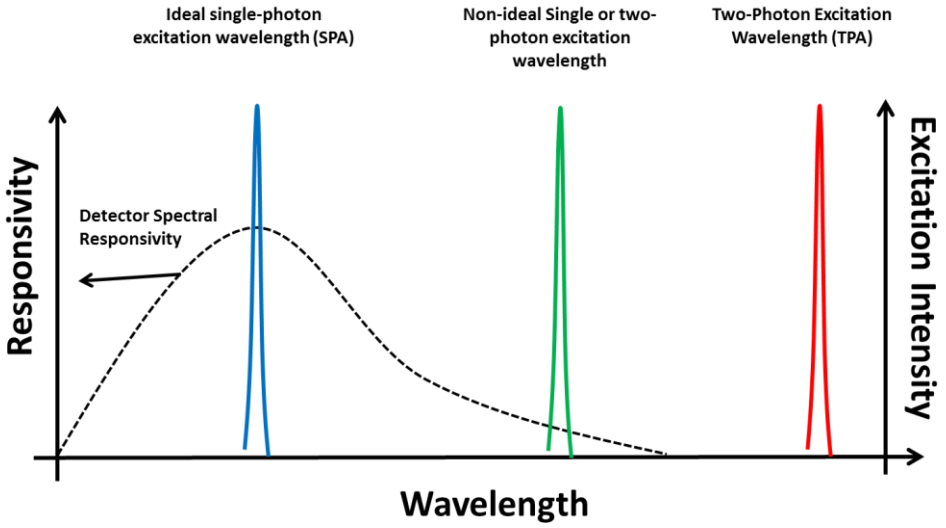

Figure 3-7 – An illustration of how SPA or TPA (or non-ideal combinations of both) may arise for any given detector's spectral responsivity and the laser excitation wavelength.

3.3. Linear and Non-linear Cross-Correlator with Temporal Pulse Positioning

This section describes a first proof of principle of the OSBERT technique, referred to here as 'Temporal Pulse Positioning' (TPP), and is the precursor demonstration to using the technique in order to *actively* scan across some temporal range.

3.3.1. Experimental Setup

This temporal pulse positioning technique requires the same configuration as the cross-correlation setup described previously; a means to control the repetition rate of the MLLD via a change in reverse bias to the saturable absorber, and a passive delay line of suitable length determined by expression (15), see Figure 3-8 for a detailed illustration of the experimental setup used.

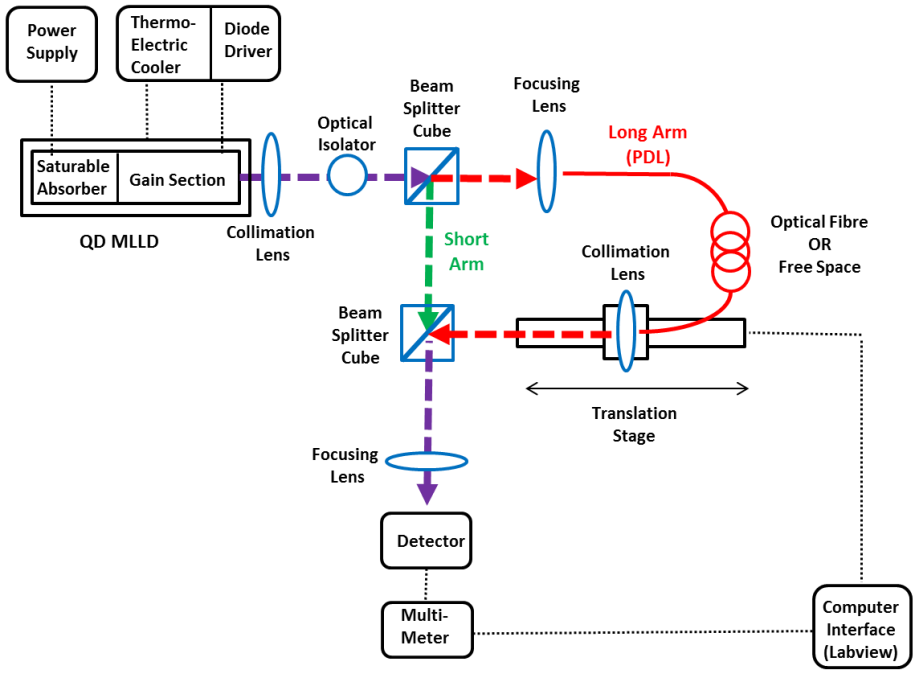

Figure 3-8 – Setup design for temporal pulse positioning. The MLLD is placed into a setup consisting of a PDL and the ability to control the repetition rate of the device using the power supply to alter the bias applied to the saturable absorber section.

In essence this is a cross correlation device, whereby the original pulse train is split into two copies. The first is sent either on a free-space delay line or into an optical fibre several metres long (the PDL), and the second is sent via free space on a significantly shorter path of fixed length (the short arm). In the case of experiments carried out using the tapered-waveguide device, only free-space PDLs were used as the device malfunctioned irreparably before the arrival of optical fibres. The delay between the arms means that, unlike in an autocorrelator, the pulse does not interfere with a copy of itself, but rather with another pulse altogether as outlined in the previous section. The benefit of using a fibre is that even extreme lengths may be coiled into a small space, whereas the free-space path is limited by the space available on the optical bench, and may suffer from beam divergence and alignment issues. In the case of a fibre setup, the beam emerging from the fibre is then collimated with a fibre-coupled collimation package, which consists of an xyz translation stage (*Thorlabs MBT616D/M 3-Axis Microblock Compact Flexure Stage*) which the fibre is secured to using a fibre holder (*Thorlabs HFB005 - FC/APC-Connectorized Fibre Holder)*, whose output is then directed towards a collimation lens (*Thorlabs C330TME-C aspheric lens, f=3.1mm*). The entire fibre collimation is then mounted on a 30-cm-long mechanical translation stage (*Thorlabs LTS 300mm, 0.1µm step-size*). Unless stated otherwise, when a fibre PDL of any length is used, it is a *Thorlabs*

SMF28E-FC design. Both beams may then be combined via a further beam splitter, and directed towards a photodetector, whose electrical output may be acquired with a multi-meter (*Agilent 34401A Multimeter*). In order to gain the maximum signal, an aspheric lens is used to focus the beam onto the detector's active region (*Thorlabs C230TME-C aspheric lens, f=4.51*) which is coupled to a long pass filter in order to eliminate any stray signal contributing to background levels (*Thorlabs FELH1000, 1000nm cut-on wavelength*).

For the purposes of the investigation, two main photodetectors were used for the detection of the cross-correlation. Given the significantly higher peak output power of the tapered device, this was selected to achieve a non-linear response from a silicon-based biased photodetector (*Thorlabs 2GHz DET025AL/M*). The spectral responsivity of the silicon detector spans a range of around 200-1100nm (see Figure 3-9), whereas the central emission wavelength of the tapered device is 1260nm, and thus it is potentially possible to generate two-photon absorption given high enough incident power as described previously, giving rise to non-linear intensity cross-correlations. The narrow-ridge device (also with an emission wavelength around 1260nm) was used in conjunction with a similar biased photo-detector which was instead Indium-Gallium-Arsenide (InGaAs) based (*Thorlabs 5GHz DET08CL/M*). The InGaAs detector's spectral responsivity spans across an infrared band of around 800nm to 1600nm (see also Figure 3-9), meaning that OSBERT scans used with this laser and detector combination shall have a linear (or single photon absorption) response.

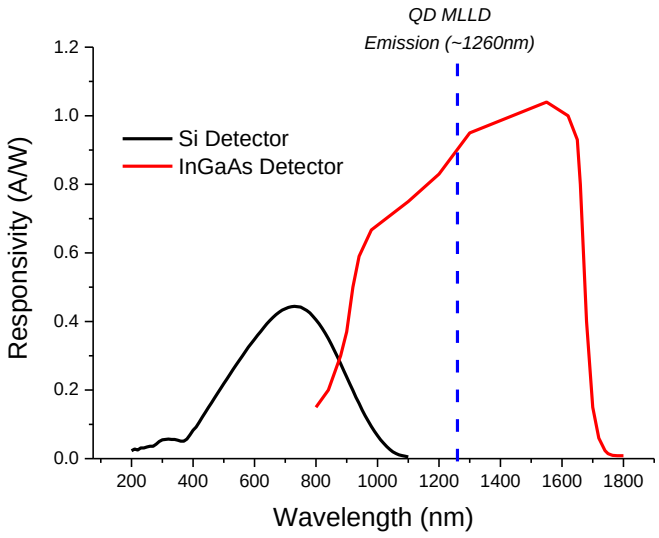

Figure 3-9 – The spectral responsivity of the two detectors used throughout the project with the indicated (blue dashed) emission wavelength of the tapered and narrow QD MLLDs. Detector responsivity data publicly available from Thorlabs [127].

As an indication of the trace we can expect from both possible device and detector combinations, we take a simple cross-correlation using the mechanical stage optical sampling technique. For this, we must select biasing conditions which lead to stable ultrashort pulses for each device within their respective MLRs (760mA forward current and 3.80V reverse bias for the tapered device, and 210mA and 4.60V for the narrow-ridge device). These conditions correspond to 2.25W peak and 77mW average power from the tapered device, and 215mW peak and 6mW average power from the narrow device. In separate experiments with a steady repetition rate established, the mechanical stage position is moved such that the pulses from the long and short arms interfere, where the output voltage from the detector is recorded from the multi-meter, see Figure 3-10.

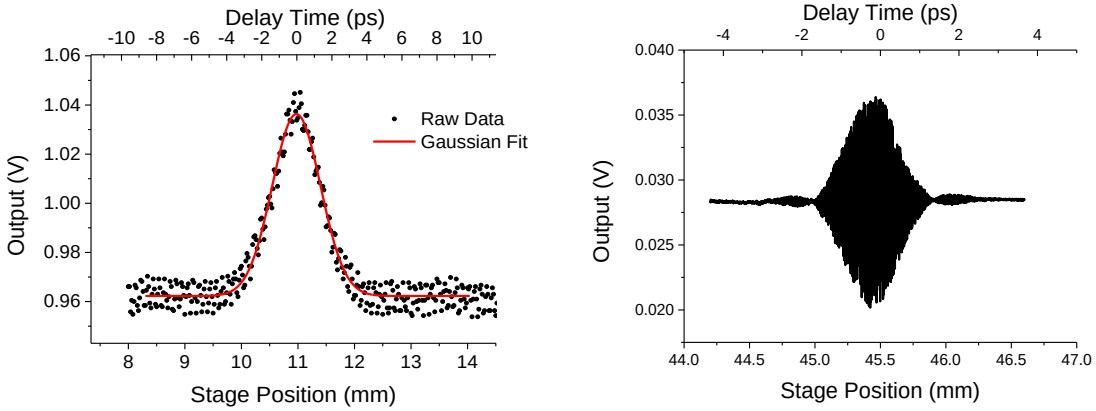

Figure 3-10 – Left, the non-linear TPA cross-correlation trace from the tapered device and Si detector, acquired with a step size of 20µm. Right, the linear SPA cross-correlation resulting from the narrow-ridge device and InGaAs detector, acquired with a step size of 1µm.

As can be seen, the non-linear TPA cross-correlation from the tapered device and silicon detector takes a Gaussian shape (as fitted to the trace), qualitatively resembling the SHG autocorrelations discussed in Chapter 2. Whereas the SHG autocorrelation under these operational conditions had a duration of 3.04ps (2.15ps when the Gaussian co-factor of 0.707 is applied), the TPA cross-correlation had a FWHM of 3.33ps without applying a co-factor. The broadening of the trace is likely due to dispersion in the long free space path. The noise levels throughout the trace are thought to be evidence of a fringe pattern, caused by poor free-space alignment over such a large distance leading to a partially interferometric cross-correlation, and was not fully optimised before the device malfunctioned. Though not ideal, this does not impede the ability of the device to demonstrate OSBERT. This is in contrast with the narrow-ridge device and the InGaAs detector cross-correlation, which has a typical first order interferometric response.

3.3.2. Scan range calculation for each device for TPP

Given that the mechanical cross-correlation principle has been demonstrated as a basic optical sampling technique under static biasing conditions, it is now necessary to pave the way for the OSBERT TPP effect. Revisiting the tunability of each of the two devices (the narrow-ridge and the tapered waveguide device) we may convert the exact reverse bias applied into the known repetition rate at that value, giving the repetition rate tunability Δf, see Figure 3-11.

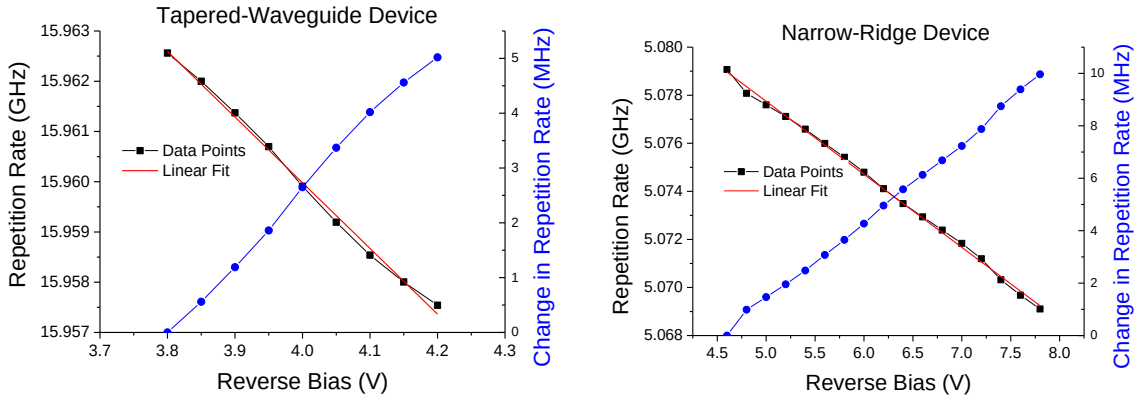

Figure 3-11 – The repetition rates f_{rep} detected under each reverse bias for left, the tapered-waveguide and right, the narrow-ridge devices, overlaid with the relative repetition rate tunability Δf.

Fitting a linear function to the results for the narrow-ridge device shown in Figure 3-11 gives us the direct relationship between reverse bias V in volts and the resultant repetition rate f_{rep} in Hz

$$f_{rep} = -3.03799 \times 10^6 V + 5.09294 \times 10^9 \, [Hz] \tag{23}$$

Each step in voltage may now be independently converted to a repetition rate value according to expression (23), which in turn may be calculated as a change in the original repetition rate. Similarly for the tapered waveguide device, we may approximate the relationship between the repetition rate and the applied reverse bias with a linear fit

$$f_{rep} = -1.3076 \times 10^7 V + 1.60123 \times 10^{10} [Hz] \tag{24}$$

We may now apply the described theory to determine the maximum scan range made available by the two devices using expression (14), were they to be tuned from their minimum to maximum reverse biases (though in reality, any subset of the biasing range could be used and give a relative scan range based on the repetition rate tunability

attributed to it). We must take into account that although the change in repetition rate through changes in reverse bias levels was approximated with a linear fit to the data, in reality this is not perfectly the case, which may affect the results in experiment.

In the case of the tapered waveguide device, free-space experiments at 0.67m and 1.79m passive delay length were conducted, whereas the narrow-ridge device was used in combination with a variety of fibre lengths at 1m, 2m and 5m, see Figure 3-12. It is important to recall that due to the refractive index of the fibre, *n = 1.46*, this means that 1m of fibre is equivalent to 1.46m of free space passive delay line in terms of the scan range achieved from expression (19).

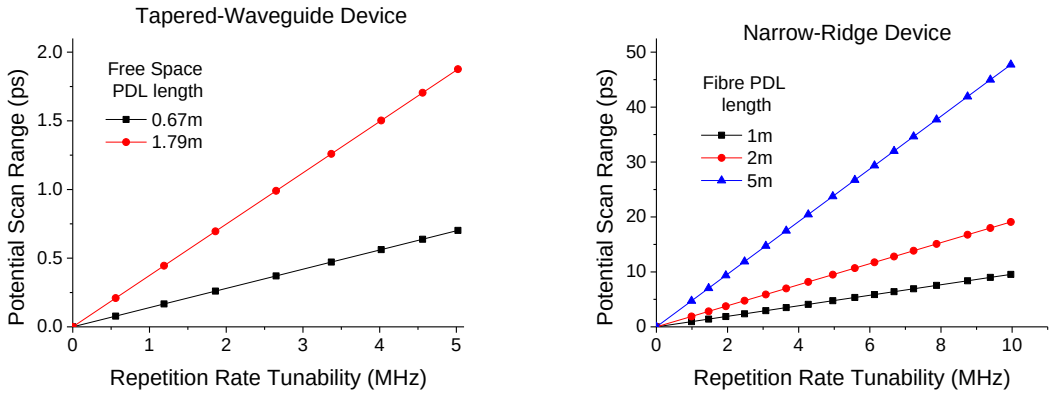

Figure 3-12 – Assuming the full repetition rate tunability brought about by the variation in reverse bias is applied, the potential scan range of each device is now plotted as a function of the various passive delay line lengths available. Left, that of the tapered device, and right, that of the narrow-ridge device.

As such, with these experimental configurations in the laboratory, the maximum temporal scan range available to the tapered device is around 2ps, whilst that of the narrow-ridge device is around 50ps. Even comparing similar lengths of passive delay line between the two devices, we find the narrow-ridge device consistently has the competitive edge in scan range, which as previously discussed is due to their difference in controllability factor β.

Due to the nature of the OSBERT method, taking a series of mechanical stage cross-correlations, each acquired fully under a different reverse bias within the MLR, should theoretically lead to a shift in the position required to find the cross-correlation along the mechanical stage axis; the OSBERT-induced temporal shift (according to equation (14)) will essentially apply to the entire cross-correlation spatial position. Figure 3-13 represents the

results of the calculations which predict the offset in stage position when using the 15.9GHz tapered waveguide device with a totally tunability of 5MHz across both of the available free-space passive delay line lengths, 0.67m and 1.79m. In each trace the only difference is the level of reverse bias applied leading to a change in repetition rate[5].

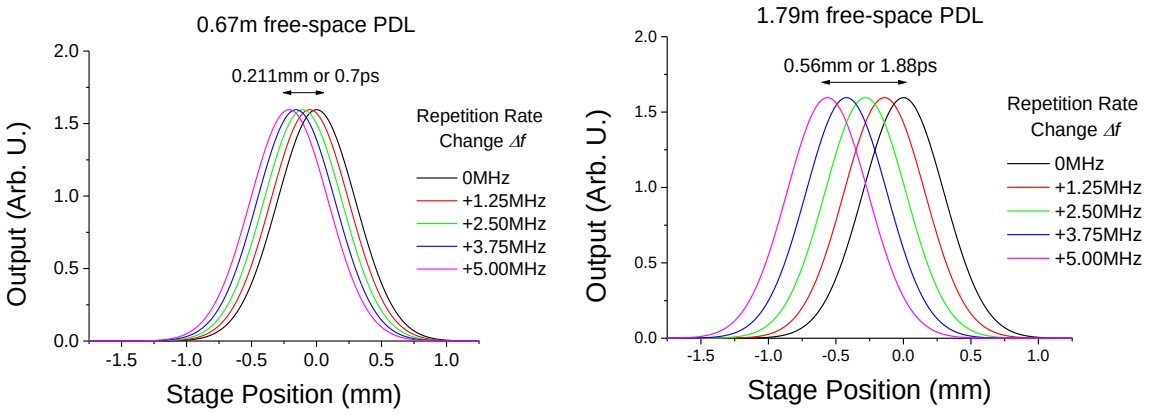

Figure 3-13 – Diagram illustrating at which position on the mechanical stage a cross-correlation will be found for increasing reverse bias levels to the tapered-waveguide device for free-space passive delay line lengths of left, 0.67m and right, 1.79m.

As can be seen, approximately 0.7ps and 1.9ps scanning range should theoretically be made available by 0.67m and 1.79m of free-space PDL respectively, illustrating the theorised increase in scanning range expected for an increase in PDL length.

We then take the example from the narrow-ridge MLLD also with pulse widths of 2ps, a fundamental repetition rate of 5.07GHz and a repetition rate tunability of 10MHz, see Figure 3-14. Three different fibre-based passive delay line lengths of 1m, 2m and 5m with refractive index $n = 1.46$ were used in order to demonstrate the PDLs ability to scale the temporal scanning range. In reality, depending on the position of the mechanical stage within the PDL (long arm) and the difference in free-space between the long and short arms, there may also exist a free-space component which adds to the PDL. In these cases, the free-space component is included in the calculations. When these parameters are placed in the fundamental equation (14) for temporal delay, it becomes possible to determine the full scan range of the system, as well as predict which position on the mechanical stage we should expect a cross-correlation.

[5] Note, for this theoretical illustration of temporal displacement, the additional changes in output characteristics outlined in chapter 2 were not included, such as the change in pulse duration, average and peak powers, or central wavelength, and so a 2ps pulse duration with arbitrary intensity is a simplification.

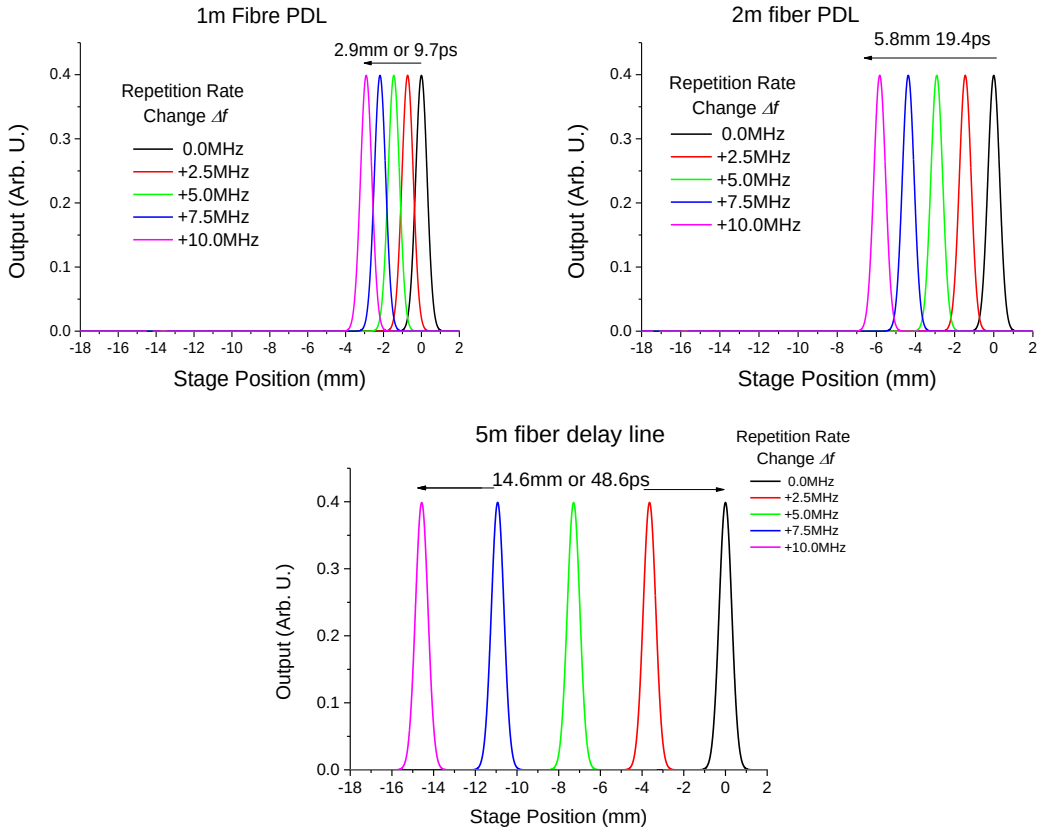

Figure 3-14 – Diagram illustrating the offset in temporal (or spatial) position of the cross-correlation when the reverse bias is altered in order to detune the repetition rate (based on the characteristics of the narrow-ridge-waveguide device and three optical fibre PDL lengths; 1m, 2m and 5m).

According to these calculations, approximately 10ps, 20ps and 50ps scanning range are made available by 1m, 2m and 5m lengths of optical fibre PDL respectively. Again we should note the bonus in both the ability to coil the far longer fibre delay line into a small space, and the greater refractive index which gives rise to longer scan ranges than a free-space delay line.

3.3.3. Single and two-photon experimental results

As illustrated in the experimental setup, a custom LabVIEW program[6] allows the mechanical stage at the long arm to move in small increments with respect to the short arm and collect the output at the multi-meter for each step taken, thus leading to a cross-correlation trace. As per the theoretical calculation, this is repeated under various increments of reverse bias applied to the absorber section. In the case of the tapered-waveguide device, the gain section has a forward current of 760mA applied, and cross-

[6] Note, this LabVIEW program was previously built for use with a smaller translation stage within the group, and was simply updated for use with the 30cm Thorlabs Translation Stage used throughout the project.

correlation traces are taken when the saturable absorber is biased at five discrete voltages within the MLR from 3.80V to 4.20V. The process is repeated when the free-space PDL is increased from 0.67m to 1.79m, see Figure 3-15[7].

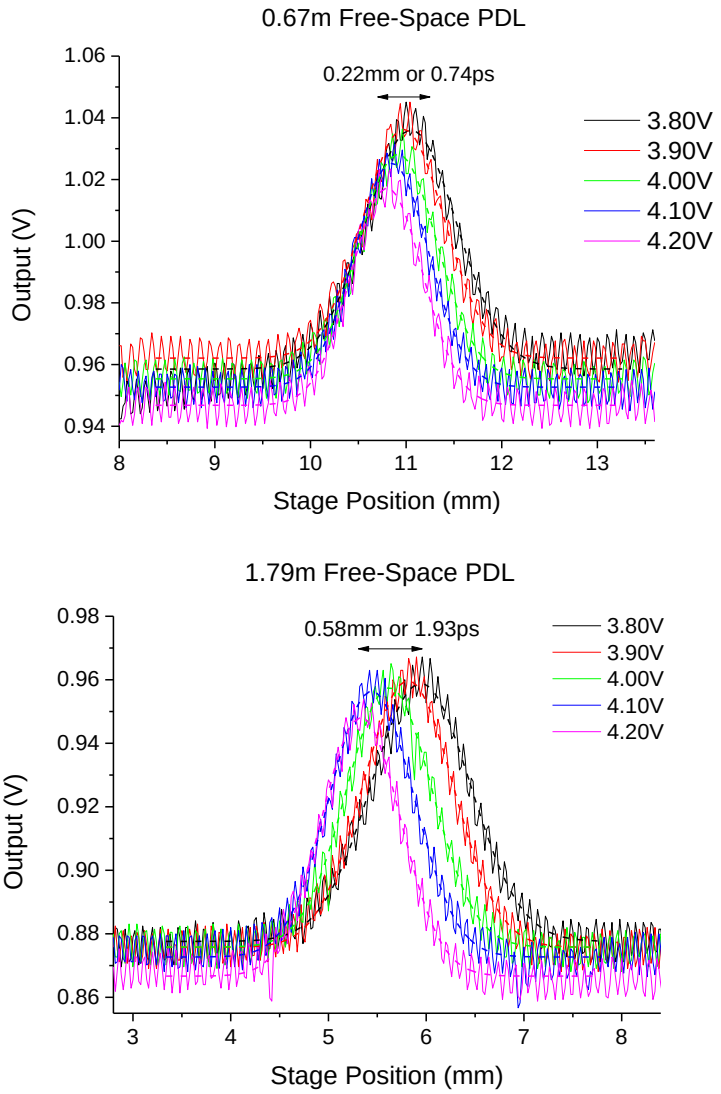

Figure 3-15 - Temporal pulse positioning traces using the tapered-waveguide device for above, 0.67m PDL and below, 1.79m PDL. Increasing the reverse bias detunes the repetition rate creating a temporal displacement between cross-correlation positions. Dashed lines represent the Gaussin fit for each trace.

As can be seen, varying the reverse bias applied to the absorber from the minimum to maximum voltage within the MLR has caused a spatial shift in each cross-correlation, leading to a total 0.22mm displacement, corresponding to a temporal range of 0.74ps in

[7] Note, For the purposes of the experimental results throughout this project, when 'Stage Position (mm)' is given as the x-axis of a trace, this is not reflective of the position of the stage within the entire length of the long arm of the setup, but only of the arbitrary local position on the 300mm of available travel. The exact imbalance in free space and optical fibre is always provided and used in calculations.

the case of the 0.67m free-space PDL. This was calculated by fitting a Gaussian to each trace in order to determine the central peak value of each cross-correlation before finding the difference in peak position. Similarly, in the case of the 1.79m free-space PDL, a total spatial shift of 0.58mm (or a temporal shift of 1.93ps) was measured. Both measured temporal displacements are in good agreement with the theoretically predicted values of 0.7ps and 1.88ps for the 0.67m and 1.79m PDL lengths respectively, as illustrated previously in Figure 3-13.

The minor discrepancy in the theoretical and experimental values of temporal displacement is likely due to the actual repetition rate tunability, which was fit as a linear function of applied reverse bias, whereas in reality this is not perfectly the case and is not accounted for in the conversion to delay time; neither, it should be noted, are the differences in optical spectrum, average and peak powers, or pulse durations for each value of reverse bias used. In addition, the measurement of the length of free-space PDL is subject to a reading error of ±2mm, whilst there is also an additional error in the mathematical determination of the central peak during the Gaussian fit. Of interest also is the narrowing of each cross-correlation trace for increasing reverse bias, see Figure 3-16.

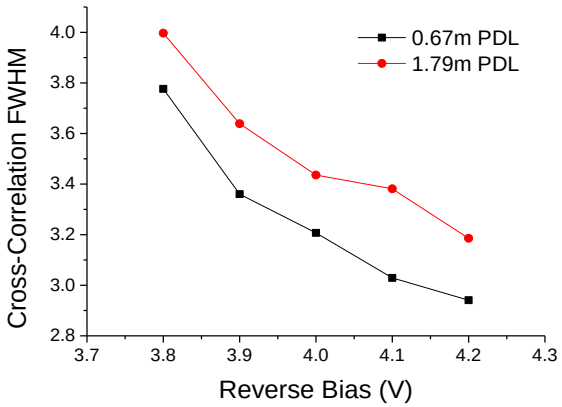

Figure 3-16 – The cross-correlations FWHM for increasing reverse bias is seen to decrease, whilst the effects of dispersion are evident in the broader FWHMs of the longer PDL.

The narrowing of the individual cross-correlations across both PDL studies may be attributed to the narrowing of the original pulses which were used to construct them, for which we can refer to their autocorrelation traces (see chapter 2, Figure 2-36). Additionally, the increase in PDL length appears to have slightly broadened the cross-correlations. This is likely due to dispersion in the longer free-space delay, but was also shown by Tourrenc *et al* to be an artefact of increased timing jitter for increased

imbalances within a cross-correlator [128]. This is discussed further in Chapter 4. It is important therefore to note that across a reverse bias range, as well as all the original pulse parameters (such as pulse duration, optical spectra, repetition rate and peak and average powers) the cross-correlation traces will themselves be distorted to an extent.

Analogously, in the case of the narrow-ridge device, the gain section has a forward current of 210mA applied, and cross-correlation traces are taken when the saturable absorber is biased at five discrete voltages within the MLR from 4.60V to 7.80V, see Figure 3-15. The procedure is repeated for the three lengths of optical fibre PDL available; 1m, 2m and 5m with refractive index $n = 1.46$.

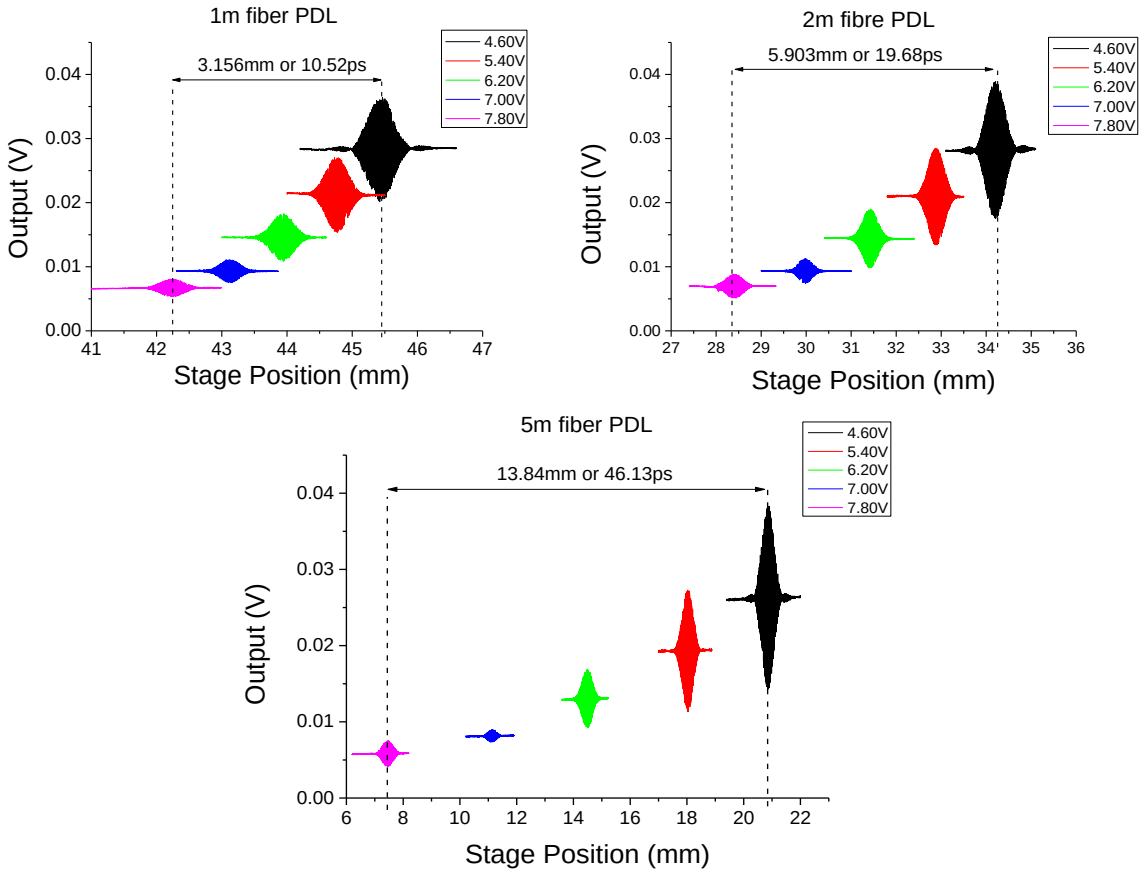

Figure 3-17 -Temporal pulse positioning traces using the narrow-ridge device and InGaAs detector for 1m, 2m and 5m PDL lengths composed of optical fibre of refractive index *n = 1.46*.

As with the tapered device, the experimental results are in strong agreement with the corresponding narrow-ridge model, which calculated temporal displacements of 9.7ps, 19.4ps and 48.6ps for PDL lengths of 1m, 2m and 5m respectively. Experimentally, varying the reverse bias applied to the absorber from the minimum to maximum voltage within

the MLR caused a spatial shift in each cross-correlation, leading to an overall 3.16mm displacement, corresponding to a temporal range of 10.52ps in the case of the 1m fibre PDL. In the case of the 2m fibre PDL, a spatial shift of 5.90mm (or a temporal shift of 19.68ps) was found, and for the 5m fibre PDL a spatial shift of 13.8mm (or a temporal shift of 46.13ps) was found. As with the tapered device, the errors associated with the minor discrepancy may be attributed to reading the length of PDL at +/-2.0mm, fitting Gaussians to the upper envelopes in order to determine the central peak, the slightly non-linear nature of the repetition rate tunability for reverse bias as compared with the linear fit, and the changing pulse characteristics for each reverse bias applied, which are not taken into account.

In the case of each device's TPP experiments, for any given PDL length, the only change between each cross-correlation trace is the level of reverse bias applied to the absorber, and we may therefore conclude that the combination of PDL and repetition rate tuning has led to a temporal delay. What is evident in both experiments is a reduction in the intensity of each cross-correlation trace, corresponding to each increase in the reverse bias applied during their acquisition. As discussed in chapter 2, an increase in reverse bias means an increase in absorption, leading to a decrease in average power. This is realised as a reduction in the output voltage from each detector due to the reduced optical power incident upon their active region, also resulting in a reduction in the background level. Also discussed in chapter 2, whilst the narrow-ridge device is capable of 10MHz tunability, it exhibits a characteristic tunability of 3.125 MHz/V whilst the tapered device demonstrates 12.5 MHz/V with a tunability of 5MHz. Quantitatively speaking, the narrow-ridge device must tune across 3.20V reverse bias, which leads to a final 76% reduction in average power across this range, evident in the TPP traces. Conversely, the tapered-waveguide device must tune over only 0.4V reverse bias, leading to only a 7% total reduction in average power.

Ultimately, these mechanical stage cross-correlation scans successfully prove the fundamental principle of OSBERT; that is to say that increasing the reverse bias applied to the saturable absorber tunes the repetition rate, and as a result due to the PDL, shifts the pulse positions temporally, giving rise to a total scan range whose magnitude is dependent on the controllability factor β and the length l of passive delay line.

3.4. Slow-OSBERT: Automated, Non-Mechanical Scanning

3.4.1. Single and Two-Photon Experimental Setup

As described, whilst Temporal Pulse Positioning (TPP) successfully demonstrated the principle, S-OSBERT (a Slow-OSBERT scan) is the next major step in demonstrating the capability of this optical sampling technique. Instead of simply varying the position at which we may find a cross-correlation through discrete increases to the absorber bias levels as with TPP, we may now (having found a suitable cross correlation position) instead linearly increase the voltage across the entire scan range, through the cross-correlation position. Essentially this means instead of moving the mechanical stage by a short distance and collecting a data point from the detector at each position, we hold the mechanical stage absolutely stationary, centred at the expected peak position of a cross-correlation, and simply increase the reverse bias to the absorber, detuning the resultant repetition rate, and ultimately temporally displacing each successive point. At each increase of the reverse bias, a voltage readout is now taken from the detector, resulting in delay time data point. The setup is similar to that described using the TPP, however the newly customised LabVIEW program now controls the same power supply which has been used throughout the project (*Agilent E36447A*), and applies the reverse bias to the absorber section and then reads the value of the detector (which is based on the incident optical power), see Figure 3-18.

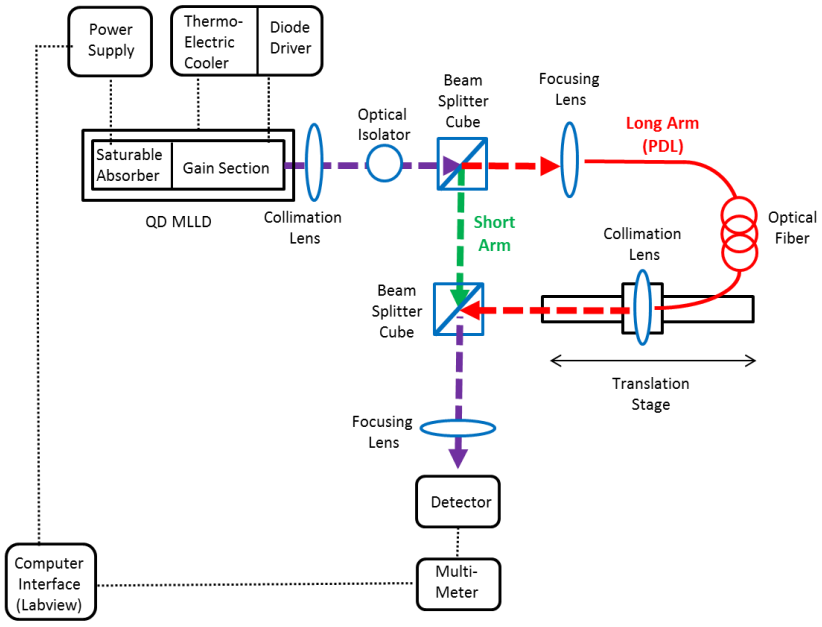

Figure 3-18 – The experimental setup is altered from TPP and mechanical stage optical sampling to SOSBERT. The mechanical stage simply aids the demonstration and is stationary during these scans, serving only to overlap the pulse train exiting the PDL precisely with that of the short arm.

It is important to note that although the translation stage still exists within the setup, it does not itself conduct any manner of temporal scanning; it serves only to align the short and long arm of the interferometer into an optimum position where a SOSBERT scan may now enable the acquisition of a cross-correlation independently.

It should be noted that the term ‘slow’ is applied here to differentiate from fast OSBERT (F-OSBERT) scans which are discussed in Chapter 4. SOSBERT scans are acquired using discrete steps of reverse bias (and thus discrete steps in repetition rate) rather than the sweeping scans and various complexities of FOSBERT, and are therefore comparable to the discrete step size in stage position used during mechanical stage scans. That is to say the purpose of OSBERT is to effectively replace the moving mechanical stage with a power supply. Therefore, SOSBERT scans occur over similar time-scales to mechanical stage scans (several minutes per cross correlation) and as such do not at this point compete with other optical sampling techniques such as ASOPS in terms of scan rate.

3.4.2. Narrow-Ridge Device: linear SPA Experimental Results

To begin with, a standard mechanical stage cross correlation trace is acquired, which serves a number of purposes. Firstly, it provides us with the stage position required which will produce a cross-correlation under the SOSBERT technique. Secondly it provides a reference trace for comparison with the SOSBERT technique. Thirdly, it provides us with the duration of the event. This means we may select either the PDL length or the fraction of the available repetition rate tunability (or both) in order to best scan the feature. Typical first order cross-correlations have exhibited full spatial widths of less than 2mm (corresponding to a temporal widths of less than 7ps), and as such when using the choice of 1m, 2m or 5m fibre PDL lengths we may now calculate the optimum reverse bias range (repetition rate tunability) required to scan a minimum delay of one cross-correlation.

The narrow-ridge device is typically tuned from 4.60V to 7.80V (a total range of 3.20V) reverse bias, which gives rise to 10MHz repetition rate tunability. We may in fact reduce the reverse bias range as scanning the full range will not be necessary for the acquisition of single cross-correlations, and as such for each length of fibre a reverse bias range of 5.35V to 6.45V is selected at a step-size of 0.5mV. We therefore apply the previously used value of forward current (210mA) to the gain section of the narrow-ridge device, and

5.90V reverse bias to the absorber section, before acquiring a standard mechanical-stage scan at one of the spatial positions along the axis of the stage which would result in a cross-correlation between two pulses, see Figure 3-19.

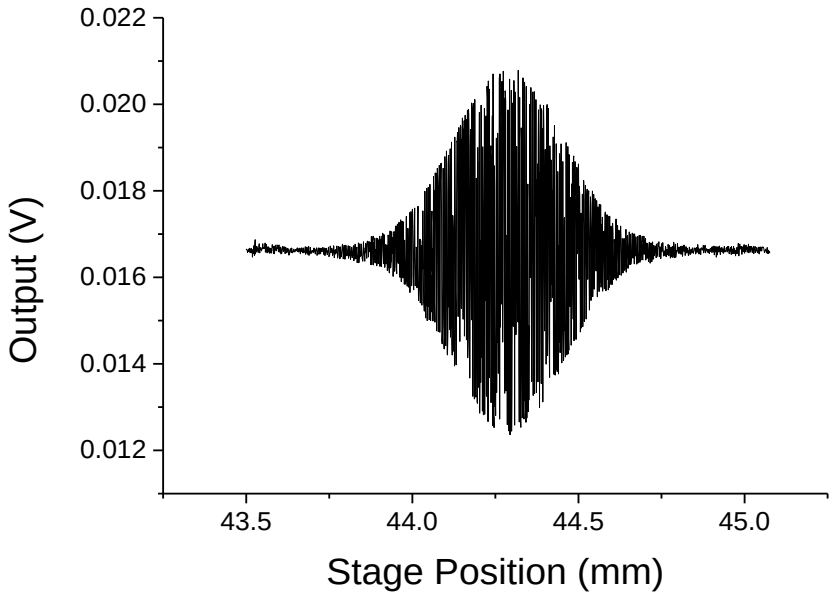

Figure 3-19 – Standard mechanical stage cross-correlation trace taken at 210mA forward current to the gain section and 5.90V reverse bias to the absorber section. The central peak occurs approximately at position 44.20mm, and the step-size is 1µm.

At a step-size of 1µm, the trace covers 1.5mm, corresponding to a temporal step-size of 3.33fs and a scan range in this case of 5ps. The mechanical stage cross-correlation indicates that an ideal position to conduct the same trace using the SOSBERT technique will be at or around 44.20 mm on the mechanical stage[8].

The stage is then moved to this position whilst the device is still biased under the same conditions. This means that whilst the gain section's forward current is held constant at 210 mA, with the SOSBERT technique the reverse bias will be scanned from 5.35V to 6.45V in 0.5mV steps, inducing a repetition rate change that will scan through the cross-correlation position, instead of moving the mechanical stage itself. This process is then repeated for three lengths of PDL; 1m, 2m and 5m, see Figure 3-20.

[8] Note, of course a cross-correlation position will occur at every spatial position analogous to a roundtrip period, in this case 5GHz gives a roundtrip period of around 200ps indicating a cross-correlation will occur at approximately every 60mm in free-space. Therefore on the 300mm translation stage we would expect to find at least five separate cross-correlation positions.

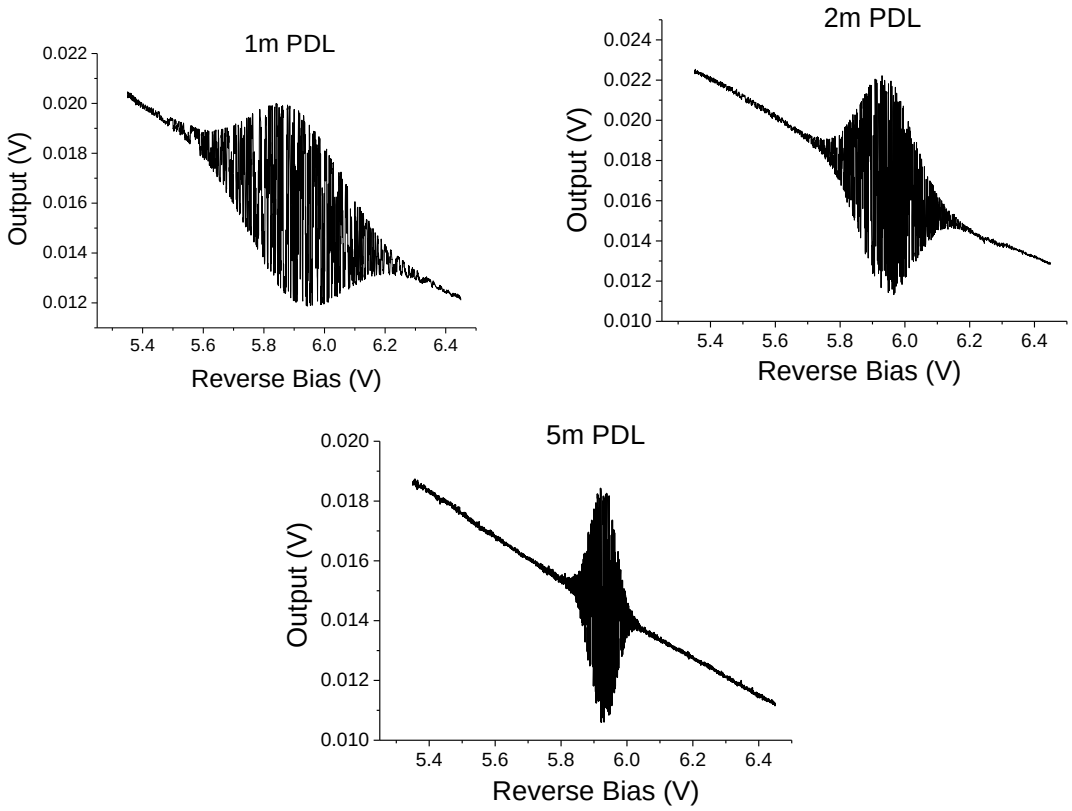

Figure 3-20 – The first SOSBERT traces, whereby increase in reverse bias applied to the absorber section detunes the repetition rate and enables a temporal scan which scales with the length of the 1m, 2m and 5m PDL used.

As can be seen, the method has successfully scanned a full cross-correlation trace using only a change in reverse bias, with no mechanical or moving parts required. The only difference in the experimental parameters leading to each trace is the length of PDL used (1m, 2m and 5m respectively), and as can be seen in each case, the exact same sweep of the reverse bias leads to greater scan ranges. Since the 1.10V reverse bias range corresponds to a repetition rate tunability of 3.34MHz, theoretically we expect under these conditions that the 1m, 2m and 5m PDLs will give rise to scan ranges of 3.2ps, 6.4ps and 16ps respectively, according to expression (14).

Notable, however, is the skewedness of the traces. As in the case of the TPP technique, this is due to the inherent decrease in average power as the reverse bias applied to the absorber section is increased. By subtracting a reference trace which was taken at a baseline position where no cross-correlation occurs while using the same reverse bias range and setup parameters, this effect can be removed. An example is presented using the SOSBERT scan acquired using the 1m PDL, see Figure 3-21.

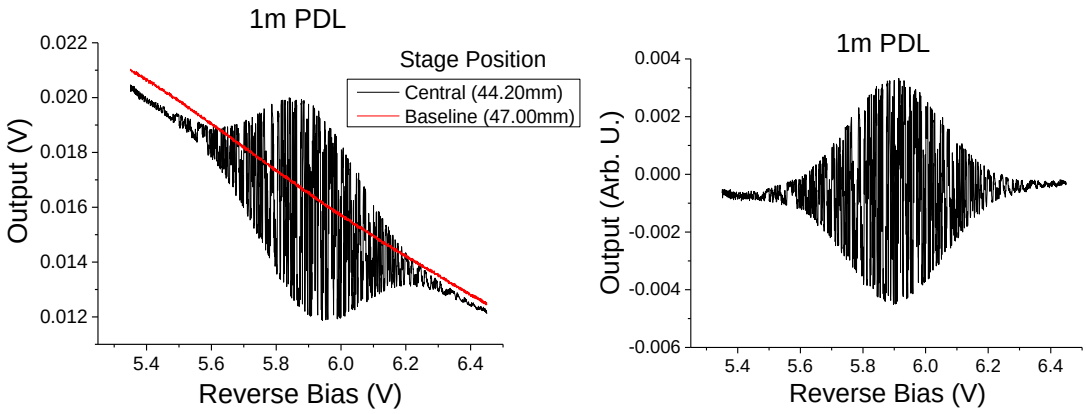

Figure 3-21 – The original 1m-PDL SOSBERT trace, left , from which the red reference baseline trace is subtracted in order to account for the decrease in average power, leading to the corrected trace, right.

As can be observed, the baseline subtraction has not been a perfect tool in removing the skewed nature of the original trace, as there are minor differences in each baseline which occur due to the slight differences in beam alignment at the different positions of each scan. This has resulted in an offset reduction from the left to the right of the trace. This method, however, aids in the analysis of each trace, which for future experiments must have peak functions such as Gaussians fit to their upper envelopes, which proved difficult unless the baseline was subtracted.

The next step in the deconvolution process is to convert the x-axis from an applied reverse bias value, to the corresponding change in repetition rate using expression (23) with reference to Figure 3-11, and finally to the temporal delay by combining this tunability Δf with the PDL lengths l of 1m, 2m and 5m into expression (14), see Figure 3-22. Note that in the case of this experiment, the ~40cm free-space component of the long arm may be excluded, since the free-space before fibre coupling and after fibre collimation was approximately equal to the free-space short arm[9].

[9] Note, throughout the project, when the free space of the short and long arms does not balance, the free-space component is explicitly included in the calculation and the discussion.

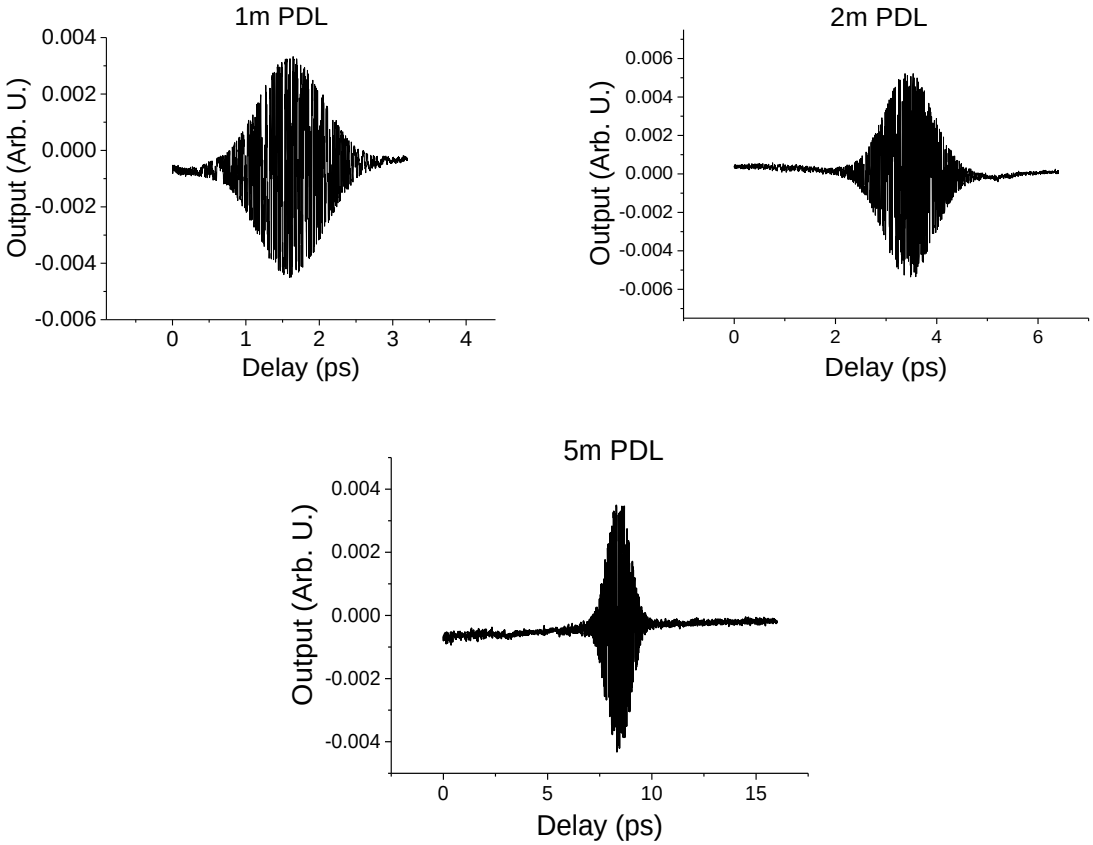

Figure 3-22 – Fully deconvolved SOSBERT scans acquired for 1m, 2m and 5m PDL lengths. In each case the same reverse bias range was applied, and then converted to a temporal scanning range.

Of interest to note is the fact that although the same step-size in reverse bias voltage was used for each length of PDL, the scaling factor of the delay length actually increases the step-size of the temporal delay, which explains the apparent change in resolution between traces. As such, the temporal step-size during the 2m and 5m fibre PDL experiments will be twice and five times as large as that of the 1m fibre PDL respectively, see Figure 3-23 where these effects are summarised.

PDL length (n = 1.46)	Reverse Bias Step-Size	Repetition Rate Tuning Step-Size	Temporal Step-Size	Scan Range for 5.35V to 6.45V
1m	0.5mV	1.52kHz	1.45fs	3.2ps
2m	0.5mV	1.52kHz	2.90fs	6.4ps
5m	0.5mV	1.52kHz	7.25fs	16.0ps

Figure 3-23 – Tabulation of the difference in temporal step-size which arises due to the scaling of the scan range brought about by the increase in PDL length, despite the same reverse bias step-size.

For a full comparison, the SOSBERT trace acquired using the 5m PDL is normalised and plotted alongside a normalised version of the original mechanical stage cross-correlation (Figure 3-19), overlapped, and plotted on a delay time axis, see Figure 3-24.

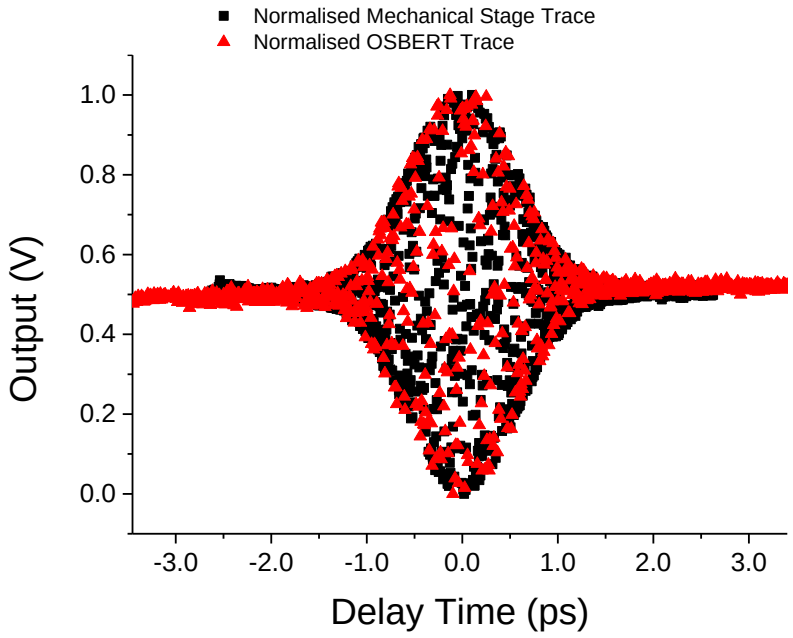

Figure 3-24 – The OSBERT trace acquired using a 5m PDL is superimposed on the original mechanical stage trace for comparison; both have been normalised. Whilst the mechanical stage scan has a step-size of ~3.33fs, the OSBERT scan has approximately double the step-size of ~7.2fs.

What is clear is that the skewedness of the OSBERT trace has not been entirely removed, as previously discussed. However, the OSBERT scan has captured the same features present in the mechanical stage cross-correlation. Under these circumstances, half the voltage step size in reverse bias would need to be used in order to meet the resolution of the mechanical stage.

3.4.3. Tapered-Waveguide Non-linear TPA Experimental Results

The same SOSBERT scanning method and deconvolution process may equally be applied to the tapered-waveguide device (or indeed, any MLLD whose repetition rate may be tuned via altering the biasing conditions).

A standard mechanical stage cross-correlation scan is acquired under selected mode-locking biasing conditions (760mA forward current applied to the gain section of the device, and 4.00V reverse-bias applied to the absorber section - the centre of the reverse bias range of 3.80V to 4.20V), see Figure 3-25.

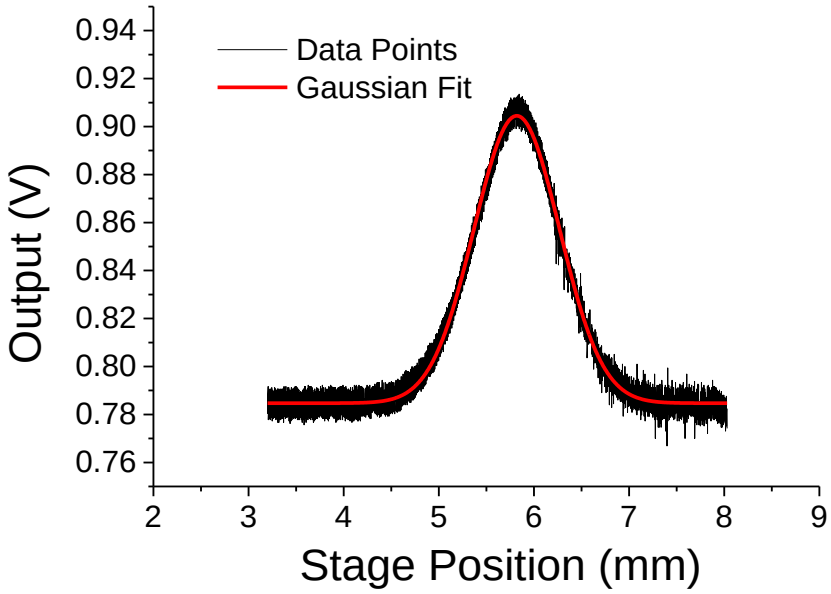

Figure 3-25 – Mechanical stage TPA Cross-correlation taken using the tapered-waveguide device at 4.00V reverse bias and 760mA forward current. A Gaussian function is fit to the data in order to establish the central peak position (5.8mm).

We then fit a Gaussian function to the data in order to mathematically determine the central peak position (in this case, 5.8mm). The stage is then centred on this position and kept stationary, resulting in a full free-space PDL of 1.79m in order to carry out a SOSBERT scan. Sweeping the reverse bias through the MLR from 3.80V to 4.20V produces the first OSBERT-based TPA trace, see Figure 3-26.

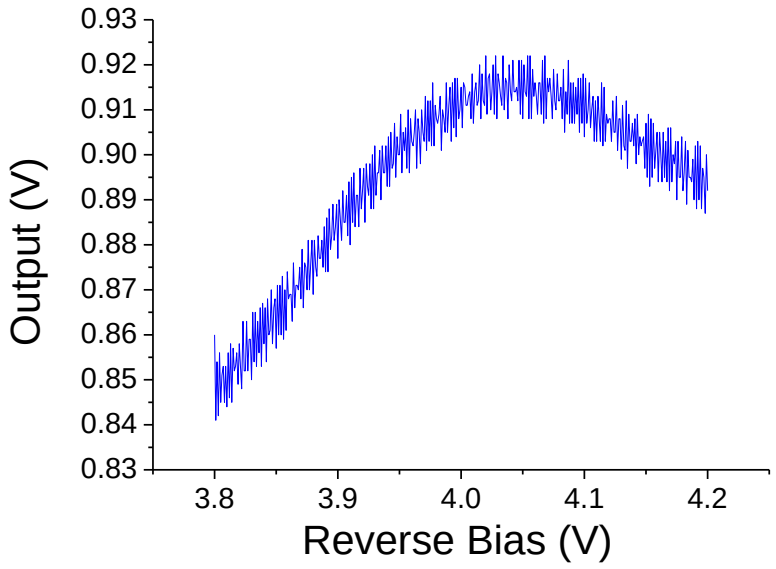

Figure 3-26 – A SOSBERT TPA trace taken whilst the stage was centred to 5.80mm (the centre of the cross-correlation peak) using the full repetition rate tunability of 5MHz via 0.4V reverse bias change.

On first inspection, this may seem an unusual response, barely resembling the results achieved with the mechanical stage. However, when we consider that the Δf and I parameters for the tapered device result in less than a 2ps scan range (as previously found theoretically in Figure 3-13 and then practically in Figure 3-15 in TPP experiments), it is not surprising that only the upper peak of the TPA trace could be scanned. In fact, in order to represent the full cross-correlation we would have to take SOSBERT traces at multiple positions of the translation stage, see Figure 3-27.

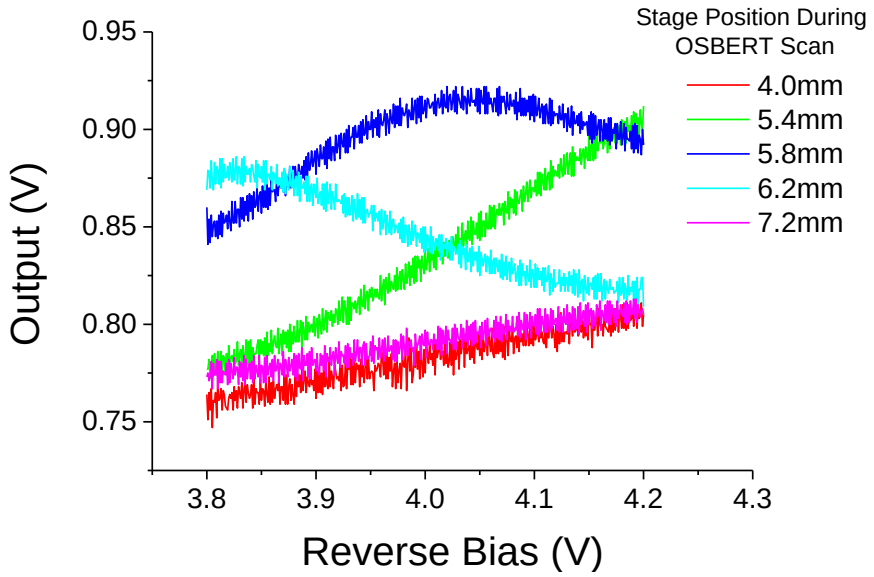

Figure 3-27 – Multiple TPA SOSBERT traces taken at five different positions of the mechanical translation stage in order to scan various features of the cross-correlation. All were taken using the same reverse bias range, at 1mV step-size.

Each trace was acquired using the exact same reverse bias range and under all the same conditions, with the only exception being that the mechanical stage was centred on a different part of the expected cross-correlation position in each instance. These positions (4.0mm, 5.4mm, 5,8mm, 6.2mm and 7.2mm) were chosen with respect to the mechanical stage trace (Figure 3-25) in order to scan a range of features of the cross-correlation, from the baseline, through the wings and the entire peak and again on the opposite side.

If we now apply the deconvolution procedure used in section 3.4.2 with the narrow-ridge device to the tapered laser's parameters, we may easily place each individual trace at its scanned position and superimpose it upon the original mechanical stage scan. Firstly the x-axis reverse bias is converted to a repetition rate tunability Δf using expression (24) with reference to Figure 3-11, and converted to a temporal scan range using expression (14),

and then to a spatial range in order to match that of the mechanical stage scan (Figure 3-25). The position in which each OSBERT scan was acquired is then simply added to the x-axis data in order to superimpose the OSBERT scan with the mechanical stage position it was taken, see Figure 3-28.

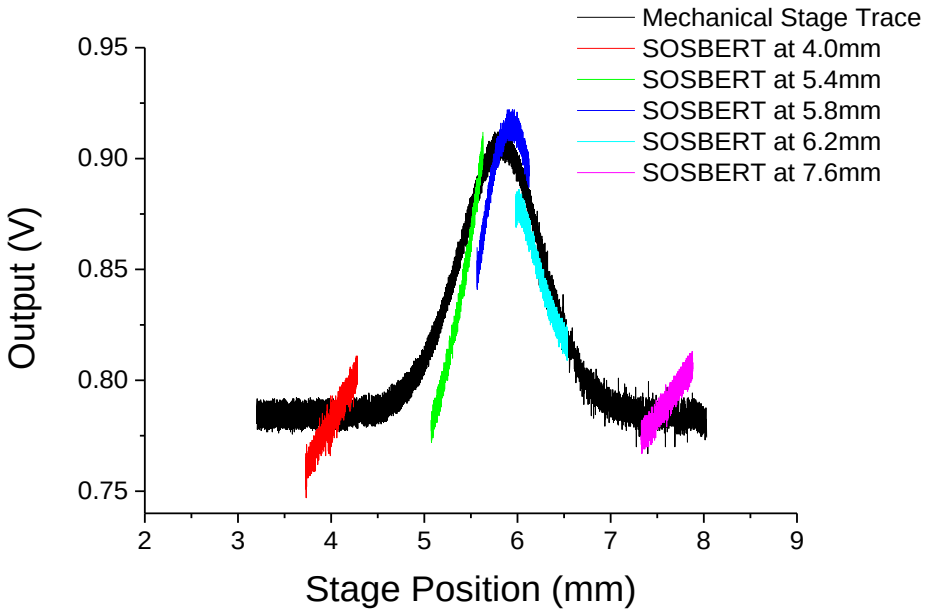

Figure 3-28 – The SOSBERT traces for each position are converted from a reverse bias to a spatial position corresponding to the superimposed cross-correlation trace taken using the mechanical stage.

We now begin to see the validity of each individual SOSBERT scan as the underlying features of the cross-correlation become apparent. However, as in the case of the narrow-ridge device, we now face a similar problem regarding the skewedness of each trace; however in this non-linear case the trend increases due to the peak power increase with increasing reverse bias. In particular this is pronounced in the degree of skewedness, which is far sharper when the trace increases through the left hand side wing, and becomes shallower when decreasing through the right hand side. The solution remains the same, however, which is to subtract a reference point from each individual trace, in this case that of the baseline. Whilst this effectively straightens each OSBERT trace, it also re-scales it with respect to the detector output voltage, and as such both the OSBERT and the mechanical stage traces are normalised for greater comparison see Figure 3-29. In this case the individual OSBERT traces have been concatenated in order to do so effectively, giving one continuous data set.

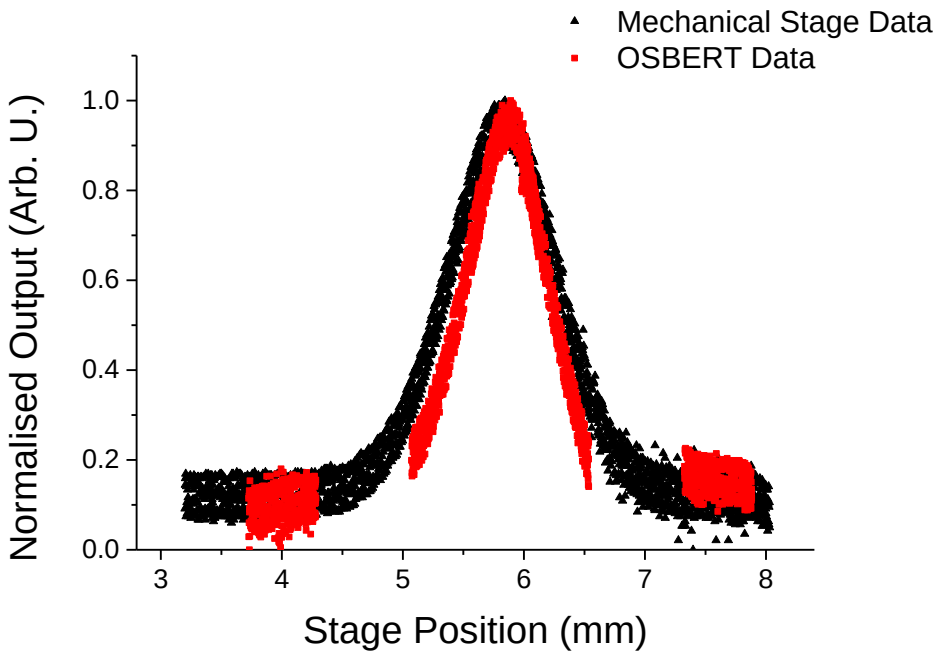

Figure 3-29 – The final normalised deconvolved SOSBERT traces are combined (red) on the positions they were acquired, showing a full TPA cross-correlation trace using the OSBERT method, once again compared to the equivalent normalised mechanical stage scan (black).

Following the same deconvolution steps, we now see several SOSBERT traces which combined now represent the original two-photon-absorption cross-correlation trace very well, at the cost of losing the exact detector output values having normalised the full curve along with the superimposed mechanical stage trace. We find the OSBERT cross-correlation is in fact narrower than the mechanical stage counterpart. This is likely due to the fact that during an OSBERT trace, the reverse bias is increasing, leading to an increase in peak power and a reduction in pulse duration. As a result, since the final OSBERT trace is made up of five individual OSBERT traces of increasing reverse bias, each portion of the trace tends towards an increasingly narrowed trace[10]. Whilst technically the mechanical stage was required to reconstruct the entire cross-correlation in this particular case, if the PDL was longer, or indeed the cross-correlation was narrower, the scan would have been totally acquired under a single sweep of the reverse bias. Thus, these traces validate the notion of a non-linear two photon absorption trace acquired using only one MLLD, driven entirely non-mechanically by electrically varying the reverse bias to the saturable absorber, indicating great potential for future studies requiring non-linear optics.

[10] Note, this marks the final experiment conducted using the tapered-waveguide device before its irreparable malfunction part way into the project. As such, the remaining chapters, unless stated otherwise, contain experimental results obtained using the narrow-ridge device only.

3.5. Testing Applications with OSBERT

The following section describes a number of proof of principle applications which were tested using the above SOSBERT technique in order to determine its validity and accuracy. In each case, the forward current applied to the gain section of the MLLD was held constant throughout at 210mA, whilst the entire device temperature was kept at 20°C.

3.5.1. Introduction

An application for optical sampling techniques is time-of-flight or absolute distance measurements, such as LIDAR (Light Detection And Ranging) [129]. These involve using a pulsed laser source to direct the pulses towards a target of interest, and then gathering the reflections from its surface in such a manner as to calculate the time taken for the return trajectory, before calculating either the distance of the target or indeed the distance the target has moved in a set period of time. For such applications, several time-of-flight distance measurements have been reported which are also based upon optical sampling techniques, and have involved the use of conventional mechanical delay lines [130, 131].

Of particular interest, is the work of Yang *et al* [62], who reported an experimental demonstration of remote OSCAT-based motion tracking using a highly imbalanced Mach-Zehnder interferometer, where the distance to the target was several kilometres. Given the similarities between OSCAT and OSBERT, this work is highly relevant and as such will be discussed in greater detail in Chapter 4. The OSBERT method of the basic table-top proof of concept representation of LIDAR remains similar in essence.

In the context of an imbalanced Mach-Zehnder interferometer, a long passive delay line such as an optical fibre is coiled on the optical bench and represents the distance between the detector and the target, see Figure 3-30. The laser pulses are directed along the course of the long PDL towards some target, which for the sake of this demonstration is a reflective mirror, such that the reflected pulses return on the original trajectory, and may interfere with another pulse which has traversed the significantly shorter arm. Their cross-correlation and its resultant spatial (or temporal) displacement when the mechanical stage moves, gives rise to the calculation of the distance moved.

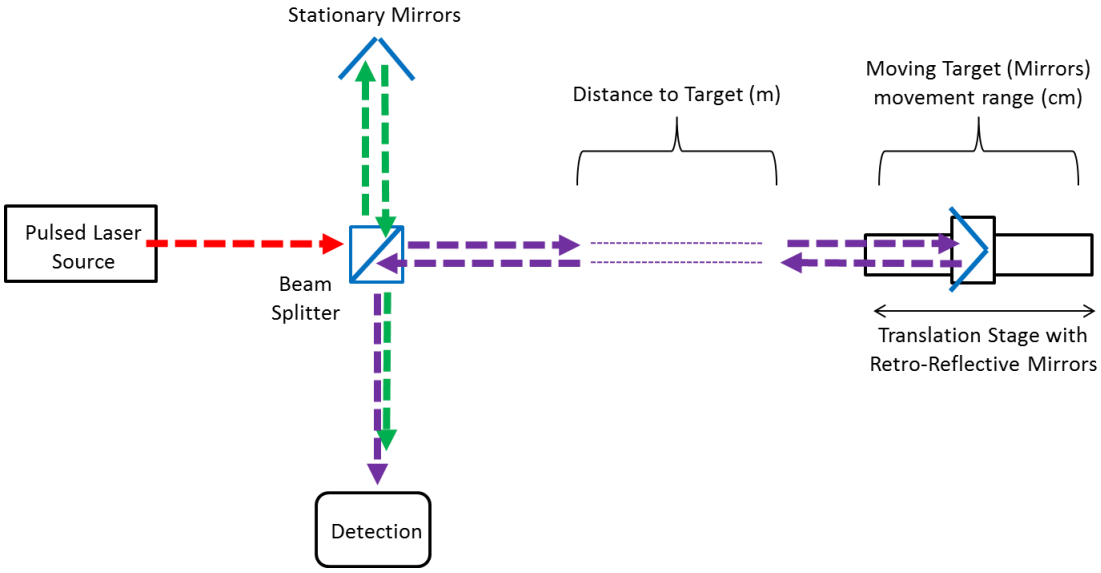

Figure 3-30 –Diagram of a displacement measurement setup within an imbalanced interferometer.

3.5.2. Determining the displacement of a target using SOSBERT

Taking the same approach as those OSBERT scans described in section 3.4.3 which were taken at multiple stage positions, we now turn our attention to the narrow-ridge device which has a considerably greater scan range (given the combination of repetition rate tunability and coiled optical fibre PDL lengths). We refer to the diagram of Figure 3-30 in conjunction with the actual experimental setup of Figure 3-18.

A SOSBERT trace is taken under a selection of reverse bias ranges, leading to interferometric cross-correlations as described. The process is repeated however, when moving the target (in this case the fibre port mounted on the mechanical stage) to various positions, thus off-setting the position we would expect to find an OSBERT cross-correlation, see Figure 3-31. We demonstrate the principle using the 5m optical fibre, and compare a range of reverse bias (and therefore repetition rate tunability) applied to the absorber section for each experiment, namely 5.60V - 6.20V, then 5.30V - 6.50V, and finally 4.70 - 7.10V. Using expression (23), these 0.60V, 1.20V and 2.40V reverse bias ranges correspond to 1.82MHz, 3.65MHz and 7.30MHz repetition rate tunability respectively.

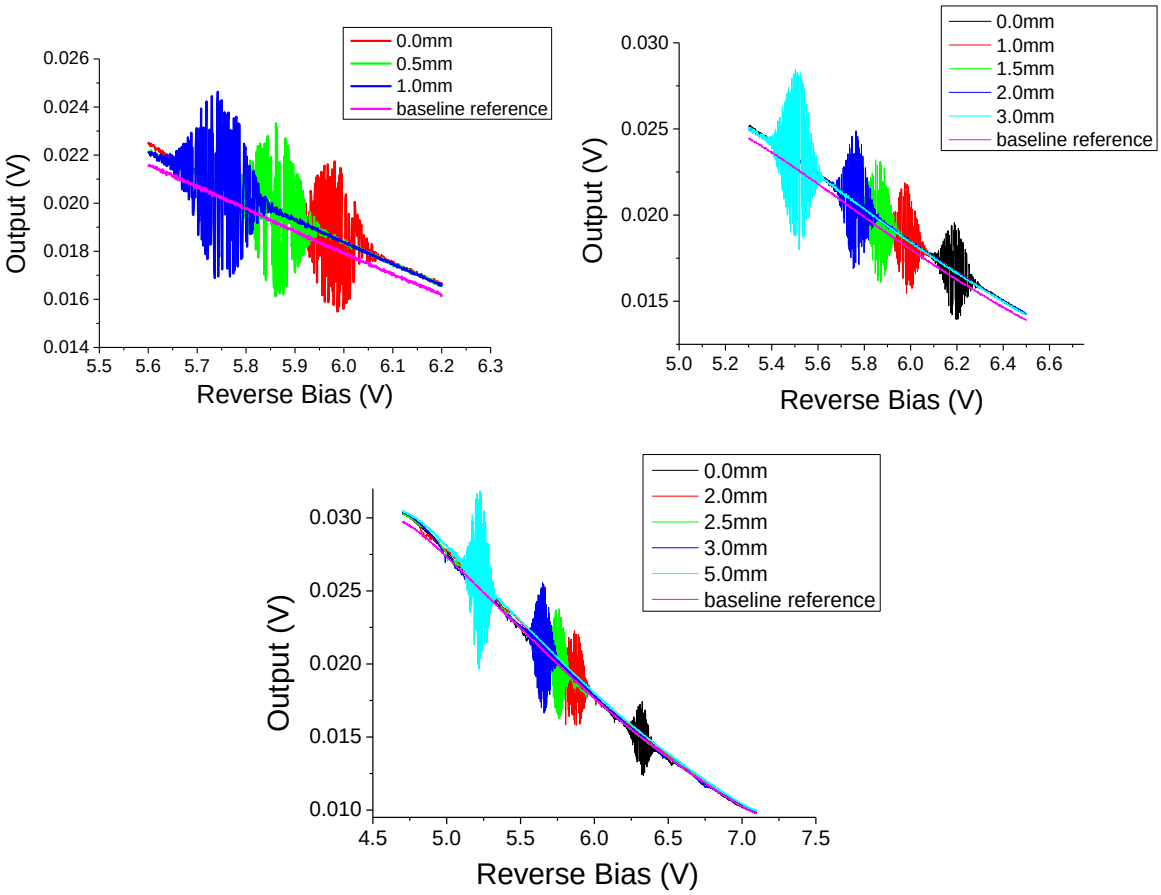

Figure 3-31 – SOSBERT traces taken at several different stage positions using a 5m PDL. In each case, the reverse bias range (or repetition rate tunability) is increased.

As was previously demonstrated in section 3.4.2, increasing the length of PDL whilst keeping the range of reverse bias constant increased the scan range. Here, the contrary scenario is demonstrated for proof of principle, where increasing the range of reverse bias applied in each experiment has increased the scan range for a constant 5m length of PDL. We then apply the same deconvolution process as described in section 3.4.2, whereby the reverse bias applied is converted to a corresponding repetition rate, and then to a scan range. A baseline reference is then subtracted from each successive cross-correlation trace, see Figure 3-32. It is prudent to reiterate that the reference-subtraction phase of the trace deconvolution is not entirely necessary; the central position of each peak remains the same in the time domain, and as in previous sections it serves only to aid in the mathematical fitting procedures.

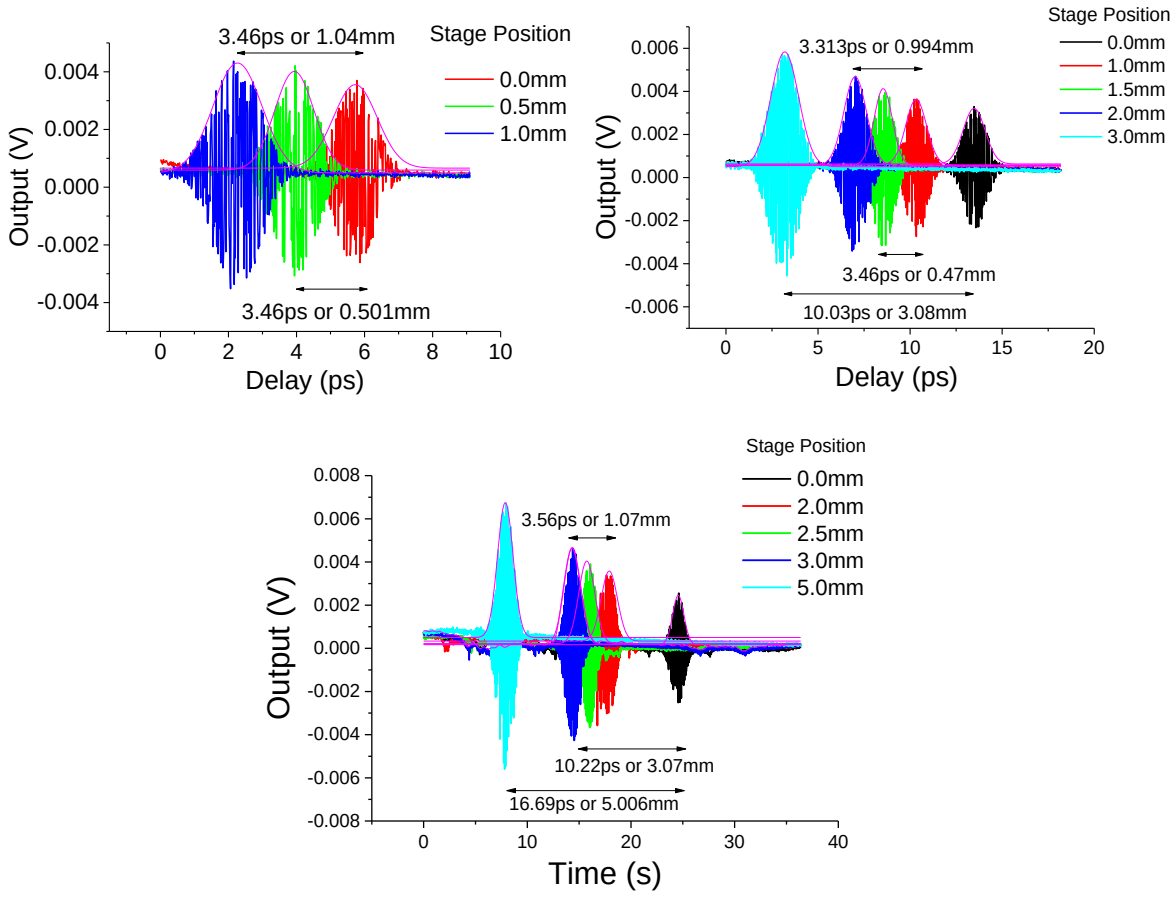

Figure 3-32 – Having deconvolved each SOSBERT trace and converted to the scan range, the central position of each peak may be measured by fitting a Gaussian (purple) to the upper envelopes.

We now have cross-correlations taken from the target displacements converted to a temporal domain. In order to determine the relative distance between each trace as accurately as possible, we fit the upper envelope of the traces with Gaussian functions, providing us with a repeatable mathematical value for the peak's central position in each case. From here we may easily calculate the various displacements of the target, which, as can be seen, are in good agreement with the actual known displacement in each case, see Figure 3-33.

Reverse Bias Range	OSBERT for 0.5mm Stage Displacement	OSBERT for 1.0mm Stage Displacement	OSBERT for 3.0mm Stage Displacement	OSBERT for 5.0mm Stage Displacement
0.6V	0.50mm	1.04mm		
1.2V	0.47mm	0.99mm	3.08mm	
2.40V	0.54mm	1.07mm	3.07mm	5.01mm

Figure 3-33 – Tabulation of the target displacement experiment, where each value measured using OSBERT is compared with the known displacement tracked using the mechanical stage.

The results encouragingly indicate that OSBERT scans can be accurate as to the targets displacement to within a few tens of micrometres, and this does not appear to be dependent upon the range of reverse bias used. The error associated with each value may (as in previous experiments) be attributed to the variation in output characteristics as the reverse bias is increased, and in the Gaussian fitting process.

3.5.3. Determining the refractive index of a material using SOSBERT

One test of OSBERT's abilities is to consider the calculation of the refractive index of some material situated within the experimental setup. In this example, we use the narrow-ridge device to calculate (and confirm) the refractive index of the optical fibre used as the PDL. Similarly to the above described experiments, OSBERT traces are taken of the cross-correlations using the method of tuning the repetition rate via tuning the reverse bias applied to the absorber section. In this case, the process is repeated after the position of the mechanical stage is arbitrarily altered, see Figure 3-34.

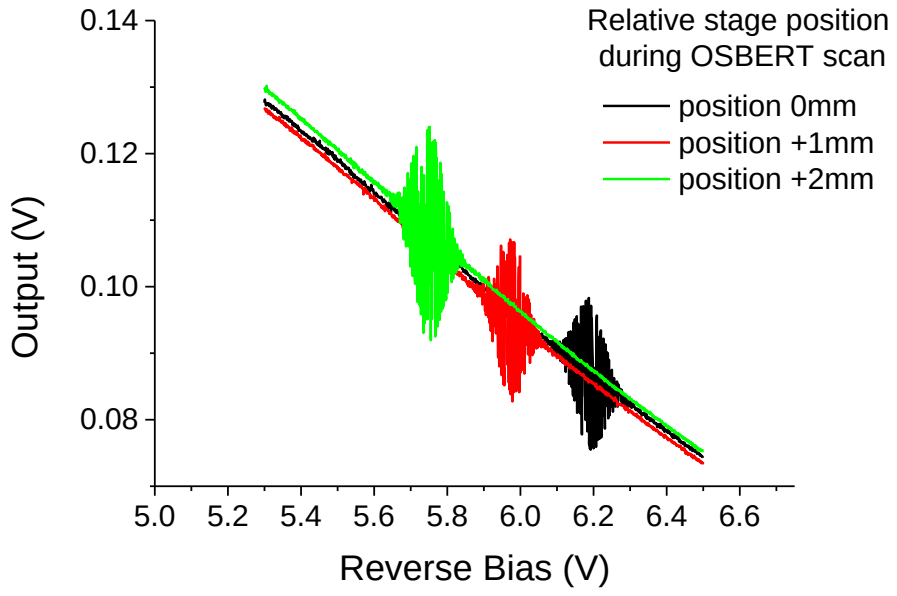

Figure 3-34 – SOSBERT traces taken at three different stage positions set a total of 2.00mm apart. In each case the same reverse bias range was applied, using the 5m fibre.

We then apply the conversion process described in the previous section to convert from a reverse bias to a delay time using expression (14). In this case we have used the 5m fibre PDL, however have assumed no knowledge of its refractive index, and as such may consider that $n = 1$, see Figure 3-35.

In addition, as the beam emerges from the fibre, there is an additional 30mm of free space delay left in the long arm before meeting with the short arm beam at the detector, giving a total assumed PDL length of 5.30m

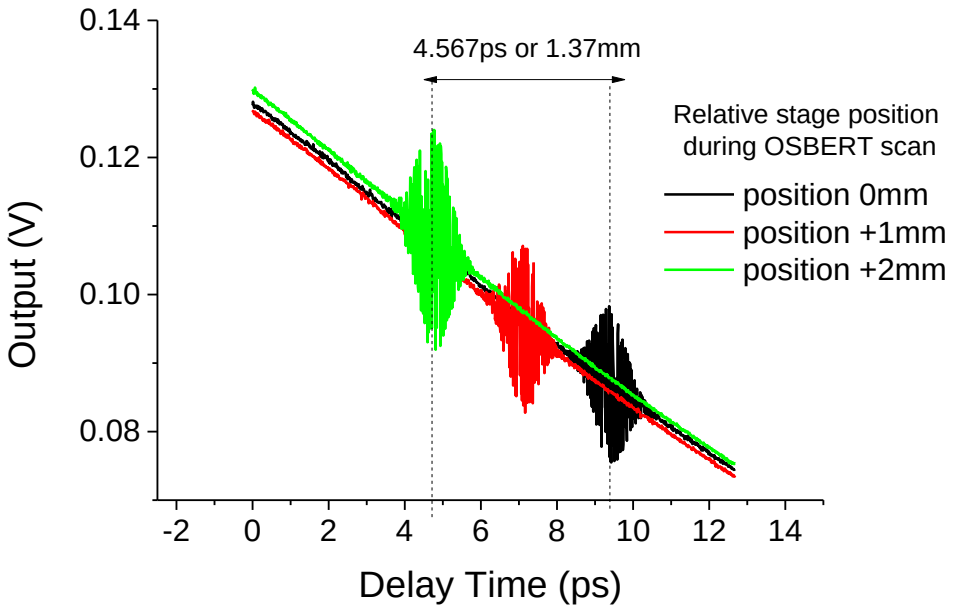

Figure 3-35 – Assuming the total 5.30m PDL is entirely free-space (*n = 1*), the conversion from reverse bias to delay time results in a mechanical stage displacement of 1.37mm in contrast with the actual 2.00mm displacement. This is because 5.00m of the PDL is optical fibre of unknown (greater) refractive index.

As can be seen, assuming the entire PDL is free-space (with *n = 1*), the distance between OSBERT traces is calculated as only 1.37mm, compared with the known value of 2.00mm. This 31.5% discrepancy is due to the incorrect assumption of the refractive index. This can be calculated as follows.

The optical fibre is 5.00m long, and has a refractive index n_{fiber}. We may assume the additional 30cm of free-space delay has a refractive index $n_{free\text{-}space} = 1$. As such, the fibre section of the PDL contributes 94% of the total delay, whilst the free-space section contributes 6% where $\Delta t_{tot} = \Delta t_{n_{fibre}} + \Delta t_{n_{free-space}}$. In terms of the measured 1.37mm of scanning, this relates to 1.32mm and 0.08mm respectively of the total scan. In reality, we know that 2.00mm was moved through between the OSBERT traces, and so applying the PDL percentage contributions we calculate that again 94% or 1.92mm should have come from the 5m fibre. We now have an expected and a measured value of the contribution of the scan range made by the 5m fibre alone, and for this reason may ignore the free-space 30cm. We now find that $n_{fiber} = 1.92/1.32 = 1.454$. Comparing this value

with the specifications provided by the manufacturer we find good agreement, where the refractive index of the fibre core is given as n_{core} = 1.457. We may now repeat the above conversion process instead using the newly calculated refractive index value of 1.46, see Figure 3-36.

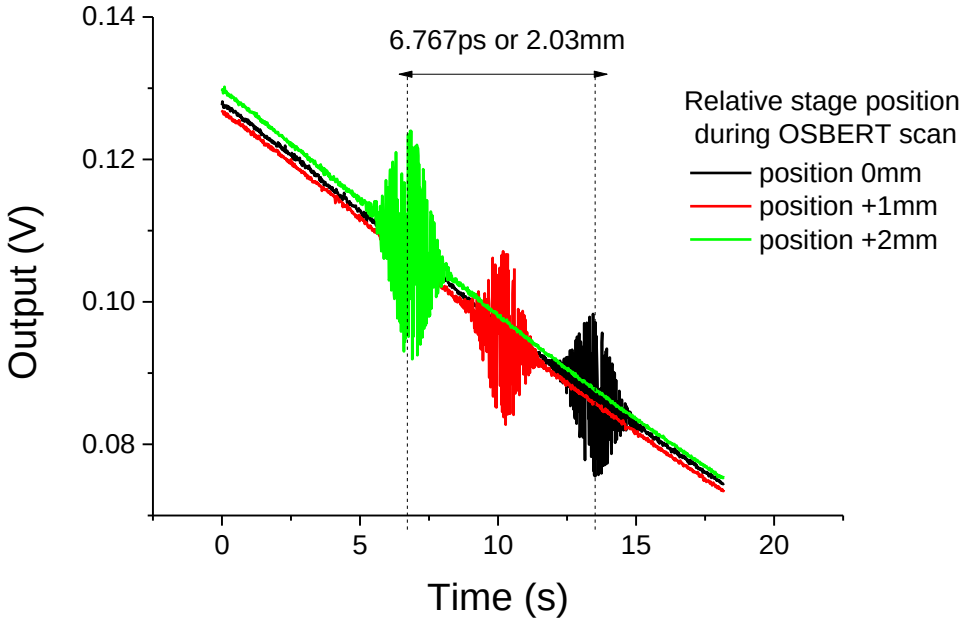

Figure 3-36 – Assuming now the total 5.30m PDL is 5m of n = 1.46 fibre and 0.3m of n = 1 free-space, the conversion from reverse bias to delay time now gives a mechanical stage displacement of 2.03mm in contrast with the actual 2.00mm movement. This is a significant boost in the accuracy of the movement compared to the previously calculated 1.37mm.

As can be seen, the conversion process has now significantly increased the accuracy of the known displacement, where the SOSBERT traces have indeed been separated by ~2mm due to the movement of the mechanical stage, improving on the original calculation of 1.37mm, when it was assumed the refractive index was that of air[11]. In essence, this simply involved rearranging the fundamental OSCAT expression (14) to find any unknown parameter (in this case, refractive index) when all other parameters are known; equally we may have repeated this process assuming, for example, the PDL length (acting as the distance to the target) was unknown and all other parameters were known.

[11] Note, any refractive index value may have been assumed for the PDL, as the same calculations would still give rise to the true refractive index value.

3.5.4. Measuring the thickness of a sample

Another application-based proof of principle of the OSBERT method is to measure the thickness or the refractive index of a sample, where one of these parameters is unknown; the OSREFM technique was used to accomplish this by delaying a terahertz signal through silicon windows of various thicknesses [72]. The typical OSBERT setup is simplified in order to illustrate how the thickness (or refractive index) of a sample inserted in one of the arms gives rise to an optical path difference between both arms, see Figure 3-37.

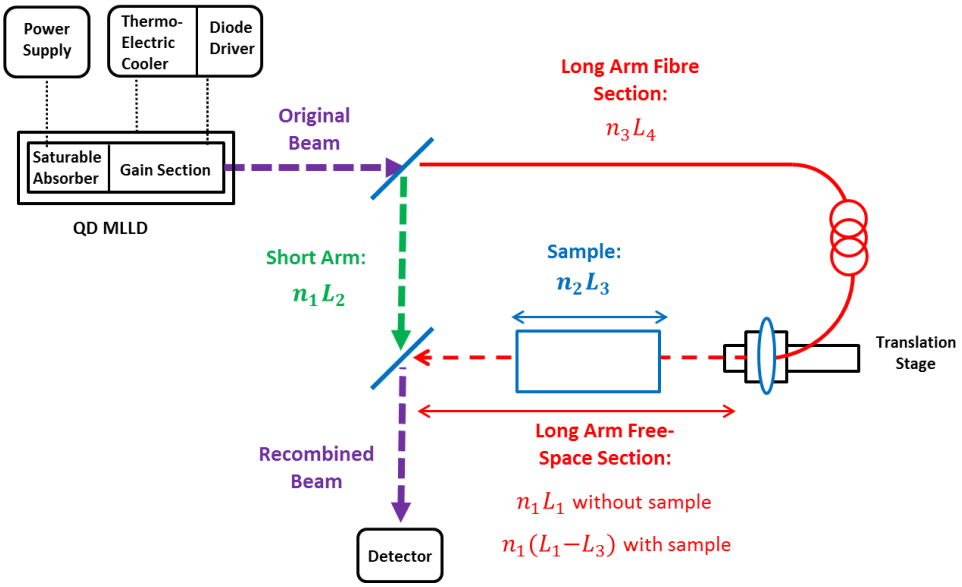

Figure 3-37 – Diagram showing all optical path components of both the short and long arms, with and without a sample present in the long arm's free-space component, based on the experimental setup described in Figure 3-18.

If a mechanical stage cross-correlation is taken when a sample is not present and again when it is, its trace will have shifted due to the change in refractive index of the sample causing an additional delay. The results may then be repeated whilst the stage is held stationary and an OSBERT trace is acquired with and without a sample present.

Consider D_1 is the optical path length of arms 1 and 2 combined without a sample, consisting of the free-space beam in the short arm of relative optical path $n_1 L_2$, and in the long arm the fibre-coupled component $n_3 L_4$ plus the free-space component after beam collimation $n_1 L_1$, such that

$$D_1 = n_1 L_1 + n_1 L_2 + n_3 L_4 \tag{25}$$

Where $n_1 = 1.0$ is the refractive index of air and $n_3 = 1.46$ is the refractive index of the 5m-long optical fibre. D_2 is therefore the optical path length of arms 1 and 2 when a sample whose own optical path is $n_2 L_3$ is present. In this case the sample's own length replaces a portion of the free-space path in the long arm, such that

$$D_2 = n_1 L_2 + n_1 (L_1 - L_3) + n_2 L_3 + n_3 L_4 \tag{26}$$

Where L_3 is the thickness of the sample and n_2 is its refractive index. The optical path difference (OPD) is therefore the difference in optical path lengths, where

$$OPD = D_2 - D_1 = n_2 L_3 - n_1 L_3 \tag{27}$$

Throughout this experiment, known lengths are $L_1 = 30cm$, $L_2 = 30cm$, and $L_4 = 5m$. In this case the sample is a neutral density (ND) wheel of unknown thickness L_3 composed of fused silica (*Thorlabs NDC-100C-4 Unmounted Continously Variable ND filter*), which was rotated to the minimum (near-zero) attenuation position and placed in the path of the long arm. We ascertain that the fused silica has a refractive index of around 1.45 [132] for the 1260nm wavelength of the narrow-ridge MLLD, and so we may therefore measure its thickness. A mechanical stage cross-correlation was taken for comparison with the OSBERT scan, where the reverse bias was constant at 6.0V throughout, see Figure 3-38.

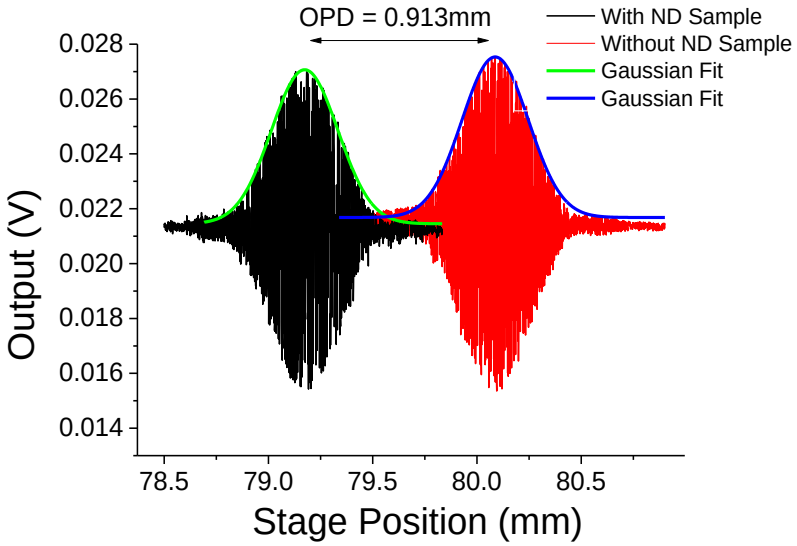

Figure 3-38 – Mechanical stage cross-correlations each acquired with a reverse bias was of 6.0V. The presence of the ND sample leads to an OPD causing the cross-correlation position to change.

Measuring directly we find the OPD induced by the presence of the fused silica ND sample is 0.913mm, which we may substitute into expression (27) to find the length (thickness) L_3 of the sample is 2.03mm, in good agreement with the known thickness of 2.00mm given by the vendor. Sources of error giving rise to inaccuracies within a few tens of microns lie within the absolute thickness of the sample which is likely to have surface imperfections, with the Gaussian peak-fitting procedure being imperfect leading to an error in the central value, and with the dynamic acquisition of the traces, which occurred over several minutes each, during which time fluctuations in pulse timing, temperature, and bias controls may vary.

The scan was then repeated using the SOSBERT method, where in both instances the mechanical stage within the setup remained stationary, allowing the scan to be acquired by reverse bias variation only, converting in the usual manner to a temporal delay via the OSCAT equation (14) and converting the applied reverse bias to a change in repetition rate using equation (23), see Figure 3-39. In this case the fibre length of the long arm was 5m, and the reverse bias applied corresponded to a repetition rate tunability of 3.33MHz.

In this case, the OPD induced by the presence of the fused silica sample in the long arm of the OSBERT setup was found to be 0.908mm, giving rise to a sample thickness of 2.02mm, in good agreement with both the supplier's specifications of 2.00mm, and with the 2.03mm result measured by the mechanical stage method above.

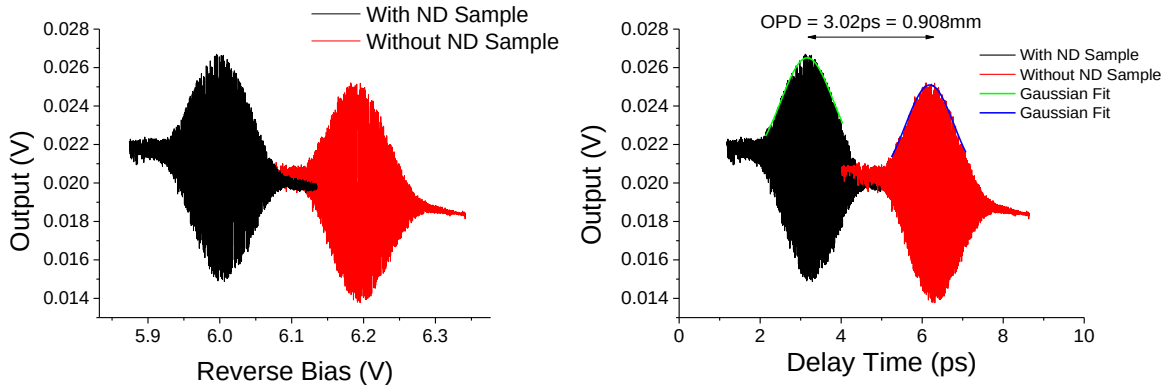

Figure 3-39 – SOSBERT scans analogous to Figure 3-38 where the mechanical stage is held stationary throughout, and instead the reverse bias is swept for a respective 3.33MHz repetition rate tunability, and for a PDL fibre length of 5m. Left, raw data traces acquired by varying the reverse bias applied, and right, those traces converted to a delay time.

As with the mechanical stage scan, sources of error leading to the similar few tens of microns inaccuracy include fluctuations in the lasers output over the several minutes acquisition time. Whilst the position of the stage during the OSBERT scan remains constant (unlike in the mechanical stage scan method, where beam alignment and divergence may lead to errors), the OSBERT traces are composed of a fairly wide variation in output characteristics due to the changes in reverse bias, and may lead to errors in the calculation, as well as the fitting of the Gaussians in order to determine the central peak value. It should be noted that either the refractive index or the sample thickness could have been calculated, depending on which factor was considered unknown.

3.6. Conclusions

This chapter has proven the underlying principles of the OSBERT technique, firstly in temporal pulse positioning, which demonstrates the scan range available to each MLLD is dependent upon its repetition rate tunability and the PDL length used in the long arm; that is to say, all that is required to produce a temporal delay under these conditions is a change in reverse bias applied to the saturable absorber section of the MLLD.

Next, the active scanning capabilities of the method were demonstrated, showing that the same calculated temporal scan range found from temporal pulse positioning may now be found whilst actively scanning using the SOSBERT technique. It was proven that no moving or mechanical parts were required in order to carry out these cross-correlation scans; simply linearly varying the reverse bias applied to the absorber section tuned the repetition rate without a need for an intra-cavity stepper motor, and without a translation stage to drive the scan. As such, temporal scanning was achieved using only one laser - a two-section quantum dot passively mode-locked laser diode. Thus OSBERT may have the potential to compete with two-laser techniques such as ASOPS and ECOPS, with absolutely no moving parts necessary to conduct the scan. To the best of my knowledge, this is the first time such a technique has been demonstrated.

Both linear (single photon absorption) and non-linear (two photon absorption) techniques gave rise to proof of principle demonstrations, including target displacement measurements and calculations of the thickness (or refractive index) of a material, which were carried out successfully and accurately using the SOSBERT technique and compared

with a conventional mechanical translation stage optical sampling technique. Specifically, both the target displacement and the thickness of the sample were accurately measured to within a few tens of microns, showing accuracies very similar to the conventional mechanical stage method. Scans were acquired with femtosecond level step-size, across various scan ranges up to 40 picoseconds when using a 5m PDL and the full 10MHz repetition rate tunability of the narrow-ridge device.

It is important to note that given expression (14) any unknown parameter may actually be measured using the OSBERT method, provided the others are known. For example, it is possible to instead rearrange the above experiment and calculate the length of passive delay line used, and as such a distance measurement may be set up which measures the distance from the laser to some target given a known target displacement.

Although the entire underlying principle of OSBERT is now proven (single-laser optical sampling with absolutely no moving parts), the scan itself does occur very slowly – a standard cross-correlation such as those described can take several minutes to acquire, and therefore in terms of scan rate is only on par with the mechanical stage scans used for comparison. Therefore, in the next chapter we turn our attention to the ability to not only scan continuously, but also several orders of magnitude faster.

4. Fast-OSBERT: Theory, Development and Analysis

This chapter discusses the final improvement in the OSBERT technique, which in addition to optical sampling with just one inexpensive and compact laser (a two-section quantum dot passively MLLD) without any mechanical or moving parts, is to scan repetitively at fast scan rates in order to compete with the state of the art on all levels. Additional theory surrounding the drawbacks associated with longer passive delay line lengths and increased scan rates are also discussed. Ultimately, cross-correlations are acquired without issue up to scan rates of tens of kilohertz, with promising indicative results up to megahertz scan rates. The proof of principle for so-called Fast-OSBERT is demonstrated as a target displacement measurement device, and is accurately presented at scan rates of 10kHz.

4.1. OSCAT and Displacement Measurement

Mode-locked lasers within a Michelson interferometer configuration present a method of measuring long distances as well as target displacements over long distances. Cui *et al* [131] performed distance measurements in air using a femtosecond frequency comb laser up to free-space distances of 50m by measuring cross-correlations in an imbalanced Michelson interferometer, where the delay was tunable via a mechanical translation stage. Absolute Distance Measurements (ADMs) have also been realised using the ASOPS technique, though as is inherent to ASOPS, two pulsed laser sources were required to perform such measurements, inflating the costs and increasing the complexity [41, 133, 134].

Owed to the requirement of a long passive delay line (PDLs), the OSCAT method described in the previous chapters lends itself particularly well to displacement measurement techniques over long distances, since the large in-built imbalance in the interferometer arms serves as the distance between a target and a detector. Wu *et al* successfully demonstrated long distance measurements at 47m [135] and 60m [136] based on the OSCAT technique.

Similarly, Yang *et al* [62] recently used OSCAT to demonstrate LIDAR (Light Detection And Ranging), using a repetition-rate tunable femtosecond fibre laser in conjunction with a PDL equivalent to over 2km. Their study was sufficiently sensitive to detect target

vibrations as little as 15µm at a scan rate of 50Hz. Inherent to the OSCAT technique, the scans were acquired by mechanically tuning the repetition rate of the laser, which was also the major limitation of their scan rate. As stipulated in the following sections, it is the work of Yang *et al* which forms some of the theoretical basis of this chapter and the development of FOSBERT.

4.2. Dynamic OSCAT model

In order to drive the OSBERT scan faster than the step-by-step version demonstrated by S-OSBERT in chapter 3, we must fundamentally be able to modulate the repetition rate from a minimum to a maximum value, which in the case of MLLDs means fast modulation of the amplitude of reverse bias applied to the saturable absorber section. F-OSBERT (Fast-OSBERT) differs from Slow-OSBERT by only one key factor; whereas in SOSBERT the repetition rate was tuned gradually and linearly in a time frame equivalent to that of the standard mechanical stage it successfully replaced, a FOSBERT scan requires fast modulation of the repetition rate via a signal generator (which replaces the static power supply), typically by a sinusoidal function at a rate of multiple scans per second. Faster acquisition methods such as an oscilloscope are also therefore required, rather than the multi-meter used previously.

This conceptual difference requires that the fundamental OSCAT equation [59] used throughout chapter 3 has a repetition rate which may be continuously modulated over real time. The static (or unmodulated) equation for scan range Δt_{unmod} remains as follows:

$$\Delta t_{unmod} = a\left(\frac{1}{f_{rep}} - \frac{1}{f_{rep} + \Delta f}\right) = \frac{l n f_{rep}}{c}\left(\frac{1}{f_{rep}} - \frac{1}{f_{rep} + \Delta f}\right) \tag{28}$$

Where as in previous chapters the pulse index *a* is the difference in the number of pulses which propagate a passive delay line (PDL) of length *l*, *n* is the refractive index of the PDL, *c* is the speed of light in a vacuum, f_{rep} is the repetition rate and Δf is the repetition rate tunability. In contrast, the modulated case is described with an additional sinusoidal

component[12], the full derivation of which may be found in [62] and is simply restated here. This gives rise to the dynamically modulated scan range $\Delta T_m(t)$ as a function of real time *t*, such that

$$\Delta T_m(t) \approx \delta T_0 + \frac{\Delta f \Delta T_0}{f_{rep}} sin\left[2\pi f_m\left(t + \frac{\Delta T_0}{2}\right)\right] \tag{29}$$

Where $\Delta T_0 = l \cdot n/c$ is the equivalent temporal delay of the PDL of length *l* and refractive index *n* and *c* is the speed of light. f_m is the modulation frequency of the sine wave (also therefore equivalent to the scan rate) and as always f_{rep} and Δf are the repetition rate and repetition rate tunability respectively. δT_0 is a small offset delay resulting from the difference between the exact PDL temporal delay ΔT_0 and the number designated as the pulse index; the integer number of pulses which may in reality propagate the delay line. The factor was simply used in [62] in order to give an extra degree of freedom in where their scan range was centralised or offset, and so was not used in this project.

A few key differences in the modulated case must be taken into account. Whilst in both the static and modulated cases an increase in repetition rate tunability will increase the scan range, in the modulated case only the scan range will *not* increase indefinitely with increasing PDL length represented by ΔT_0. According to expression (29) when the imbalance becomes so large that the condition is not met where the product $f_m \Delta T_0 \ll 1$ the scan range will peak when $\Delta T_0 = 1/2f_m$ and disappear when $\Delta T_0 = 1/f_m$, which is to say that scan rates whose period is proportional to the delay brought on by the PDL will lead to a reduction in the scan range. The dependence of the scan range on the modulation frequency and the imbalance of the interferometer is calculated to form a contour plot, see Figure 4-1, which was built for comparison with that presented by Yang *et al*. This simulation is constructed assuming the characteristics of the narrow ridge device; $\Delta f = 10MHz$, $f_{rep} = 5.07GHz$, and all PDL lengths assume an optical fibre of refractive index $n = 1.46$. As can be seen, in practice there is a trade-off between the scan rate and the scan range when the interferometer imbalance is sufficiently large. Given the longest PDL length available in the lab is just 25m, the effect of 'negative scanning' or scan

[12] Note that although a sine function is used to sweep the minimum to maximum repetition rate, saw-tooth or triangular functions were also successfully tested. The signal generator available offered faster scan rates using the sine function, whilst minimising the frequency components supplied to the MLLD.

range reduction is avoidable up to around 1MHz scan rate. We may examine this closer by extracting profile slices of each decade of scan rate from the contour plot, see Figure 4-2.

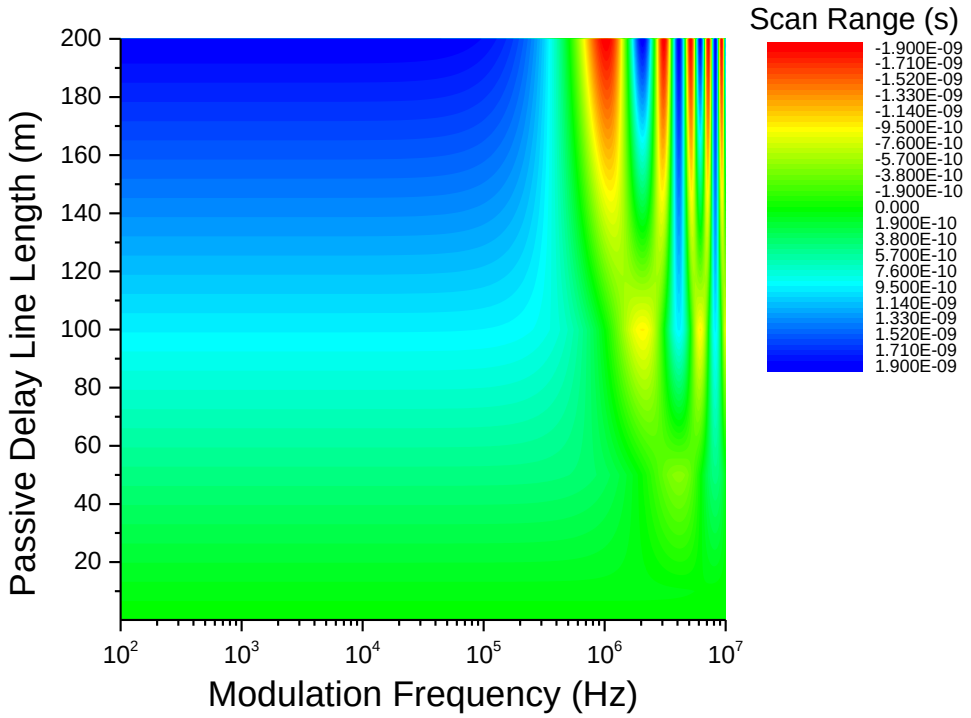

Figure 4-1 - Contour plot showing the consequences on scan range of increasing the modulation frequency for increasing PDL lengths assuming the characteristics of the narrow-ridge device, based on expression (29). A linear plot version is included in the Appendix, section 7.3.1, Figure 7-1.

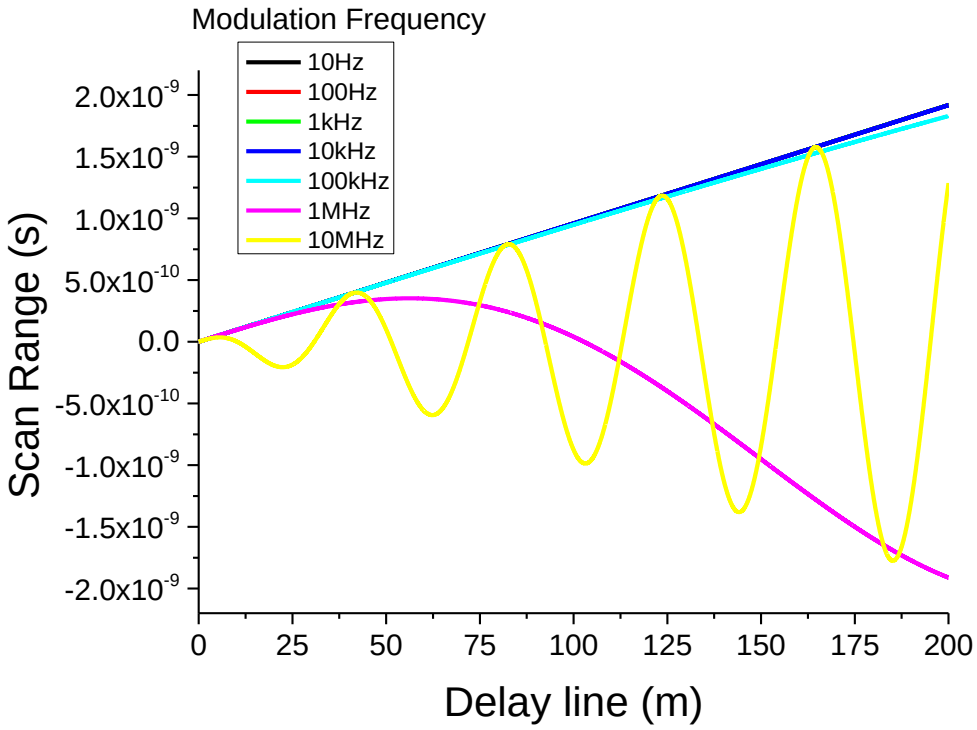

Figure 4-2 – Profile Slices from Figure 4-1 showing 'negative' scanning which occurs for particularly fast modulation frequencies (or scan rates) even at short PDL lengths. Note that this issue does not occur for scan rates of 10Hz to 1kHz, and are hidden behind the 10kHz trace which is also unaffected.

In agreement with both expression (29) and the contour plot, we can clearly see that the scan range will not be affected even up to 200m PDL length for scan rates of up to 10kHz, such that a slight dip in scan range is found at 100kHz scan rate. 1MHz scan rates however begin to degrade after around 30m PDL, and 10MHz scans periodically scan positively and negatively, making this an unsuitable scan rate beyond a few metres of delay line.

Finally, it is important to check that the modulated case of expression (29) is equivalent to the unmodulated case of expression (28). Beginning with expression (28), we may rearrange to find

$$\Delta t_{unmod} = a\left(\frac{\Delta f}{f_{rep}(f_{rep}+\Delta f)}\right) \tag{30}$$

In this sense f_{rep} may be considered the minimum repetition rate and the quantity $(f_{rep}+\Delta f)$ may be considered the maximum. If we then make the special case that Δf is significantly smaller than f_{rep} (in particular that 10*MHz* << 5*GHz*), we find that the expression approximates to

$$\Delta t_{unmod} \approx a\left(\frac{\Delta f}{f_{\mathrm{rep}}^2}\right) \tag{31}$$

Returning to the fast modulation case, we recall (29), where we consider that the maximum scan range $(\Delta T_m)_{max}$ will occur when the sinusoidal component gives rise to a value of +1/2 (where the repetition rate has been tuned by $+\frac{\Delta f}{2}$) giving $\delta T_0 + \frac{1}{2}\frac{\Delta f \Delta T_0}{f_{rep}}$ and that the minimum scan range $(\Delta T_m)_{min}$ will occur when the sinusoidal component has a value of -1/2 (where the repetition rate has been tuned by $-\frac{\Delta f}{2}$), giving $\delta T_0 - \frac{1}{2}\frac{\Delta f \Delta T_0}{f_{rep}}$. Therefore, the scan range may be given by

$$\Delta T_m \approx (\Delta T_m)_{max} - (\Delta T_m)_{min} \approx \frac{\Delta f \Delta T_0}{f_{rep}} \tag{32}$$

We may then consider the equivalency that $\Delta T_0 = a/f_{rep}$ and so we have

$$\Delta T_m \approx a\left(\frac{\Delta f}{f_{rep}^2}\right) \approx \Delta t_{unmod} \tag{33}$$

Finally, moving away from the OSCAT definitions, we can extend this case to the OSBERT regime where the controllability factor $\Delta f / f_{rep}$ or β-ratio is replaced into the expression

$$\Delta T_m \approx a\left(\frac{\beta}{f_{RO}}\right) \approx \Delta t_{unmod} \tag{34}$$

Therefore as demonstrated, both the modulated and unmodulated cases of OSBERT (or OSCAT) have the same theoretical background.

As this regime will be applied in an OSBERT fashion (to the narrow-ridge 2-section quantum dot mode-locked laser diode described in chapter 3), we recall that the repetition rate tunability will once again be driven by an electrical modulation of the saturable absorber section, and as such the concept of the modulated case of OSBERT is illustrated in Figure 4-3.

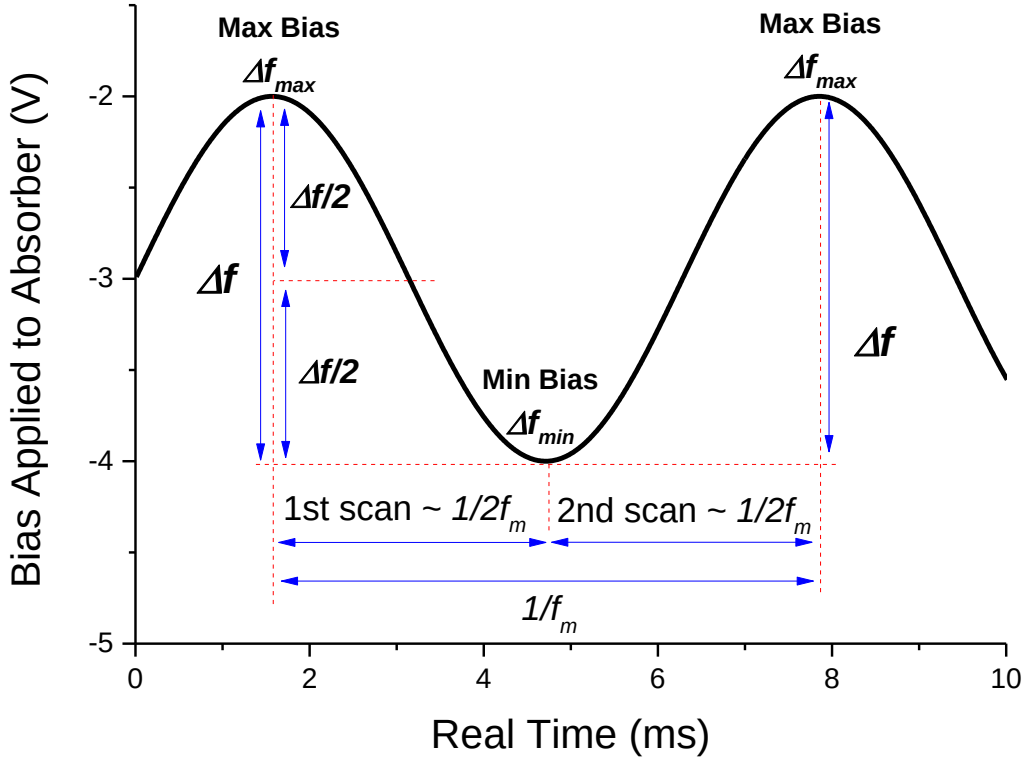

Figure 4-3 – A representation of how the sinusoidal modulation of the reverse bias applied to the saturable absorber of an MLLD relates to a real time scan.

Noteworthy is the fact that scanning will occur between alternating sets of minimum and maximum reverse biases, which accounts for the half period of the modulation frequency. Therefore essentially two scans will occur in one period of modulation, and it could be said that, for example, a 100Hz scan is actually occurring at 200Hz. However, for clarity, a 100Hz modulation frequency shall always be discussed as an equivalent 100Hz scan rate for the purposes of this project; i.e. the scan rate is the modulation frequency.

4.3. F-OSBERT Experimental Setup & Considerations

The experimental setup of FOSBERT is similar to that of SOSBERT, except for the key features described, whereby the power supply used for biasing the saturable absorber is replaced with a signal generator (*Keysight Technologies 33612A Waveform Generator, 80MHz*). Secondly, the static multi-meter (which reads the output of the detector) is replaced with an oscilloscope (*Teledyne Lecroy HDO4104, 1GHz bandwidth*), see Figure 4-4. The InGaAs detector (*Thorlabs 5GHz DET08CL/M*) remains the same as in the SOSBERT cases associated with the narrow-ridge device in chapter 3, along with all other components.

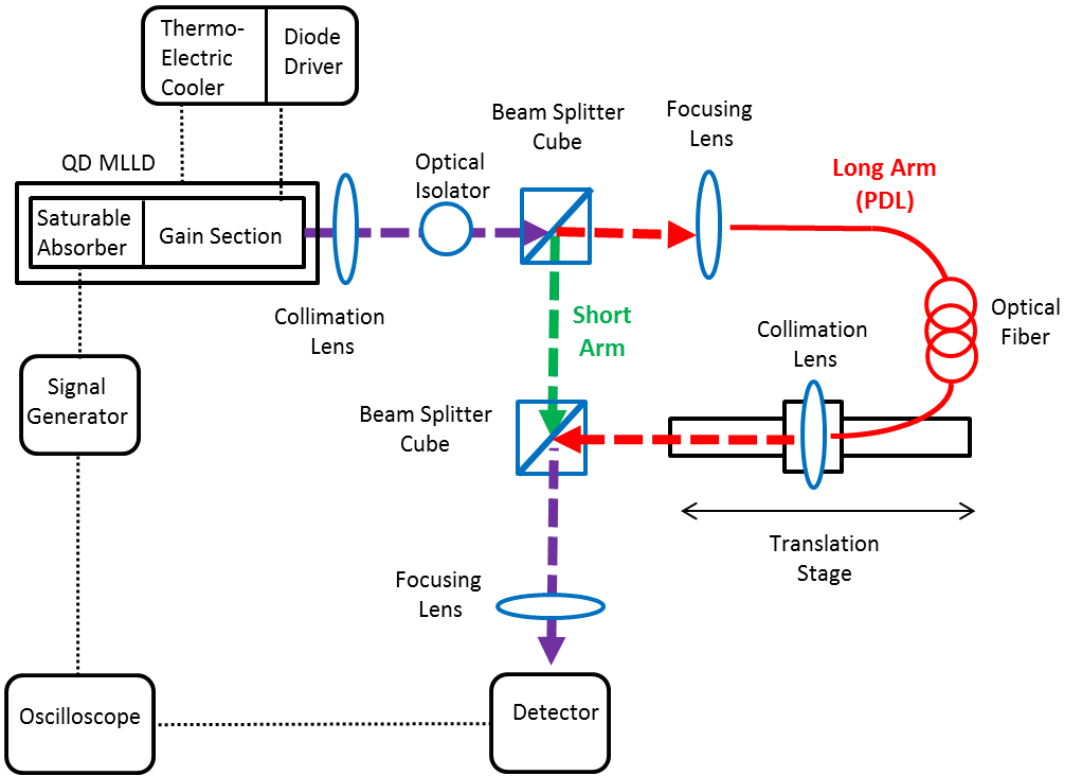

Figure 4-4 – New experimental setup required to drive the OSBERT technique at several scans per second; with respect so SOSBERT, in FOSBERT the power supply has been replaced with a signal generator and the multimeter has been replaced with an oscilloscope.

Another consideration we must make when biasing the absorber section via the signal generator as opposed to the DC power supply is the fact that the signal generator displays the voltage assuming it is being terminated into a 50Ω Load. In this sense, the resistance of the narrow-ridge device itself plays a role in the biasing conditions. Consider the following formula

$$V_{exp} = V_{set}\left(\frac{R_{load}}{R_{sig.\ gen.} + R_{load}}\right) \tag{35}$$

Where the voltage experienced V_{exp} by the device varies from the voltage set at the signal generator V_{set} depending on the difference between the load of the device R_{Load} and the 50Ω output of the signal generator. In order to determine the difference, we calculate the resistance of the narrow-ridge device across the MLR by reading the photocurrent generated and using Ohm's Law to determine the resistance at each discrete reverse bias value, see Figure 4-5. For these measurements, the forward current supplied to the gain section of the MLLD was held constant throughout at 210mA, whilst the entire device temperature was held constant at 20°C.

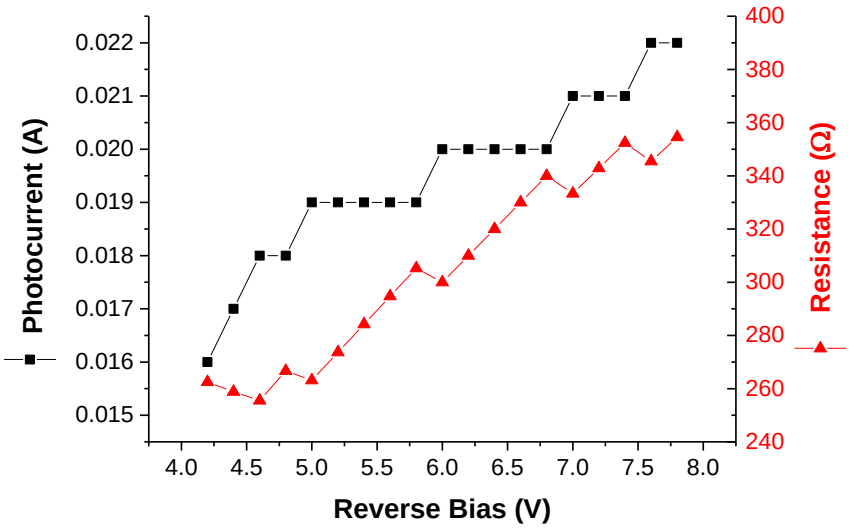

Figure 4-5 – The photocurrent generated by the saturable absorber section of the narrow-ridge device is measured for each value of reverse bias applied. Ohm's Law then gives the resistance of the saturable absorber across the MLR.

Note that the coarse step-wise increase of the readable photocurrent is an artefact of the minimum detectable current on the power supply, which was 1mA. In the case of the extremely low resistance power supply used for SOSBERT in Chapter 3, the change in voltage supplied versus voltage experienced was insignificant according to expression (35).

However, in the case of using the signal generator as the voltage supply to the absorber section, the 50Ω impedance channel was used, meaning that the MLR of 4.60V to 7.80V would not be applied using these settings. A calibration curve was thus created in order to determine the correct voltage to set on the signal generator to ensure the experienced voltage would be that of the MLR, see Figure 4-6. This was done by plotting the set voltage against the experienced voltage which was a function of the resistance under that particular reverse bias.

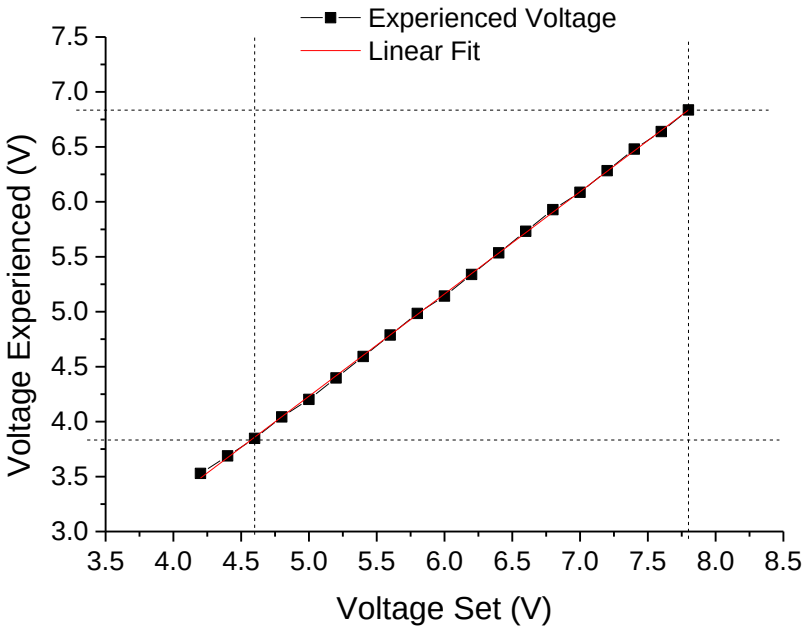

Figure 4-6 – Calibration curve with a linear mathematical fit which determines which voltage will be experienced by the absorber section depending on the voltage set at the signal generator.

As can be seen, a linear fit to the calibration curve results in the relationship

$$V_{exp} = 0.93057 * V_{set} - 0.42187\ [V] \tag{36}$$

Where the result is in volts. And so, setting the full MLR of 4.60V to 7.80V in the case of FOSBERT would result in an experienced voltage of between3.86V and 6.84V, which means the system would be attempting to scan without an established repetition rate, using a non-MLR bias, and would not reach its full potential of 7.80V at the upper limit. Using the same expression we determine that in order to experience the full MLR bias range, we must instead set the signal generator to sweep from anywhere within the range of 5.397V and 8.835V.

In terms of a sinusoidal function driving the reverse bias applied to the absorber section, signal generators typically operate under the principal of selecting a central offset voltage V_{off} and a voltage amplitude from peak to peak of the sinusoid V_{pp}, see Figure 4-7.

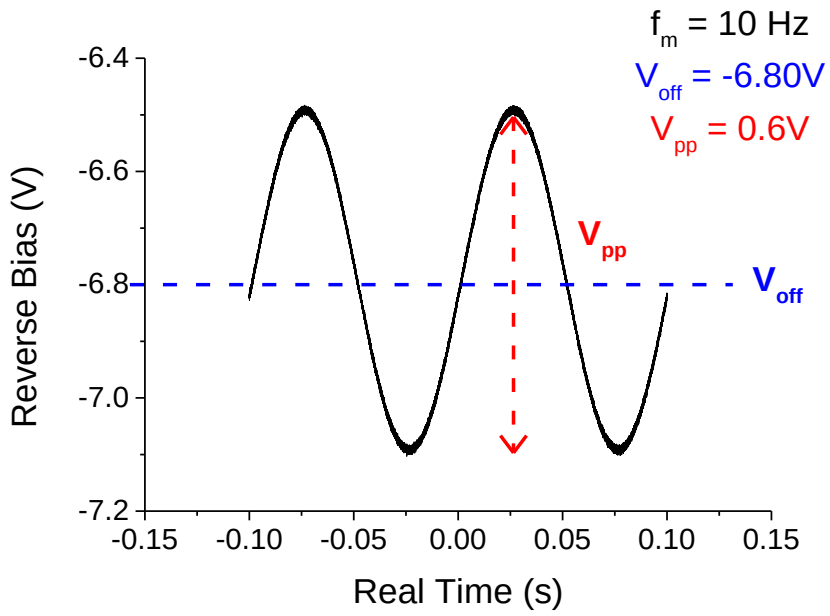

Figure 4-7 – Example of a 10 Hz sinusoidal function driven by the signal generator and applied to the absorber section of the device. V_{off} represents the central voltage required within the MLR and V_{pp} represents the amplitude (or range) of voltage needed for repetition rate tuning.

Throughout the investigation, several combinations of modulation frequencies (scan rates), and voltage offsets and amplitudes within the MLR were used. In particular, in order to demonstrate the full potential of the repetition rate tunability within the MLR, this translates from the SOSBERT range of 4.60V to 7.80V, to the FOSBERT driving parameters $V_{off} = -7.10V$ and $V_{pp} = 3.40V$ using expression (36).

It should be noted as in previous cases that the full tuning range is not a requirement of running the FOSBERT system; any subset of offsets and amplitudes may be applied, provided electronically they fall within the MLR. As such, using smaller sub-sets of the tunability means fewer corresponding changes to the output characteristics such as power, wavelength or pulse duration; critically, smaller values of reverse bias ranges will scan using increased average powers, whereas greater values of reverse bias ranges will scan using shorter pulse durations. Depending on the application, the range and consequent changes to output characteristics may be minimised as necessary, at the cost of reducing the scan range. As discussed, however, the scan range may be increased

without interfering with the output characteristics of the device by simply increasing the PDL. As such, the scan range is highly customisable depending on the overall tunability of the device, or the PDLs which are available or practically implementable.

4.4. First repetitive FOSBERT scans using three PDL lengths

In order to demonstrate the principle of FOSBERT, the following experimental conditions are implemented to measure the distance travelled by a target, as with that of SOSBERT in Chapter 3.

4.4.1. Investigating 10Hz Scans

Firstly, the input signal from the signal generator is set as such to provide the full reverse bias tuning range to the absorber section of the device, V_{off} = -7.10 V and V_{pp} = 3.40 V, corresponding to approximately 9.6MHz repetition rate tunability.

For a first proof of concept, the frequency of the sinusoidal signal was then set to 10Hz in order to demonstrate continuous scanning. As with the SOSBERT method, the mechanical stage was then moved into a position which would result in a cross-correlation at the detector. When the signal generator is activated, the trace is acquired at the Oscilloscope and saved for each stage position. The procedure is repeated in all aspects across three fibre PDL lengths (1m, 2m and 5m), see Figure 4-8, where only the full distance moved by the stage is increased respectively in order to demonstrate the increased temporal scanning range brought on by increasing the PDL length, whilst the repetition rate tunability remains constant.

Of interest is the expected sinusoidal output response in FOSBERT traces which is synchronised with the sinusoid input from the signal generator. In this case only one period has been acquired in order to showcase the detail within the scans, however as with any repetitive system, any number of periods may be acquired at the expense of resolution.

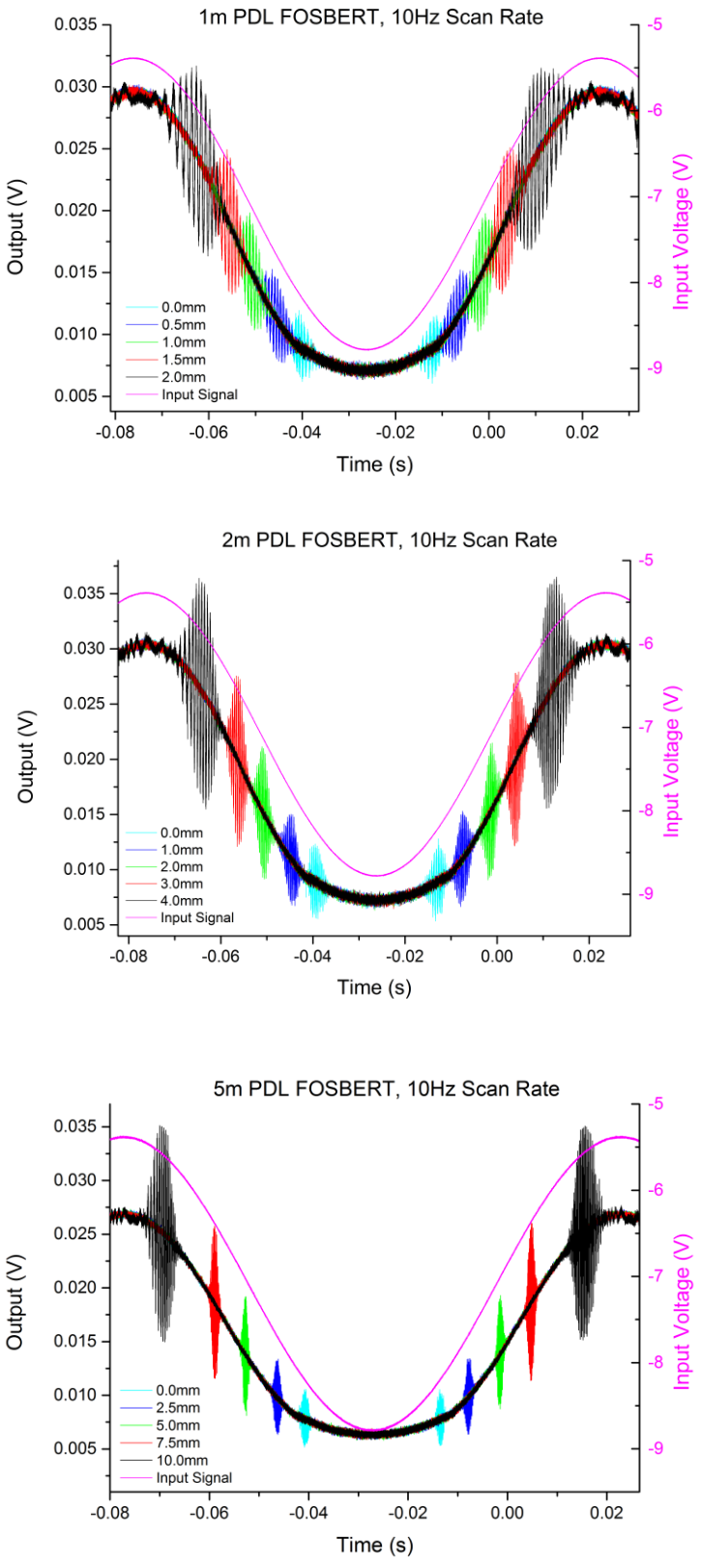

Figure 4-8 – 10 Hz FOSBERT scans are acquired for three fibre PDL lengths, in each case using the exact same input sinusoidal voltage range supplied by the signal generator[13].

[13] Note, throughout the project, differences in the amplitudes of OSBERT scans between PDL lengths result only from any variation in the efficiency of the optical fibre coupling, which was not normalised. Each fibre length was otherwise identical in composition.

Unlike the SOSBERT method which scans once from a minimum to a maximum reverse bias value, as previously discussed, these repetitive FOSBERT scans actually acquire two scans per period; that is to say a 'downward' scan as the response falls from peak to trough, and a repeated 'upward' scan from the same trough to the following peak and so forth.

As can be seen, the input signal which drives the full range reverse bias to the absorber remains the same in each experiment, as does the driving frequency. Despite this, the increase in PDL length is enough to allow the stage to move a greater distance and acquire greater scan ranges. For fibre lengths of 1m, 2m and 5m, scan ranges of at least 2mm, 4mm and 10mm were achieved respectively, also proving that the scan range increases linearly with increasing PDL lengths as expected from the outlined theory.

4.4.2. Deconvolution Process

The deconvolution process to convert the raw FOSBERT scans from real time to delay time is similar to that discussed in Chapter 3 regarding SOSBERT scans, the main difference being that SOSBERT scans were instead were converted directly from reverse bias applied to delay time.

Firstly, the scan from one half of a modulation period is selected, which is to say one full FOSBERT scan either between a trough and a peak or between a peak and a trough is selected. This raw data is essentially cut from anywhere within the trace for processing, however most commonly those traces associated with the 0-second time-base value of the oscilloscope are taken throughout the project; that is to say, the oscilloscope was triggered such that the mid-point between crest and trough of the sine waves of the input signal and the resultant OSBERT signals were centred on 0 seconds on the time-base of the oscilloscope.

Referring now to expression (29) from the previous section, we may replace the constant variables as discussed; the fundamental repetition rate, $f_{rep} = 5.07GHz$, the repetition rate tunability according to the reverse bias conversion is $\Delta f = 9.6MHz$, and the modulation frequency is $f_m = 10Hz$. The 1m, 2m and 5m optical fibre PDL lengths were acquired with additional minor free-space imbalances of 22cm, 11cm and 5cm

respectively, giving rise to total passive delay periods of $\Delta T_0 \approx 5.6\text{ns}$, 10.1ns and 24.5ns respectively. Additionally, due to two scans occurring per period of modulation, we halve the resultant temporal scan range (that is simply to say, one FOSBERT scan range is acquired per half modulation period). The real-time values may now easily be converted to delay time values, and subsequently converted to spatial values in millimetres in order to more readily compare the motion of the target, see Figure 4-9.

The scans are now converted from real-time to spatial scanning ranges based upon the length of PDL used for each experiment. Although the sinusoidal carrier response has now clearly been removed from the traces, the inherent average output power drop is still evident in the new baseline, consistent with the SOSBERT traces in Chapter 3, and the measured average power in Chapter 2.

It is interesting to note that the FOSBERT traces at this stage are comparable to those Temporal Pulse Positioning (TPP) scans acquired Chapter 3, section 3.3.3, particularly with reference to Figure 3-17. Whereas the FOSBERT scans shown in Figure 4-9 are gathered by holding the stage position constant and varying the reverse bias, the TPP scans from Chapter 3 were acquired with a reverse bias held constant whilst the mechanical stage was allowed to move.

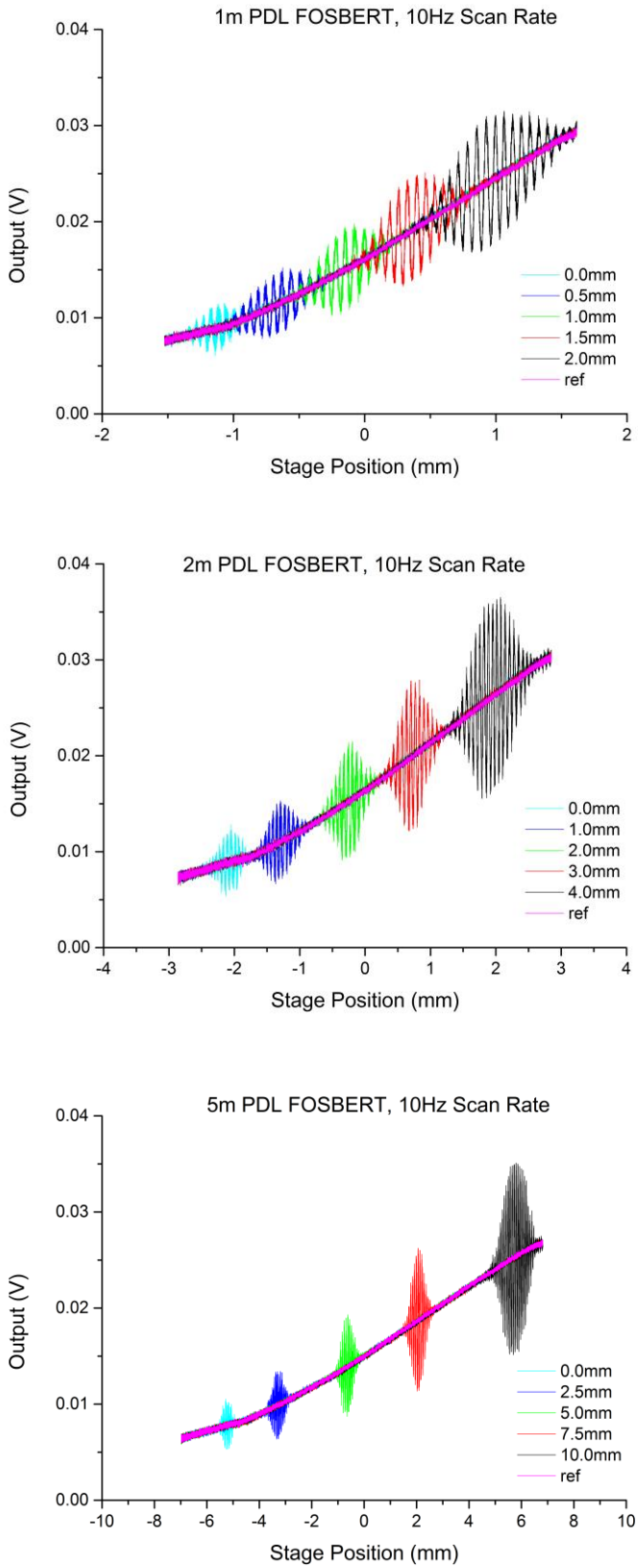

Figure 4-9 – The raw real-time data has been converted firstly to a temporal scanning range and then subsequently to spatial positions in millimetres. A reference (ref) scan is superimposed from a trace where no cross-correlation was present.

As with the SOSBERT scans, the final step in the deconvolution is to subtract from each trace a 'baseline reference' scan (one which did not include a cross-correlation within the trace), see Figure 4-10.

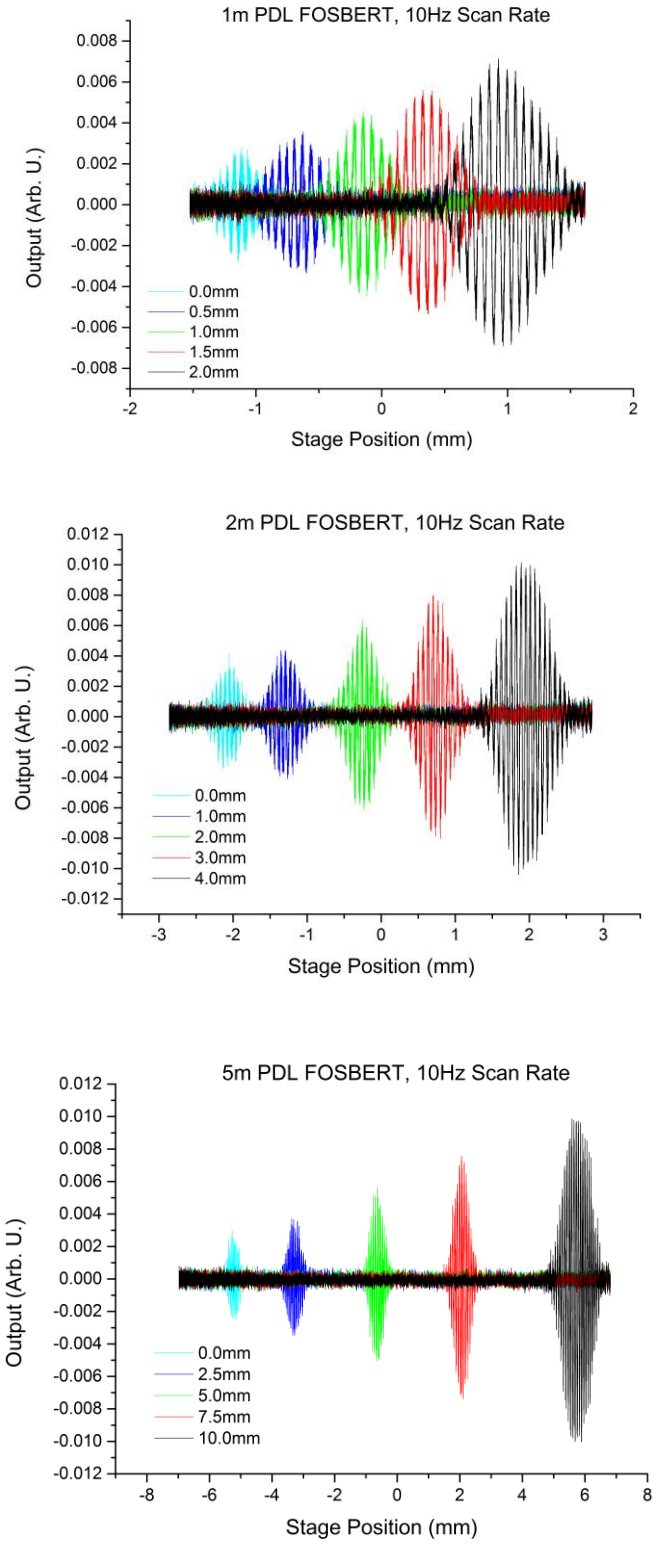

Figure 4-10 – The Baseline reference scan is now subtracted from the traces in order to remove their skewedness, resulting in a linear baseline and corresponding traces.

As can be seen, the baseline between individually positioned scans is now linear and normalised at the cost of losing the exact output values from the detector, which are now arbitrary units (Arb. U.). However, each trace now clearly resembles the analogous standard mechanical cross-correlation traces acquired under individual reverse biases discussed in Chapter 3. As with the SOSBERT deconvolution process, a Gaussian may be fit to the upper envelope of each FOSBERT trace in order to consistently mathematically determine the central peak position. In particular, for the 1m, 2m and 5m PDL lengths a total target displacement of 2.0mm, 4.0mm and 10.0mm was known, compared with the measured displacement of 2.1mm, 4.2mm and 11.0mm[14].

With the procedure outlined, these same deconvolution steps may now be applied to future scans, provided the correct input voltage ranges are converted to the appropriate repetition rate tunability. Importantly, for the first time, the concept of continuous scanning has been demonstrated.

4.5. Maximising the Scan Range

As well as the ability to maximise the scan rate, we shall also consider the options for maximising the scan range. Up until now we have only discussed three passive delay line lengths (1m, 2m and 5m), which combined with the narrow-ridge device's repetition rate tunability of 10MHz have given rise to maximum scanning ranges of 9.6ps, 19.2ps and 47.9ps respectively. We now consider the scan range typically available via the ASOPS technique, which by design is automatically the full roundtrip period of the laser's repetition rate (e.g. two ~100MHz repetition-rate lasers using the ASOPS system may walk through a maximum scan range of 10 nanoseconds before the scan repeats again).

We investigate the length of passive delay line which must be implemented in order to maximise the scan range to incorporate the full roundtrip period given the characteristics of the narrow-ridge device. Since the fundamental repetition rate is 5.07GHz, the roundtrip period may be calculated as its inverse, which is just under 200 picoseconds (or

[14] The discrepancy in these results came to light towards the end of the project when a high speed RF analyser was borrowed, and is discussed further in Section 4.6.2, rather than during this proof of principle whose purpose was to demonstrate repetitive scanning (compared to SOSBERT) and show an analogous experiment to Temporal Pulse Positioning.

0.2 nanoseconds). In order to scan this range, we substitute it into expression (14) to find a PDL length requirement of 20.6 metres (assuming a refractive index of 1.46 and a repetition rate tunability of 10MHz). Considering this will scan the roundtrip period and no more, we opt for a 25 metre optical fibre of the exact same design as the others used as a PDL, in order to ensure two full cross-correlations may be present in one scan. As such the expected scan range is now calculated as 239.5 picoseconds, or 71.9 millimetres, slightly exceeding the maximum useful scan range purely for the purposes of this demonstration.

In order to see the full roundtrip period (and thus, two cross correlations) within just one scan, we must consider the position of the target. We centre the stage approximately half way between two expected cross-correlation positions, and displace it to three different positions such that the measurement may be made multiple times for proof of concept, see Figure 4-11.

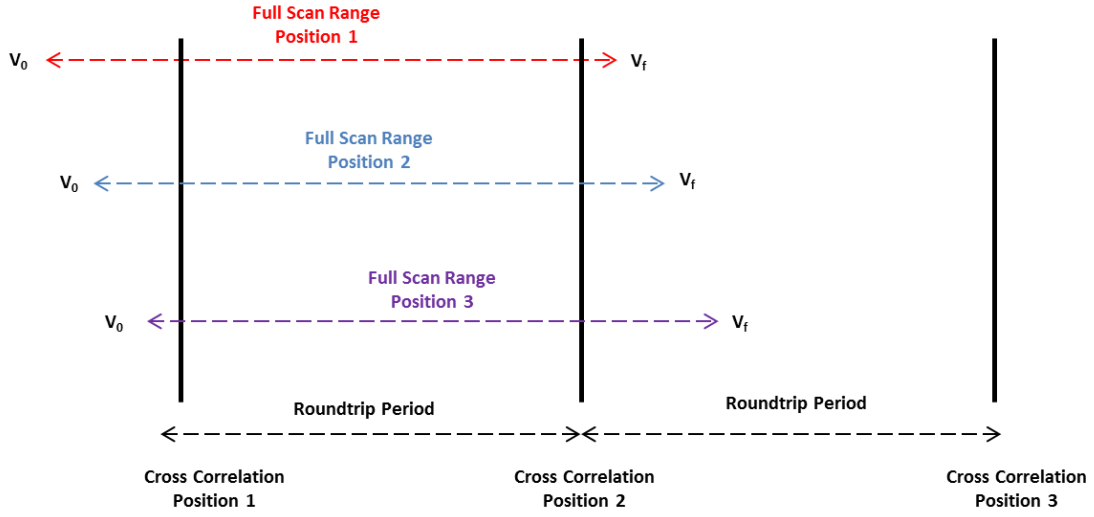

Figure 4-11 – The approach taken which will ensure two cross-correlations will be present in one FOSBERT scan given a 25m long PDL. Repeating the scan as the stage moves through three positions allows for several measurements. V_0 and V_f denote the minimum and maximum reverse bias values for the selected 10MHz repetition rate tunability.

Implementing this technique using the maximum scan range settings gives the first FOSBERT scans which clearly demonstrate the entire roundtrip period, where two cross-correlation traces are present in one scan, see Figure 4-12.

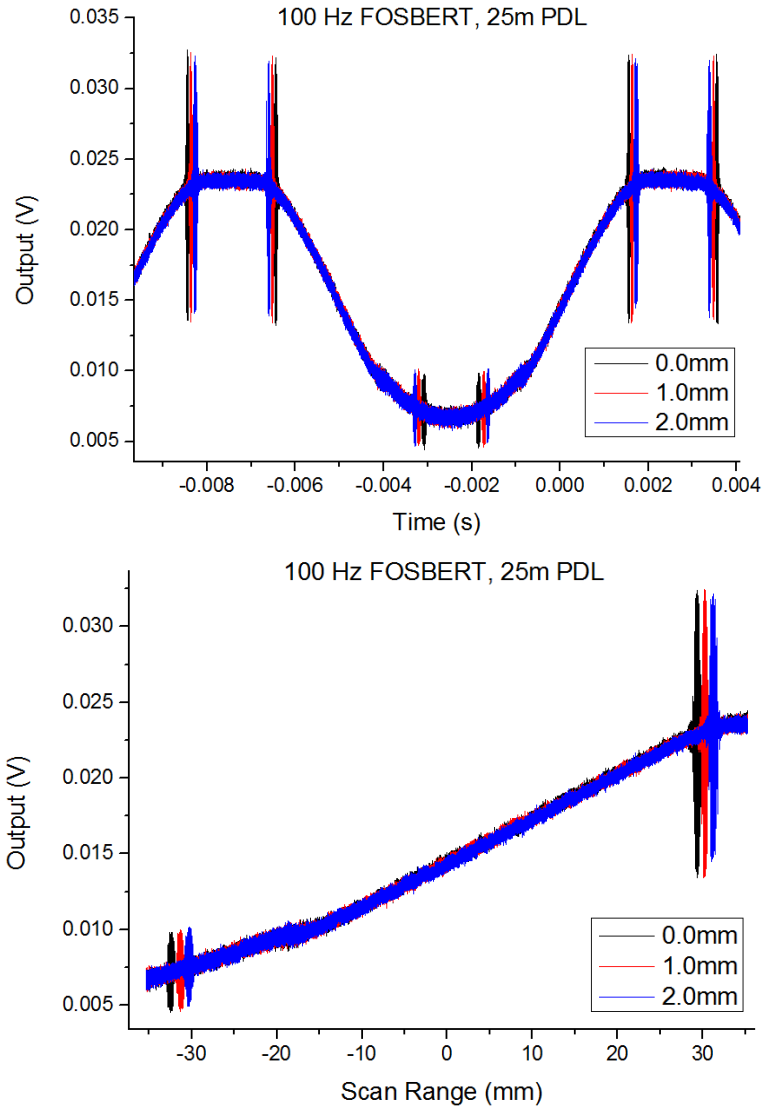

Figure 4-12 – Left, the real time trace at 100 Hz showing three stage positions, each providing two cross-correlations. Left, the trace converted to a scan range according to expression (29), giving a ~60mm spatial difference between pulse positions, equating to the expected ~ 5GHz repetition rate.

Applying the described deconvolution process measures the ~200ps or ~60mm roundtrip period between the two cross-correlation positions, giving a measured ~5GHz Repetition rate. As expected, the cross correlations exhibit a large difference in amplitude due to the range in reverse bias applied across the scanning range.

4.6. Increasing the Scan Rate

The first examples of repetitive scans were kept at relatively low scan rates of 10Hz (and 100Hz, above) in order to gather a reference as to how these scans will alter as the modulation frequency is increased. This section discusses the bandwidth of the experimental components and their impact on the quality of the FOSBERT scans as the scan rate is increased.

4.6.1. Experimental Results

Given that we are currently only interested in the effects of increasing the scan rate of the FOSBERT system, we do so using a simplified subset of experimental parameters. These include demonstrating the effects using only the 5m PDL, and using V_{off} = -6.80V and V_{pp} = 1.20V, equivalent to ~3.4 MHz repetition rate tunability as opposed to the full 10 MHz which is available. The stage position is also held stationary, and as such only single FOSBERT cross-correlation scans are acquired for each decade increment in frequency modulation. As in the previous sections, the forward current supplied to the gain section of the MLLD was held constant throughout at 210 mA, whilst the entire device temperature was held constant at 20°C. This is to say each trace is identical in all parameters other than the scan rate.

We firstly acquire a 10Hz scan where two periods of scanning are acquired on the time-base of the oscilloscope in the first instance, as well as a zoomed-in trace in order to see the detail of the cross-correlation, see Figure 4-13.

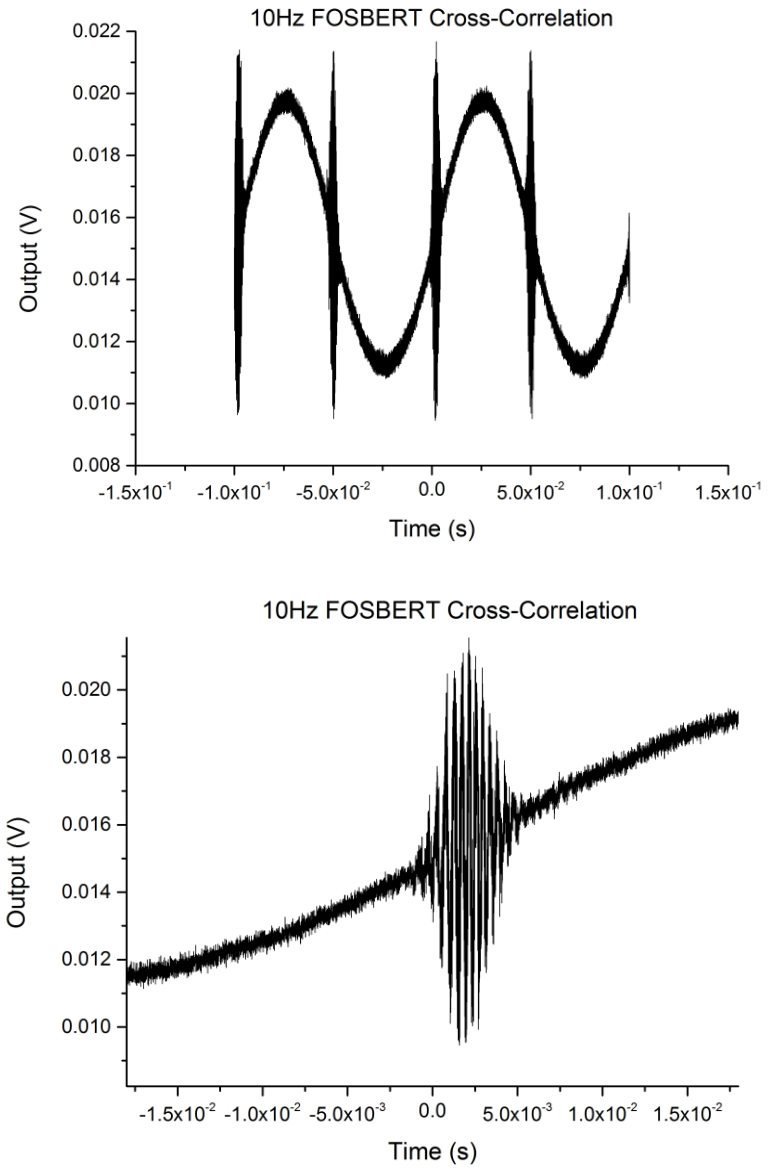

Figure 4-13 – 10Hz FOSBERT scans are shown within a two-period time-base, above, and an accompanying zoomed trace, below.

The process was repeated under the exact same parameters, with the modulation frequency now increased to 100Hz, see Figure 4-14.

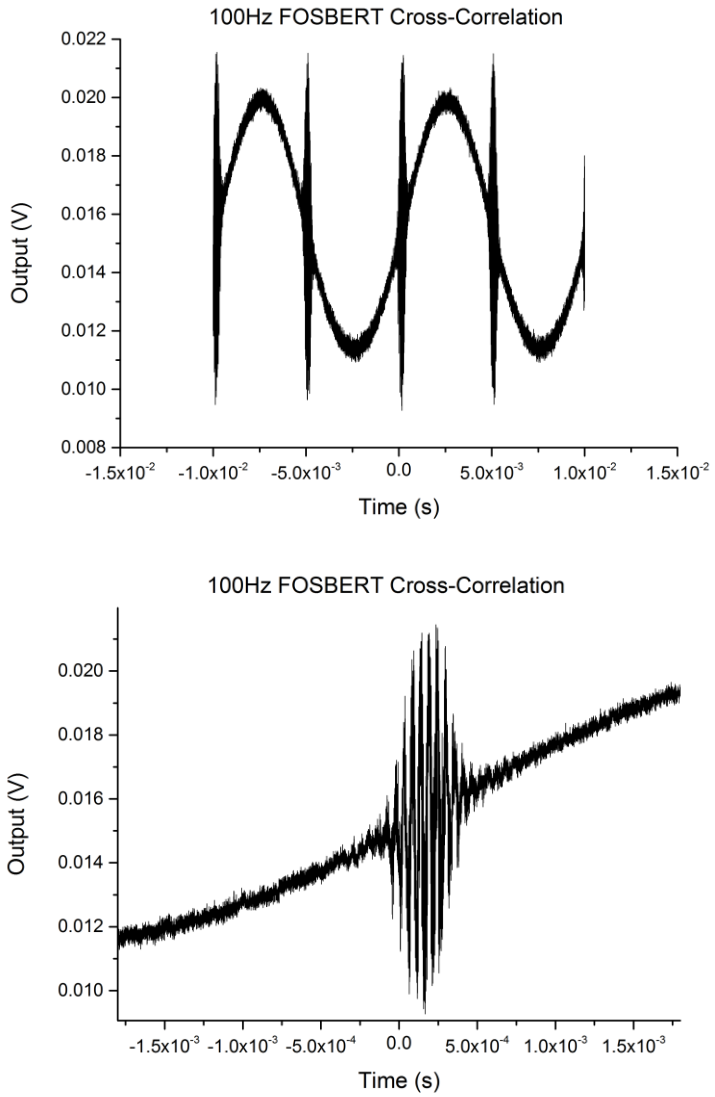

Figure 4-14 –100Hz FOSBERT scans are shown within a two-period time-base, above, and an accompanying zoomed trace, below.

As can be seen, there is little to distinguish the traces which are separated by an order of magnitude in scan rate; the cross-correlation traces (which have not been deconvolved) qualitatively appear similar.

The scan rate is then increased to show scans acquired at 1kHz and 10kHz in order to demonstrate kilohertz scan rates for the first time, see Figure 4-15 and Figure 4-16. What is notable between these scans and the sub-kilohertz counterparts is a reduction in the number of fringes detected in each cross-correlation.

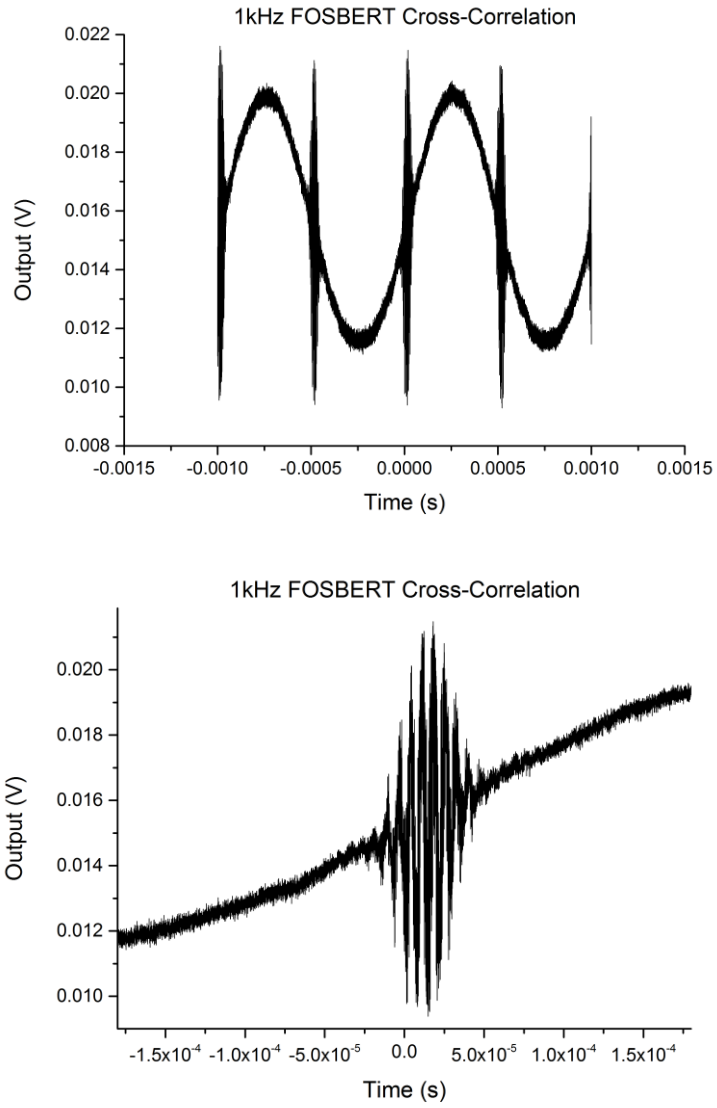

Figure 4-15 - 1kHz FOSBERT scans are shown within a two-period time-base, above, and an accompanying zoomed trace, below.

The overall amplitude, position and shape remain constant from 10Hz up to 10kHz, however the faster scan rates mean that the sharp temporal features of each fringe (that is, the rise time associated with an individual fringe) may be less clearly detectable.

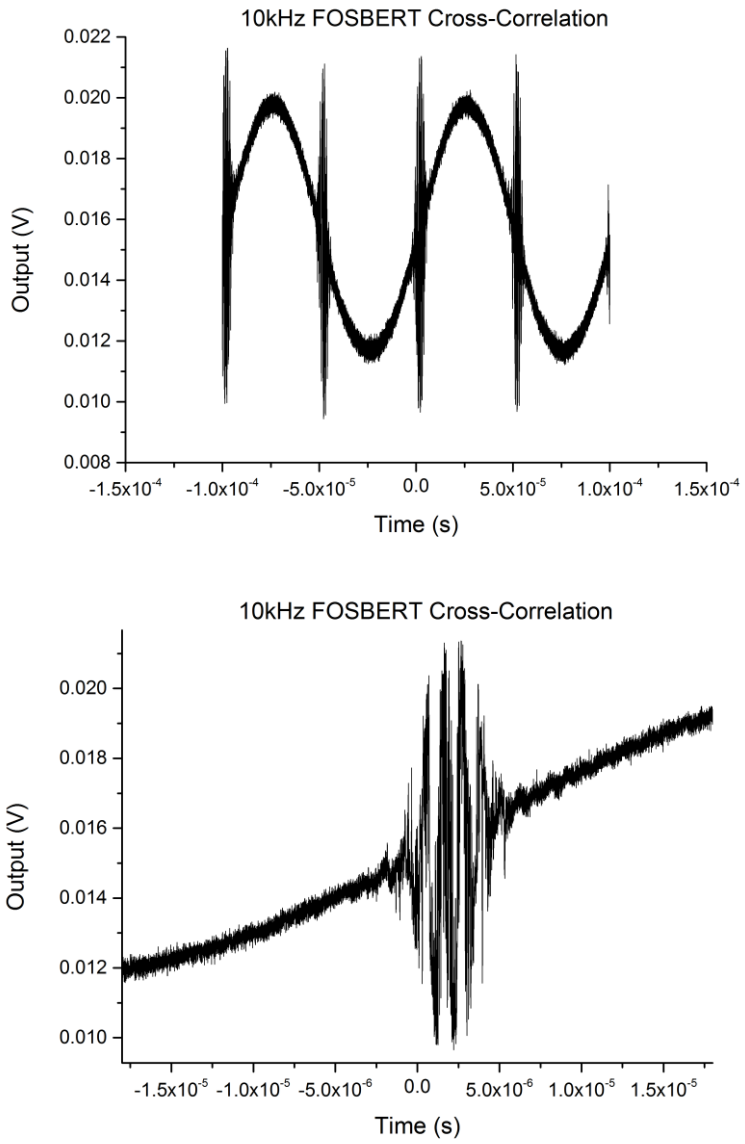

Figure 4-16 - 10kHz FOSBERT scans are shown within a two-period time-base, above, and an accompanying zoomed trace, below.

Interestingly this effect becomes significantly more pronounced as the modulation frequency is increased from 10kHz to 100kHz. In fact, what was found was with each 10-kHz increase the number of detected fringes within the cross-correlation rapidly decreased, leading to only one or two fringes at 100kHz, see Figure 4-17.

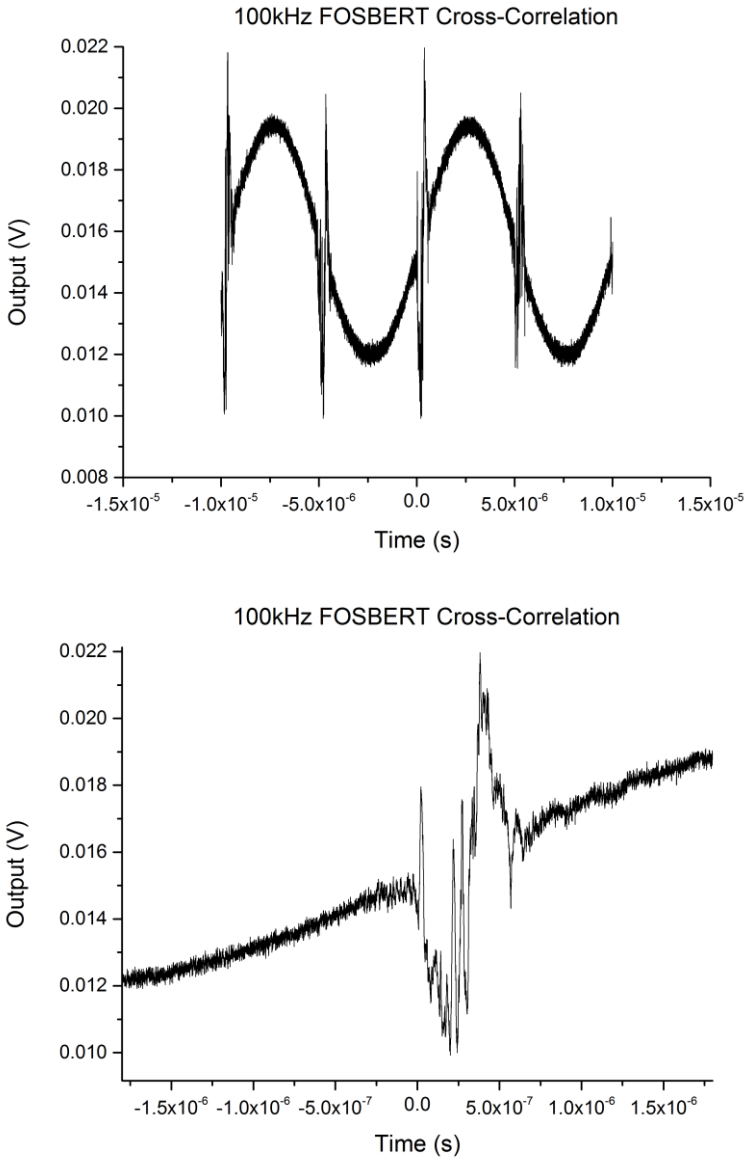

Figure 4-17 – A 100kHz FOSBERT scan is shown within a two-period time-base, above, and an accompanying zoomed trace, below. In comparison with lower modulation frequencies, the number of fringes within the cross-correlation has significantly reduced.

This significant reduction in the number of fringes within the cross-correlation may have been explained, as above, due to the bandwidth limitations of the acquisition. However, when the modulation frequency is increased further, eventually we find the number of detected fringes begins to gradually increase at around 1MHz, see Figure 4-18.

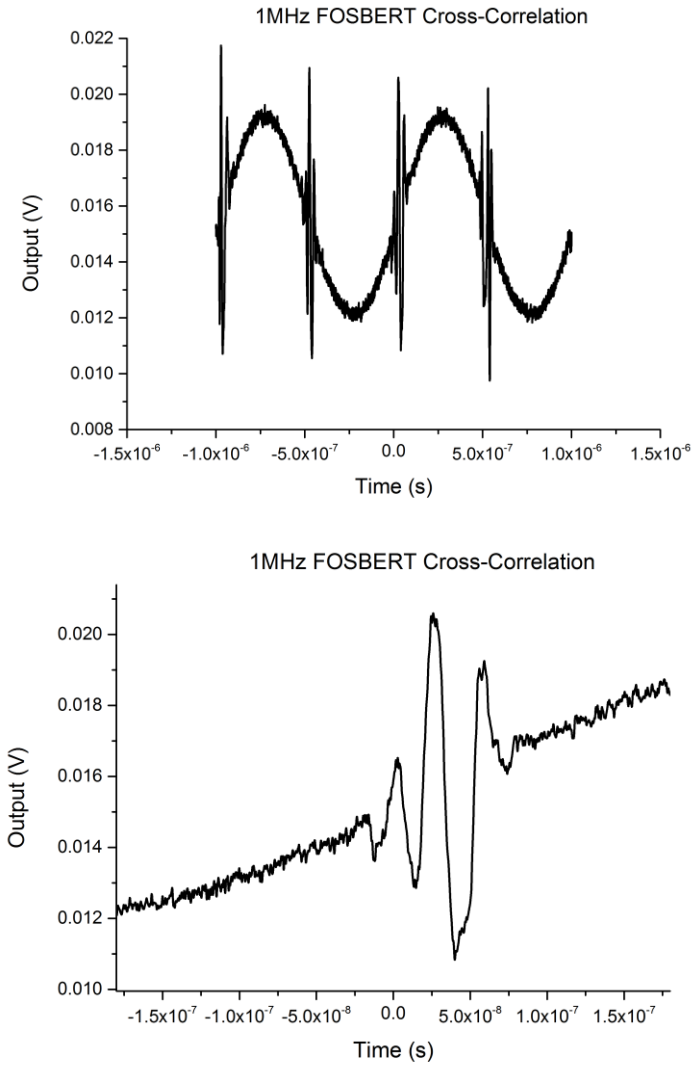

Figure 4-18 - 1MHz FOSBERT scans are shown within a two-period time-base, above, and an accompanying zoomed trace, below.

This trend of slightly increasing fringes appears to continue until around 3MHz scan rate, see Figure 4-19. Beyond around 3MHz and approaching 10MHz scan rate, we find the trace begins to completely destabilise, where the cross-correlation fringes blend into the surrounding baseline, gradually losing all obvious features. This may be an artefact of the 'negative scanning' associated with particularly fast scan rates (Figure 4-2) where it was noted that at 10MHz scan rates, even a few metres of PDL would have degraded scans.

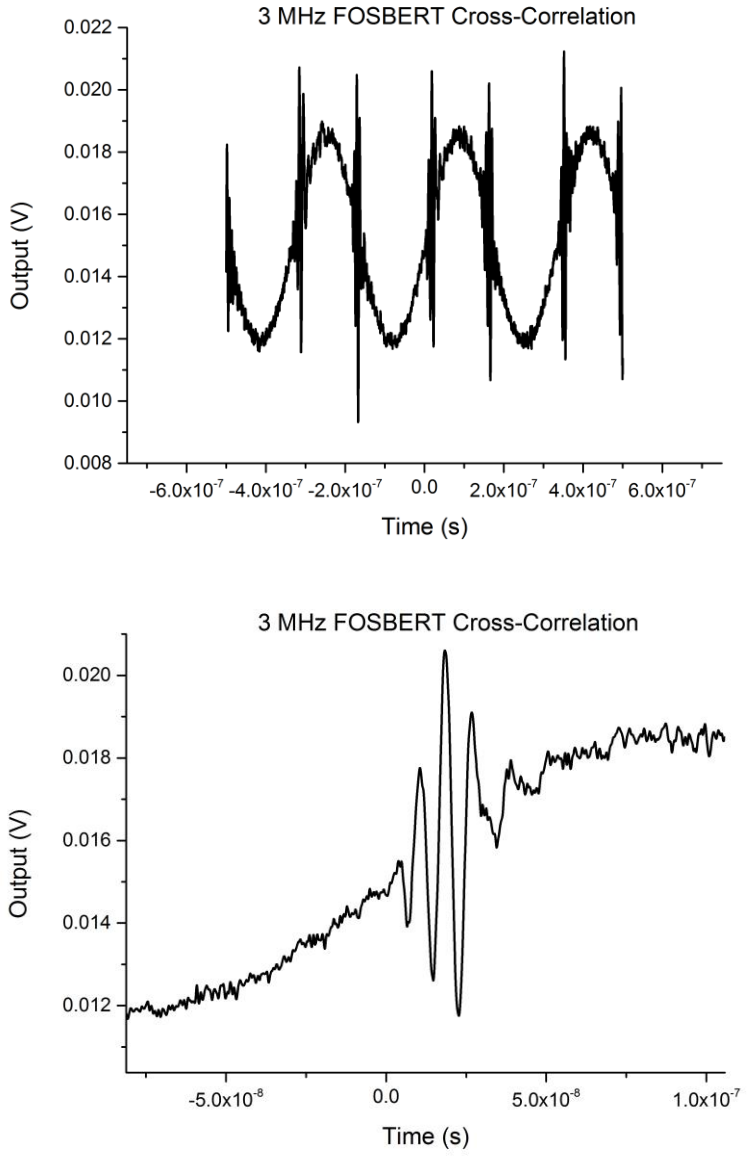

Figure 4-19 - 3MHz FOSBERT scans are shown within a-period time-base, above, and an accompanying zoomed trace, below. The number of fringes appears to increase compared to that of the 100kHz scan rate.

Across all traces at all scan rates from 10Hz to 3MHz, what is clear is the overall shape of the traces remains the same and in the same real-time position, given the mechanical stage remains stationary. What changes is simply the quality of the trace in terms of the number of distinguishable fringes of each, though it should be noted that longer PDL lengths gave rise to inconsistencies within each trace whose fringes were noisier and tended to oscillate – this is attributed to a combination of dispersion, and in particular to pulse-to-pulse jitter, discussed further in section 4.8.

Whilst bandwidth limitations have likely played a role, it seems unlikely that these traces should lose their features at 100kHz in a 1GHz system. We consider then that individual SOSBERT scans were acquired over a period of several minutes each. Given the repetition rate of the narrow-ridge device is over 5GHz, this means more than 5 billion pulses are present during each second of acquisition, maximising the probability of a cross-correlation data point due to pulse overlap. Extending this concept, only 500 million pulses are present during the 10Hz scan, and a mere 5000 are present during the entirety of the 1MHz scan. That is to say, the number of pulses present per second (the repetition rate) will dictate the ultimate potential for data point acquisition. Due to the 'erosion' of fringes, it was found that fitting a Gaussian to the envelope of traces beyond scan rates of 10kHz proved too inaccurate for this method, and were excluded from analysis henceforth. Clearly though, there is promising potential for MHz level scanning, owed to the repeatable presence of cross-correlations themselves.

To an extent we can show the erosion of fringes for increasing scan rates due to this under-sampling induced by the presence of fewer pulses during faster scan rates. We simulate the electric field *E* of both a stationary and a translatable pulse over time *t* as;

$$E(t) = \frac{1}{2}\sqrt{I(t)}e^{i\omega_0 t - \phi(t)} \tag{37}$$

Where $\phi(t)$ is the phase which contributes to chirp, and is set to zero for the purposes of this simulation, and $\omega_0 = 2\pi f$ is the carrier frequency, such that the wavelength of the pulse $\lambda = c/f$ where c is the speed of light in a vacuum. $I(t)$ represents the time-dependent intensity, which we adopt as a Gaussian such that

$$I(t) = y_0 + \frac{A}{w\sqrt{\pi/2}}e^{-2\frac{(t-t_c)^2}{w^2}} \tag{38}$$

Where y_0 and t_c represent x-axis and y-axis offsets which are both set to zero throughout the simulation, and *A* represents an amplitude scale which is set to one throughout. Finally, *w* represents the width of the function, which is related to the pulse-width such that it's $FWHM = w\sqrt{\ln 4}$. We construct the original pulse copies with 200as resolution,

based upon a wavelength of 1260nm, and an autocorrelation was simulated[15] in the same fashion as that discussed previously in Chapter 2, Section 2.3, Figure 2-16, however for a first order interferometric autocorrelation, across a 20ps scan range[16]. The autocorrelations were then constructed assuming 50000, 5000, 500 and 50 pulses were present during the scan, corresponding to scan rates of 100kHz, 1MHz, 10MHz and 100MHz respectively, see Figure 4-20.

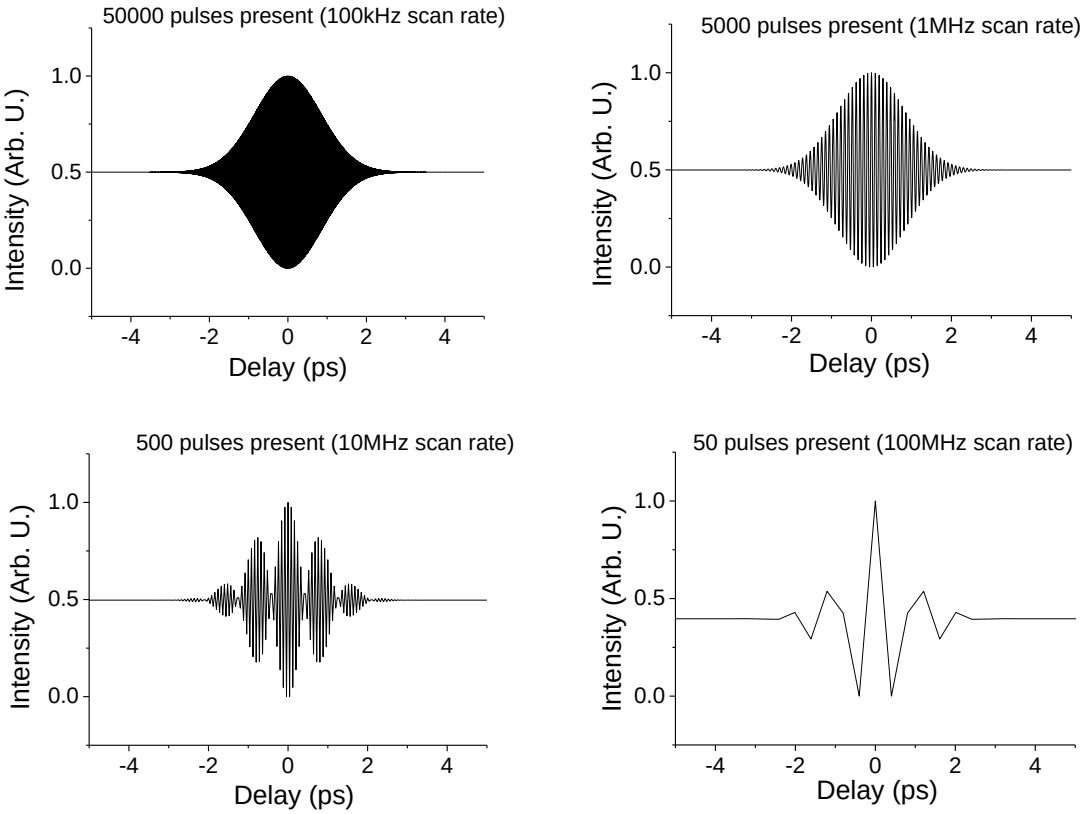

Figure 4-20 – Simulation showing autocorrelations where 50000, 5000, 500 and 50 pulses are present, representing scans acquired at 100kHz, 1MHz, 10MHz and 100MHz scan rates respectively, assuming a 5GHz repetition rate.

As can be seen, the general trend of fringe erosion can be demonstrated under the principle of increasing scan rate, however the simulation shows this to a lesser extent than the experiments in reality, where a fairly well constructed trace is found at 1MHz; in fact it is not until an assumed 100MHz scan rate that a similar level of features are seen to compare with that of an experimental 1MHz scan rate. This approximate factor of 100

[15] Note that this does simulate an autocorrelation, not a cross-correlation, and does not take into account the various dynamic changes in MLLD output characterisation; the purpose is merely to illustrate the reduction in fringes due to the presence of fewer pulses per second.

[16] Note that whilst the simulation was carried out over a 20ps scan range, the figures were drawn to show only 10ps in order to clearly see the resultant features.

between experimental and simulated results could be due to the bandwidth limitations of the 1GHz oscilloscope. We can test this by measuring the rise time of the fringes of a 10Hz experimental scan, see Figure 4-21.

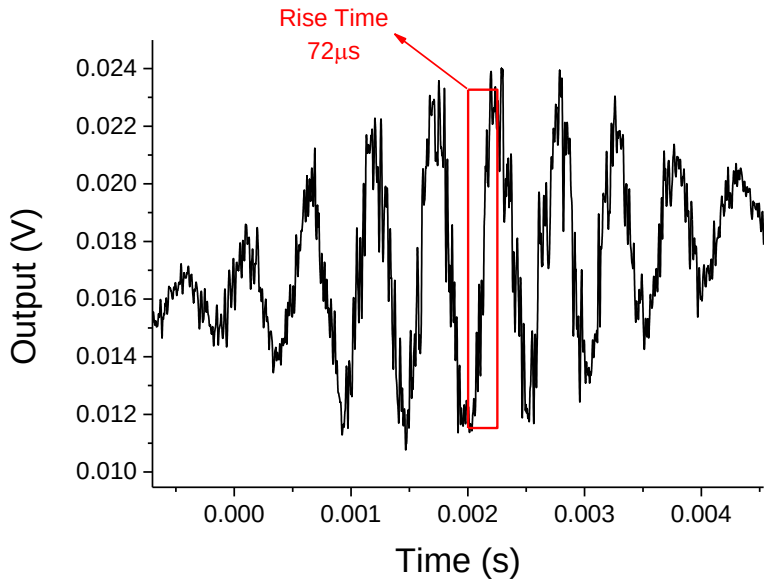

Figure 4-21 – Experimental 10Hz FOSBERT trace with a red highlighted region of interest which was used to calculate a rise time of 72µs, corresponding to a frequency component of 13.9kHz.

If we consider that at 10Hz, the fringes in the cross-correlation have a rise time of 72µs corresponding to a 13.9kHz frequency component, then by extrapolation if the scan rate is increased by a factor of 100,000 (to 1MHz), in order to maintain this level of detail the system would need to be capable of detecting at 100,000 times 13.9kHz, i.e. frequency components of 1.4GHz. In order to realise such fast components the oscilloscope bandwidth would have to be significantly greater to overcome the Nyquist criteria, however the system would still be incapable of competing with the small number of pulses which are physically present during each scan.

The simulation, as well as not being constructed around the varying output characteristics of each pulse used in the cross-correlation, does not take into account the effects of jitter, dispersion, power and temperature fluctuations which induce noise; all of which are likely to contribute to the differences in the experimental versus the simulated results.

Despite these technical drawbacks, the potential of the system is well highlighted in this section. Regardless of the quality, cross-correlations from a two-section quantum dot mode-locked laser diode were detected and acquired at up to megahertz scan rates, using

only a single laser, with absolutely no moving parts, demonstrating the proof of concept of repetitive scanning by applying an electrical signal to the absorber section of the diode in the context of an imbalanced interferometer.

Note, for the remainder of this chapter (unless stated otherwise), the forward current applied to the gain section was increased slightly from the usual 210mA to 220mA in order to improve the peak to baseline ratio and aid in the precision of the deconvolution and fitting processes. According to the mode-locking region (MLR) measured in Chapter 2, this gave rise to slightly different reverse bias and repetition rate tunability ranges, the specifics of which are provided in the Appendix, section 7.3.2. As such, a full repetition rate tunability of 5.67MHz was found for a static (power supply) reverse bias range of 5.00V to 7.00V, and therefore a modulated (signal generator) sinusoidal reverse bias range of $V_{offset} = -7.09V$ and $V_{pp} = 2.28V$ when corrected for the voltage drop across the new device resistance ranges. This also aids in the demonstration of these devices as versatile, entirely electronically controlled pulsed laser sources, where the outputs can be tuned essentially at the touch of a button.

4.6.2. Reduction in Repetition Rate Tunability Amplitude

Though the bandwidth of the oscilloscope is 1GHz, and that of the InGaAs detector is 5GHz, we do not have any certain way of determining how effectively the device itself may respond to fast modulation of one of its sections (the small saturable absorber). In order to gather some information regarding this, a typical FOSBERT scan was set up, however the longer arm of the interferometer was blocked. With the gain section forward biased at a constant 220mA, a continuously modulated reverse bias is applied to the absorber section. The output of the narrow-ridge device is then collected at the InGaAs detector directly via the free-space delay line only, disallowing the opportunity for a cross correlation. The output of the detector is then sent to the oscilloscope, along with a copy of the original input modulation signal from the signal generator, see Figure 4-22. Scans are acquired from 10Hz to 1MHz. What is immediately evident is that whilst the input biasing signal maintains its form and amplitude up to modulation speeds of 1MHz, the same cannot be said for the performance of the MLLD. After approximately 100Hz, the device begins to show signs of degraded response to the input signal, as the amplitude from the detector begins to drop.

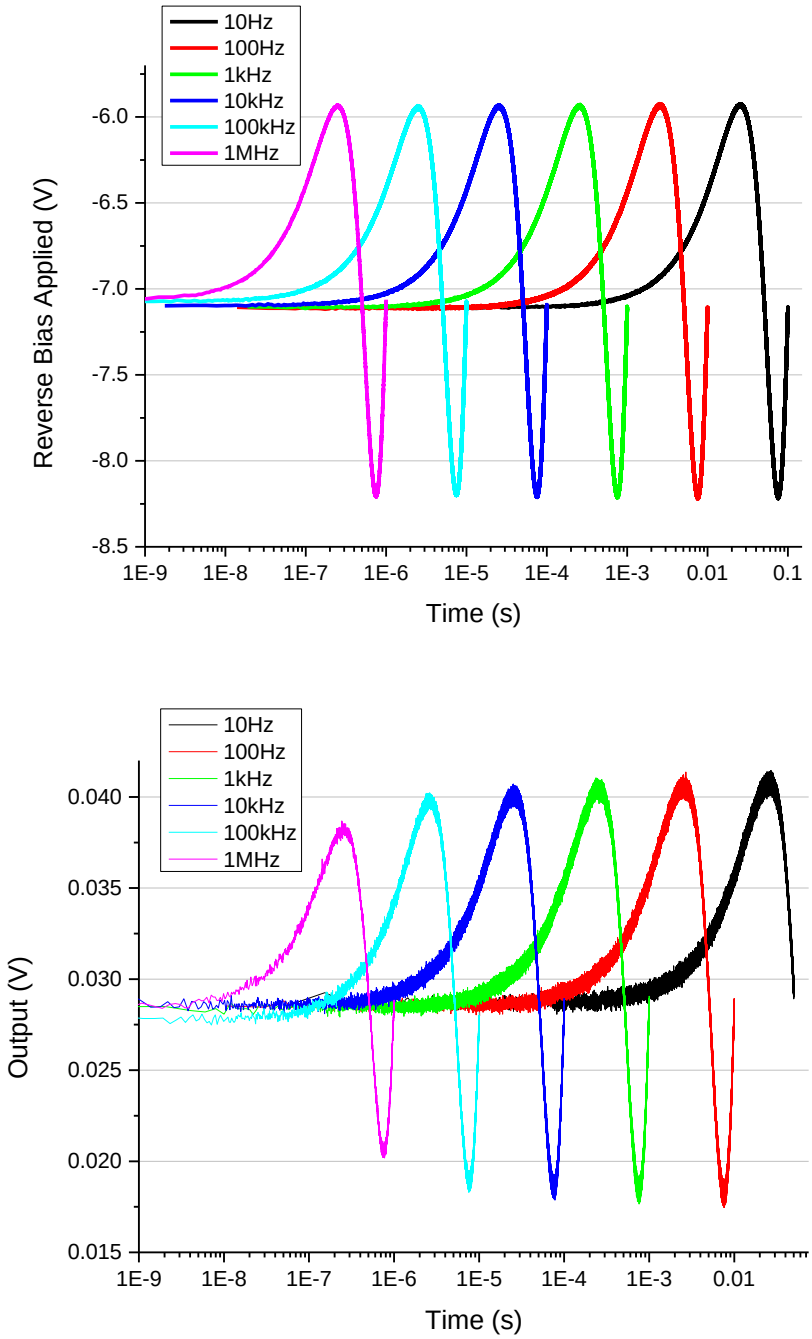

Figure 4-22 – Above, the reverse bias signal applied to the absorber section of the MLLD across several modulation frequencies. Below, the detector output across the same modulation frequencies.

The amplitude reduction has further implications when considering the conversion from real time to scanning time. Considering slow modulation or SOSBERT scans, we know that a specific value of reverse bias to the absorber section should result in a specific voltage output at the InGaAs detector. That is to say, the output of the detector (being directly proportional to the average output of the laser) is also then directly related to the reverse bias applied to the absorber section as demonstrated in Chapter 2. As such, if there is a

reduction in the extremes of the sinusoid, this suggests firstly that the extremes in maximum and minimum average power have not been electrically realised, which could signify that the extremes in maximum and minimum reverse bias were never realised either. Since the biasing levels are also related to the repetition rate tunability, this could mean the tunability has somehow reduced due to faster modulations. If not taken into account, this will appear to dilate the trace when it is converted from reverse bias (repetition rate tunability) to a scan range, leading to inaccurate or inconsistent measurements.

In order to examine this, in the final stages of the project a high speed RF analyser (*Tektronix RSA51126B*) was used over a short period to determine if there was a correlation between the falling average power amplitude and the repetition rate tunability via the sinusoidal reverse bias. The full repetition rate tunability is known to be 5.67MHz under static drive by a power supply over a reverse bias range of 5.0V to 7.0V. The equivalent reverse bias range for this repetition rate tunability driven by the signal generator, as discussed is $V_{offset} = -7.09V$ and $V_{pp} = 2.28V$.

When this reverse bias range is supplied in sinusoidal form to the absorber section and the output delivered to the high speed RF analyser, we may observe how the repetition rate tunability changes for increasing scan rates using the real-time Digital Phosphor Technology (DPX) spectrum function, which resembles the maximum-hold function available on standard RF analysers. With the span set to 10MHz, markers are placed on opposite extremes of the trace as the signal is acquired at 10Hz, 100Hz, 1kHz and 10kHz scan rates, see Figure 4-23. Note that screen-shots are taken of the live data during the acquisition, and the results of the markers are gathered for later use. Additionally, due to limitations of the High Speed RF Analyser, traces were not acquired for 100kHz or 1MHz scan rates due to the unreliability in reading the repetition rate tunability reduction.

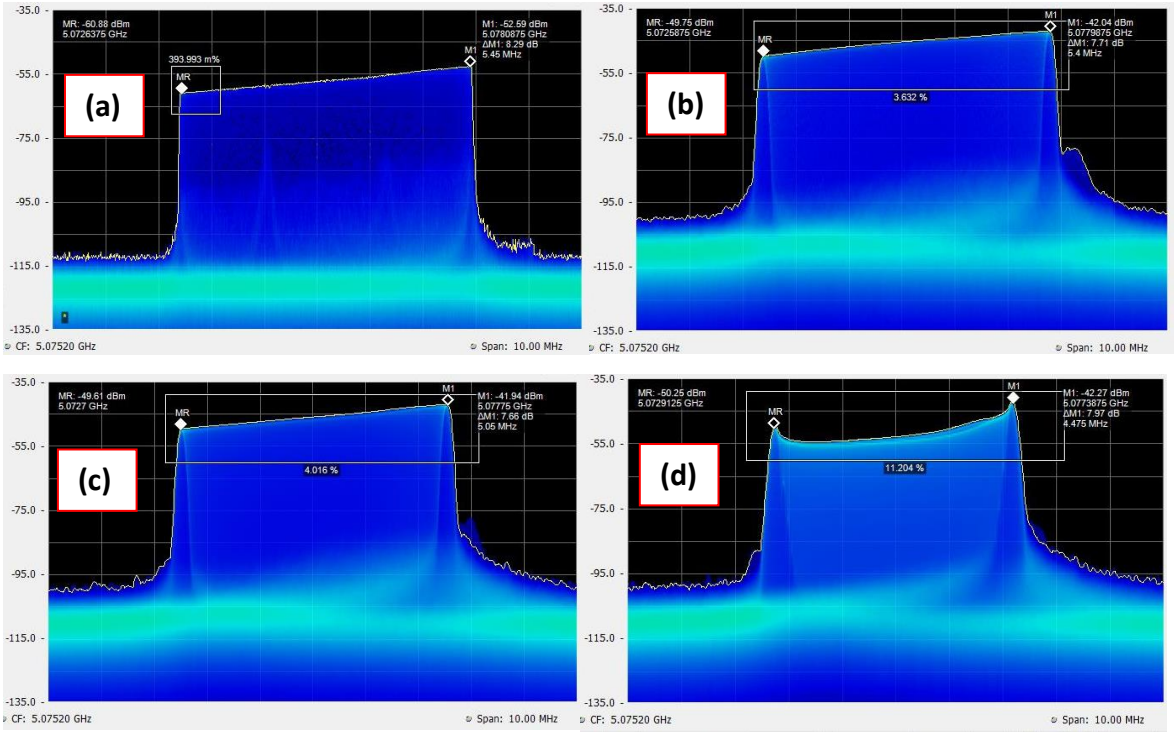

Figure 4-23 – Screen shots from a High Speed RF Analyser showing how the repetition rate tunability decreases for increasing scan rates a) 10Hz b) 100Hz c) 1kHz and d) 10kHz

The results clearly show a reduction in repetition rate tunability for increasing scan rates compared to the static power supply, and are plotted for comparison where a reading error of ±50kHz is assumed (a twentieth of one x-scale division) based on the ability to reasonably manually measure the maximum peak of each extreme, see Figure 4-24.

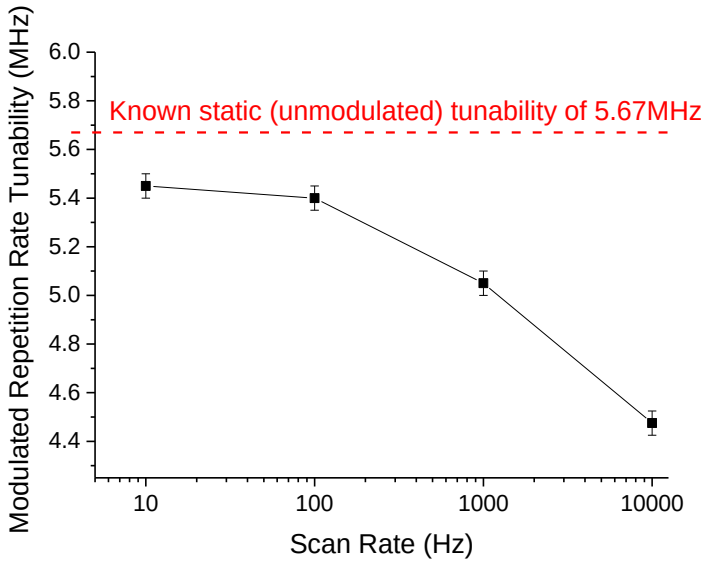

Figure 4-24 – The measured repetition rate tunability for increasing scan rates as compared to the known repetition rate tunability of the static (unmodulated) case (red dashed line).

The cause of the reduction in the amplitude of the repetition rate tunability for faster scan rates is not understood at present. It is possible that the fast modulation of the small absorber section compared to the statically biased larger gain section leads to discrepancies in the temperature of the active region, which was shown in chapter 2 to influence the repetition rate. It is also possible that higher quality driving equipment is required, such as shortening and replacing the SMA cables between the signal generator and the absorber section with higher bandwidth alternatives.

In the following section, the accuracy of the displacement measurements was found to decrease for increasing scan rates when the static tunability of 5.67MHz was used throughout the experiments. The scan rate-dependant repetition rate tunability was then used as a comparison, and the accuracy of these more robust tests is discussed.

4.7. FOSBERT Displacement Measurement

In this Section, having previously demonstrated the deconvolution process for FOSBERT displacement at 10Hz, as well the considering the reduction in quality and even amplitude of scans acquired at faster scan rates and the ability to increase the scan range through longer PDLs, this section aims to quantitatively assess the accuracy of FOSBERT for a variety of scan ranges and scan rates. As with other OSBERT studies, this is cross-examined over a number of combinations of PDL lengths and repetition rate tunability ranges.

4.7.1. Experimental Approach

Two main experimental designs were investigated. Firstly, one which could assess the accuracy of extremely small sub-millimetre target displacements of 100 micrometres. This was undertaken using a short PDL length of 2m (equating to a free-space distance of around 3m) and an applied reverse bias range corresponding to 5.67MHz repetition rate tunability, giving a total scan range of 10.86 picoseconds (or 3.26 millimetres in terms of potential target displacement) according to expression (14). The second experiment consisted of an identical approach however using a longer PDL length of 25m (equating to over 36m free-space), corresponding to a far longer total scan range of 135.7 picoseconds (or 40.7 millimetres target displacement) according to expression (14). The scans were then reanalysed using the repetition rate tunabilities acquired under scan rates of 10Hz, 100Hz, 1kHz and 10kHz according to Figure 4-24 above. In the case of the 2m PDL

experiments, an additional free-space element of 45cm was measured as the imbalance between the short and long arms, whilst an additional 48cm was measured in the case of the 25m PDL experiments, adding 1.68ps and 1.79ps scan range respectively – these were taken into account during all calculations.

In the case of 2m PDL study, the target position was moved through several spatial positions, each 100µm apart, such that a series of target movements could be calculated and assessed for their accuracy. This process was repeated at several scan rates. The approach for the 25m PDL study was identical, however the greater scan range was taken advantage of, and instead several individual 1.0mm target positions were acquired.

4.7.2. Analysis and Discussion

Firstly we look at the scans acquired using the 2m PDL, and deconvolved the scan as per the method described in section 4.4.2, see Figure 4-25. Note that although four scan rates were assessed, presented here as leading examples are the scans acquired under the maximum scan rate of 10kHz.

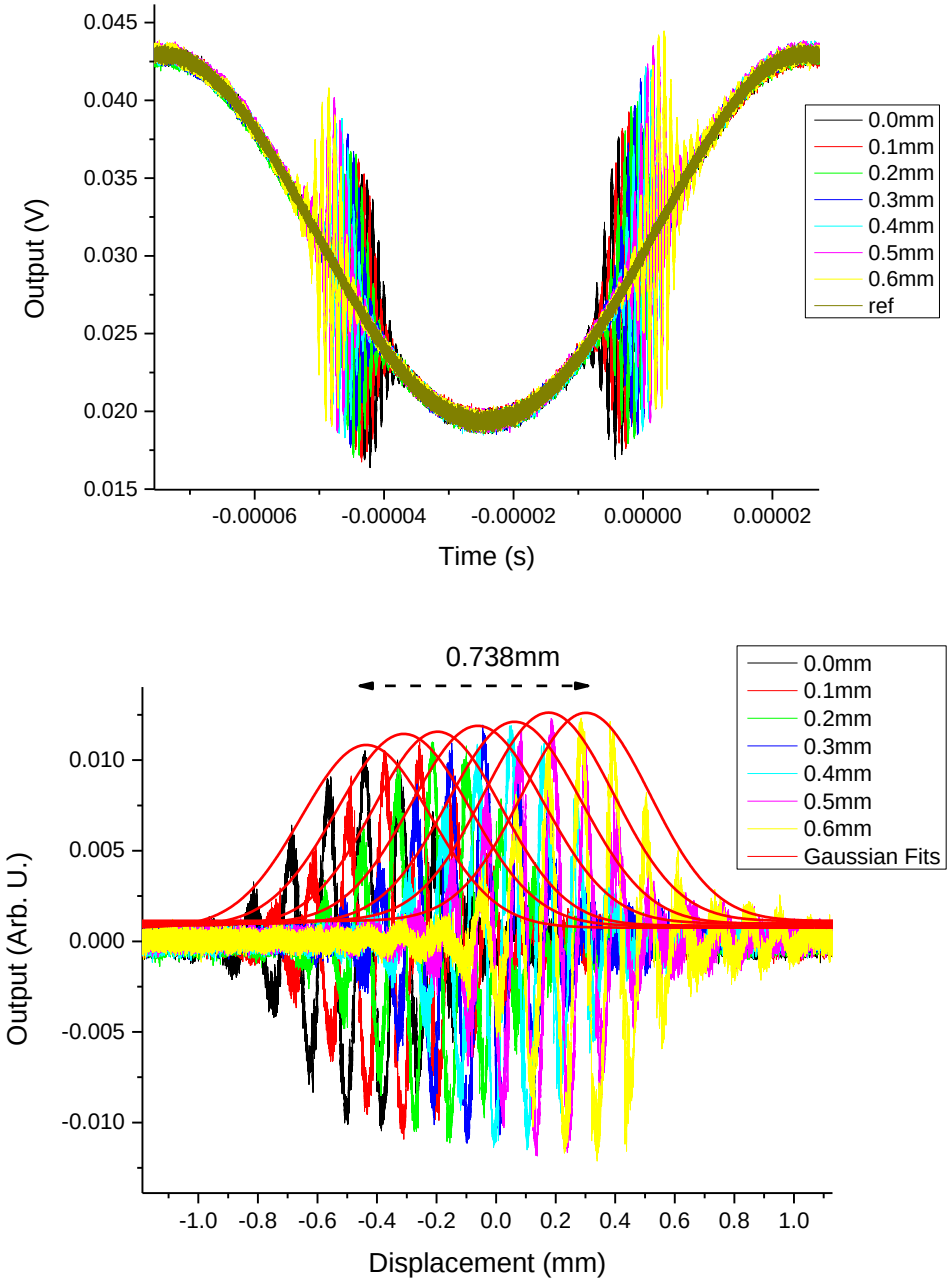

Figure 4-25 – Above, 10kHz target displacement scans using the 2m PDL show several target positions. Below, the deconvolved scans plotted over the spatial domain and fitted with Gaussians.

Though the target displacement via the translation stage was known to total a distance of 0.6mm, the deconvolution of these OSBERT traces has given rise to a total measured displacement of 0.738mm. This inaccuracy is expected to be caused by the reduced repetition rate tunability amplitude discussed in the previous section, and as such the analysis was repeated under the exact same deconvolution process, where only the repetition rate tunability was replaced with 4.475MHz as per Figure 4-24 above. The results were then replotted, see Figure 4-26.

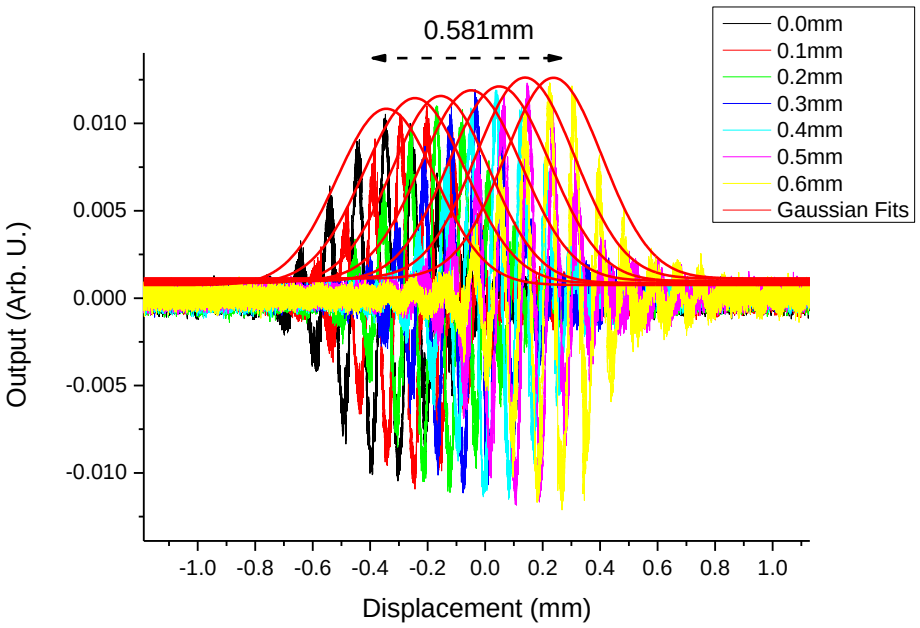

Figure 4-26 – The 10kHz OSBERT target displacement scans are replotted taking into account the reduction in repetition rate tunability brought on by increasing scan rates.

As can be seen, the re-analysed traces have been deconvolved into a more accurate total displacement of 0.581mm. The remaining inaccuracy as compared to the known displacement of 0.6mm is likely due to a combination of the envelope fitting process, the inexactly linear relationship between reverse bias and repetition rate, and the inexactly linear relationship between the set and experienced voltages due to the resistance of the narrow ridge device. For each scan rate, the individual 100µm steps were then plotted against an ideal reference for both the uncorrected version of the measurements and that which was corrected for the reduction in repetition rate tunability, see Figure 4-27.

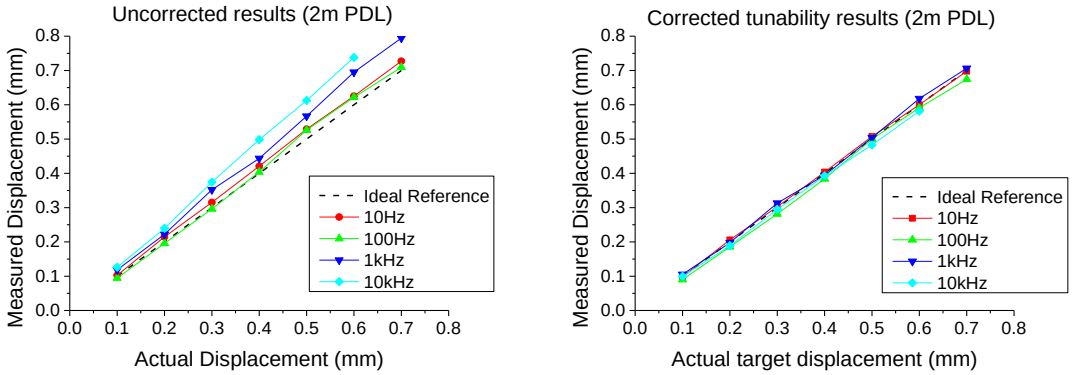

Figure 4-27 – The individual 100µm steps are plotted alongside an ideal reference for each scan rate. Left, the original uncorrected results and right, having been corrected according to Figure 4-24.

As can be seen, simply reanalysing the data altering only the repetition rate tunability Δf according to the measured reduction has greatly increased the accuracy of each individual step, confirming the source (though not the cause) of the error.

Therefore the 25m PDL experiments were conducted and analysed in the same manner. Firstly we plot the raw traces from the oscilloscope and deconvolved them assuming the tunability does not decrease, see Figure 4-28 and Figure 4-29.

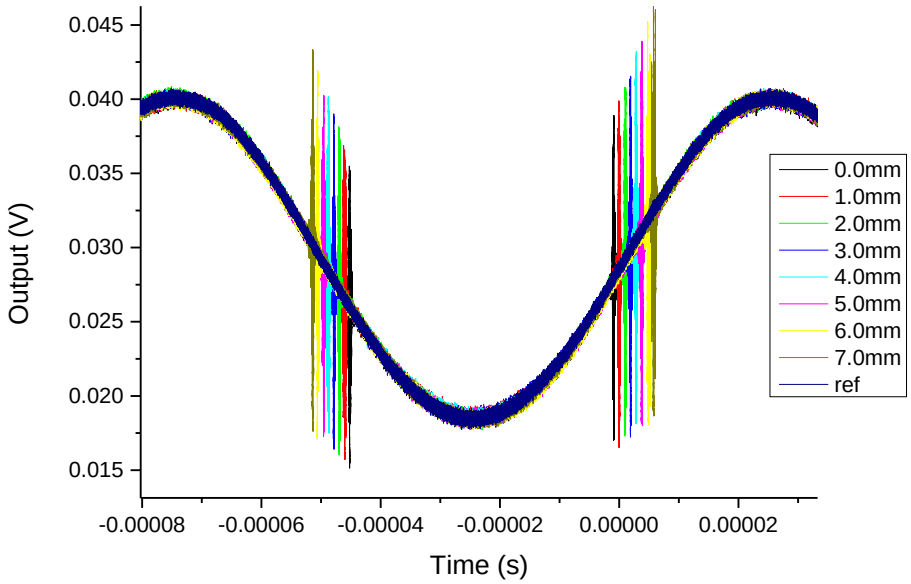

Figure 4-28 - 10kHz target displacement scans using the 25m PDL show several target positions.

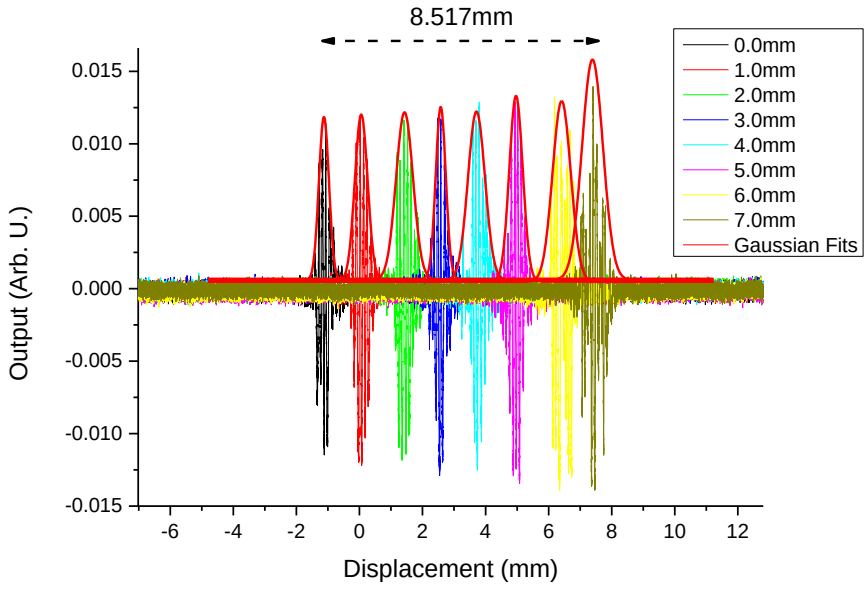

Figure 4-29 – The deconvolved scans plotted over the spatial domain and fitted with Gaussians.

Out of the known total displacement of 7.0mm, 8.517mm was measured using the 10kHz OSBERT method. As with the 2m PDL experiments, the data was then reanalysed where the repetition rate tunability was substituted with the 4.475MHz found in Figure 4-24, see Figure 4-30.

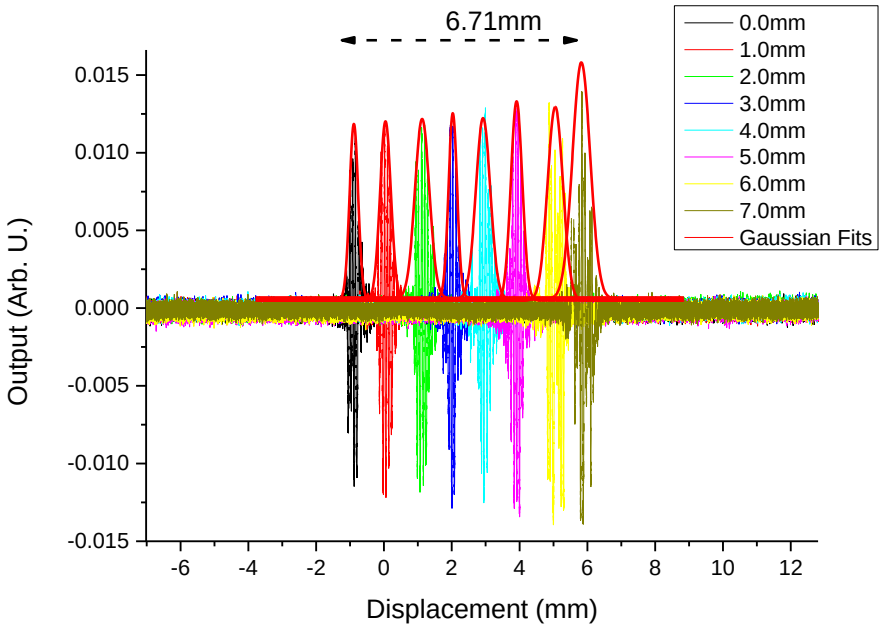

Figure 4-30 - The 10kHz OSBERT target displacement scans are replotted taking into account the reduction in repetition rate tunability brought on by increasing scan rates.

As can be seen, the re-analysed traces have been deconvolved into a more accurate total displacement of 6.71mm. As with the 2m PDL experiments, the remaining inaccuracy as compared to the known displacement of 7.0mm is likely due to the inexactly linear relationship between reverse bias and repetition rate, and the inexactly linear relationship between the set and experienced voltages due to the resistance of the narrow ridge device. Evidently the traces acquired using a 25m PDL are of slightly poorer quality in so far as the individual fringes are more difficult to resolve, and therefore the fitting of the Gaussians was less precise. This is thought to be due to a combination of dispersion over a longer length, and timing jitter, discussed further in section 4.8. These additional factors may account for the slightly larger error than that found in the 2m PDL experiments. For each scan rate, the individual 1.0mm steps were then plotted against an ideal reference for both the uncorrected version of the measurements and that which was corrected for the reduction in repetition rate tunability, see Figure 4-31.

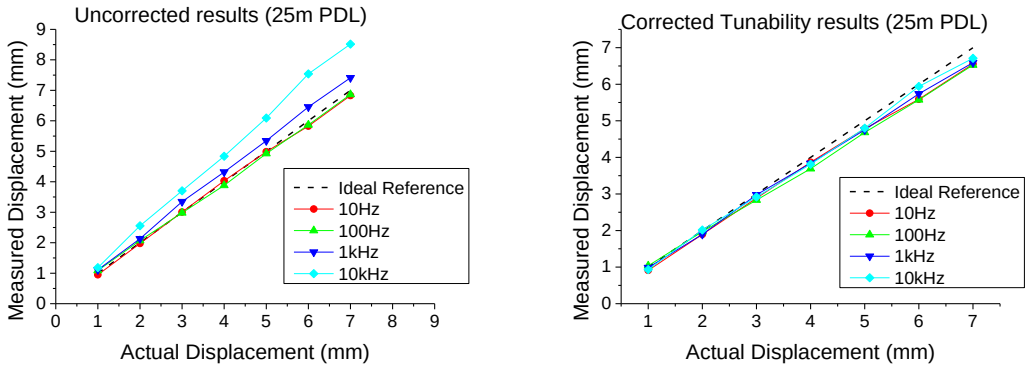

Figure 4-31 - The individual 1.0mm steps are plotted alongside an ideal reference for each scan rate. Left, the original uncorrected results and right, having corrected for the reduction in repetition rate tunability.

As can be seen, the corrected target displacements exhibit far greater accuracy across the increasing scan rates than before, however there also appears to be a drop in accuracy compared to the ideal reference as the target moves to the final position. The reason for this is not understood as (aside from the PDL length) the traces were acquired under identical conditions to the 2m PDL counterpart experiments. Since we can rule out the correction in repetition rate tunability, or the motion of the target if a software issue occurred with the accurate reporting of the stage position – this could be the case since the accuracy seems to particularly fall off past 3.0mm total displacement.. The error in reading the free-space component, as in Chapter 3, was considered to be +/- 2.0mm, and in this context would correspond with a scan range error of only +/- 7.4fs or 2.2µm, and is therefore not considered a major contributor towards the error.

Finally, both PDL experiments were compared over each scan rate by averaging the individual 100µm and 1.0mm steps in the target displacement for the 2m PDL and 25m PDL experiments respectively. As a guide for accuracy and repeatability, the averaged results were plotted alongside accompanying error bars which are the standard deviation of each average, see Figure 4-32 and Figure 4-33. Each experiment is plotted both with and without the repetition rate tunability correction.

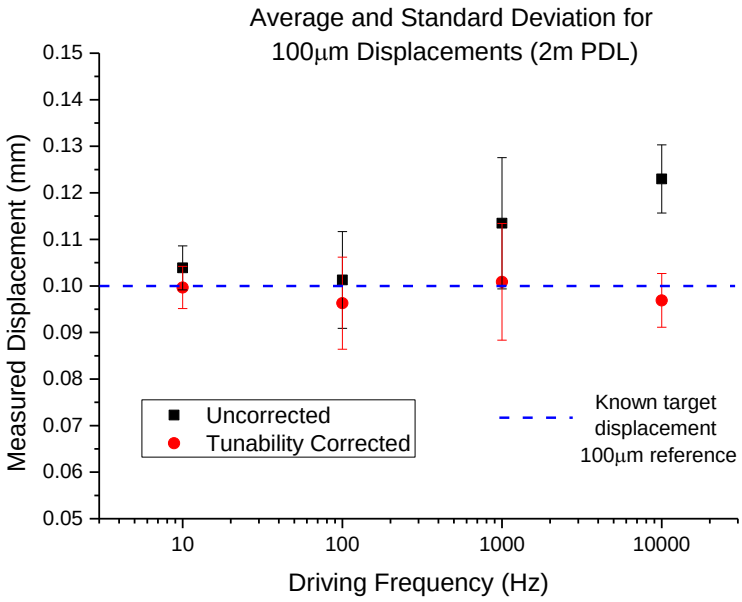

Figure 4-32 – The average displacements for the 2m PDL experiments are plotted for both uncorrected and corrected repetition rate tunability, and contrasted against the known target displacement.

Immediately the benefit of correcting for the repetition rate tunability may be seen, as up to 10kHz scan rates, the average 100µm displacements are within error as compared to the actual target displacement. Ultimately, a target displacement as small as 100µm was successfully measured to within an error of between ±5µm and ±10µm, at a distance of 2m. The procedure was therefore completed in the same fashion for the 25m PDL experiment, see Figure 4-33.

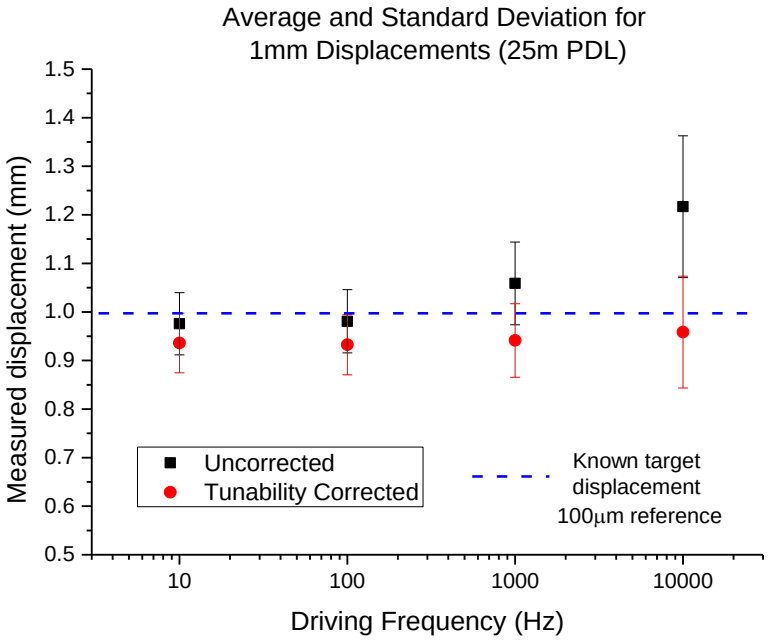

Figure 4-33 - The average displacements for the 25m PDL experiments are plotted for both uncorrected and corrected repetition rate tunability, and contrasted against the known target displacement.

As can be seen, the average displacement is within error of the known target displacement of 1.0mm after repetition rate tunability correction. There does however, still appear to be a systematic error whereby the correction has given a consistent average displacement of around 0.95mm. As with the individual steps shown in Figure 4-31, the reason is not known exactly, as all parameters were constant between the 2m and 25m PDL experiments. For this experiment, a target displacement as small as 1.0mm was successfully measured to within an error of between ±50µm and ±100µm, at a distance of 25m, equating to a free space distance of over 36m when the free-space component is take into account.

4.8. Jitter Considerations

4.8.1. Brief Introduction to Jitter

Timing jitter is the deviation of a signal from an ideal periodicity; in the context of pulsed lasers this means to what extent the pulses are emitted at exactly the repetition rate. With regards to semiconductor laser diodes, both active and hybrid mode-locking techniques are generally found to exhibit superior jitter performances than their passively mode-locked counterparts [137] due to the restorative active process of pulse train emission in the former. Similarly, quantum dot MLLDs have demonstrated superior jitter performance than their quantum well counterparts [138], due to the reduced amplified spontaneous emission (brought on by greater carrier confinement) which is the primary source of jitter in passive mode-locked lasers [128, 139].

Both RMS and pulse-to-pulse timing jitter methods were compared by Lin *et al* [140] who suggested that the latter method is more suitable for passively mode-locked laser diodes, since without the active influence, the timing of each pulse is dependent upon the timing of the previous one, which is to say the timing jitter is cumulative, and therefore best measured in a pulse-to-pulse format such as that of the cross-correlation method [128, 141].

In particular, since OSBERT is an inherently time-sensitive cross-correlation technique, it is sensible to take into account the pulse to pulse timing jitter. Kefelian *et al* [142] have shown that the pulse to pulse timing jitter may be extracted using the RF linewidth $\Delta\upsilon$ of

the RF spectrum as a figure of merit for the magnitude of jitter, which is found to increase for the increasing number of periods *N* between pulse pairs, where

$$\sigma_{pp}(N) = T_{rep}\sqrt{\frac{\Delta\upsilon N T_R}{2\pi}} = \frac{1}{f_{rep}}\sqrt{\frac{\Delta\upsilon N}{2\pi f_{rep}}} \tag{39}$$

This is particularly relevant since OSBERT is based partly upon the OSCAT technique, where greater scan ranges are brought about by increasing the passive delay line within the cross-correlator, and therefore increasing the number of roundtrip periods. As discussed, degradations occur within the OSBERT cross correlations for two main factors; increasing the scan rate towards megahertz levels, and increasing the passive delay line length, the latter of which may be explained by the pulse to pulse timing jitter increasing for increasing PDL lengths.

4.8.2. Estimating the pulse-to-pulse timing jitter

Using the Kefelian approach, RF spectra shown in Chapter 2 were fit with a lorentzian function in order to determine their linewidth, which were around 15kHz. It is expected that this linewidth would decrease for increasing reverse bias due to the increased stability in mode-locking, however the RF Analyser available was not sensitive enough to discern a reliable difference between RF traces, hence 15kHz was an upper limit on the linewidth. Substituting this into expression (39), we may plot the results according to an increasing passive delay length, see Figure 4-34. As a means of comparison, 5kHz, 10kHz and 20kHz linewidths were also simulated and superimposed.

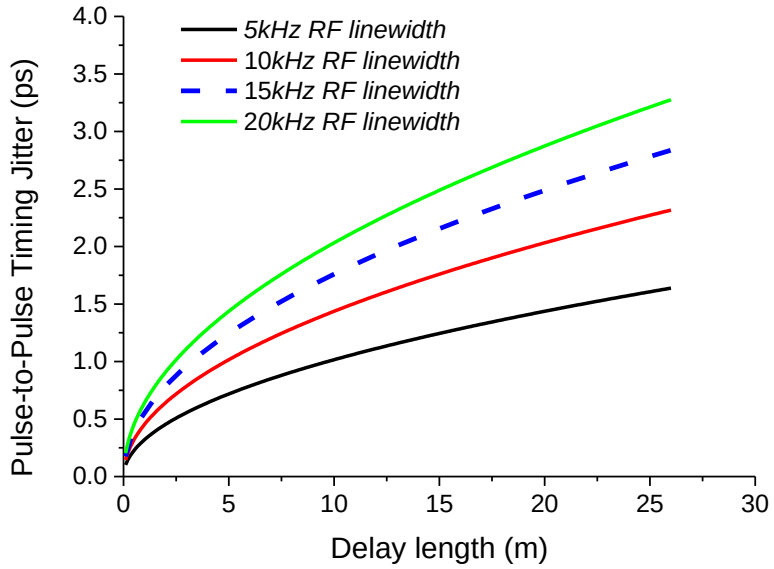

Figure 4-34 – Simulation showing that increasing the linewidth of the RF spectra or the length of delay line will increase the pulse to pulse timing jitter for a 5.07GHz repetition rate laser.

As can be seen, theoretically a few hundred femtoseconds to a few picoseconds of pulse to pulse timing jitter may have been present in the OSBERT system depending on the PDL lengths used (1m, 2m, 5 and 25m). This would at least qualitatively explain the reduction in quality and fringe pattern stability observed for increasing PDL lengths.

4.9. Conclusions

In this chapter, the final improvements were made to the OSBERT technique. In order to compete with the state of the art, the technique was tested for increasing both the scan range and the scan rate.

A number of additional considerations had to be taken into account when conducting Fast-OSBERT experiments as compared with the static (unmodulated) case of Slow-OSBERT experiments, demonstrated in Chapter 3. Firstly, whilst the repetition rate was still tuned by the reverse bias applied to the absorber section, the source was a signal generator with a 50Ω output resistance, compared to the minimal resistance of a power supply used for SOSBERT. As such, the voltage drop experienced by the resistance of the device had to be accounted for and calibrated.

Additionally, it was found (though not entirely understood) that the tunability decreased for increasing scan rates, which also had to be compensated for as the reduction in repetition rate tunability led to a reduction in scan range, without which the scans were increasingly inaccurate.

Compared to SOSBERT, the FOSBERT scans also exhibited quality reduction as the scan rate was increased, namely in a reduced number of detectable fringes within the interferogram traces. Despite this, cross-correlations were still acquired at megahertz scan rates, which highlights the potential of such a system having absolutely no mechanical parts. Additionally, a 25m version of the 1m, 2m and 5m PDLs used during the project was introduced in order to maximise the scan range to that of the laser's 200ps roundtrip period as proof that this limit can indeed be reached.

In terms of a proof of principle demonstration, target displacement measurement was adopted. Using a 2m PDL length, target displacements of 100µm were measured to within 10µm accuracy at an equivalent free-space distance of over 3m when the refractive index of the fibre and the free-space component is taken into account. Scans which were corrected for the repetition rate tunability losses were achieved at 10Hz, 100Hz, 1kHz and 10kHz scan rates. Similarly, using a 25m PDL length, target displacements of 1mm were measured to within 100µm accuracy at an equivalent free-space distance of over 36m when the refractive index of the fibre is taken into account. Scans which were corrected for the repetition rate tunability losses were also achieved at 10Hz, 100Hz, 1kHz and 10kHz scan rates. Preliminary investigations of megahertz level scan rates were shown to have potential for realisation, particularly if a higher speed RF analyser would be required in order to measure and compensate for the tunability reduction at such high scan rates. Additionally, whilst only PDL lengths as long as 25m were used, it is possible that far longer effective distances could be realised, particularly if dispersion compensating fibres were used. Additionally, longer PDL lengths were shown to potentially increase the pulse to pulse jitter within the system, and so this must also be taken into consideration.

Whilst most OSCAT-type systems (including OSREFM) achieved sub-kHz scan rates, OSBERT achieved a minimum of 10kHz, additionally contending with two-laser systems such as ASOPS and ECOPS, see Appendix Section 7.1.1.

Ultimately, this chapter marks the final improvement in the OSBERT system in terms of proof of principle demonstrations. To the best of my knowledge, for the first time an optical sampling technique has now been demonstrated using only a single compact, inexpensive two-section quantum dot passively mode-locked laser diode. Though based partly on the OSCAT technique, OSBERT differs in that the repetition rate is tuned electronically, without the need for any mechanical parts whatsoever. This has opened up the realisation of scan rates on the order of tens of kilohertz, whilst showing great potential for megahertz level scan-rates.

5. Single-Laser-ECOPS and the Virtual Laser

In this chapter, the groundwork suggestions and theory are discussed for a second unique optical sampling technique which was mathematically developed during the final analysis of OSBERT in the previous chapters. The theoretical technique for Single-Laser Electronically Controlled Optical Sampling (SLECOPS) is firstly introduced as a means of performing an ASOPS or ECOPS type scan using only one laser, as opposed to two, partially taking advantage of the single-laser OSCAT premise. The concept of a second 'virtual' laser originating from the source laser is discussed, and a mathematical relationship between ASOPS and OSCAT is derived. The potential for increased scan rates among other advantages as a result of this technique are presented in the form of cross-correlation simulations, and the limitations of practically implementing such a system are considered.

5.1. Introduction

Asynchronous type sampling, demonstrated in ASOPS and ECOPS systems, have thus far been described as inherently two-laser techniques, whereas in fact ASOPS has to date been performed using only a single mode-locked fibre laser [143], whose cavity was designed such that it resulted in dual-wavelength output pulses at slightly different repetition rates. SLECOPS (essentially, Single Laser ECOPS) is a theoretical suggestion for a new optical sampling technique which combines several of the previously introduced state-of-the-art methods for many of their advantages, whilst losing many of their disadvantages. Namely, SLECOPS competes with the speed and basic asynchronous principle of ASOPS, the selectable and customisable scan range of ECOPS, and the single-laser operation of OSCAT (or OSBERT) by use of a passive delay line in a highly imbalanced interferometer. It is important to note that whilst OSBERT is based exclusively on MLLDs with repetition-rates tunable via selective biasing conditions, SLECOPS is a method which is potentially applicable to any single pulsed laser source whose repetition rate can be modulated (including MLLDs).

SLECOPS is achieved initially very similarly to OSBERT, by splitting the pulse train of a single pulsed laser source of some tunable repetition rate into two copies which traverse two independent paths; one far longer than the other, such as that found in a highly imbalanced interferometer, and the premise of the OSCAT technique [59]. Provided the

repetition rate of the pulsed laser source is tunable to some degree between a minimum and maximum frequency, and the passive delay line is sufficiently long, a temporal delay will occur between the two recombined pulse train copies at some target position. The combination of the passive delay line length and the amplitude of repetition rate tunability will determine the maximum scan range of the system. The concept of the 'virtual laser' may be seen as replacing one of the physical lasers of the two-laser ECOPS (or ASOPS) techniques with a long PDL and square wave or 'switching' tunability of the physical laser. As in ECOPS, this ultimately leads to two extreme repetition rates being alternately present at the target position, see Figure 5-1, giving rise to asynchronous sampling in a manner similar to that of ASOPS.

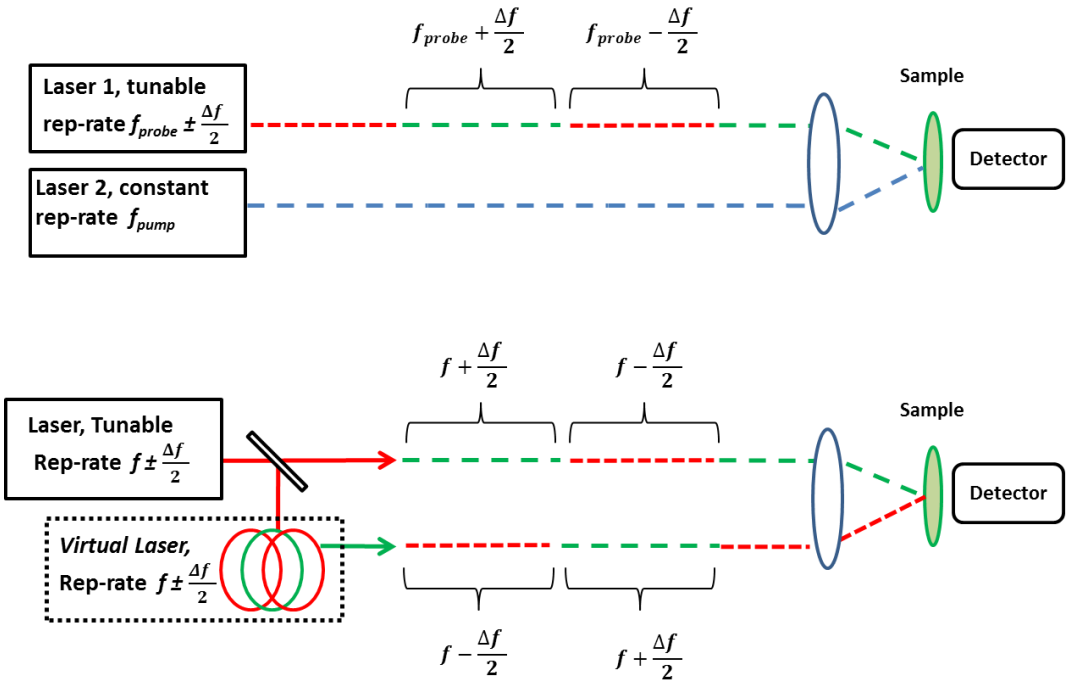

Figure 5-1 – Diagram showing how the second laser of an ECOPS system can be removed, giving rise to a Single Laser ECOPS technique (SLECOPS). The concept of the virtual laser shows how square wave modulation and a passive delay line can give rise to an alternating repetition rate difference at the target, the principle of ECOPS as a special case of asynchronous optical sampling.

The switching modulation of the repetition rate at the laser source via square wave is inspired by ECOPS, and occurs in such a manner as to allow, for example, the beam with the minimum repetition rate pulse train to propagate in one arm, whilst the beam with maximum repetition rate is delayed within the longer arm. The result is that two distinct repetition rates are detected at some target position upon the recombination of both pulse trains. The process is reversed upon switching the laser source to the opposite repetition rate in such a manner to allow scanning to be repeated periodically, for example using square wave modulation.

From the outset it is important to differentiate SLECOPS from the other optical sampling methods described throughout the project. Whereas OSCAT uses a controlled linear [59] (or sinusoidal [62]) increase of the repetition rate to directly control the scan rate, steadily acquiring data points along the way, SLECOPS instead switches instantly from the minimum to the maximum repetition rate, and allows the setup to scan through itself asynchronously. That is to say, the scan occurs passively at the moment of switching, rather than be guided by a steady increase or decrease in repetition rate, and therefore only two repetition rates are ever used.

Whereas the scan does occur in an asynchronous manner like that of ASOPS [40], SLECOPS uses only one laser, where the second laser may be thought of as effectively replaced by a long passive delay line (the 'virtual laser'). Similarly, although ECOPS [54] as discussed previously may solve ASOPS' problem of unwanted dead time, it does so by introducing a mechanical means of tuning one of the lasers repetition rates, a further limitation to add to the fact it is performed with two lasers. SLECOPS uses only one laser, where the pulse train traversing the passive delay line may be said to act as the 'second' or virtual laser on recombination.

In order to have the full selectable scan range within the entire roundtrip period, it is necessary to select a passive delay line which will allow this when combined with the preferred repetition rate tunability (though such a scan range is not actually necessary in order to accomplish the SLECOPS method). That is, as with the OSBERT method any combination of repetition rate tunability and passive delay line length may be adopted, giving a maximum possible scanning window up to one full roundtrip period of the pulse train (as in the case of ASOPS). A preferred scan range within that window may then be further selected by varying the amplitude and offset of the switching function controlling the repetition rate tuning. Thus scan ranges can be instantly limited to only meaningful temporal windows where information is required. As such, Single Laser ECOPS as described in this chapter is a proposal for a technique where ECOPS-type scanning can actually occur using only one laser.

.

5.2. Theory

We firstly examine in more detail a typical OSCAT setup, where the pulsed output of a mode-locked laser is split into a short and a long arm in the format of an imbalanced interferometer. As previously described in chapter 3, the combination of the ability to tune the repetition rate f_{rep} by Δf and the length *l* of a passive delay line (PDL) of refractive index *n* will give rise to a scan range Δt [60] such that

$$\Delta t = \frac{l \cdot n \cdot f_{rep}}{c}\left(\frac{1}{f_{rep}} - \frac{1}{f_{rep} + \Delta f}\right) = a\left(\frac{1}{f_{rep}} - \frac{1}{f_{rep} + \Delta f}\right) \tag{40}$$

Where *c* is the speed of light in a vacuum and *a* is the pulse-index; the difference in pulse number due to the interferometric arm imbalance. We now consider the mode-locked laser is pulsing at some repetition rate f_1. The pulses from each arm will temporally overlap at some target position, assuming in this case the temporal delay induced by the PDL is proportional to a multiple of the roundtrip period, see Figure 5-2. Note, the temporal delay of the PDL is simply defined as the delay in time for the length *l* such that $T_{PDL} = ln/c$.

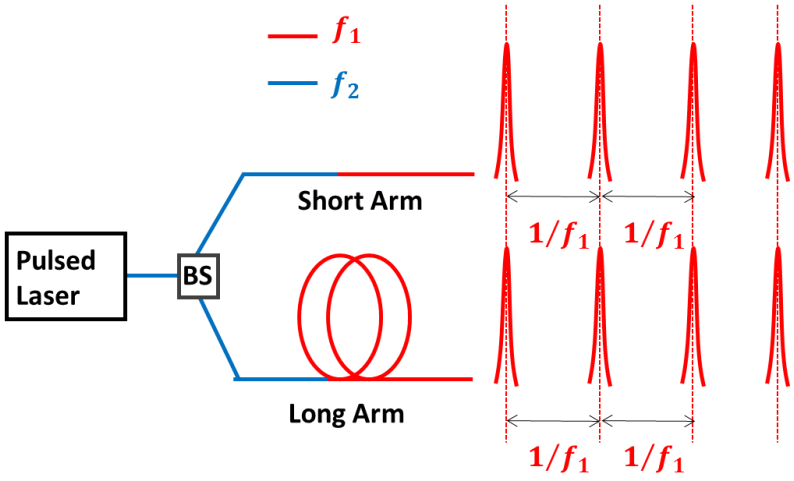

Figure 5-2 – An OSCAT setup showing how the consecutive pulses from the long and the short arm are temporally (and spatially) aligned, given a PDL whose temporal delay is proportional to one roundtrip period. The imbalance of the long arm means at the point of switching to a new repetition rate f_2, the former repetition rate f_1 will have a longer optical path to cross (temporarily) than that of the short arm.

Once the pulse train with repetition rate f_1 propagates both arms and then recombines, at some point in time OSCAT requires the next sub-step in repetition rate to be selected, giving rise to a different f_2 at the source (blue in Figure 5-2). It is clear to see that the

pulse train with f_2 will traverse the short arm far sooner than the pulse train in the long arm, which is to say the repetition rate change itself is delayed by the imbalance. As a result, for a brief period proportional to the length of the imbalance, two pulse trains with different repetition rates will temporarily overlap at the target position, see Figure 5-3, also known here as the catch-up phase.

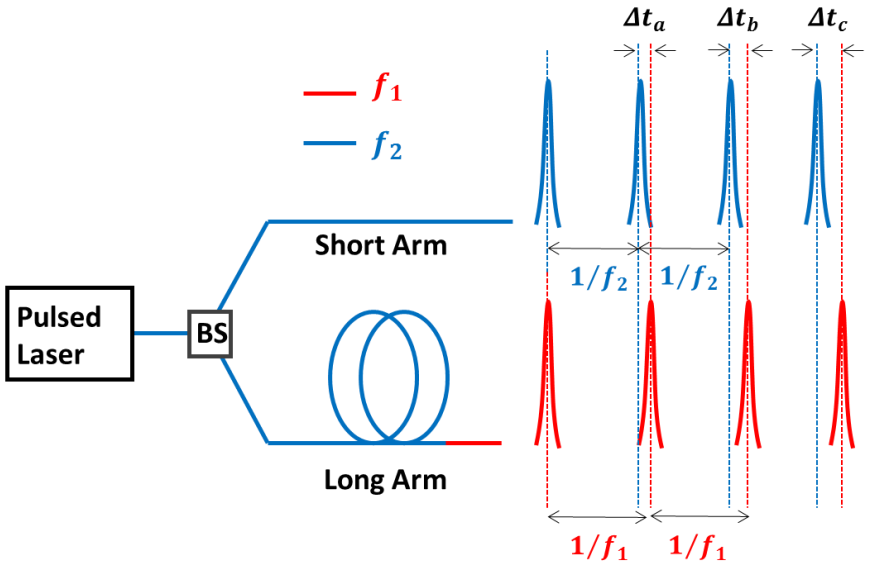

Figure 5-3 – The new pulse train with f_2 has traversed the far shorter arm and reached the target, however the pulse train in the long arm still exhibits the former repetition rate f_1. As a result, two different repetition rates are temporarily present at the target position, giving a sucessive temporal delay $\Delta t_{a,b,c}$.

During this 'catch-up' phase which is proportional to the imbalance, both f_1 and f_2 will interfere, and as outlined in the figure above, two discrete repetition rates present at one target will scan asynchronously, where each successive pulse is delayed in increments like that of ASOPS; Δt_a, Δt_b, Δt_c and so forth. However, in the case of OSCAT presented here, this will not continue indefinitely, as eventually the new repetition rate f_2 will complete its progress through the long arm, and the previous repetition rate will no longer exist simultaneously. At this point, the output of both arms has a repetition rate f_2, however due to the asynchronous step-wise nature of the previous phase, the pulses from each arm no longer overlap, but are left delayed with respect to each, see Figure 5-4. In finer detail, and closer inspection, this is the mechanism upon which OSCAT is built by successive incremental changes in repetition rate; the final delay between discrete OSCAT data points comes about due to the temporary mismatch of repetition rates exhibited in each arm requiring a catch-up phase between increments of repetition rate.

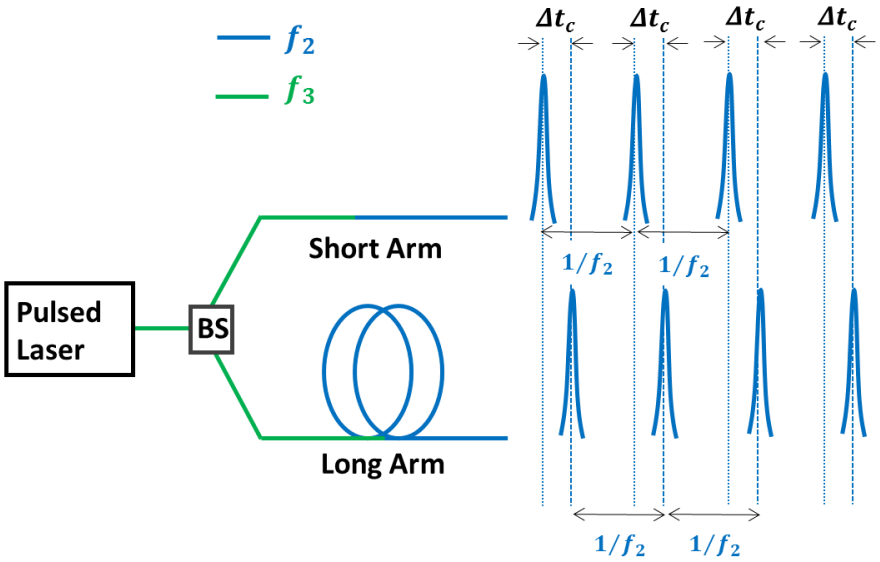

Figure 5-4 – After a time equal to the delay of the PDL, the temporary ASOPS-type scan caused by the presence of two repetition rates f_1 and f_2 at the detector has now ceased, and once again the same repetition rate (now f_2) is present at the detector in both arms.

As such, this final phase represents a new data point in the OSCAT scanning regime, as there is now a consistent delay between successive pulses from both arms, the entire object of that technique. The process will repeat as illustrated through the succession of the previous three figures at each moment the repetition rate is detuned again resulting in a new repetition rate, and therefore a new delay time and a new OSCAT data point.

The scenario corresponding to the transitions between the situations depicted in Figure 5-2, Figure 5-3 and Figure 5-4 may then be represented numerically. Consider a single pulsed laser of repetition rate $f_1 = 10\text{GHz}$, (and roundtrip period $1/f_1 = 100ps$) where the PDL has a length corresponding to a pulse index of $a = 4$. If the repetition rate is tuned by Δf = 500MHz to $f_2 = 10.5\text{GHz}$, this would represent a temporal delay of 20ps according to expression (40). Continuing in OSCAT fashion, a further Δf = 500MHz increase will give rise to another data point delayed by a further 20ps, and so forth (as similarly demonstrated in SOSBERT, Chapter 3). However, as indicated, the transition mechanism for this delay occurs due to this previously unexplored “catch-up” period, as the difference in roundtrip periods finish propagating the long and short arms, where the PDL represents their imbalance, see Figure 5-5.

Short Arm roundtrip period (ps)	Long Arm roundtrip period (ps)	Description of long and short arm repetition rates	Delay between pulse pairs (ps)	Description of delay-type
100	100	Repetition rate $f_1 = 10GHz$ with period $1/f_1$ is present in both arms at the target position.	0	There is zero delay between successive pulses as the PDL is aligned to allow this, and Δf = 0MHz
200	200		0	
300	300		0	
400	400		0	
500	500		0	
600	600		0	
700	700		0	
800	800		0	
895	900	Whilst the new rep rate $f_2 \sim 10.5GHz$ exits the short arm, f_1 finishes traversing the long arm; two rep rates exist at once	5	ASOPS-type scan with step-size δt~5ps due to rep rate mismatch
990	1000		10	
1085	1100		15	
1180	1200		20	
1275	1295	After the catch-up period of the long arm, Repetition rate f_2 with period $1/f_2$ is present in both arms at the target position.	20	Constant OSCAT-type delay due to new step ~Δf = 500MHz increase
1370	1390		20	
1465	1485		20	
1560	1580		20	
1650	1675	Whilst the new rep rate $f_3 \sim 11GHz$ exits the short arm, f_2 finishes traversing the long arm; two rep rates exist at once	25	ASOPS-type scan with step-size δt~5ps due to rep rate mismatch
1740	1770		30	
1830	1865		35	
1920	1960		40	
2010	2050	After the catch-up period of the long arm, Repetition rate f_3 with period $1/f_3$ is present in both arms at the target position.	40	Constant OSCAT-type delay due to new step ~Δf = 1000MHz increase
2100	2140		40	
2190	2230		40	
2280	2320		40	

Represents the PDL where $a = 4$

Represents the PDL where $a = 4$

Figure 5-5 – A representation of the concept of the ASOPS dynamic occurring within the OSCAT regime.

If the ASOPS-type dynamics within this OSCAT scan are ignored, essentially three OSCAT-type delay data points Δt are represented here, one for each Δf value. Note that unless the repetition rate is then altered again, the OSCAT scan would simply repeat at the same delay time, represented here by arbitrarily sustaining the time delay for four roundtrip periods; in reality of course, this depends on the speed of acquisition.

The temporal step-size of this ASOPS-type dynamic under these conditions is $\delta t = 5ps$, which is to say four such steps are taken before the OSCAT data point at 20ps is reached from the initial 0ps temporal delay; one ASOPS-type step per pulse propagating the delay line. In other words, the number of points is equal to the pulse index a of the PDL of length l. If we now rename the variables such that $f_1 = f_{min}$ and $f_2 = f_{max}$, (the minimum

and maximum repetition rates considered in the ASOPS-type phase) the step-size may then be given by

$$\delta t = \frac{\Delta f}{f_{min} f_{max}} \tag{41}$$

which is the same relationship for step-size given by true ASOPS [144]. By extension, since the number of points is equal to the pulse index *a*, it follows that the total scan range is the product of the step-size and pulse index,

$$\Delta t = a \cdot \delta t = a \cdot \frac{\Delta f}{f_{min} f_{max}} \tag{42}$$

As expected this is simply a rearrangement of the main OSCAT expression (40) and was previously expressed as an approximation in Chapter 4, surrounding expression (31). Substituting the values used to simulate Figure 5-5, we find that *4* pulses at 5ps step-size indeed amount to 20ps total scan range. In this example, a pulse index of 20 would give rise to a scan range Δt equivalent to the entire roundtrip period of $1/f_{rep} = 100$ps. This corresponds to a PDL length of just 0.6m, assuming 500MHz total repetition rate tunability. In such a system, only two values of repetition rate would be required; f_{min} and f_{max} where $\Delta f = f_{max} - f_{min}$. As such, if instead of ramping linearly from f_{min} to f_{max} (as in the case of an OSCAT scan), we could instantaneously switch between the values, and this would allow an ASOPS-type scan to occur. For example, in the case of Slow-OSBERT scans (discussed in Chapter 3) where the reverse bias corresponding to a repetition rate is gradually increased through the mode-locking region, we would instead simply switch from the lowest to the highest voltage, omitting any need to access any intermediate repetition rates. In the current example, due to the catch-up period in a 0.6m long PDL (equivalent to a pulse index of 20), the scan will proceed according to Figure 5-6.

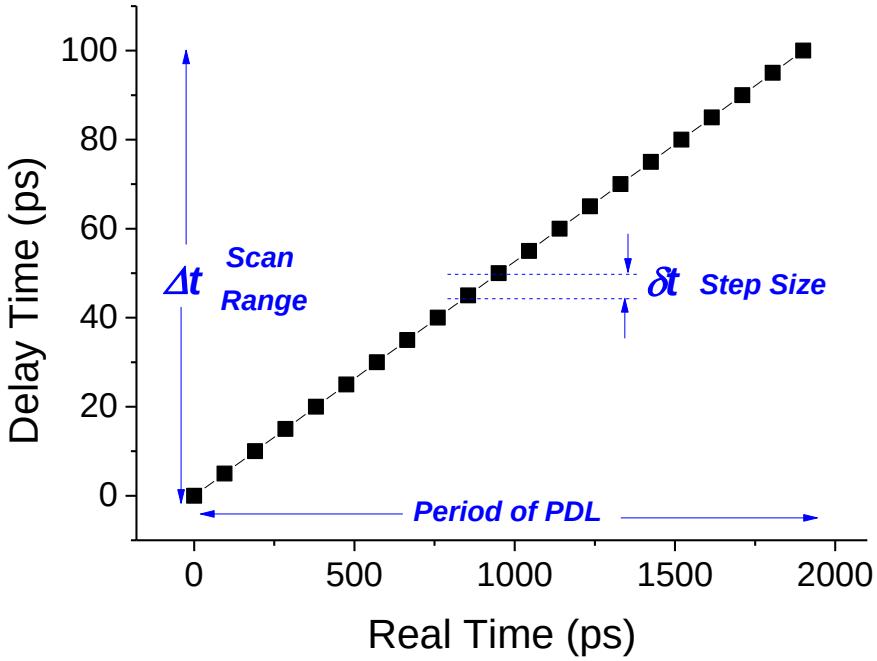

Figure 5-6 – If the intermediate repetition rate steps used for a complete OSCAT scan are omitted, and only the maximum and minimum value selected, an ASOPS type scan will occur as one pulse train will propagate with the minimum repetition rate the other will propagate with the maximum repetition rate.

In the case of ASOPS, the scan range is always the entire roundtrip period associated with the laser's repetition rate [40], $\Delta t = 1/f_{rep}$. For SLECOPS, the scan range, as shown, is still completely determined by the parameters comprising the OSCAT equation, expression (40), where here we have adopted the special case of variables leading to a scan range equal to the roundtrip period in order to take advantage of the maximum possible range. In this case, if we were to shorten the PDL length, the scan range would be reduced, alongside the number of acquisition points, whilst the step-size would remain constant. The real-time acquisition, whose duration as shown is proportional to the length of the PDL, would also reduce. If the repetition rate tunability were reduced, the scan range would also reduce (as in the case of the reduced PDL). The step-size would also reduce giving rise to higher resolution according to expression (41), however the real-time acquisition would remain constant, as this is still determined entirely by the length of PDL. Also we note that a reduction in step-size would also occur at lower repetition rates, though the roundtrip period would increase.

In the example outlined above, the full scan occurs over a real-time period of 2000ps, which at 2ns could potentially be equivalent to 500MHz scan rate, however the scan only propagates once through the 0.6m PDL and then terminates as soon as both arms exhibit the same repetition rate, see Figure 5-7, where only figure (d) represents an ASOPS-type scan.

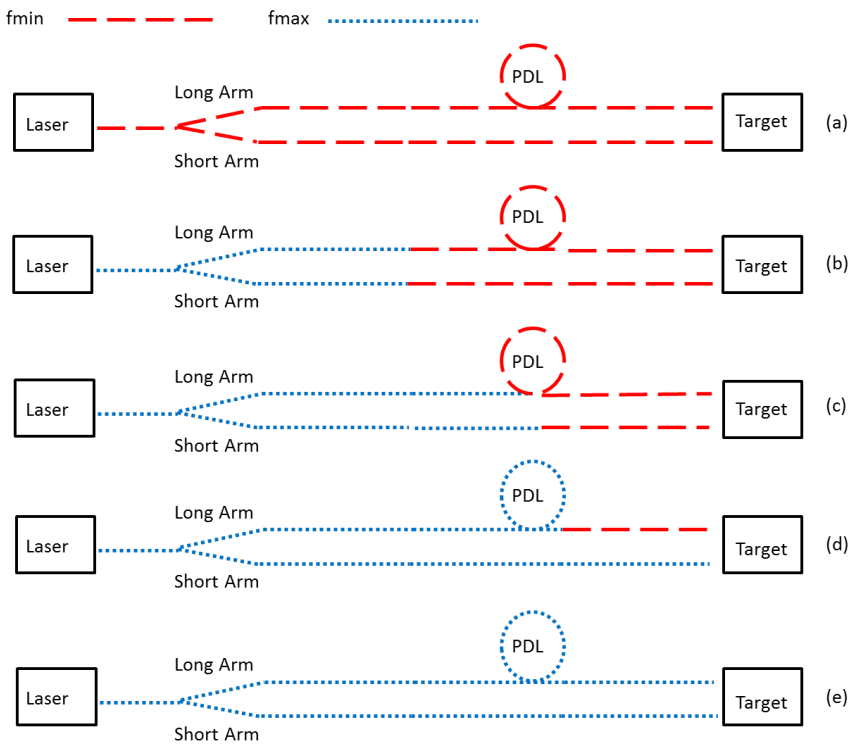

Figure 5-7 – a) The original minimum repetition rate is propagating each arm. b-c) The beam with the maximum repetition rate has been set and begins propagating both arms. d) Whilst the beam with maximum repetition rate has reached the target via the short arm, it is still delayed via the long arm. Consequently both repetition rates may be detected in an ASOPS type fashion. e) With the maximum repetition rate having caught up to that of the short arm at the target via the PDL, the scan is terminated.

In order to scan repetitively, we must be able to alternate the minimum and maximum repetition rates at the source in a manner which will allow two different repetition rates to be present periodically at the target position, for example, by using a waveform generator (WFG) to modulate the repetition rate as a square wave between minimum and maximum values. In a laser cavity with bulk optics this could be done, as in the OSCAT or ECOPS techniques, by simply moving the intra-cavity mirrors between two positions. In the case of MLLDs, this could be accomplished as in the OSBERT method, by driving the reverse bias applied to the absorber section as a square wave, see Figure 5-8.

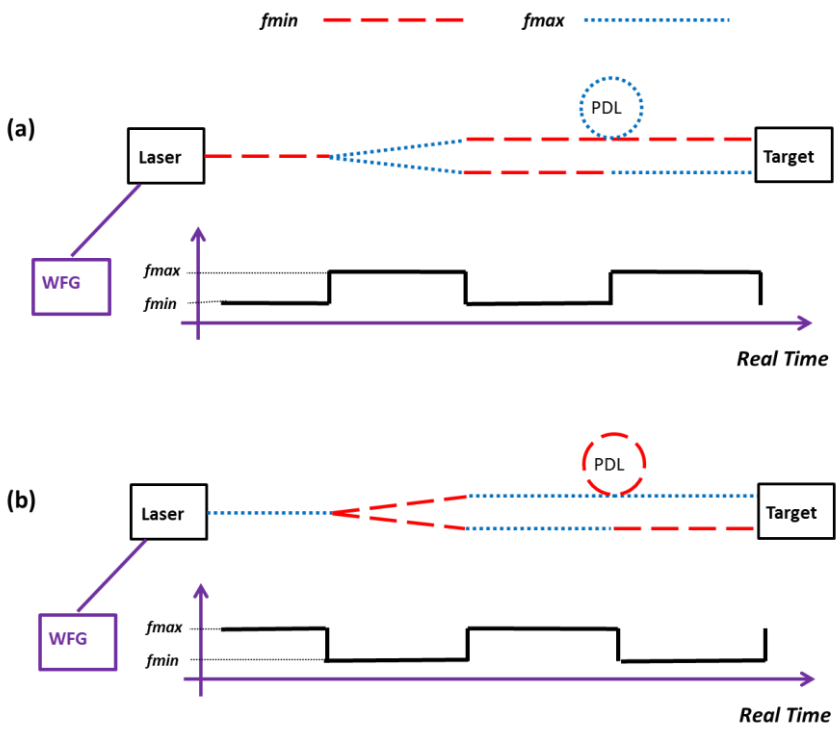

Figure 5-8 – a) The repetition rate of the laser is modulated as a square wave via a WFG, where the PDL of the long arm causes both maximum and minimum repetition rates to be present at the target position. b) Half a period later, as the square wave propagates, the repetition rates constantly swap whether they are present in the long or short arm, a similar principle as that shown in ECOPS.

In particular, if the period of the square wave T_{sq} is exactly double that of the passive temporal delay T_{PDL} introduced by the PDL of length *l* where $T_{PDL} = l/c$, the repetition rates will constantly switch with respect to each other in an ECOPS-type scan, where

$$T_{sq} = 2T_{PDL} \tag{43}$$

As previously discussed, the usable scan rate is determined entirely by the length of the PDL used. If this length does not satisfy expression (43), if too short then dead-time will occur within the period of the square wave, see Figure 5-9. Ultimately, the picture of modulating the square wave at a scan rate whose period is proportional to double the temporal delay of the PDL is in essence the same as that of ECOPS – the major advantage being that only one laser is used, hence, Single Laser Electronically Optical Sampling is conceived.

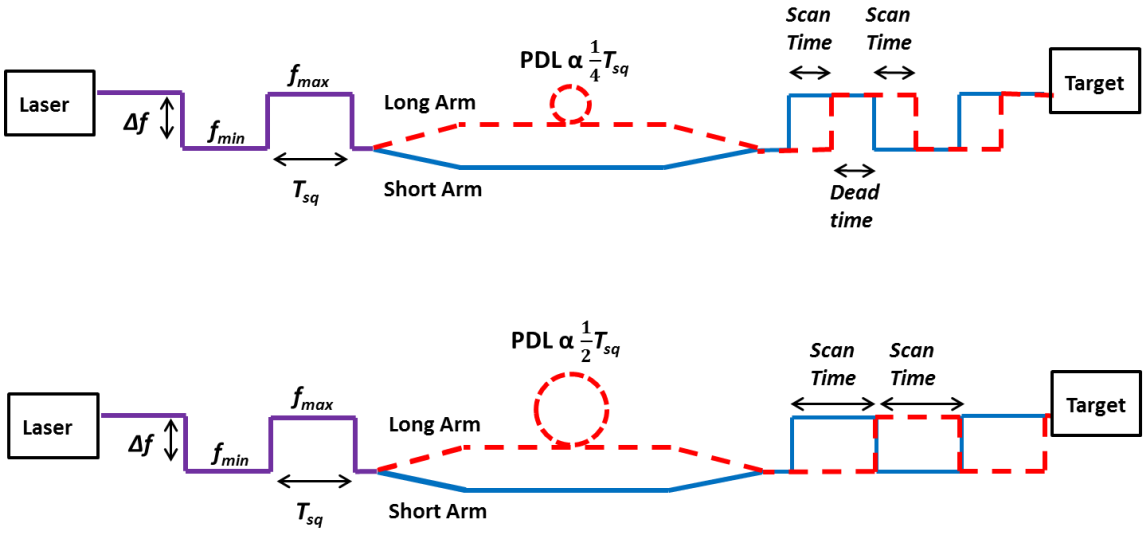

Figure 5-9 – A square wave modulation of the repetition rate at the source laser gives rise to a phase difference in the square wave brought on by the imbalance between the two arms. Above, a PDL whose temporal delay is shorter than the square wave's half-period will lead to combinations of scanning and dead time. Below, a PDL whose temporal delay is equal to that of the square wave's half-period will lead to alternating ECOPS-type scanning, using only one laser.

It should be noted, however, that it is not essential to satisfy expression (43). The scan will still propagate within the period of the square wave, depending on the length of PDL used, and provided the ratio of dead-time is known, the useable scan period may still be utilised (as per the upper diagram in Figure 5-9. It is, of course, advantageous to reduce the period of the square wave as far as is practically possible to limit the dead time and increase the actual scan rate. That is to say, whilst the outright scan rate by definition is the inverse of the temporal delay of the PDL $r_{PDL} = \frac{1}{T_{PDL}}$ the frequency of the square wave used to modulate the repetition rate is given by the inverse of the square wave period, $r_{sq} = \frac{1}{T_{sq}}$. In the event that expression (43) is satisfied, we may unambiguously assert the scan rate of SLECOPS is the inverse of the passive real-time delay introduced by the PDL, which accommodates a-1 pulses of roundtrip period $\boldsymbol{T_{rep}}$, such that

$$r_{SLECOPS} = \frac{1}{T_{PDL}} = \frac{1}{(a-1)\cdot T} = \frac{f_{rep}}{(a-1)} \tag{44}$$

Note, the factor (a - *1*) is simply representative of the fact that the roundtrip periods occur in-between pulses, and there will always be one fewer roundtrip period than pulses. For comparison, the ASOPS scan rate is given by the inverse of the sample interval $1/\Delta f$ [15] which is the difference in the repetition rate of each laser, such that

$$r_{ASOPS} = \Delta f \tag{45}$$

And as noted, the scan range of the ASOPS system is simply one full roundtrip period T_{rep}; the inverse of the repetition rate, $\frac{1}{f_{rep}} = T_{rep}$, whereas the scan range of SLECOPS is still defined by the fundamental OSCAT formula, expression (40).

The step-size of SLECOPS has already been defined by expression (41) as the same as the step-size of ASOPS, and the number of points in an ASOPS scan N_{ASOPS} is given by

$$N_{ASOPS} = \frac{f_{min}}{\Delta f} = \frac{1}{T} \cdot \frac{1}{\Delta f} \tag{46}$$

Whilst the number of points of SLECOPS has been defined as equal to the pulse index *a*, (essentially by the length of PDL) such that

$$N_{SLECOPS} = a = \frac{ln f_{min}}{c} \tag{47}$$

In fact it is possible to unite the mathematical description of single laser SLECOPS technique with the double laser ASOPS technique based on this information. For example, if we simply set the number of points of the SLECOPS system equal to one (essentially one delay step), this is the same as setting *a = 1* to the full scan range in expression (40), such that

$$\Delta t = 1\left(\frac{1}{f} - \frac{1}{f + \Delta f}\right) = \frac{1}{f_{max}} - \frac{1}{f_{min}} = \frac{f_{max} - f_{min}}{f_{max} \cdot f_{min}} = \frac{\Delta f}{f_{max} \cdot f_{min}} \tag{48}$$

This is in perfect agreement with the simulated model and expressions (41) and (42). Similarly, if the desired scan range of SLECOPS is the full roundtrip period, the scan rate of the ASOPS and OSCAT systems become comparable as SLECOPS. If we set the special case where the required scan range Δt of SLECOPS (defined by expression (40)) to $1/f_{rep}$ or equivalently T_{rep} (where as in ASOPS f_{rep} in this case is equal to f_{min}) we find

$$\Delta t = a\left(\frac{1}{f_{rep}} - \frac{1}{f_{rep} + \Delta f}\right) = \frac{1}{f_{rep}} = T_{rep} \tag{49}$$

Rearranging for the substitution where $\frac{1}{f_{rep}} = T_{rep}$ we then find

$$T_{rep} = aT_{rep} - \frac{a}{\frac{1}{T} + \Delta f} \tag{50}$$

The following steps of rearranging and substitution follow in turn

$$T_{rep} - aT_{rep} = T_{rep}(1 - a) = -\frac{a}{\frac{1}{T_{rep}} + \Delta f} \tag{51}$$

$$T_{rep} = -\frac{a}{\frac{1}{T_{rep}} + \Delta f}\frac{1}{(1 - a)} \tag{52}$$

$$T_{rep}\left(\frac{1}{T_{rep}} + \Delta f\right) = -\frac{a}{(1 - a)} \tag{53}$$

$$1 + T_{rep}\Delta f = -\frac{a}{(1 - a)} \tag{54}$$

$$T_{rep}\Delta f = -\frac{a}{(1 - a)} - 1 = \frac{1}{(a - 1)} \tag{55}$$

Finally giving rise to the final expression

$$\Delta f = r_{ASOPS} = \frac{1}{(a - 1)T_{rep}} = r_{SLECOPS} \tag{56}$$

As can be seen, expression (56) has successfully united SLECOPS expression (44) and ASOPS expression (45) for scan rate, but *only* in the special case that the required scan range is equal to the roundtrip period. Since this has been derived via the same special

case of OSCAT, this proves mathematically that the two optical sampling techniques are not entirely mutually exclusive, and are built around similar premises.

A brief summary of the salient points of how both *l* and Δf impact various SLECOPS scanning parameters, including the number of points, the step-size, the scan range and the scan rate is tabulated in Figure 5-10 for clarity and for future reference.

	Effect on SLECOPS Scanning Parameter (relevant expression)			
Parameter To Increase	***Number of Pulses* (47)** $a = \frac{lnf_{rep}}{c}$	***Step-Size* (41)** $\frac{\Delta f}{f_{min} f_{max}}$	***Scan Range* (42)** $a \cdot \delta t$	***Scan Rate* † (44)** $\frac{f_{rep}}{(a-1)}$
PDL length ***l***	Increases	Unchanged	Increases	Decreases
Repetition Rate tunability $\boldsymbol{\Delta f}$	Unchanged	Decreases	Increases	Unchanged

Figure 5-10 – For a given fundamental pulse repetition rate, how will increasing the PDL length or the repetition rate tunability affect the number of pulses, the temporal step-size, the scan range and scan rate of a SLECOPS scan.

† Note as discussed, for the case of scan rate we assume expression (43) is satisfied such that $T_{sq} = 2T_{PDL}$, and so of course the square wave period will be selected according to the desired PDL length, though this condition does not have to be met. One could keep the preferred PDL length but perhaps be limited in having to use a far slower square wave, in which case the scan may be realised but at significantly lower scan rates due to the extended dead times. The square wave could also be significantly faster than the requirement, meaning that the available legitimate scan time is reduced (which of course may be an advantage for shorter events of interest in pump probe spectroscopy for example). Therefore it is reasonable to also say that the scan rate is ultimately decided by the frequency of the square wave chosen for the scan, in which case the PDL length has no effect on the scan rate, but as is described above, will impact the number of pulses present during the scan.

5.3. SLECOPS Simulation

In order to visualise how the variables which make up a SLECOPS scan may result in optical sampling, a SLECOPS cross-correlation simulation was developed. The simulation firstly creates an ultrashort pulse which is stationary with respect to a second pulse which may be temporally delayed such that the two may cross-correlate. The stationary pulse represents that which has exited the short arm, whilst the second represents that which has traversed the PDL of the longer arm, and their resultant optical cross-correlation is simulated to exhibit the properties of a SLECOPS type scan.

From the outset it is important to note the limitations of such a simulation, which is presented as a illustrative demonstration of the described theory. Firstly, the simulation does not directly take into account the difference between short arm and long arm pulse pairs, such as dispersion or differences in laser's output characteristics related to the repetition rate difference. Secondly, the square wave nature of SLECOPS is not included, simply the result of a single instant switch from minimum to maximum repetition rates in the context of an imbalanced interferometer. Therefore, in order to simplify the simulation we may effectively assume the square wave period is selected such that any dead time is eliminated, and expression (43) is satisfied.

As in the case of the simulator described previously in chapter 4 to demonstrate the erosion of fringes, the electric field *E* of both the stationary and translatable pulse over time *t* are described as follows;

$$E(t) = \frac{1}{2}\sqrt{I(t)}e^{i\omega_0 t - \phi(t)} \tag{57}$$

Where and $\phi(t)$ is the phase which contributes to chirp, and is set to zero for the purposes of this simulation, and $\omega_0 = 2\pi f$ is the carrier frequency, such that the wavelength of the pulse $\lambda = c/f$ where *c* is the speed of light in a vacuum. *I(t)* represents the time-dependent intensity, which we adopt as a Gaussian such that

$$I(t) = y_0 + \frac{A}{w\sqrt{\pi/2}}e^{-2\frac{(t-t_c)^2}{w^2}} \tag{58}$$

Where y_0 and t_c represent x-axis and y-axis offsets which are both set to zero throughout the simulation, and A represents an amplitude scale which is set to one throughout the simulation. Finally, *w* represents the width of the function, which is related to the pulse-width such that it's $FWHM = w\sqrt{\ln 4}$. If these expressions are combined, we can fully mathematically describe a pulse for use in the simulation, which is that of a first order linear interferometric cross-correlation as described in Chapter 3. As in previous cases, the autocorrelation function is given by

$$A^{(2)}(\tau) = \int_{-\infty}^{\infty} E(t)E(\tau - t)dt \tag{59}$$

For the purposes of demonstrating how the PDL length and repetition rate tunability each affect the characteristics of a SLECOPS scan, two main cross-correlation simulations are presented. In both cases the pulse characteristics were set to be similar to that of the narrow-ridge device discussed in the previous two chapters. Parameters common to both simulation 1 and simulation 2 are tabulated in Figure 5-11.

Parameter	Value
Original Pulse Wavelength	1260nm
Original Pulse Duration	10.0ps
Original Pulse Resolution	0.2fs
Repetition Rate	5.07GHz
PDL refractive index	1.46

Figure 5-11 – Table summarising the constant parameters common to both SLECOPS simulations.

Whilst the original pulse of the short arm is simulated to remain stationary at a temporal delay position of zero, the translatable pulse of the long arm is set to an initial position calculated as half the available scan range away from the zero-position, such that one full scan would translate the second pulse through the entire available scan range. The original pulse is simulated such as to show its 200 attosecond resolution required for the simulation of 1260nm wavelength, see Figure 5-12.

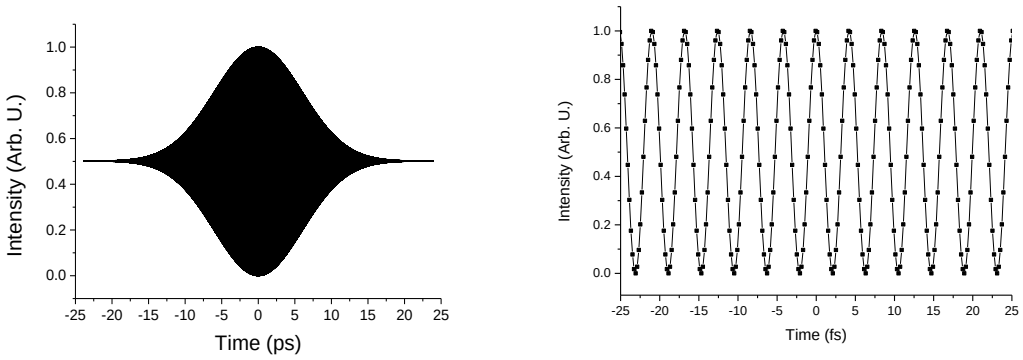

Figure 5-12 – Left, a simulation of the original pulse used for the cross-correlation simulation, and right, the central 50fs show the 200as resolution in the fringe pattern.

Additionally we may take a Fast Fourier Transform of the simulated pulse in order to check the spectral components in the fringe pattern are of a frequency corresponding to the wavelength of the light, see Figure 5-13.

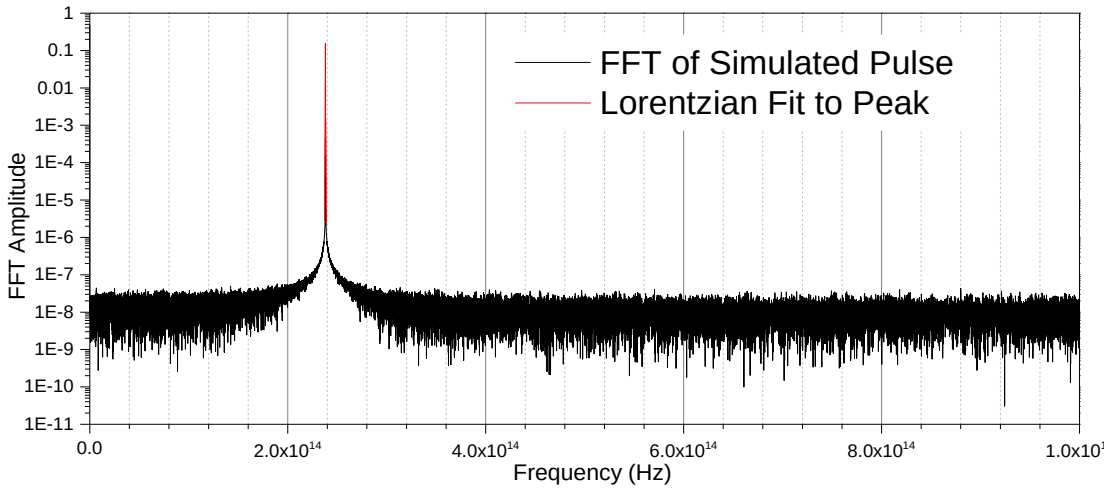

Figure 5-13 – FFT of the original simulated pulse with Lorentzian fit to its peak.

When fit with a Lorentzian, we find the RF peak is centred at 2.38×10^{14} Hz, which indeed corresponds to a wavelength of 1260.5nm. The slight deviation from the simulated 1260.0nm is likely a combination of the goodness of fit of the Lorentzian, and the resolution used to create the original pulse trace.

Before applying the SLECOPS method to the cross-correlation simulator, it is firstly set up such as to simulate a trace brought on by a standard mechanical translation stage. The simulator was set to cross-correlate the original pulse described above at a step-size of

1.0μm (or 3.33fs) - a resolution the Thorlabs translation stage used in the previous chapters was capable of, see Figure 5-14.

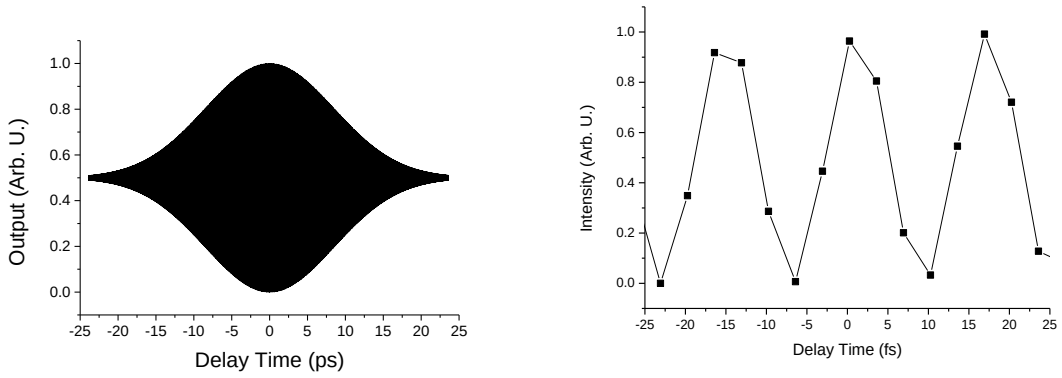

Figure 5-14 - Left, a simulated mechanical stage cross-correlation of the original pulse taken with a step-size of 3.33fs, and right, the central 50fs show the equivalent resolution in the fringe pattern.

As can be seen, and as is generally the case in reality, the cross-correlation has been under-sampled in that the original pulse fringe pattern has not been created, and rather a Nyquist effect has led to the appearance of a misleading fringe pattern. This is because the 3.33fs resolution is over 10x the original pulse resolution. This translation stage version may now be contrasted with those of the SLECOPS method under similar conditions.

Although the original pulses are created with a resolution of 0.2fs, the cross-correlation step-size (among other characteristics) is determined by the SLECOPS parameters. In Simulation 1, the difference in repetition rate is $\Delta f = 10MHz$ and the PDL has length $l = 25m$. As discussed, the number of steps is governed by the pulse index $a = 617$ as in expression (47), the scan range $\Delta t = 240ps$ as in expression (42) and the step-size $\delta t = 389fs$ as in expression (41), see Figure 5-15. Since the SLECOPS scan progressed with a step-size which was almost 2000x that of the original pulse, and over 100x that of the mechanical delay stage cross-correlation, the significantly lower resolution of the cross-correlation is expected.

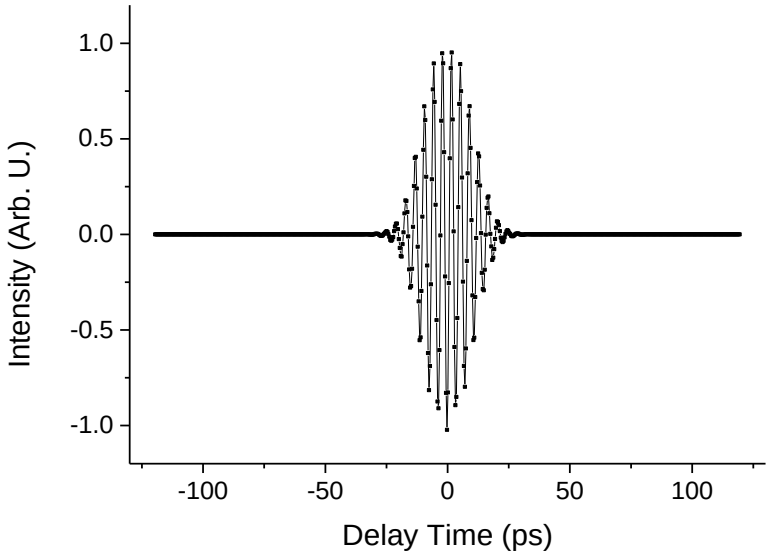

Figure 5-15 –The resultant SLECOPS cross-correlation for a PDL length of 25m and a repetition rate tunability of 10MHz.

The scan rate, however, is the most important aspect of the SLECOPS scan. Its inverse, the sample interval, was 122ns, according to expression (44), which is proportional to the 25m PDL length used, see Figure 5-16.

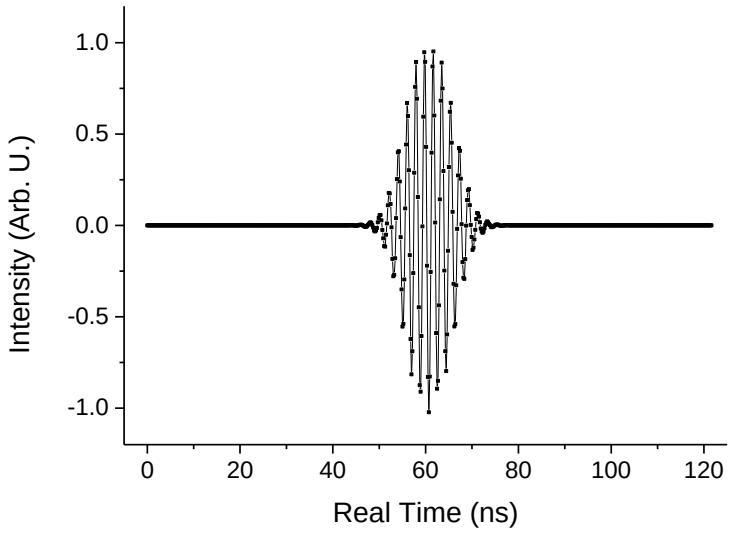

Figure 5-16 – The cross-correlation acquired under the parameters of simulation 1 plotted instead for the real 122ns acquisition time.

This would require a square wave modulation frequency of 8.2MHz to avoid dead time. As discussed, it is possible to control the resolution by varying the repetition rate tunability, however this will also alter the scan range. We can therefore make alterations to both the PDL length and the repetition rate tunability to keep the same scan range, whilst

increasing the resolution. We do so by extending the PDL length by five times to 125m, whilst also reducing the repetition rate tunability by five times to 2MHz, see Figure 5-17.

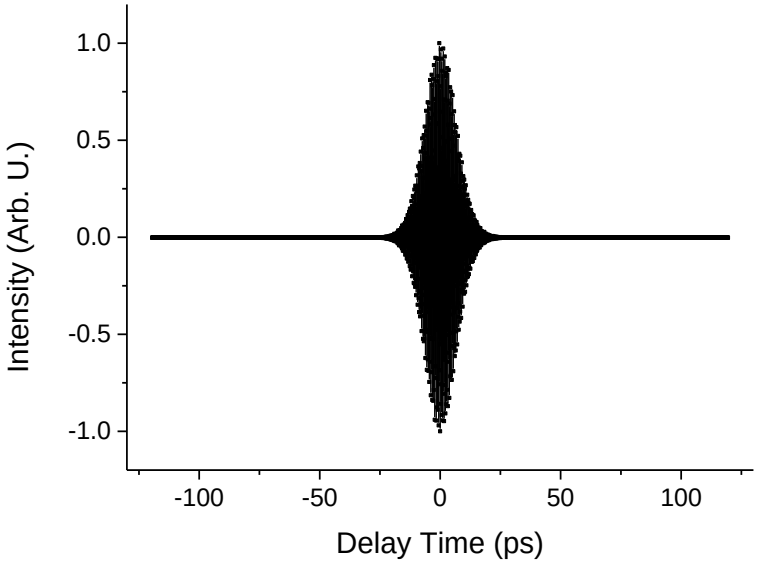

Figure 5-17 – The resultant SLECOPS cross-correlation for a PDL length of 125m and a repetition rate tunability of 2MHz

This has had the effect of increasing the number of points to 3084 and decreasing the step-size to 78fs, whilst the scan range, as can be seen, has remained the same as in simulation 1. The caveat, of course, is that such a scan will take longer to acquire due to the significantly longer PDL length, see Figure 5-18.

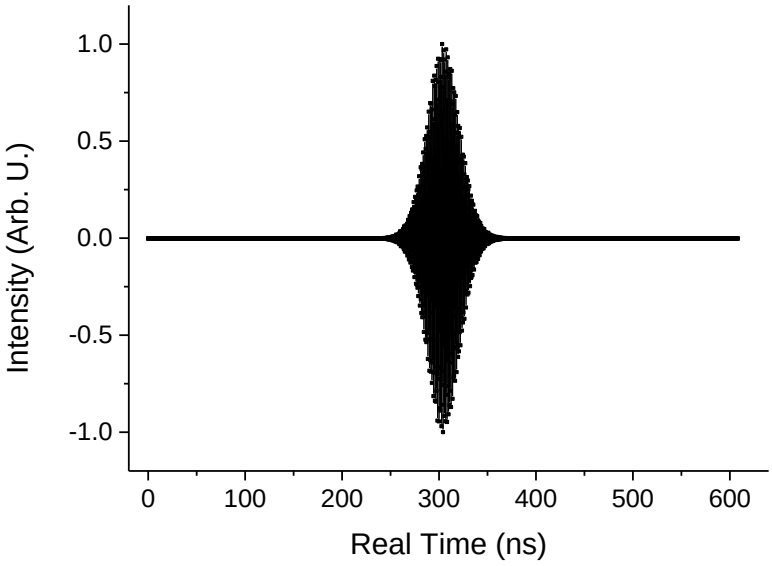

Figure 5-18 - The cross-correlation acquired under the parameters of simulation 2 plotted instead for the real 608ns acquisition time.

Such a scan, if repeated via square wave, would require modulation at a frequency of 1.6MHz to avoid dead time. The input parameters and output parameters of both simulations are summarised and tabulated, see Figure 5-19.

	Simulation 1	**Simulation 2**
Parameter	**Input**	
PDL Length ***l***	25m	125m
Rep Rate Tunability ***Δf***	10MHz	2MHz
Parameter	**Output**	
Number of Points N_{pt}	617	3084
Step-Size δt	389fs	78fs
Scan Range Δt	240ps	240ps
Sample Interval T_{PDL}	122ns	608ns
Equivalent Scan Rate $1/T_{PDL}$	8.2MHz	1.6MHz

Figure 5-19 - Table summarising how both simulations were conducted in terms of the difference in input parameters, and the resultant output parameters of each.

These results may then be retrospectively contrasted with the general predictions associated with SLECOPS in Figure 5-10. Clearly there are multiple trade-offs between scan range, scan resolution and scan rate brought about by the combinations of PDL length and repetition rate tunability. If the experiment in question was designed to measure significantly shorter events, the user would need to take these conditions into account.

5.4. Practical Considerations on SLECOPS experimental implementation

In order to give a practical indication of the future potential of the SLECOPS technique, an example is drawn from the work of previous chapters within this project. Whilst the simulation of the previous section would provide potential users with insight into which conditions to drive their SLECOPS scan, this section discusses the reality of doing so.

From the previous chapter, we recall that the narrow-ridge device achieved its maximum scan range of over one pulse cavity roundtrip period under the following conditions: a repetition rate $f_{rep} = 5.07GHz$, a repetition rate tunability $\Delta f = 10MHz$, and a PDL of length $l = 25m$ and refractive index $n = 1.46$. Using expression (40) this gave rise to a

total scan range of $\Delta t = 239.5ps$, capable of demonstrating two cross-correlations in one scan due to the ~200ps roundtrip period.

Applying this information to the SLECOPS technique, we may calculate the operational parameters. Firstly, the number of points is found to be $N_{SLECOPS} = a = 617$ using expression (47). Next, the step-size is calculated as $\delta t = 390fs$ using expression (41). Finally, according to (44) the scan rate associated with such a scan is $r_{SLECOPS} = 8.26MHz$, corresponding to a real-time sample interval equivalent to $T_{PDL} = 121ns$.

If we take the example of a 1MHz square wave, this means that the square repetition rate modulation in the long arm of such a system will be delayed by 121ns with respect to the square repetition rate modulation in the short arm, see Figure 5-20.

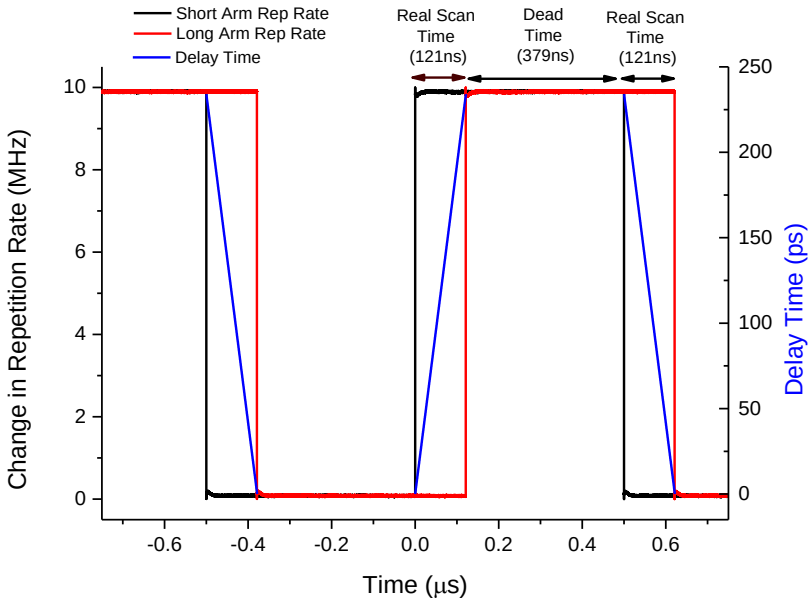

Figure 5-20 – Diagram showing a square wave change in repetition rate of 10MHz. The PDL has caused a phase shift between the repetition rates found in the long and short arms, during which scanning occurs, and outside of which dead time occurs.

As can be seen, a 1MHz square wave corresponds to a half period of $\frac{T_{sq}}{2} = 500ns$ leading to a dead-time of 379ns where no scanning can occur. There are a number of methods in which this dead-time can be avoided.

Firstly, and most obviously, the square wave frequency could be increased to satisfy expression (43), where the square wave period $T_{sq} = 2T_{PDL} = 242ns$, corresponding to a

square wave modulation of 4.13MHz. This would maximise the scan rate by reducing dead-time, whilst having no effect on other parameters such as scan range, step-size or the number of points contributing to the scan, see Figure 5-21.

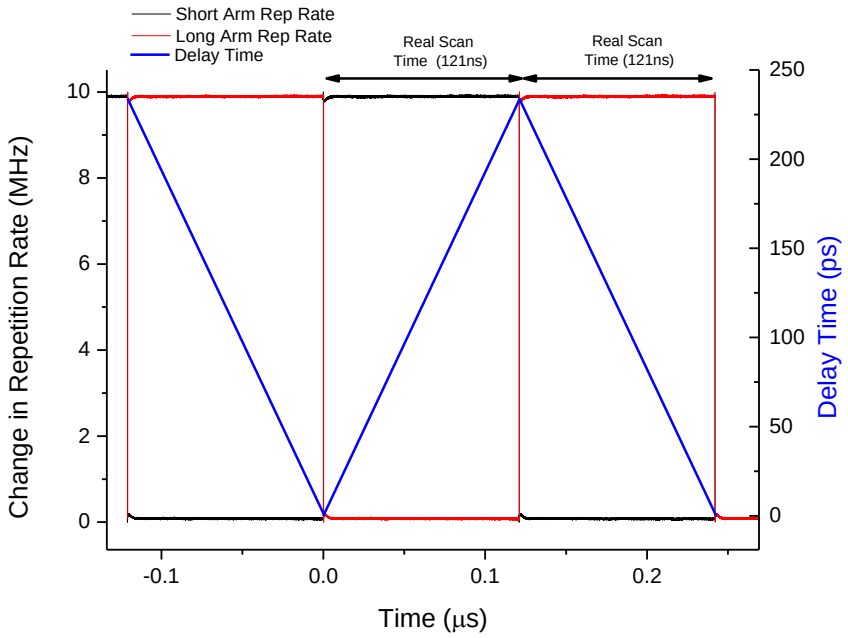

Figure 5-21 – Diagram showing how a sufficiently short square wave period reduces the dead-time of the SLECOPS scan, ensuring maximum and minimum repetition rates are always alternately present at the detector position, as the PDL has phase shifted the square waves in each arm by one half period.

Another method of reducing dead-time is to increase the length of PDL such that it increases from the 121ns calculated to match that of the 500ns half-period of the square wave. This method comes with a number of pros and cons. In terms of cons, the fibre would have to be extended to a length of around 100m in order to achieve this, quadrupling the length which (for the example of the narrow-ridge MLLD) in chapter 4 had already begun to show signs of quality reduction, timing jitter and dispersion. Furthermore, according to expression (40), lengthening the fibre will of course lengthen the scan range. In this case, however, the maximum usable scan range has already been exceeded - the roundtrip period. Therefore, as much as this would reduce unusable dead time and replace it with pseudo-usable (largely unecessary) scan time, this would give multiple full roundtrip period scans in one modulation square wave, and each successive scan will be more susceptible to the described adverse effects than the last.

This unnecessary scan time may be overcome by simply reducing the repetition rate tunability by a factor of 4, such that $\Delta f = 2.5MHz$; in other words increasing the PDL length by four times whilst reducing the repetition rate tunability by four times. This leads to a number of advantages. Although the adverse effects of a longer PDL will persist, the step-size will reduce by a factor of 4, giving $\delta t = 97.5fs$ and therefore increasing resolution. Considering, for example, the linear cross-correlations acquired for OSBERT scans in the previous chapter had durations of around 10ps, this resolution is significantly more appealing than the previous step-size of 390fs.

Additionally, if we consider an MLLD as the source laser, in terms of a square wave bias to the absorber section, if a lower *Δf* is used, this represents using a lower range of reverse bias characteristics within the MLR (Mode-Locking Region), meaning the pulse and spectral characteristics associated with the maximum and minimum repetition rate will be more similar in value than a wider *Δf.* This is in fact another major advantage of SLECOPS over OSBERT; whilst OSBERT cross-correlates one characteristic through another in step-wise fashion throughout the MLR upon each small increment of the reverse bias, SLECOPS allows only two pulse characteristics to interfere at once, eliminating all the wide ranges in pulse duration, peak and average powers and optical spectra used to acquire each successive point. In reality, we have seen degradations to a sine wave OSBERT modulation at 1MHz, and considering the additional frequency components required to construct a square wave, it is likely that these would distort, and so lower scan rates (and potentially longer PDL lengths) may have to be used.

As an additional example from the literature, in [62] the PDL length *l* used in the OSCAT setup is 2.02km equivalent free-space which has a temporal delay T_{PDL} of 6.73μs, and a pulse index of a = 1682, equivalent to the number of data points. Performing a SLECOPS scan with such a long PDL according to expression (44) would require a square wave modulation whose frequency was $1/T_{sq} = 74.2$kHz in order to satisfy expression (43). The maximum useable scan range *Δt* of the $f_{rep} = 250$MHz laser used is the roundtrip period of $T = 1/f_{rep}$= 4ns. According to expression (40) this would require a repetition rate tunability *Δf* of only 148.6kHz to achieve, giving rise to a step-size of δt = 2.37ps. One of the longest PDL lengths successfully used in an OSCAT setup has been 10km [145], which

with a temporal delay of 33µs would require a square wave modulation of 15kHz, giving rise to a scan rate of 15kHz.

In terms of intra-cavity repetition rate tuning using a mechanical piezo electric actuator, frequency bandwidths of a few kilohertz to a few tens of kilohertz are common, for which PDL lengths would likely need to be in the order of several kilometres. As this technology develops, bandwidths of hundreds of kHz are being realised [58, 146], and could significantly reduce the length of PDL required.

5.5. Conclusions

In conclusion, the concept of a second 'virtual' laser constructed from a length of PDL and square wave repetition rate modulation originating from the physical source laser was discussed. Groundwork theory was derived which provides a mathematical connection between the ASOPS, ECOPS and OSCAT methods, culminating in a new theoretical model for a unique optical sampling technique: SLECOPS.

The potential for increased scan rates among other advantages as a result of the technique are suggested, as well as the limitations of practically implementing such a system. In particular, in the case of an electrically modulated MLLD-based SLECOPS scanner, applying a high-speed square wave modulation may be possible but the results are potentially highly dependent upon the dynamics of the laser itself. In the case of commercially available lasers with repetition rates which are tunable using mirrors mounted on piezo electric actuators, there may be a limit on scan rates which would require long PDL lengths. However, considering timing jitter, dispersion, and the resultant practically accessible scan resolutions, the choice of PDL length and repetition rate tunability is clearly non-trivial.

Interestingly it may be possible in the future to take advantage of the 'virtual laser' premise to separate other output characteristics from one laser and combine them in the alternating fashion described by SLECOPS. For example in the case of MLLDs whose optical spectra may be varied by varying the bias conditions [6, 147] (demonstrated in chapter 2). If instead of using the PDL to delay a repetition rate, either using a continuous wave or mode-locked output, two wavelengths could be separated by extremes of biasing

conditions (of either the gain or the absorber sections) and directed towards the target, see Figure 5-22

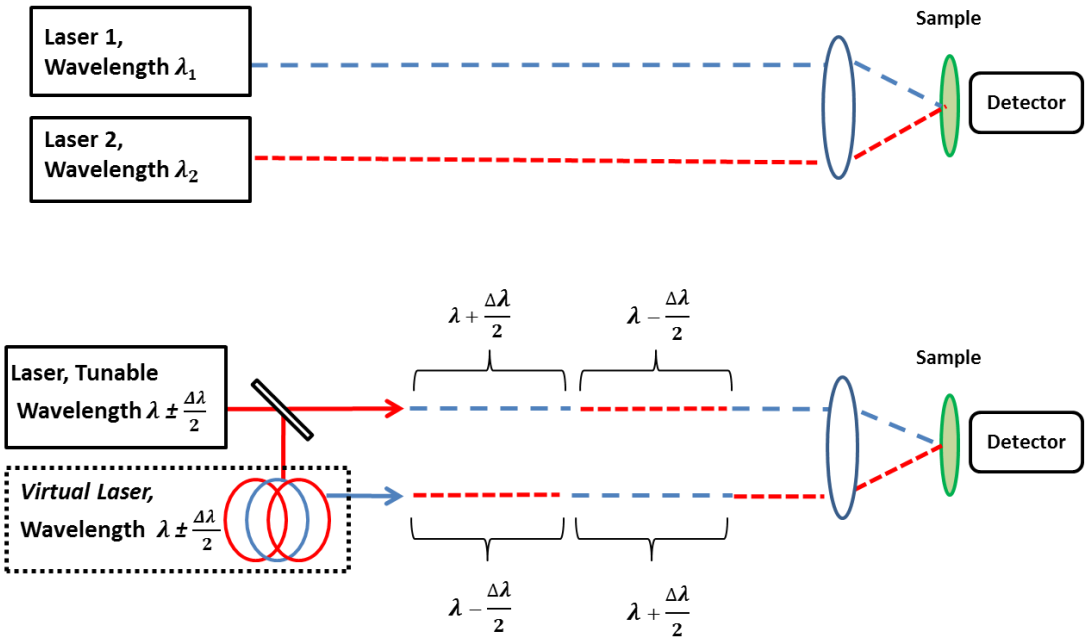

Figure 5-22 – Diagram which represents a modification of SLECOPS which may allow any tunable characteristic, such as the output wavelength, to be alternately combined from one laser into a detector.

With sufficient wavelength tunability, this technique could be deployable in two-colour optical sampling techniques [47], or simply as a means to filter out the pump beam from the detection in pump-probe spectroscopy by utilising finely tuned spectral filters which allow only the probe beam to be detected.

Ultimately, SLECOPS theoretically represents a possibility for typically two-laser optical sampling systems such as ASOPS and ECOPS to be performed using only one laser at potentially far greater scan rates provided the desired scan range is less than the laser's roundtrip period. It also has the potential to improve upon the OSBERT technique because only two pulse characteristics (two reverse bias values within the MLR) are ever used in one scan, rather than a wide range. In addition, SLECOPS offers highly customisable scans, where the optimum combination of PDL length and repetition rate tunability allows for simple and effective control of the scan range, scan rate and scan resolution, whilst reducing dead-time.

For clarity and quick reference the potential advantages and disadvantages of SLECOPS over contending optical sampling systems is summarised, see Figure 5-23.

Comparison Technique	SLECOPS Potential Advantages	SLECOPS Potential Disadvantages
ASOPS	1 Laser over 2 Reduced Dead-Time Faster Scan Rates	Long PDL leading to greater jitter Long PDL leading to dispersion
ECOPS	1 Laser over 2 Faster Scan Rates	
OSCAT	Faster Scan Rates	May require even longer PDLs (scan rate, range and resolution dependent)
OSBERT	Only two characteristics interfered when using MLLDs Applicable to any tunable laser	

Figure 5-23 – Summary of the potential advantages and disadvantages of SLECOPS over contending optical sampling techniques.

As is anticipated, due to SLECOPS essentially being a hybrid technique of ASOPS and OSCAT type techniques, its disadvantages over ASOPS and ECOPS, and over OSCAT and OSBERT respectively are identical.

6. SUMMARY AND FUTURE OUTLOOK

In this chapter, the final conclusions on the project are drawn and discussed, whilst suggestions for future development of the work are provided. The conclusions and discussions here may be contrasted with the research goals outlined in Chapter 1.

6.1. Project Summary & Conclusions

In this project, novel high speed optical ampling techniques were developed using two-section quantum dot passively mode-locked laser diodes.

As outlined in the introduction, a number of techniques exist which compete for increasing scan rates and optimum scan ranges. Whilst OSCAT and ECOPS are ultimately limited by mechanical parts, both ASOPS and ECOPS were limited by the fact they require two (often expensive) pulsed lasers within a complicated setup. The combination of pros and cons between each technique therefore provided the ultimate motivation for this project; to develop a technique which required only one laser, in particular a compact and inexpensive MLLD. Additionally, this technique would require absolutely no moving parts to function within an optical sampling context. And finally, on top of these improvements, the newly developed technique would be capable of competing with the others in terms of scan rate.

Firstly the OSBERT method (Optical Sampling By Electronic Repetition-rate Tuning) has been demonstrated, and to my knowledge is the first demonstration of a single, quantum dot, passively mode-locked, two-section semiconductor laser diode in such an optical sampling configuration, where scanning is achieved electrically via reverse biasing the absorber section within an imbalanced interferometer setup. A proof of principle demonstration was set up for displacement measurements at scan rates of 10kHz, where target displacements between 100µm and 1.0mm were detected at 2m and 25m optical fibre distances (effective free-space distances of over 3m and 36m respectively including the free-space components), exhibiting accuracies to within ~10µm and ~100µm respectively. The maximum usable scan range (the roundtrip period of a ~5GHz repetition rate laser, ~200ps) was also realised by utilising the maximum available combination of electronic repetition rate tunability and passive delay line length. Additionally,

demonstrative cross-correlations were acquired at up to 1MHz scan rates, demonstrating great potential for real-time scanning. All scans were performed by modulating the electrical biases applied to a single quantum dot semiconductor passively mode-locked laser diode, with absolutely no mechanical parts required whatsoever. Referring to the original Figure 1-12, which in Chapter 1 plotted a selection of the scan rates and scan ranges achieved by the existing optical sampling techniques, an overall summary of the achievements of OSBERT found throughout the project are now superimposed respectively in Figure 6-1.

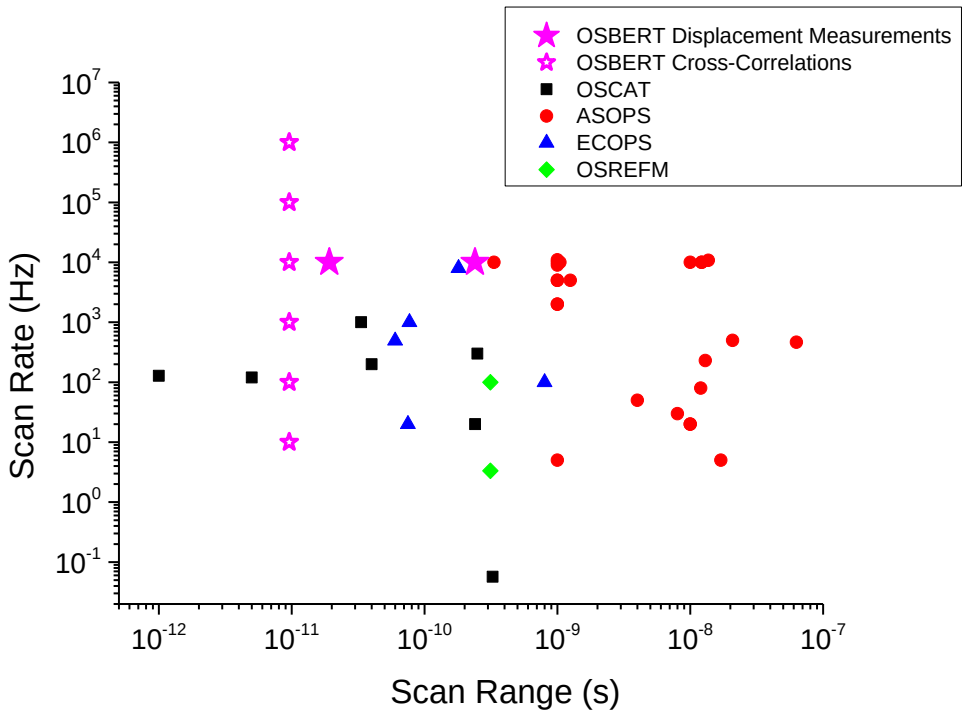

Figure 6-1 – Referring to the original Figure 1-12, the summary of the project is illustrated here. In particular, OSBERT has been accurately demonstrated to 10kHz scan rates, for scan ranges accessed by the use of increasing passive delay line lengths between 1m and 25m, with demonstrative cross-correlations acquired at up to 1MHz.

As can be seen, OSBERT has been accurately demonstrated experimentally as a contender to all the major techniques, sitting at the top end of the scan rates presented from the literature, where the cross-correlations acquired at megahertz scan rates are displayed for the potential of the technique. Though the scan range (competing with OSCAT and ECOPS) was selectable by the repetition rate tunability and PDLs available, it was ultimately limited practically by the 200ps roundtrip period of this particular laser. As such, lower repetition rate MLLDs (particularly external cavity MLLDs) could provide scan ranges

exhibited by ASOPS if necessary. With first demonstration limitations in mind, the primary research goals of this project were ultimately met.

A second technique, SLECOPS (Single-Laser Electronically Controlled Optical Sampling), was developed from first principles, and although theoretically well suited to the electrical tunability of MLLDs, it is attractive because it is potentially suited to any type of laser whose repetition rate may be tuned via square wave modulation, and as such may be adopted by a variety of laser systems and their respective optical sampling requirements. SLECOPS is of particular interest due to the novelty of its ability to perform asynchronous-type scanning (such as that shown by ASOPS or ECOPS) using only one laser instead of two, owed to the concept of the virtual laser. Cross-correlations were simulated under various theoretical conditions in order to show the ability to select the scan range, scan rate and step-size depending on the requirements of the study, particularly the available repetition rate tunability, PDL length and the practical feasibility in square wave modulation.

The summary and primary advantages and disadvantages of SLECOPS and OSBERT are finally tabulated and compared with those in the literature, see Figure 6-2.

In conclusion, SLECOPS and particularly OSBERT sit well within the state of the art optical sampling techniques as reasonable contenders. The ability to select the scan range through the optimum combination of amplitude of repetition rate modulation and passive delay line length, alongside the competitive scan rates pave the way for such ultrafast semiconductor passively mode-locked laser diodes to be deployed in fast, low-cost and compact optical sampling systems such as the pump probe spectroscopy approach adopted in biomedical microscopy, imaging and other sensing applications. With the wide array of wavelengths, peak powers, repetition rates and pulse durations of MLLDs available, this has essentially opened up the potential for reducing the costs and complexities demonstrated within the current trends, and since both linear (SPA) and non-linear (TPA) techniques were demonstrated (and contrasted with conventional mechanical translation stage methods), there is great potential for cutting edge optical sampling techniques, particularly if amplification and pulse compression techniques were built into the setup.

Technique	Scan rate dictated by:	Scan range dictated by	Advantages	Disadvantages
OSBERT	Ability to fast-modulate reverse bias to absorber section	- repetition rate *f* - repetition rate tunability *Δf* - PDL length *l*	- 1 Laser - Fast Scan Rates - Inexpensive MLLD - Scan range customisable - No mechanical parts	- long PDLs lead to dispersion and jitter issues
SLECOPS	- PDL length - Ability to modulate repetition rate via square wave	- repetition rate *f* - repetition rate tunability *Δf* - PDL length *l*	- 1 Laser - Fast Scan Rates - Scan range customisable	- long PDLs lead to dispersion and jitter issues
Translation Stage	The mechanical speed of a physical motor	The length of the translation stage	- 1 Laser - Simple setup -Scan range customisable	- Low scan rates limited by mechanical parts
ASOPS	The offset *Δf* between both lasers	The roundtrip period *T = 1/f*	- Fast scan rates and long scan ranges (depending on laser characteristics) - No mechanical parts	- 2 Lasers - Double Costs - Complex phase-locking system -Scan range not customisable
ECOPS	The fraction of roundtrip period *T = 1/f* selected by the offset *Δf* between both lasers	The offset *Δf* between both lasers	- Fast scan rates and long scan ranges (depending on laser characteristics) -Scan range customisable	- 2 Lasers - Double Costs - Complex phase-locking system - limited by mechanical parts
OSCAT	Intracavity mirror motor speed	- repetition rate *f* - repetition rate tunability *Δf* - PDL length *l*	- 1 Laser - Scan range customisable	- long PDLs lead to dispersion and jitter issues - limited by mechanical parts
OSREFM	The ability to modulate the repetition rate and the carrier dynamics of the material concerned	- repetition rate *f* - repetition rate tunability *Δf* - PDL length *l*	- 1 Laser - Inexpensive SLD - Scan range customisable - No mechanical parts	- Complex phase locking electronics - low scan rates demonstrated - High pulse to pulse timing jitter

Figure 6-2 – OSBERT and SLECOPS are added to the summary of optical sampling techniques with respect to the original Figure 1-11, including how in each case the scan rate and scan range are determined, and the relative advantages and disadvantages of each system.

6.2. Suggestions for Future Investigations

Though the major goals of the project were met, a number of investigations could follow the successes and limitations of the project, in order to address some of their respective challenges and potential which were discussed throughout the thesis.

For OSBERT, though a number of devices were tested with varying degrees of repetition rate tunability *Δf* (two of which were included in the thesis) and paired with various lengths of passive delay line *l*, the magnitude of the β-ratio, $\Delta f/f_{rep}$ was still relatively small

due to the MLLDs high repetition rates f_{rep}. The scan range scales with this ratio and with the length of passive delay line, however increasing *l* can increase the cumulative jitter and thus decrease the reliability of the system. It would therefore be a significant step to modify the system such that an external cavity was used; not in order to mechanically tune the repetition rate as in OSCAT or ECOPS, but instead to *set* the fundamental repetition rate to a few hundred megahertz which could then still be electronically tuned by varying the biasing conditions. A longer external cavity will reduce the repetition rate, and thus increase the β-ratio, decreasing the required length of fibre and thus decreasing both adverse dispersion and jitter effects in the system.

An illustrative demonstration of Fast-OSBERT as an optical sampling technique for non-linear optics would highlight its attractiveness. Whilst TPA traces were acquired for Slow-OSBERT, it would be interesting to see how effectively the second order cross-correlation traces could be realised at fast scan rates as compared to the linear interferometric traces which were acquired. In particular, a benefit of FOSBERT over SOSBERT was in fact the ability to finely tune the alignment of the system in real time. During SOSBERT scans, only small methodical adjustments could be made to the beam alignment between the optical components and the detector, followed by a full scan, followed by further adjustments between scans until the signal was as optimised as possible. This laborious process could be significantly reduced from tens of minutes to mere seconds whilst scanning even at a few Hz, watching the signal improve in moments and finely tuning the alignment of the system. If this were applied to the tapered waveguide device and the TPA traces, the quality could have improved and a greater peak to baseline ratio could have been found.

A parametric study of repetition rate tunability brought on by reverse bias, forward current and temperature could help categorically determine the exact mechanism involved. Several devices could be tested which are identical in all but one key feature per set of devices, for example gain to absorber length ratios, device structure (both physical and chemical), quantum wells, dashes and dots as the active medium etc. Additionally, when the tunability across reverse bias, forward current and temperature are known, it could be possible to simultaneously modulate all three to optimise the tunability per volt, per amp and per degree centigrade and reduce the knock-on effects to the other

parameters such as pulse duration, peak and average powers and central output wavelength – in essence to stabilise the tuned output.

An investigation in the loss in repetition rate tunability amplitude would be a great advantage to the project, as the source in not currently understood. Higher bandwidth detectors, cables and driving equipment may aid in this, or at least in realising more fringes at faster scan rates. Additionally, if the high speed RF Analyser had been available throughout the project, it would have been useful to begin the project from the outset knowing the reduction in tunability and applying it directly during each experiment.

Also, a broader study of the jitter in the system would be hugely beneficial, particularly the pulse-to-pulse jitter brought on by increasing the PDL length. A comparison of RMS jitter could also be included if a high resolution RF Analyser with a timing jitter module was made available, as this is a useful characteristic to be able to quote.

It would be more ideal to use PDLs of several kilometres, and study the effects of both dispersion and jitter in order to determine the reality of implementing MLLDs in such a system. Dispersion compensating measures could be implemented in the form of dispersion-compensating fibres or post-fibre compensation. In addition, the pulses could potentially be compressed in order to compete with the femtosecond pulse duration of commercial systems, and the power amplified (for example using an SOA).

Steps may also be taken to minimise the design of OSBERT. For example, the translation stage is not required to provide temporal scanning; it merely facilitates the ability to demonstrate standard translation stage scans within the same study. Using the 25m PDL was sufficient to provide the maximum scan range in excess of the roundtrip period, and therefore a scan would always be present on the oscilloscope in the context of a cross-correlation, regardless the offset between long and short arms. This means that in fact both arms could consist of specially designed lengths of coiled fibre if the beam splitters were replaced with fibre mating sleeves, see Figure 6-3. With any combination (or indeed an array) of two-section passively mode-locked laser diodes of various wavelengths, repetition rate tunabilities, pulse durations and optical powers, an OSBERT device could be designed much like that of the Tera-OSCAT [148] produced by Menlo Systems.

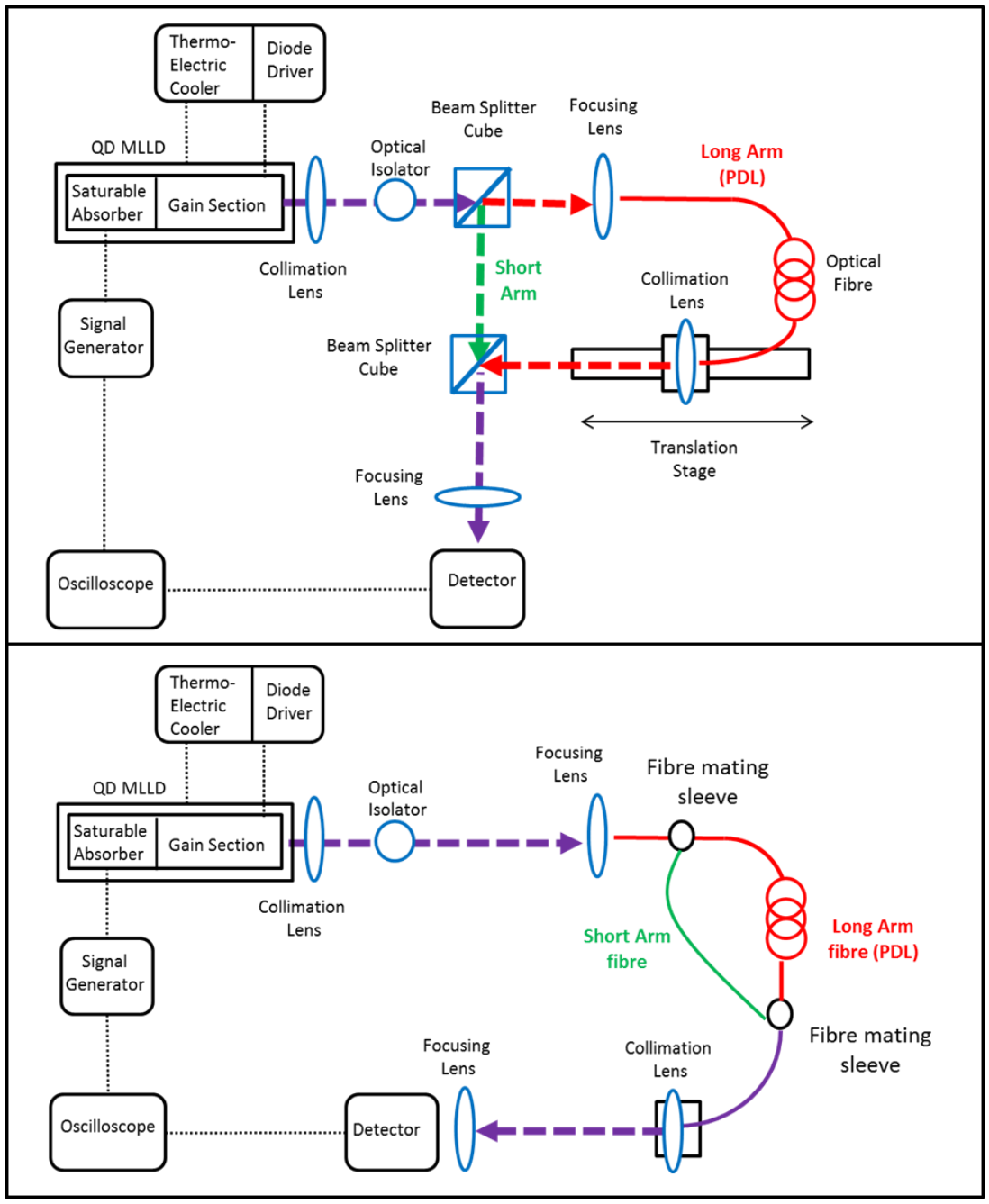

Figure 6-3 – Above, OSBERT as has been presented in this project. Below, OSBERT as could be realised when both arms are combined in an entirely fibre-optic design.

Finally, though it was out-with the scope of the project, a practical test of the SLECOPS technique would need to be carried out in order to confirm the theoretical basis. Ideally this could be done with both a tunable MLLD and with a commercial solid state system with motorised repetition rate control for comparison. An investigation into the practical issues surrounding fast square waves applied to the system should be carried out, as well as a parametric study of various PDL lengths, square wave periods and repetition rate tunabilities.

7. APPENDICES

7.1. Chapter 1 Appendices

7.1.1. Optical Sampling Systems

The tabulation of optical sampling techniques used to generate Figure 1-12. Note that whilst other works are discussed throughout the thesis, only those which had a clear scan range and scan rate value are tabulated here and plotted in Chapter 1 and Chapter 6.

OSCAT									
Ref	**Laser**	***f*** **(Hz)**	***Δf*** **(Hz)**	**t_{pulse} (fs)**	**λ (nm)**	**Scan Range (ps)**	**P_{av} (mW)**	**l_{delay} fibre (m)**	**Scan Rate (Hz)**
[60]	Menlo Systems M-Comb Fibre	250E6	0.0035E6	63	1560	1.0	600	14.4	128
[62]	Menlo Systems M-Comb Fiber	250E6	0.14864E6	700	1560	33.33	32	2020	100
[24]	Yb-Doped Fibre	1000E6	~10E6	95	1038	250	30	266.5	300
[149]	Menlo Erbium Fibre	100E6	0.325E6		1550	325		20	0.057
[145]	Menlo Erbium Fibre	100E6	0.0005E6	40000	1550	240		10000	20
[148]	Menlo TERA OSCAT	250E6	2E6	90	1560	40		50	200
[150]	Fibre Menlo Systems	250E6	0.0035E6	80	1550	5		80	120

OSREFM									
Ref	**Laser**	**f (Hz)**	**Δf (Hz)**	**t_{pulse} (fs)**	**λ (nm)**	**Scan Range (ps)**	**P_{av} (mW)**	**l_{delay} fibre (m)**	**Scan Rate (Hz)**
[71]	GSLD into fibre	39.72E6	0.5E6	200	775	313	15	7.5	100
[72]	GSLD into fibre	39.72E6	0.5E6	200	775	313	15	7.5	3.33

ASOPS[17]								
Ref	**Laser**	**f (Hz)**	**Δf (Hz)**	**t_{pulse} (fs)**	**λ (nm)**	**Scan Range (ps)**	**P_{av} (mW)**	**Scan Rate (Hz)**
[151]	Nd:YAG Dye	82E6	0.01E6	15000 1000	532 600	12200	400 85	10E3
[45]	Ti:Saph	1000E6	0.005E6	1000	800	1000		5E3
[152]	Dual ML Fibre	15.753170E6 15.752704E6	0.000466E6	1.56 1.15	1532 1554	63000	0.504 0.029	0.466E3
[46]	Ti:Saph	1000E6	0.011E6	30	820	1000	500	11E3
[153]	Ti:Saph	1000E6	0.002E6	40	800	1000		2E3
[154, 155]	Dual Fibre	250E6	0.00005E6	50	1550	4000	500	0.05E3
[156]	Menlo ASOPS C-Fibre	100E6	0.02E6	150 110	1560 780	10000	30 65	10E3
[144]	Nd:YAG Ti:Saph	78E6 78E6	0.0108E6	28000 14	266 800	13700	2000 400	10.8E3
[51]	Ti:Saph	80E6	80	100	800	12000	1000 500	0.08E3
[47]	Ti:Saph	76E6	230	300	800	13000		0.23E3
[157]	Ti:Saph	125.13E6	29.93	10	800	8000	500	0.02993E3
[158]	Ti:Saph	1000E6	0.009E6	30	830	1000	500	9E3
[159]	Ti:Saph	1000E6	0.005E6		790 810	1000	100 10	0.005E3
[160]	Ti:Saph	800E6	0.005E6	50	790 820	1250	70 5	5E3
[48]	Ti:Saph	100E6	20	20 10	800	10000		0.02E3
[161]	VECSEL Ti:Saph	1000E6 1000E6	0.01E6	370	1048 825	333	12 900	10E3
[162]	Ti:Saph	1000E6	0.005E6	35	800	1000	700	5E3
[163]	Ti:Saph	1000E6	0.005E6	45	800	1000	800	5E3
[49]	Ti:Saph	100E6	0.00002E6	10		10000		0.02E3
[164]	Er Fibre	56.124E6	5	50	1550	17000		0.005E3
[25]	Ti:Saph	1000E6	0.002E6	40		1000	650	2E3
[165]	Ti:Saph	956E6	10000	50	800	1046	600	10000
[50]	Yb:KYW	48E6	0.0005E6	330	1027	20833	1000	0.5E3

[17] Note, where information regarding both pump and probe lasers is clearly known (or where they differ from each other), they are included as two characteristics in the same cell.

ECOPS							
Ref	**Laser**	**f (Hz)**	**t_{pulse} (fs)**	**λ (nm)**	**Scan Range (ps)**	**P_{av} (mW)**	**Scan Rate (Hz)**
[166]	Er Fibre	100E6	300	1550	800		0.1E3
[167]	Ti:Sapp	100E6	10	800	77		1E3
[57]	Er Fibre	100E6	140	1560	180	80	8E3
[168]	fs fibre	100E6	50	1560	60	8.4	0.492E3
[169]	Er Fibre (Toptica)	82E6		1550	75		0.02E3

7.2. Chapter 2 Appendices

7.2.1. Thermal Expansion

The thermal expansion of Gallium Arsenide [170] was calculated in order to determine if the increase in the length *L* of the laser cavity could lead to the extent of repetition rate tunability found in the temperature study. We know the repetition rate f_{rep} to be given by

$$f_{rep} = \frac{c}{2nL} = \frac{1}{T_{rep}} \tag{60}$$

Where *c* is the speed of light in vacuum, *n* is the refractive index of the material and T_{rep} is the roundtrip period. Thus if the length *L* of the internal cavity were to change by ΔL then the resultant repetition rate would tune by Δf_{rep} such that

$$\Delta f_{rep} = \frac{c}{2nL} - \frac{c}{2n(L+\Delta L)} = \frac{c}{2n}\left(\frac{1}{L} - \frac{1}{L+\Delta L}\right) \tag{61}$$

Conversely, if we have a known repetition rate tunability we may find by how much the internal cavity length may have changed

$$\Delta L = \frac{L \cdot c}{c - L \cdot 2n \cdot \Delta f_{rep}} - L = \frac{L^2 \cdot 2n \cdot \Delta f_{rep}}{c - L \cdot 2n \cdot \Delta f_{rep}} \tag{62}$$

For our device, we have a length of 8.00mm and refractive index *n* = 3.5, therefore a tunability of 1MHz would correspond to lengthening the internal cavity by ~1.5µm. In fact we know from Chapter 2 that the repetition rate tunes by ~3.5MHz over a temperature

increase of 8°C. Therefore proportionally we would expect this to be representative of a 5.25µm change in length. Assuming a linear thermal expansion coefficient α_L of 6.0×10^{-6} [171] for near-room temperature operation of GaAs we know

$$\Delta L = \alpha_L \Delta T L \tag{63}$$

This change in temperature would only correspond to a change in length of 0.38µm, which would only give rise to a repetition rate tunability of ~0.25MHz. In conclusion, though the repetition rate change will likely in part be due to thermal expansion, it does not account for the entire tunability which was found by over an order of magnitude. Therefore, other influences such as those brought about by pulse shaping and carrier dynamics, are the likely major cause.

7.3. Chapter 4 Appendices

7.3.1. Linear Version of Contour Plot

A linear version of the logarithmic plot is shown in order to visually demonstrate the periodic relationship between scan range, scan rate and passive delay line length.

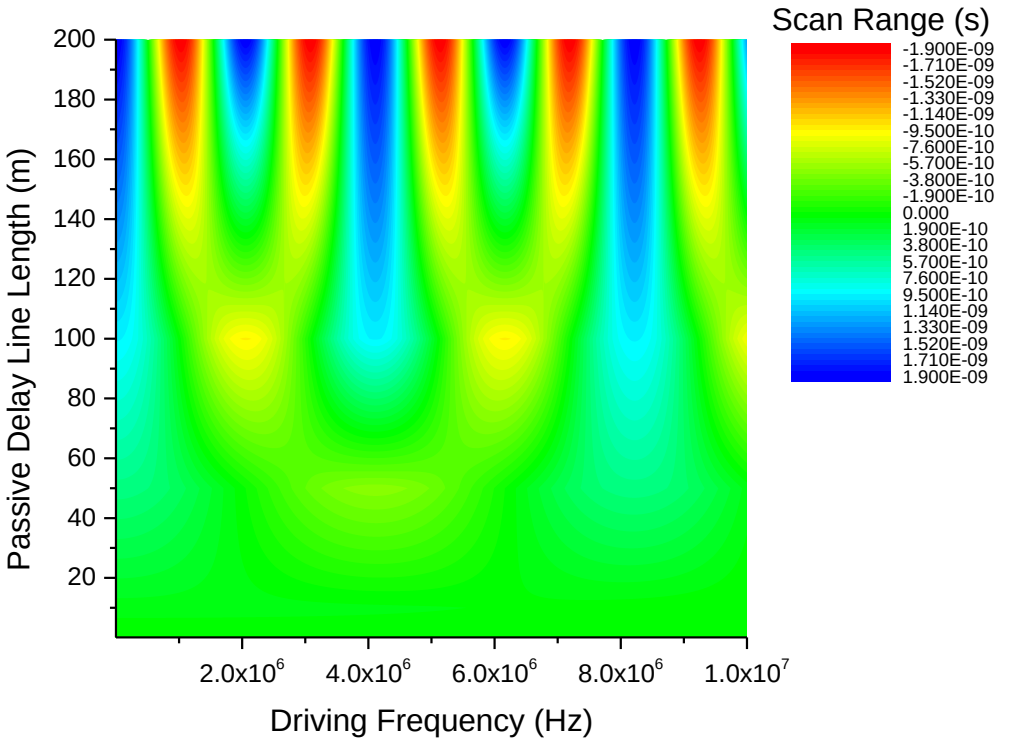

Figure 7-1 – Linear (non-logarithmic) version of the contour plot showing the consequences of increasing the driving (modulation) frequency for increasing passive delay line lengths using the full 10MHz repetition rate tuning characteristics of the narrow-ridge device.

7.3.2. Tunability and electrical calibration for 220mA forward current

The repetition rate tunability for reverse bias and the electrical calibration under the 220mA forward current regime as compared with the 210mA regime.

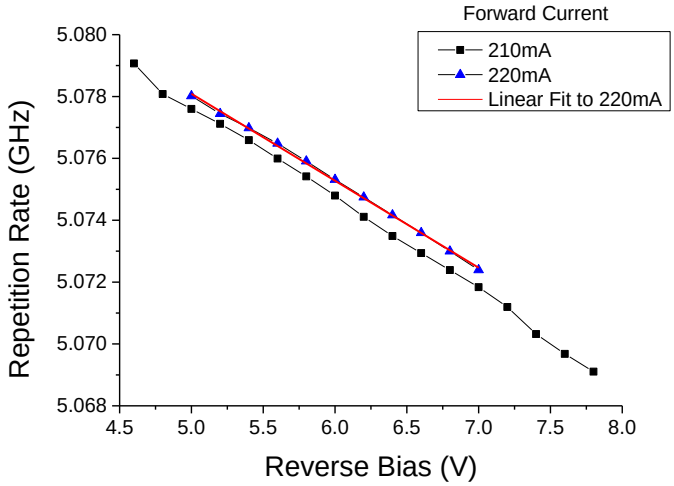

Figure 7-2 - Repetition rate tunability for reverse bias under the 220mA regime compared to the 210mA regime.

The linear fit of the repetition rate tunability (Hz) in the 220mA gives the relationship for reverse bias in volts

$$\boldsymbol{f_{rep}} = -2.81176 \times 10^{6}\boldsymbol{V} + 5.09215 \times 10^{9}\ [Hz] \tag{64}$$

The electrical calibration for use with the signal generator under the 220mA regime is then compared with the 210mA regime with a linear fit.

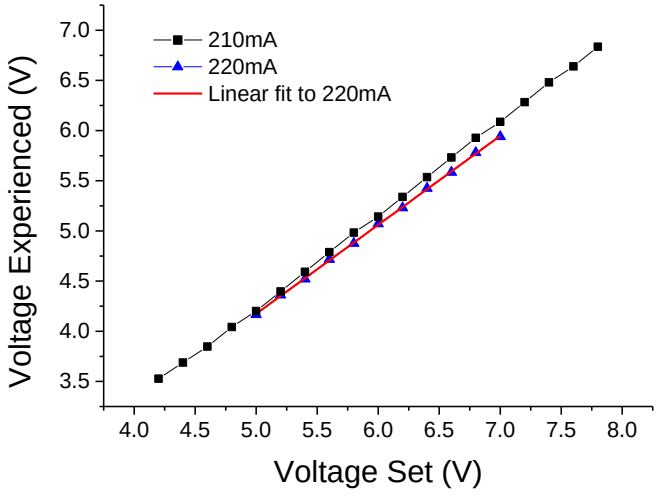

Figure 7-3 – Voltage experienced by the absorber for the voltage set in both the 210mA and 220mA forward current regimes.

The linear fit for the 220mA regime as used in the deconvolution of the OSBERT target displacement scans is thus

$$\boldsymbol{V_{exp}} = 0.88649\boldsymbol{V_{set}} - 0.25809\ [V] \tag{65}$$

These expressions were used for the deconvolution of any OSBERT study conducted whilst the forward current setting was 220mA.

8. REFERENCES

1. Li, M.-F., Ni, H.-Q., Ding, Y., Bajek, D., Kong, L., Cataluna, M.A., and Niu, Z.-C., *Optimization of InAs/GaAs quantum-dot structures and application to 1.3-μm mode-locked laser diodes.* Chinese Physics B, 2014. **23**(2): p. 027803.
2. Wang, H., Kong, L., Forrest, A., Bajek, D., Haggett, S.E., Wang, X., Cui, B., Pan, J., Ding, Y., and Cataluna, M.A., *Ultrashort pulse generation by semiconductor mode-locked lasers at 760 nm.* Optics Express, 2014. **22**(21): p. 25940-25946.
3. Kong, L., Wang, H.L., Bajek, D., White, S.E., Forrest, A.F., Wang, X.L., Cui, B.F., Pan, J.Q., Ding, Y., and Cataluna, M.A., *Deep-red semiconductor monolithic mode-locked lasers.* Applied Physics Letters, 2014. **105**(22): p. 221115.
4. Kong, L., Wang, H., Bajek, D., Haggett, S., Forrest, A., Wang, X., Cui, B., Pan, J., Ding, Y., and Cataluna, M.A. *Semiconductor monolithic mode-locked laser for ultrashort pulse generation at 750 nm*. in *24th IEEE International Semiconductor Laser Conference*. 2014. Palma de Mallorca, Spain: Institute of Electrical and Electronics Engineers. p. 137-138.
5. Wang, H., Kong, L., Bajek, D., Haggett, S., Wang, X., Cui, B., Pan, J., Ding, Y., and Cataluna, M.A. *760-nm Semiconductor Passively Mode-Locked Monolithic Laser for Picosecond Pulse Generation*. in *CLEO: 2013*. 2013. San Jose, California: Optical Society of America. p. JTh2A.20.
6. Cataluna, M.A., Ding, Y., White, S.E., Bajek, D., and Krakowski, M. *High-power ultrafast and broadly-tunable quantum-dot lasers*. in *SPIE Photonics West: Quantum Sensing and Nanophotonic Devices XII*. 2015. San Francisco; United States. p. 93702D-93702D-93706.
7. Einstein, A., *Zur Quantentheorie der Strahlung.* Physikalische Zeitschrift, 1917. **18**: p. 121-128.
8. Maiman, T.H., *Stimulated Optical Radiation in Ruby.* Nature, 1960. **187**(4736): p. 493-494.
9. Bookey, H.T.G. and Kar, A.K., *Characterisation and optimisation of a dual-channel picosecond gain-switched DFB laser system for use as a pump–probe source.* Optics Communications, 2005. **248**(1–3): p. 229-239.
10. Hargrove, L.E., Fork, R.L., and Pollack, M.A., *Locking of He-Ne laser modes induced by synchronous intracavity modulation.* Applied Physics Letters, 1964. **5**(1): p. 4-5.
11. Zakhar'yash, V.F., Kashirskii, A.V., and Klement'ev, V.M., *Active mode-locking in semiconductor lasers.* Optoelectronics, Instrumentation and Data Processing, 2015. **51**(6): p. 553-559.
12. Ippen, E.P., Shank, C.V., and Dienes, A., *Passive mode locking of the cw dye laser.* Applied Physics Letters, 1972. **21**(8): p. 348-350.
13. Thompson, M.G., Rae, A.R., Penty, R.V., White, I.H., Kovsh, A.R., Mikhrin, S.S., Livshits, D.A., and Krestnikov, I.L. *Absorber length optimisation for sub-picosecond pulse generation and ultra-low jitter performance in passively mode-locked 1.3 /spl mu/m quantum-dot laser diodes*. in *Optical Fiber Communication Conference, 2006 and the 2006 National Fiber Optic Engineers Conference. OFC 2006*. 2006. p. 3 pp.
14. Spence, D.E., Kean, P.N., and Sibbett, W., *60-fsec pulse generation from a self-mode-locked Ti:sapphire laser.* Optics Letters, 1991. **16**(1): p. 42-44.
15. Bartels, A., Hudert, F., Janke, C., Dekorsy, T., and Köhler, K., *Femtosecond time-resolved optical pump-probe spectroscopy at kilohertz-scan-rates over nanosecond-*

time-delays without mechanical delay line. Applied Physics Letters, 2006. **88**(4): p. 041117.

16. Porter, G., *Flash Photolysis and Spectroscopy. A New Method for the Study of Free Radical Reactions.* Proceedings of the Royal Society of London A: Mathematical, Physical and Engineering Sciences, 1950. **200**(1061): p. 284-300.
17. Zhao, K., Zhang, Q., Chini, M., Wu, Y., Wang, X., and Chang, Z., *Tailoring a 67 attosecond pulse through advantageous phase-mismatch.* Optics Letters, 2012. **37**(18): p. 3891-3893.
18. Paul, P.M., Toma, E.S., Breger, P., Mullot, G., Augé, F., Balcou, P., Muller, H.G., and Agostini, P., *Observation of a Train of Attosecond Pulses from High Harmonic Generation.* Science, 2001. **292**(5522): p. 1689-1692.
19. Hasted, J.B., *Milli-microsecond pulse generation by electron bunching.* Proceedings of the Physical Society, 1948. **60**(4): p. 397.
20. Kerns, Q.A., Kirsten, F.A., and Cox, G.C., *Generator of Nanosecond Light Pulses for Phototube Testing | Rev. Sci. Instrum. - Review of Scientific Instruments.* Rev. Sci. Instrum., 1958. **30**.
21. Armstrong, J.A., *Measurement of Picosecond Laser Pulse Widths.* Applied Physics Letters, 1967. **10**: p. 16-18.
22. Diels, J.C. and Stryland, E.V., *Generation and measurement of 200 femtosecond optical pulses.* 1978. **25**(1): p. 93–96.
23. Liu, Y., De Silvestri, S., Magni, V., Laporta, P., and Svelto, O. *38-Femtosecond pulse generation from a simple linear-cavity synchronously pumped dye laser*. in *International Conference on Optoelectronic Science and Engineering '90*. 1990. Beijing, China: Proceedings of SPIE - The International Society for Optical Engineering. p. 333-335.
24. Romann, A., Mohr, C., Ruehl, A., Hartl, I., and Fermann, M.E., *Mode-Locked Yb-Fiber Laser for Rapid Dual Pulse Scanning Applications.* Advances in Optical Materials (2011), paper JWA2, 2011.
25. Bartels, A., Klatt, G., Gebs, R., Janke, C., and Dekorsy, T. *High-speed ASOPS based THz time-domain spectrometer*. in *2009 34th International Conference on Infrared, Millimeter, and Terahertz Waves*. 2009. p. 1-3.
26. Ding, Y., Aviles-Espinosa, R., Cataluna, M.A., Nikitichev, D., Ruiz, M., Tran, M., Robert, Y., Kapsalis, A., Simos, H., Mesaritakis, C., et al., *High peak-power picosecond pulse generation at 1.26 μm using a quantum-dot-based external-cavity mode-locked laser and tapered optical amplifier.* Optics Express, 2012. **20**(13): p. 14308-14320.
27. Li, M.-F., Ni, H.-Q., Ding, Y., Bajek, D., Kong, L., Cataluna Maria, A., and Niu, Z.-C., *Optimization of InAs/GaAs quantum-dot structures and application to 1.3-μm mode-locked laser diodes.* Chinese Physics B, 2014. **23**(2): p. 027803.
28. Spectra-Physics. *Insight DS+*. 2016; Available from: http://www.spectra-physics.com/products/ultrafast-lasers/insight-ds#1.
29. Pfeifle, J., Shkarban, I., Wolf, S., Kemal, J.N., Weimann, C., Hartmann, W., Chimot, N., Joshi, S., Merghem, K., Martinez, A., et al. *Coherent terabit communications using a quantum-dash mode-locked laser and self-homodyne detection*. in *Optical Fiber Communication Conference, OFC 2015*. 2015. p. 1-3.
30. Pfeifle, J., Watts, R., Shkarban, I., Wolf, S., Vujicic, V., Landais, P., Chimot, N., Joshi, S., Merghem, K., Calò, C., et al. *Simultaneous phase noise reduction of 30 comb lines from a quantum-dash mode-locked laser diode enabling coherent tbit/s data transmission*. in *Optical Fiber Communication Conference, OFC 2015*. 2015. p. 1-3.

31. Khayatzadeh, R., Poette, J., and Cabon, B., *Impact of phase noise in 60-GHz radio-over-fiber communication system based on passively mode-locked laser.* Journal of Lightwave Technology, 2014. **32**(20): p. 3529-3535.
32. Kuramoto, M., Kitajima, N., Guo, H., Furushima, Y., Ikeda, M., and Yokoyama, H., *Two-photon fluorescence bioimaging with an all-semiconductor laser picosecond pulse source.* Optics Letters, 2007. **32**(18): p. 2726-2728.
33. Corkum, P.B. and Krausz, F., *Attosecond science.* Nature Physics, 2007. **3**(6): p. 381-387.
34. Zewail, A.H., *Laser femtochemistry.* Science, 1988. **242**(4886): p. 1645-1653.
35. Matthews, T.E., Wilson, J.W., Degan, S., Simpson, M.J., Jin, J.Y., Zhang, J.Y., and Warren, W.S., *In vivo and ex vivo epi-mode pump-probe imaging of melanin and microvasculature.* Biomed Opt Express, 2011. **2**(6): p. 1576-1583.
36. Archundia-Berra, L.C. and Delfyett, P.J., *External cavity multiwavelength semiconductor mode-locked lasers gain dynamics.* Opt Express, 2006. **14**(20): p. 9223-9237.
37. Wan, Q. and Applegate, B.E., *Multiphoton coherence domain molecular imaging with pump-probe optical coherence microscopy.* Opt Lett, 2010. **35**(4): p. 532-534.
38. Kwong, K.F., Yankelevich, D., Chu, K.C., Heritage, J.P., and Dienes, A., *400-Hz mechanical scanning optical delay line.* Optics Letters, 1993. **18**(7): p. 558-560.
39. Gambetta, A., Galzerano, G., Rozhin, A.G., Ferrari, A.C., Ramponi, R., Laporta, P., and Marangoni, M., *Sub-100 fs pump-probe spectroscopy of Single Wall Carbon Nanotubes with a 100 MHz Er-fiber laser system.* Optics Express, 2008. **16**(16): p. 11727-11734.
40. Elzinga, P.A., Lytle, F.E., Jian, Y., King, G.B., and Laurendeau, N.M., *Pump/Probe Spectroscopy by Asynchronous Optical Sampling.* Applied Optics, 1987. **26**(19): p. 4303-4309.
41. Yasui, T., Kabetani, Y., Ohgi, Y., Yokoyama, S., and Araki, T., *Absolute distance measurement of optically rough objects using asynchronous-optical-sampling terahertz impulse ranging.* Applied Optics, 2010. **49**(28): p. 5262-5270.
42. Dekorsy, T., Klatt, G., Gebs, R., Janke, C., and Bartels, A. *Asynchronous optical sampling with GHz repetition rate femtosecond lasers for high precision terahertz spectroscopy*. in *General Assembly and Scientific Symposium, 2011 XXXth URSI,*. 2011. Istanbul. p. 1-4.
43. Krauß, N., Nast, A., Heinecke, D.C., Kölbl, C., Barros, H.G., and Dekorsy, T., *Fiber-coupled high-speed asynchronous optical sampling with sub-50 fs time resolution.* Optics Express, 2015. **23**(3): p. 2145-2156.
44. Good, J.T., Holland, D.B., Finneran, I.A., Carroll, P.B., Kelley, M.J., and Blake, G.A., *A decade-spanning high-resolution asynchronous optical sampling terahertz time-domain and frequency comb spectrometer.* Review of Scientific Instruments, 2015. **86**(10).
45. Janke, C., Forst, M., Nagel, M., Kurz, H., and Bartels, A., *Asynchronous optical sampling for high-speed characterization of integrated resonant terahertz sensors.* Opt Lett, 2005. **30**(11): p. 1405-1407.
46. Bartels, A., Hudert, F., Janke, C., Dekorsy, T., and Köhler, K., *Femtosecond time-resolved optical pump-probe spectroscopy at kilohertz-scan-rates over nanosecond-time-delays without mechanical delay line.* 2006.
47. Adachi, S., Takeyama, S., and Takagi, Y., *Dual wavelength optical sampling technique for ultrafast transient bleaching spectroscopy.* Optics Communications, 1995. **117**(1–2): p. 71-77.

48. Kim, Y.-C., Jin, K.-H., Ye, J.-C., Ahn, J.-W., and Yee, D.-S., *Wavelet Power Spectrum Estimation for High-resolution Terahertz Time-domain Spectroscopy.* Journal of the Optical Society of Korea, 2011. **15**(1): p. 103-108.
49. Moon, K., Han, Y., Jung, E., Lim, M., Im, C., and Han, H. *Real-time terahertz time-domain spectroscopy based on asynchronous optical sampling*. 2009.
50. Abbas, A., Guillet, Y., Rampnoux, J.M., Rigail, P., Mottay, E., Audoin, B., and Dilhaire, S., *Picosecond time resolved opto-acoustic imaging with 48 MHz frequency resolution.* Optics Express, 2014. **22**(7): p. 7831-7843.
51. Kafka, J.D., Pieterse, J.W., and Watts, M.L., *Two-color subpicosecond optical sampling technique.* Optics Letters, 1992. **17**(18): p. 1286-1288.
52. Antonucci, L., Solinas, X., Bonvalet, A., and Joffre, M., *Asynchronous optical sampling with arbitrary detuning between laser repetition rates.* Optics Express, 2012. **20**(16): p. 17928-17937.
53. Antonucci, L., Bonvalet, A., Solinas, X., Jones, M.R., Vos, M.H., and Joffre, M., *Arbitrary-detuning asynchronous optical sampling pump-probe spectroscopy of bacterial reaction centers.* Optics Letters, 2013. **38**(17): p. 3322-3324.
54. Tauser, F., Rausch, C., Posthumus, J.H., and Lison, F. *Electronically controlled optical sampling using 100 MHz repetition rate fiber lasers*. in *Commercial and Biomedical Applications of Ultrafast Lasers VIII*. 2008. San Jose, CA; United States: Proceedings of SPIE - The International Society for Optical Engineering.
55. Sucha, G., Fermann, M.E., Harter, D.J., and Hofer, M., *A new method for rapid temporal scanning of ultrafast lasers.* Selected Topics in Quantum Electronics, IEEE Journal of, 1996. **2**(3): p. 605-621.
56. Yee, D.S. and Kim, Y., *High-speed terahertz time-domain spectroscopy based on electronically controlled optical sampling.* Optics Letters, 2010. **35**(22): p. 3715-3717.
57. Dietz, R.J.B., Vieweg, N., Puppe, T., Zach, A., Globisch, B., Göbel, T., Leisching, P., and Schell, M., *All fiber-coupled THz-TDS system with kHz measurement rate based on electronically controlled optical sampling.* Optics Letters, 2014. **39**(22): p. 6482-6485.
58. Chadi, A., Méjean, G., Grilli, R., and Romanini, D., *Note: Simple and compact piezoelectric mirror actuator with 100 kHz bandwidth, using standard components.* Review of Scientific Instruments, 2013. **84**(5): p. 056112.
59. Hochrein, T., Wilk, R., Mei, M., Holzwarth, R., Krumbholz, N., and Koch, M., *Optical sampling by laser cavity tuning.* Optics Express, 2010. **18**(2): p. 1613-1617.
60. Wilk, R., Hochrein, T., Koch, M., Mei, M., and Holzwarth, R., *OSCAT: Novel Technique for Time-Resolved Experiments Without Moveable Optical Delay Lines.* Journal of Infrared, Millimeter, and Terahertz Waves, 2011. **32**(5): p. 596-602.
61. Wilk, R., Kocur, S., Hochrein, T., Mei, M., and Holzwarth, R. *Imaging with THz OSCAT spectrometer*. in *36th International Conference on Infrared, Millimeter, and Terahertz Waves*. 2011. Houston, TX; United States. p. 1-2.
62. Yang, L., Nie, J., and Duan, L., *Dynamic optical sampling by cavity tuning and its application in lidar.* Optics Express, 2013. **21**(3): p. 3850-3860.
63. Yang, L. and Duan, L., *Depth-Resolved Imaging Based on Optical Sampling by Cavity Tuning.* Photonics Technology Letters, IEEE, 2015. **27**(16): p. 1761-1764.
64. Yang, L. and Duan, L., *Depth-Resolved Imaging Based on Optical Sampling by Cavity Tuning.* IEEE Photonics Technology Letters, 2015. **27**(16): p. 1761-1764.

65. Brenner, C., Friedrich, C.-S., and Hofmann, M.R., *Semiconductor Diode Lasers for Terahertz Technology.* Journal of Infrared, Millimeter, and Terahertz Waves, 2011. **32**(11): p. 1253-1266.
66. Mihoubi, Z., Wilcox, K.G., Elsmere, S., Quarterman, A., Rungsawang, R., Farrer, I., Beere, H.E., Ritchie, D.A., Tropper, A., and Apostolopoulos, V., *All-semiconductor room-temperature terahertz time domain spectrometer.* Optics Letters, 2008. **33**(18): p. 2125-2127.
67. Gebs, R., Klopp, P., Klatt, G., Dekorsy, T., Griebner, U., and Bartels, A., *Time-domain terahertz spectroscopy based on asynchronous optical sampling with femtosecond semiconductor disk laser.* Electronics Letters, 2010. **46**(1): p. 75-77.
68. Vickers, A.J., Alleston, S.B., Hassan, M., Muller, P.O., and Erasme, D. *A gain switched semiconductor laser pump-probe source*. in *Terahertz Electronics Proceedings, 1998. THz Ninety Eight. 1998 IEEE Sixth International Conference on*. 1998. p. 191-193.
69. Gong-Ru, L. and Yung-Cheng, C., *Novel Electro-Optic Sampling System with an Optoelectronic Phase-Locked Phase Shifter as a Delay-Time Controller.* Japanese Journal of Applied Physics, 2002. **41**(10R): p. 6003.
70. Vickers, A.J., Dudley, R., Henning, I., and Ma, Y., *A semiconductor based pump-probe system and its application to THz spectroscopy.* physica status solidi (c), 2007. **4**(2): p. 648-650.
71. Furuya, T., Estacio, E.S., Horita, K., Que, C.T., Yamamoto, K., Miyamaru, F., Nishizawa, S., and Tani, M., *Fast-Scan Terahertz Time Domain Spectrometer Based on Laser Repetition Frequency Modulation.* Japanese Journal of Applied Physics, 2013. **52**(2R).
72. Niehues, G., Furuya, T., Estacio, E.S., Yamamoto, K., Miyamaru, F., Nishizawa, S., and Tani, M. *Measurements using an OSREFM Fast-Scan Terahertz Time Domain Spectrometer*. in *JSAP-OSA Joint Symposia 2013 Abstracts*. 2013. Kyoto: Optical Society of America. p. 16a_D14_18.
73. Bulgarevich, D.S., Shiwa, M., Furuya, T., and Tani, M., *Gigahertz time-domain spectroscopy and imaging for non-destructive materials research and evaluation.* Scientific Reports, 2016. **6**.
74. Verdeyen, J.T., *Laser Electronics*. 1995, United States: Prentice Hall.
75. Kanzelmeyer, S., Sayinc, H., Theeg, T., Frede, M., Neumann, J., and Kracht, D., *All-fiber based amplification of 40 ps pulses from a gain-switched laser diode.* Optics Express, 2011. **19**(3): p. 1854-1859.
76. Sooudi, E., Sygletos, S., Ellis, A.D., Huyet, G., McInerney, J.G., Lelarge, F., Merghem, K., Rosales, R., Martinez, A., Ramdane, A., et al., *Optical Frequency Comb Generation Using Dual-Mode Injection-Locking of Quantum-Dash Mode-Locked Lasers: Properties and Applications.* Quantum Electronics, IEEE Journal of, 2012. **48**(10): p. 1327-1338.
77. Edik U. Rafailov, M.A.C., Eugene A. Avrutin, *Ultrafast Lasers Based on Quantum Dot Structures: Physics and Devices*. 2011.
78. Prasankumar, R.P., Attaluri, R.S., Averitt, R.D., Urayama, J., Weisse-Bernstein, N., Rotella, P., Stintz, A.D., Krishna, S., and Taylor, A.J., *Ultrafast carrier dynamics in an InAs/InGaAs quantum dots-in-a-well heterostructure.* Optics Express, 2008. **16**(2): p. 1165-1173.
79. Ledentsov, N.N.U., V. M.; Egorov, A. Yu.; Zhukov, A. E.; Maksimov, M. V.; Tabatadze, I. G.; Kop'ev, P. S, *Optical properties of heterostructures with InGaAs-GaAs quantum clusters.* Semiconductors, 1994. **28**(8): p. 832-834.

80. Liu, G., Stintz, A., Li, H., Malloy, K.J., and Lester, L.F., *Extremely low room-temperature threshold current density diode lasers using InAs dots in In_{0.15}Ga_{0.85}As quantum well.* Electronics Letters, 1999. **35**(14): p. 1163-1165.
81. Hitoshi, S., Shanmugam, S., Junji, Y., Sayoko, I., and Noriyuki, Y., *InAs Quantum Dot Lasers with Extremely Low Threshold Current Density (7 A/cm 2 /Layer).* Japanese Journal of Applied Physics, 2005. **44**(8L): p. L1103.
82. Bowers, J.E., Morton, P.A., Mar, A., and Corzine, S.W., *Actively mode-locked semiconductor lasers.* IEEE Journal of Quantum Electronics, 1989. **25**(6): p. 1426-1439.
83. Haus, H., *Theory of mode locking with a slow saturable absorber.* Quantum Electronics, IEEE Journal of, 1975. **11**(9): p. 736-746.
84. Olle, V.F., Wonfor, A., Sulmoni, L., Vasil'ev, P.P., Lamy, J.-M., Carlin, J.-F., Grandjean, N., Penty, R., and White, I.H. *Passive and Hybrid Mode-Locking From a Monolithic InGaN/GaN Laser Diode*. in *CLEO: 2013*. 2013. San Jose, California: Optical Society of America. p. CW1G.1.
85. Rafailov, E.U., Cataluna, M.A., and Sibbett, W., *Mode-locked quantum-dot lasers.* Nat Photon, 2007. **1**(7): p. 395-401.
86. Thompson, M.G., Rae, A., Sellin, R.L., Marinelli, C., Penty, R.V., White, I.H., Kovsh, A.R., Mikhrin, S.S., Livshits, D.A., and Krestnikov, I.L., *Subpicosecond high-power mode locking using flared waveguide monolithic quantum-dot lasers.* Applied Physics Letters, 2006. **88**(13): p. 133119-133113.
87. Nikitichev, D.I., Ding, Y., Cataluna, M.A., Rafailov, E.U., Drzewietzki, L., Breuer, S., Elsaesser, W., Rossetti, M., Bardella, P., Xu, T., et al., *High peak power and sub-picosecond Fourier-limited pulse generation from passively mode-locked monolithic two-section gain-guided tapered InGaAs quantum-dot lasers.* Laser Physics, 2012. **22**: p. 715-724.
88. Jensen, O.B., Hansen, A.K., Muller, A., Sumpf, B., Unterhuber, A., Drexler, W., Petersen, P.M., and Andersen, P.E., *Power scaling of nonlinear frequency converted tapered diode lasers for biophotonics.* IEEE Journal on Selected Topics in Quantum Electronics, 2014. **20**(2).
89. APE, *APE Pulse-Check Autocorrelator Manual #115279*. 2007, Plauener Str. 163-165 Haus N 13053 Berlin Germany. p. p. 6.
90. Armstrong, J.A., *Meausrement of picosecond laser pulse widths.* Applied Physics Letters, 1967. **10**(1): p. 16-18.
91. Diels, J.C.R., W., *Ultrashort Laser Pulse Phenomena*. 2, Revised ed. 2006: Academic Press, 2006.
92. Huang, X., Stintz, A., Li, H., Lester, L.F., Cheng, J., and Malloy, K.J., *Passive mode-locking in 1.3 μm two-section InAs quantum dot lasers.* Applied Physics Letters, 2001. **78**(2825): p. 2825-2827.
93. Sadeev, T., Arsenijević, D., Franke, D., Kreissl, J., Künzel, H., and Bimberg, D., *1.55-μm mode-locked quantum-dot lasers with 300 MHz frequency tuning range.* Applied Physics Letters, 2015. **106**(3): p. 031114.
94. Cheng, H.C., Wu, Q.Y., Pan, C.H., Lee, C.P., and Lin, G., *Low repetition rate and broad frequency tuning from a grating-coupled passively mode-locked quantum dot laser.* Applied Physics Letters, 2013. **103**(21): p. 211109-211109-211103.
95. Tan, W.K., Wong, H.Y., Kelly, A.E., Sorel, M., Marsh, J.H., and Bryce, A.C., *Passive modelocking of InGaAsP/InP laser diode over wide operating temperature range.* Electronics Letters, 2005. **41**(25): p. 1380-1382.

96. Mee, J.K., Crowley, M.T., Patel, N., Murrell, D., Raghunathan, R., Aboketaf, A., Elshaari, A., Preble, S.F., Ampadu, P., and Lester, L.F., *A passively mode-locked quantum-dot laser operating over a broad temperature range.* Applied Physics Letters, 2012. **101**(7): p. 071112.
97. Ќefélian, F., O'Donoghue, S., Todaro, M.T., McInerney, J., and Huyet, G., *Experimental investigation of different regimes of Mode-locking in a high repetition rate passively mode-locked semiconductor quantum-dot laser.* Optics Express, 2009. **17**(8): p. 6258-6267.
98. Cheng, H.-C. and Lee, C.-P., *Investigation of quantum dot passively mode-locked lasers with excited-state transition.* Optics Express, 2013. **21**(22): p. 26113-26122.
99. Arahira, S. and Ogawa, Y., *Repetition-frequency tuning of monolithic passively mode-locked semiconductor lasers with integrated extended cavities.* Quantum Electronics, IEEE Journal of, 1997. **33**(2): p. 255-264.
100. Kuntz, M., Fiol, G., Laemmlin, M., Meuer, C., and Bimberg, D., *High-Speed Mode-Locked Quantum-Dot Lasers and Optical Amplifiers.* Proceedings of the IEEE, 2007. **95**(9): p. 1767-1778.
101. Liu, H.F., Arahira, S., Kunii, T., and Ogawa, Y., *Frequency-tunable millimetre-wave signal generation using a monolithic passively mode-locked semiconductor laser.* Electronics Letters, 1996. **32**(8): p. 740-741.
102. Kuntz, M., Fiol, G., and Laemmlin, M., *High-Speed Mode-Locked Quantum-Dot Lasers and Optical Amplifiers.* 2007.
103. Camacho, F., Avrutin, E.A., Bryce, A.C., and Marsh, J.H. *Modelocking frequency tunability and timing jitter in an extended cavity mode-locked semiconductor laser*. in *Lasers and Electro-Optics Society Annual Meeting, 1997. LEOS '97 10th Annual Meeting. Conference Proceedings., IEEE*. 1997. San Francisco, CA. p. 207-208.
104. Murata, S., Tomita, A., and Suzuki, A., *Influence of free carrier plasma effect on carrier-induced refractive index change for quantum-well lasers.* Photonics Technology Letters, IEEE, 1993. **5**(1): p. 16-19.
105. Kuhn, K.J., Iyengar, G.U., and Yee, S., *Free carrier induced changes in the absorption and refractive index for intersubband optical transitions in $Al_xGa_{1-x}As/GaAs/Al_xGa_{1-x}As$ quantum wells.* Journal of Applied Physics, 1991. **70**(9): p. 5010-5017.
106. Miller, D.A.B., Chemla, D.S., Damen, T.C., Wood, T.H., Burrus, C.A., Gossard, A.C., and Wiegmann, W., *Band-edge electroabsorption in quantum well structures - The quantum-confined Stark effect.* Physical Review Letters, 1984. **53**: p. 2173-2176.
107. Huang, X., Stintz, A., Li, H., Rice, A., Liu, G.T., Lester, L.F., Cheng, J., and Malloy, K.J., *Bistable operation of a two-section 1.3 μm InAs quantum dot laser-absorption saturation and the quantum confined Stark effect.* Quantum Electronics, IEEE Journal of, 2001. **37**(3): p. 414-417.
108. Mokkapati, S. and Jagadish, C., *III-V compound SC for optoelectronic devices.* Materials Today, 2009. **12**(4): p. 22-32.
109. Juodawlkis, P.W.O.D., Frederick J.; Bailey, Robert J.; Plant, Jason J.; Ray, Kevin G.; Oakley, Douglas C.; Napoleone, Antonio; Watts, Michael R.; Betts, Gary E., *InGaAsP/InP quantum-well electrorefractive modulators with sub-volt $V\pi$.* Proceedings of the SPIE, 2004. **5435**: p. 53-63.
110. Kunimatsu, D., Arahira, S., Kato, Y., and Ogawa, Y., *Passively mode-locked laser diodes with bandgap-wavelength detuned saturable absorbers.* Photonics Technology Letters, IEEE, 1999. **11**(11): p. 1363-1365.

111. Stolarz, P.M., Javaloyes, J., Mezosi, G., Hou, L., Ironside, C.N., Sorel, M., Bryce, A.C., and Balle, S., *Spectral Dynamical Behavior in Passively Mode-Locked Semiconductor Lasers.* Photonics Journal, IEEE, 2011. **3**(6): p. 1067-1082.
112. Xiao-Qiong, Q. and Jia-Ming, L., *Photonic Microwave Applications of the Dynamics of Semiconductor Lasers.* Selected Topics in Quantum Electronics, IEEE Journal of, 2011. **17**(5): p. 1198-1211.
113. Novak, D., Ahmed, Z., Waterhouse, R.B., and Tucker, R., *Signal generation using pulsed semiconductor lasers for application in millimeter-wave wireless links.* Microwave Theory and Techniques, IEEE Transactions on, 1995. **43**(9): p. 2257-2262.
114. Avrutin, E.A., Marsh, J.H., and Portnoi, E.L., *Monolithic and multi-gigahertz mode-locked semiconductor lasers: constructions, experiments, models and applications.* Optoelectronics, IEE Proceedings, 2000. **147**(4): p. 251-278.
115. Karin, J.R., Helkey, R.J., Derickson, D.J., Nagarajan, R., Allin, D.S., Bowers, J.E., and Thornton, R.L., *Ultrafast dynamics in field-enhanced saturable absorbers.* Applied Physics Letters, 1994. **64**(6): p. 676-678.
116. Yang, W. and Gopinath, A., *Study of passive mode locking of semiconductor lasers using time-domain modeling.* Applied Physics Letters, 1993. **63**(20): p. 2717-2719.
117. Berger, L.I., *Semiconductor Materials*. 1996, United States: Taylor & Francis Inc. p. 139.
118. Cataluna, M.A., Malins, D.B., Gomez-Iglesias, A., Sibbett, W., Miller, A., and Rafailov, E.U., *Temperature dependence of electroabsorption dynamics in an InAs quantum-dot saturable absorber at 1.3 µm and its impact on mode-locked quantum-dot lasers.* Applied Physics Letters, 2010. **97**(12): p. 121110.
119. Agrawal, G.P. and Olsson, N.A., *Self-phase modulation and spectral broadening of optical pulses in semiconductor laser amplifiers.* IEEE Journal of Quantum Electronics, 1989. **25**(11): p. 2297-2306.
120. Varshni, Y.P., *Temperature dependence of the energy gap in semiconductors.* Physica, 1967. **34**(1): p. 149-154.
121. Xingsheng, L., Hu, M.H., Caneau, C.G., Bhat, R., and Chung-En, Z., *Thermal management strategies for high power semiconductor pump lasers.* IEEE Transactions on Components and Packaging Technologies, 2006. **29**(2): p. 268-276.
122. Kaiser, W. and Garrett, C.G.B., *Two-Photon Excitation in $CaF_2:Eu^{2+}$*. Physical Review Letters, 1961. **7**(6): p. 229-231.
123. Rulliere, C., *Femtosecond Laser Pulses*. 2 ed. Advanced Texts in Physics. 2005: Springer-Verlag New York. p. 185-195.
124. Kane, D.J. and Trebino, R., *Characterization of arbitrary femtosecond pulses using frequency-resolved optical gating.* IEEE Journal Of Quantum Electronics, 1993. **29**(2): p. 571-579.
125. Ranka, J.K., Gaeta, A.L., Baltuska, A., Pshenichnikov, M.S., and Wiersma, D.A., *Autocorrelation measurement of 6-fs pulses based on the two-photon-induced photocurrent in a GaAsP photodiode.* Optics Letters, 1997. **22**(17): p. 1344-1346.
126. Dudley, J.M., Reid, D.T., Sibbett, W., Barry, L.P., Thomsen, B., and Harvey, J.D., *Commercial Semiconductor Devices for Two Photon Absorption Autocorrelation of Ultrashort Light Pulses.* Applied Optics, 1998. **37**(34): p. 8142-8144.
127. Inc., T. *High-Speed Free-Space Detectors: Graphs*. 2016; Available from: https://www.thorlabs.de/newgrouppage9.cfm?objectgroup_id=7537.
128. Tourrenc, J.P., O'Donoghue, S., Todaro, M.T., Hegarty, S.P., Flynn, M.B., Huyet, G., McInerney, J.G., O'Faolain, L., and Krauss, T.F., *Cross-Correlation Timing Jitter*

Measurement of High Power Passively Mode-Locked Two-Section Quantum-Dot Lasers. Photonics Technology Letters, IEEE, 2006. **18**(21): p. 2317-2319.

129. Newbury, N.R., Coddington, I., and Swann, W.C., Optical frequency comb-based coherent LIDAR, US20110285980 A1, 2013
130. Balling, P., Křen, P., Mašika, P., and Berg, S.A.v.d., *Femtosecond frequency comb based distance measurement in air.* Optics Express, 2009. **17**(11): p. 9300-9313.
131. Cui, M., Zeitouny, M.G., Bhattacharya, N., van den Berg, S.A., Urbach, H.P., and Braat, J.J.M., *High-accuracy long-distance measurements in air with a frequency comb laser.* Optics Letters, 2009. **34**(13): p. 1982-1984.
132. Malitson, I.H., *Interspecimen Comparison of the Refractive Index of Fused Silica*,†.* Journal of the Optical Society of America, 1965. **55**(10): p. 1205-1209.
133. Zhang, H., Wei, H., Wu, X., Yang, H., and Li, Y., *Absolute distance measurement by dual-comb nonlinear asynchronous optical sampling.* Optics Express, 2014. **22**(6): p. 6597-6604.
134. CoddingtonI, Swann, W.C., NenadovicL, and Newbury, N.R., *Rapid and precise absolute distance measurements at long range.* Nat Photon, 2009. **3**(6): p. 351-356.
135. Wu, H., Zhang, F., Liu, T., Meng, F., Li, J., and Qu, X., *Absolute Distance Measurement Using Optical Sampling by Cavity Tuning.* IEEE Photonics Technology Letters, 2016. **28**(12): p. 1275-1278.
136. Wu, H., Zhang, F., Liu, T., Balling, P., Li, J., and Qu, X., *Long distance measurement using optical sampling by cavity tuning.* Optics Letters, 2016. **41**(10): p. 2366-2369.
137. Derickson, D.J., Helkey, R.J., Mar, A., Karin, J.R., Wasserbauer, J.G., and Bowers, J.E., *Short pulse generation using multisegment mode-locked semiconductor lasers.* IEEE Journal of Quantum Electronics, 1992. **28**(10): p. 2186-2202.
138. Thompson, M.G., A.R.Rae, M.X., Penty, R.v., and White, I.H., *InGaAs Quantum-Dot Mode-Locked Laser Diodes.* IEEE Journal of Selected Topics in Qunatum Elecctronics, 2009. **15**(3): p. 661-672.
139. Rafailov, E.U., Cataluna, M.A., and Avrutin, E.A., *Ultrafast lasers based on quantum dot structures : physics and devices*. 2011, Weinheim, Germany: Wiley-VCH.
140. Lin, C.Y., Grillot, F., Li, Y., Raghunathan, R., and Lester, L.F., *Microwave Characterization and Stabilization of Timing Jitter in a Quantum-Dot Passively Mode-Locked Laser via External Optical Feedback.* IEEE Journal of Selected Topics in Quantum Electronics, 2011. **17**(5): p. 1311-1317.
141. Jiang, L.A., Wong, S.T., Grein, M.E., Ippen, E.P., and Haus, H., *Measuring timing jitter with optical cross correlations.* Quantum Electronics, IEEE Journal of, 2002. **38**(8): p. 1047-1052.
142. Kefelian, F., O'Donoghue, S., Todaro, M.T., McInerney, J.G., and Huyet, G., *RF Linewidth in Monolithic Passively Mode-Locked Semiconductor Laser.* Photonics Technology Letters, IEEE, 2008. **20**(16): p. 1405-1407.
143. Zhao, X., Zheng, Z., Liu, L., Wang, Q., Chen, H., and Liu, J., *Fast, long-scan-range pump-probe measurement based on asynchronous sampling using a dual-wavelength mode-locked fiber laser.* Opt Express, 2012. **20**(23): p. 25584-25589.
144. Granados, E., Fuerbach, A., Coutts, D.W., and Spence, D.J., *Asynchronous cross-correlation for weak ultrafast deep ultraviolet laser pulses.* Applied Physics B, 2009. **97**(4): p. 759-763.
145. Potvin, S., Boudreau, S., Deschênes, J.D., and Genest, J., *Fully referenced single-comb interferometry using optical sampling by laser-cavity tuning.* Applied Optics, 2013. **52**(2): p. 248-255.

146. Briles, T.C., Yost, D.C., Cingöz, A., Ye, J., and Schibli, T.R., *Simple piezoelectric-actuated mirror with 180 kHz servo bandwidth.* Optics Express, 2010. **18**(10): p. 9739-9746.
147. Moskalenko, V., Williams, K.A., and Bente, E.A.J.M., *Pulse Narrowing and RF Linewidth Reduction of Integrated Passively Mode-Locked Laser in Anticolliding Design by Means of Spectral Tuning.* IEEE Photonics Journal, 2016. **8**(4): p. 1-10.
148. *High-speed THz Spectrometer | Menlo Systems*. 2014; Available from: http://www.menlosystems.com/products/thz-time-domain-solutions/tera-oscat/.
149. Potvin, S., Deschênes, J.-D., and Genest, J., *Optical Sampling by Laser Cavity Tuning with a Highly Varying Laser Cavity Length.* CLEO: 2013 (2013), paper CTu2I.4, 2013.
150. Wilk, R., Kocur, S., Hochrein, T., Mei, M., and Holzwarth, R. *Imaging with THz OSCAT spectrometer*. 2011.
151. Elzinga, P.A., Lytle, F.E., Jian, Y., King, G.B., and Laurendeau, N.M., *Pump/Probe Spectroscopy by Asynchronous Optical Sampling.* Applied Spectroscopy, Vol. 41, Issue 1, pp. 2-4, 1987.
152. Zhao, X., Zheng, Z., Liu, L., Wang, Q., Chen, H., and Liu, J., *Fast, long-scan-range pump-probe measurement based on asynchronous sampling using a dual-wavelength mode-locked fiber laser.* Optics Express, Vol. 20, Issue 23, pp. 25584-25589, 2012.
153. Dekorsy, T., Klatt, G., Gebs, R., Janke, C., and Bartels, A. *Asynchronous optical sampling with GHz repetition rate femtosecond lasers for high precision terahertz spectroscopy*. 2011.
154. Yasui, T., Iyonaga, Y., Hsieh, Y.D., Sakaguchi, Y., Yokoyama, S., Inaba, H., Minoshima, K., and Araki, T. *Frequency-swept asynchronous-optical-sampling THz time-domain spectroscopy*. 2012.
155. Yasui, T., Iyonaga, Y., Hsieh, Y.D., Inaba, H., Minoshima, K., Yokoyama, M., Araki, T., and Hashimoto, M. *Frequency-swept asynchronous-optical-sampling terahertz time-domain spectroscopy*. 2013.
156. *Asynchronous Optical Sampling System | Menlo Systems*. 2014; Available from: http://www.menlosystems.com/products/synchronization-stabilization-and-asops-systems/asops/.
157. Schliesser, A., Brehm, M., Keilmann, F., and van der Weide, D., *Frequency-comb infrared spectrometer for rapid, remote chemical sensing.* Optics Express, 2005. **13**(22): p. 9029-9038.
158. Bartels, A., Thoma, A., Janke, C., Dekorsy, T., Dreyhaupt, A., Winnerl, S., and Helm, M. *High-Resolution THz Spectrometer with kHz Scan Rates*. in *Conference on Lasers and Electro-Optics/Quantum Electronics and Laser Science Conference and Photonic Applications Systems Technologies*. 2006. Long Beach, California: Optical Society of America. p. CMCC6.
159. Bruchhausen, A., Lloyd-Hughes, J., Hettich, M., Gebs, R., Grossmann, M., Ristow, O., Bartels, A., Fischer, M., Beck, M., Scalari, G., et al., *Investigation of coherent acoustic phonons in terahertz quantum cascade laser structures using femtosecond pump-probe spectroscopy.* Journal of Applied Physics, 2012. **112**(3): p. 033517-033517-033518.
160. Schubert, M., Grossmann, M., Ristow, O., Hettich, M., Bruchhausen, A., Barretto, E.C.S., Scheer, E., Gusev, V., and Dekorsy, T., *Spatial-temporally resolved high-frequency surface acoustic waves on silicon investigated by femtosecond spectroscopy.* Appl. Phys. Lett, 2012. **101**.

161. Gebs, R., Klopp, P., Klatt, G., Dekorsy, T., Griebner, U., and Bartels, A. *THz Time-Domain Spectrometer Based on Asynchronous Optical Sampling with a Femtosecond Semiconductor Disk Laser*. in *Conference on Lasers and Electro-Optics 2010*. 2010. San Jose, California: Optical Society of America. p. CMZ6.
162. Gebs, R., Klatt, G., Schafer, H., Dekorsy, T., and Bartels, A. *Sub-100 fs time-domain spectroscopy using high-speed ASOPS*. in *Lasers and Electro-Optics 2009 and the European Quantum Electronics Conference. CLEO Europe - EQEC 2009. European Conference on*. 2009. p. 1-1.
163. Gebs, R., Klatt, G., Janke, C., Dekorsy, T., and Bartels, A. *Sub-50 fs time-domain spectroscopy using high-speed ASOPS*. 2010.
164. Nose, M., Kawamoto, K., Ihara, A., Inaba, H., Minoshima, K., Araki, T., and Yasui, T. *Fiber-based, asynchronous optical sampling terahertz time-domain spectroscopy system*. 2009.
165. Bartels, A., Cerna, R., Kistner, C., Thoma, A., Hudert, F., Janke, C., and Dekorsy, T., *Ultrafast time-domain spectroscopy based on high-speed asynchronous optical sampling.* Review of Scientific Instruments, 2007. **78**(3).
166. Tauser, F., Rausch, C., Posthumus, J.H., and Lison, F. *Electronically controlled optical sampling using 100 MHz repetition rate fiber lasers*. 2008.
167. Kim, Y. and Yee, D.-S., *High-speed terahertz time-domain spectroscopy based on electronically controlled optical sampling.* Optics Letters, 2010. **35**(22): p. 3715-3717.
168. Kray, S., Spoler, F., Hellerer, T., and Kurz, H., *Electronically controlled coherent linear optical sampling for optical coherence tomography.* Opt Express, 2010. **18**(10): p. 9976-9990.
169. Liu, J., Mbonye, M.K., Mendis, R., and Mittleman, D.M. *Measurement of Terahertz Pulses Using Electronically Controlled Optical Sampling (ECOPS)*. in *Conference on Lasers and Electro-Optics 2010*. 2010. San Jose, California: Optical Society of America. p. JWA107.
170. Towe, E., *Heterogeneous Optoelectronic Integration*. 2000, United States: SPIE Publications p. 8.
171. Feder, R. and Light, T., *Precision Thermal Expansion Measurements of Semi-insulating GaAs.* Journal of Applied Physics, 1968. **39**(10): p. 4870-4871.